Durham E-Theses

Electrical and magnetic properties of n-Cd(_1-x)Mn(_x) Te close to the metal-insulator transition

Read, Daniel Edward

How to cite:

Read, Daniel Edward (2001) *Electrical and magnetic properties of n-Cd(_1-x)Mn(_x) Te close to the metal-insulator transition*, Durham theses, Durham University. Available at Durham E-Theses Online: http://etheses.dur.ac.uk/3783/

Use policy

The full-text may be used and/or reproduced, and given to third parties in any format or medium, without prior permission or charge, for personal research or study, educational, or not-for-profit purposes provided that:

- a full bibliographic reference is made to the original source
- a link is made to the metadata record in Durham E-Theses
- the full-text is not changed in any way

The full-text must not be sold in any format or medium without the formal permission of the copyright holders.

Please consult the full Durham E-Theses policy for further details.

Academic Support Office, Durham University, University Office, Old Elvet, Durham DH1 3HP
e-mail: e-theses.admin@dur.ac.uk Tel: +44 0191 334 6107
http://etheses.dur.ac.uk

Electrical and Magnetic Properties of n-$Cd_{1-x}Mn_xTe$ Close to the Metal-Insulator Transition

The copyright of this thesis rests with the author.
No quotation from it should be published without
his prior written consent and information derived
from it should be acknowledged.

Daniel Edward Read

University of Durham 2001

A thesis submitted in partial fulfilment of the requirements for the degree of doctor of philosophy

17 SEP 2002

Abstract

Electrical transport and magnetic measurements have been made on n-$Cd_{1-x}Mn_xTe$ ($0.047 < x < 0.197$) for samples doped with In or In,Al. Results are presented for measurements made as a function of temperature ($40\ mK < T < 300\ K$), applied magnetic field ($0\ T < B < 6\ T$) and photogenerated carrier density.

Low field magnetic susceptibility measurements have identified a transition from a paramagnetic phase to a spin glass phase at low temperatures. The measured temperature dependence of the magnetic susceptibility is consistent with a cluster glass model. Measurements of the spin glass freezing temperature have been carried out on four samples having different Mn fractions The results obtained are in agreement with the limited number of previous measurements on nominally undoped samples. At low temperatures photo-induced changes in magnetism have been measured in both the paramagnetic and the spin glass phase. The change in magnetisation on illumination is due to an increased number of bound magnetic polarons formed around quasi localised s-spins. High temperature susceptibility measurements have been used to examine the parameters characterising the paramagnetic phase, and their variation with Mn fraction.

Electrical transport measurements at very low temperatures ($T < 800\ mK$) have shown a strong temperature dependent electron localisation. This has resulted in the confirmation of insulating behaviour in a sample ($x = 0.047$) having $n > n_c$. At low temperatures and in zero field an activated form of the conductivity is observed. In applied magnetic fields ($B > 50\ mT$) Efros-Shklovskii variable range hopping is observed in the insulating phase. These results are attributed to the formation of a hard gap in the density of states, having a magnetic origin. At higher fields an insulator-metal phase transition occurs. In the metallic phase the conductivity can be described by a quantum correction to the zero temperature conductivity due to the effect of electron-electron interactions. Results obtained before and after illumination are consistent with scaling theory of electron localisation, having a critical exponent close to unity, indicative of the importance of electron-electron interactions. A reduction in the value of the critical field is seen after increasing the carrier density ($B_c = 2.0$ and $1.3\ T$ for $n = 3.3 \times 10^{17}\ cm^{-3}$ and $3.8 \times 10^{17}\ cm^{-3}$ respectively).

At low temperatures an anisotropy in the resistivity has been measured for samples in the spin glass phase. Magnetoresistance measurements have shown results consistent with previous measurements, in addition to a large, low field component that is attributed to the effect of magnetic field on electrons in the variable range hopping regime.

Declaration

I hereby declare that this thesis is original and that no part of it has been submitted previously for a degree at this or any other university. All work presented in this thesis is my own unless otherwise stated. This thesis is within the word limit set by the examining body.

The copyright of this thesis rests with the author. No quotation from it should be published without their prior written consent and information derived from it should be acknowledged.

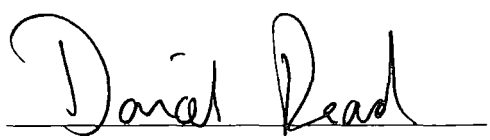

Copyright © 2001 Daniel Read

Acknowledgements

I would like to take this opportunity to thank some of the many people that have helped and assisted me throughout my postgraduate studies in Durham.

In this time two departmental heads (Prof B K Tanner & Prof M R Pennington) have provided the excellent facilities and resources that I have utilised.

I wish to thank Chris Ottley from Durham university department of geological sciences for his help with mass spectroscopy and Andrew Yates from the physics department for his time and assistance with EDAX measurements. Also Pauline Russel from the physics department has provide a number of the line drawings included in this thesis.

I wish to extend my warmest thanks to John Dobson for (amongst other things!) his fine technical assistance. He has helped me out of a tricky situation on more than one occasion and there is no object that this man cannot retrieve from the inside of a helium dewar!

Over a period of many years I have been lucky enough to have benefited from many fruitful discussions with Dr Chris Leighton (Some of which have related to the physics!). I would like to thank him for his friendship, continual support and interest in the work.

I am extremely grateful to my PhD supervisor Dr Ian Terry for his patient assistance during my time in Durham, his enthusiasm for the subject has made working with him a stimulating and enjoyable experience. In addition, his help and support since I have left Durham has been invaluable.

Over the past years I have met many good friends and colleagues, a selection of these are listed below (in no particular order!),

In Durham, Gwyn Ashcroft, Amir Rozatian, Stuart Dailey, Susan Roy, Gordon Irvine, Marek Szablewski, Phil Hands, David Unit, Adrian Sneary, Nigel Leigh, David Taylor, Nicola Morley, Simon Keys, Tom Hase, Stuart Wilkins, Hugh Jars, Neil Parkinson, James Buchanan, Damian Hampshire, Peter Hatton, Andy Brinkman, Ken Durose, Lydia Heck, David Stockdale, Andrew Hunter, Mike Cousins, Paul Edwards, Phil Amstrong, Steve Lishman, Peter Luke, Malcom Robertshaw, Kevin McGee, Chris Cavagin, Ian Milne, Ken Parkin, George Teasdale, Ian Manfren, Wayne Dobby, Paul Foley, Matt Carrick, Clive Doloughan, Norman Thompson, David Patterson, John Scott, Tom Jackson, Chris Mullaney, Chris Moore, Tom Adamson, Vicki Greener, Mike Lee, Pat Monkhouse, Penny Carse, Linda Wilkinson, Julie Bell, Angela Healer, Claire Davies, Joanne Palister, Rebbeca Dunn, Samantha Dunn, Sharon Fairless.

In Bayreuth, Girgl Eska, Reinhard Konig, Thomas Herrmansdorfer, Alex Schindler, Evgeny Navaretski, Likrougo Hrikstakos, Herbert Gotz, Kai Taubenreuther, Christine Linser.

In particular I would like to acknowledge the good doctors from number 54 John Clarke, Steven Moss and Ian Clarkson who along with the hospitality of Michael and co have provided many entertaining evenings out of the lab. Also, Andrea Li Bassi, Sarah Woodland, Brian Fulthorpe, Sean Giblin have been particularly supportive during (and

after) my time in Durham. In addition many residents of Hastings Avenue (both past and present) have also helped me out, when I was just starting out Ian Daniel gave a great deal of assistance, the Swinhoe's, Michael and Rachel have both offered support and helped me out in different ways. Most recently Nancy-Ann Hackman has been a great friend at one of the toughest times during my PhDstudies, I very much appreciate it.

Last but not least I wish to thank my parents and Chris, who have helped me out during this time in ways too numerous to mention.

I am extremely grateful to all of the above, thanks.

Contents

1	Introduction	1
1.1	Introduction and Motivation	1
1.2	Layout of Following Chapters	3
1.3	References	5
2	Introduction to the Physics of Dilute Magnetic Semiconductors	6
2.1	Crystal Structure of Dilute Magnetic Semiconductors	7
2.2	Basic Theory of Semiconductors	10
2.3	Basic Theory of Magnetism	16
2.3.1	Diamagnetism	16
2.3.2	Paramagnetism	17
2.3.3	Pauli Paramagnetism	19
2.3.4	Ferromagnetism, Antiferromagnetism and Ferrimagnetism	20
2.4	Persistent Photoconductivity	22
2.4.1	Persistent Photoconductivity due to DX Centres	23
2.5	References	27
3	Magnetism and Electrical Transport Close to the Metal-Insulator Phase Transition	29
3.1	Magnetic Properties of Dilute Magnetic Semiconductors	29
3.1.1	Paramagnetic Phase	30
3.1.2	Spin-Glass Phase	32
3.1.3	Antiferromagnetic Phase	35
3.1.4	Bound Magnetic Polarons	35
3.1.5	Photomagnetism	37
3.2	Metal-Insulator Phase Transition in Doped Semiconductors	39
3.2.1	Introduction and History	39
3.2.2	Theory	40
3.2.2.1	Mott Transition	40
3.2.2.2	Anderson Localization	41
3.2.2.3	Scaling Theory of Electron Localization	44
3.2.3	Experiment	47
3.2.3.1	Discretely Doped Samples	48
3.2.3.2	Stress Tuning	50
3.2.3.3	Field Tuning	51
3.2.3.4	Fine Tuning Using Persistent Photoconductivity	51
3.2.3.5	Open Questions	52
3.3	Electrical Properties of Dilute Magnetic Semiconductors	53
3.3.1	The Insulating Side of the Metal Insulator Transition – Hopping Conduction	53
3.3.1.1	Nearest Neighbour Hopping (NNH)	55
3.3.1.2	Variable Range Hopping (VRH)	56
3.3.2	The Metallic Side of the Metal Insulator Transition – Quantum Corrections to the Conductivity	58
3.3.3	Magnetoresistance in Dilute Magnetic Semiconductors	60
3.3.3.1	Magnetoresistance in the Hopping Regime	61
3.3.3.2	Magnetoresistance in the Weakly Localized Regime	62
3.3.3.3	Magnetoresistance of Dilute Magnetic Semiconductors	62
3.4	References	66

4	Experimental Details	71
4.1	Sample Growth and Preparation	71
4.2	Compositional Analysis of Samples Studied	73
4.3	Electrical Measurements	75
4.3.1	Experimental Details of Electrical Measurements	75
4.3.2	Details of Bayreuth Dilution Refrigerator	79
4.3.3	Effect of Strain on Samples During Cooldown	82
4.3.4	Helium-4 Measurement Systems	83
4.4	Magnetic Measurements	86
4.4.1	Basic Principle of Operation of a SQUID	86
4.4.1.1	dc SQUID	86
4.4.1.2	rf SQUID	88
4.4.2	Low Temperature SQUID Measurements	89
4.4.3	High Temperature SQUID Measurements	93
4.4.4	Vibrating Sample Magnetometer Measurements	94
4.5	References	96
5	Results of Magnetic Measurements	97
5.1	Introduction	97
5.2	Electrical Characterisation and Compositional Analysis of Samples Used for Magnetic Measurements	97
5.3	High Temperature Magnetic Measurements	99
5.4	Low Temperature Magnetic Measurements	107
5.4.1	Spin Glass Phase Transition	108
5.4.2	Photo-Induced Changes in Magnetism	114
5.5	Summary and Conclusions	123
5.6	References	124
6	Results of Electrical Measurements Close to the Metal-Insulator Transition	127
6.1	Introduction	127
6.2	High Temperature Measurements	128
6.3	Low Temperature Electrical Measurements as a Function of Illumination	135
6.4	Field Tuning the Metal-Insulator Transition	146
6.4.1	Dark Data	146
6.4.2	Saturation Illumination	152
6.5	Temperature Dependence of Low Temperature Anisotropy Ratio	157
6.6	Magnetoresistance	163
6.6.1	Magnetoresistance Close to the Metal Insulator Phase Transition	163
6.6.2	Low Field Negative Magnetoresistance	167
6.7	Summary and Conclusions	172
6.8	References	173
7	Conclusions	177
7.1	Concluding Remarks	177
7.2	Future Work	179
	Appendix A	180

1 Introduction

1.1 Introduction and Motivation

For many decades now studies of magnetic semiconductors (both dilute and concentrated systems) have been carried out by a large number of workers around the world. Initially II-VI materials (including those containing Mn) were among the most widely studied. Of the II-VI material systems, CdMnTe is arguably the most extensively studied, although PbSnMnTe is also noteworthy as the first II-VI dilute magnetic semiconductor to be shown to exhibit ferromagnetism [1]. More recently however III-V materials have also been examined as it was shown to be possible to obtain ferromagnetism with relatively high Curie temperatures in these materials [2]. Despite the obvious technological importance of these III-V DMS, II-VI materials have remained important, not least because they offer excellent systems in which to study basic physics. One such topic, which is of great interest, is the metal insulator transition (MIT). Again a greatly studied and hotly debated subject the MIT has remained relatively poorly understood, particularly in systems containing magnetic ions.

The work contained in this thesis relates to a continuing study of the metal insulator phase transition in a dilute magnetic semiconducting system. A previous study of the MIT in CdMnTe:In [3] was limited to relatively high temperatures, and thus there remained some unanswered question relating to the nature of the MIT in this particular material. Making electrical and magnetic measurements to lower temperatures, we aim to identify more important details of the mechanisms at work in this system close to the MIT. In addition to the MIT the transport properties of these materials at very low temperatures has only been examined a few times by other workers [4] and these are still relatively poorly understood.

Another subject of great interest is related to the effect of itinerant carriers (electrons in the case of CdMnTe:In) on the magnetism of the material. Currently experimental and theoretical work is being carried out on many III-V and other DMS in order to explore the area of carrier induced ferromagnetism [5].
In CdMnTe [6] and previously in other materials [7] the important role played by bound magnetic polarons has been observed. Formation of bound magnetic polarons is directly

related to the strong exchange interaction between local manganese moments and free carrier spins. In this thesis we present data obtained from magnetic measurements at different carrier densities generated utilising persistent photoconductivity. The dc magnetic measurements presented in this thesis have been obtained as low as helium-3 temperatures. This is far beyond the base temperature of most commercial magnetometers, and the challenge of obtaining data in this regime is reflected in the very small number of such previous studies. To our knowledge only one previous study [8] measured the dc magnetic properties of nominally undoped CdMnTe to comparably low temperatures. Here we present data on heavily doped n-type samples measured using a SQUID system. Such measurements have afforded us the opportunity to examine the transition from a paramagnetic to a spin glass phase at low temperatures, and thus for samples having low manganese concentrations.

Having identified the existence of a spin glass phase we can then relate the observed effects resulting from transport measurements to the samples magnetism. In many cases we have both electrical transport and magnetic data for the same sample. In particular a subject ignored by many authors is the behaviour of magnetic polarons in a spin glass phase. Clearly this is an extremely complicated situation and the experimental data is very limited. We report the observation of a very low temperature anisotropy in the resistivity and one possible explanation for this could be the dynamics of magnetic polarons in the spin glass phase. Again to our knowledge a similar anisotropy has not been previously observed or reported.

1.2 Layout of Following Chapters

In this section the layout of the subsequent chapters of this thesis will be outlined. We describe the contents of each chapter and the motivation behind the selection of material therein.

Chapter 2 is intended to introduce the reader to the material system studied in this thesis and the basic physics of dilute magnetic semiconductors (DMS). To this end we present first (section 2.1) details of the structure of DMS. Sections 2.2 and 2.3 introduce the basic physics of semiconducting materials and of magnetism respectively. In the last section of the chapter (2.4) the special property of persistent photoconductivity (PPC) is introduced. The relevance of PPC to the work contained in this thesis is highlighted.

Chapter 3 deals in greater detail with the theory of relevance to this work. Section 3.1 describes the magnetic properties specific to DMS. In section 3.2 we present a review of the theoretical ideas and the key experimental work carried on the metal insulator phase transition. After this, section 3.3 describes the theory and reviews some selected experimental results relating to the electrical transport properties of materials close to the MIT, focusing in particular on experiments relevant to DMS.

Chapter 4 examines the details of the experimental apparatus and procedures used for this study. Beginning (section 4.1) with details of the sample preparation. Next section 4.2 describes the methods used to ascertain the samples' composition. In sections 4.3 and 4.4 we describe the experimental details of the electrical and magnetic measurements respectively. In addition to presenting details of measurement systems that have been used and/or constructed we outlined the techniques employed to yield reliable and accurate results. This section is intended to inform the reader of the procedures used in order to obtain the data present in this thesis.

In the next two chapters the experimental data are presented and analysed. Chapter 5 is related to magnetic measurements made using two different SQUID systems on a number of different samples. Chapter 6 gives the results of detailed electrical transport measurements focusing on just one particular sample. Measurements were made in different ranges of temperature and magnetic field. Experimental data are analysed in terms of the observed field driven MIT. We comment on results that are in agreement

with previous work on the same or similar material systems. Where differences or unexpected results are obtained attempts are made to offer explanations for the observed effects that are consistent with the data presented.

Finally in chapter 7 we summarise and make concluding remarks about the results presented in previous chapters. In addition suggestions for important and relevant possible future work are outlined.

1.3 References

1. Story, T., *et al.*, *Carrier-Concentration Induced Ferromagnetism in PbSnMnTe.* Physical Review Letters, 1986. **56**(7): p. 777-779.
2. Ohno, H., *Making nonmagnetic semiconductors ferromagnetic.* Science, 1998. **281**(5379): p. 951-956.
3. Leighton, C., I. Terry, and P. Becla, *Metal-insulator transition in the persistent photoconductor $Cd_{1-x}Mn_xTe$: In.* Europhysics Letters, 1998. **42**(1): p. 67-72.
4. Dietl, T., *et al.*, *Interaction Effects Near the Metal-Insulator Transition in Semimagnetic Semiconductors*, in *Anderson Localization*, T. Ando and H. Fukuyama, Editors. 1987, Springer-Verlag. p. 58.
5. Munekata, H., *et al.*, *Light-induced ferromagnetism in III-V-based diluted magnetic semiconductor heterostructures.* Journal of Applied Physics, 1997. **81**(8): p. 4862-4864.
6. Leighton, C., I. Terry, and P. Becla, *Metallic conductivity near the metal-insulator transition in $Cd_{1-x}Mn_xTe$.* Physical Review B, 1998. **58**(15): p. 9773-9782.
7. von Molnar, S., *et al.*, *Local Magnetization and Magnetotransport in Magnetic Semiconductors.* Physica B, 1994. **197**(1-4): p. 151-157.
8. Novak, M.A., *et al.*, *Spin-Glass Behavior of $Cd_{1-x}Mn_xTe$ Below the Nearest-Neighbor Percolation Limit.* Journal of Applied Physics, 1985. **57**(8): p. 3418-3420.

2 Introduction to the Physics of Dilute Magnetic Semiconductors

Solid state magnetism and semiconductor physics are two of the most important areas of current research in condensed matter physics. These topics are of particular interest not only because of the great amount of basic research which is still ongoing, but also because of the enormous potential for new technology. The great importance of the semiconductor industry is clear from a wide range of currently available devices and applications, of course the most obvious example is that of silicon and it use in microelectronics. In addition to this, the use of magnetism in data storage devices and read/write head technology is providing interesting and commercially relevant research topics. In the overlap of these two areas there is currently a great deal of work carried out on magnetic semiconductors, and also dilute magnetic semiconductors (sometimes referred to as semimagnetic semiconductors). Since the late 1970's dilute magnetic semiconductors have provided physicists with an array of interesting magnetic and electrical transport properties to study. Recently magnetic semiconductors have received renewed attention as a result of work in the emerging field of spin-electronics, where the electron spin in addition to charge is utilised to provide new functionality.

In this chapter a basic introduction is given to both the crystal structure (section 2.1) of the II-VI materials and the basic physics of semiconductors (section 2.2) and magnetism (section 2.3). Finally section 2.4 gives a brief description and review of the work on persistent photoconductivity which is of relevance to the work contained in this thesis.

2.1 Crystal Structure of Dilute Magnetic Semiconductors

A dilute magnetic semiconductors (DMS) can be thought of as a solid solution of magnetic ions incorporated substitutionally into a non magnetic host. An overview of the entire family of Mn containing II-VI DMS is shown schematically in figure 2.1. The bold lines in the figure show the ranges of composition over which bulk samples can be produced. The label "cub" or "hex" indicates the crystal structures of the particular alloy to be zincblende or wurtzite respectively.

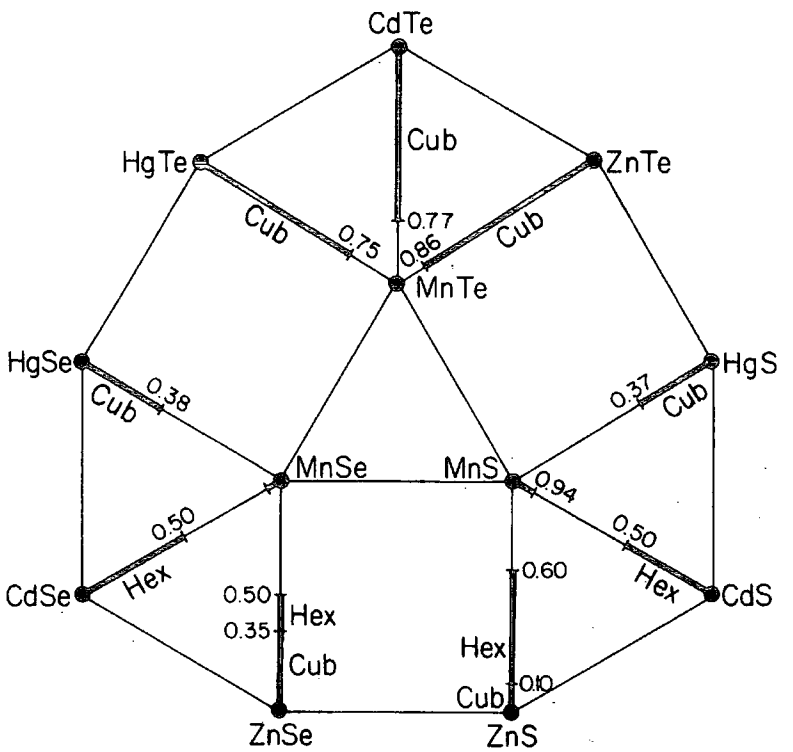

Figure 2.1 - Diagramatic overview of all Mn containing II-VI semiconductors.

Whilst the figure above gives a representative overview it should be noted that more recently higher concentrations of Mn have been incorporated into some of the systems using non-equilibrium growth techniques such as molecular beam epitaxy (MBE). One particular example is that of zincblende MnSe, which prior to successful growth by MBE [1] was only considered as a hypothetical crystal by extrapolation to x=1, MnSe normally crystallises with a rocksalt structure.

For the material of interest to the work contained in this thesis (namely $Cd_{1-x}Mn_xTe$) we can think of taking the non-magnetic semiconductor CdTe and replacing some fraction, x, of the Cd cations with Mn. As indicated in figure 2.1 bulk $Cd_{1-x}Mn_xTe$ forms with a

zincblende structure (two interpenetrating fcc lattices displaced from each other by one quarter of the body diagonal) up to manganese concentrations of approximately 77%. At higher Mn concentrations mixed phases can occur. It is interesting to note that the crystal structure remains as zincblende up to such high Mn concentrations despite the fact that MnTe itself has a Nickel Arsenide structure. Figure 2.2 below shows the zincblende crystal structure of $Cd_{1-x}Mn_xTe$.

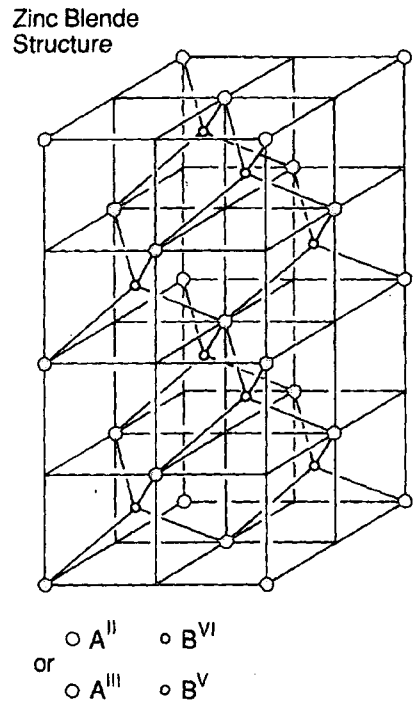

Figure 2.2 – Diagram representing the zinc blende crystal structure of $Cd_{1-x}Mn_xTe$ reproduced from [2].

In the parent material CdTe bonding is in a tetrahedral arrangement via four $s\text{-}p^3$ hybridised bonds ie two valence 5s electrons from Cd and six valence 5p electrons from Te. When Mn is substituted for Cd it contributes its $4s^2$ electrons to the $s\text{-}p^3$ bonding. Mn differs from group II elements by the fact that it has 5 unpaired electrons (with spins aligned parallel) in its 3d shell. It should be realised that energetically this is a rather stable situation as the energy required to add another electron (with by necessity opposite spin) is considerable. Thus in this respect the half filled d shell in Mn behaves very much like the completely filled $4d^{10}$ shell of Cd. Due to this Mn ions are incorporated into II-VI hosts more easily than other transition metals. By producing samples with different Mn concentrations (different values of x) it is possible to "tune" the associated material parameters such as, lattice parameter, semiconducting band gap, and also the degree of interaction between the randomly distributed magnetic ions,

which leads to the range of observed magnetic properties described later. The x dependence of the semiconductor band gap for $Cd_{1-x}Mn_xTe$ will be given in the following section (2.2) which deals with basic semiconductor theory.

The lattice parameter of all Mn containing II-VI DMS, having the general form $A_{1-x}Mn_xB$, very closely obeys Vegard's law and this is shown for the B ≡ Te compounds in figure 2.3.

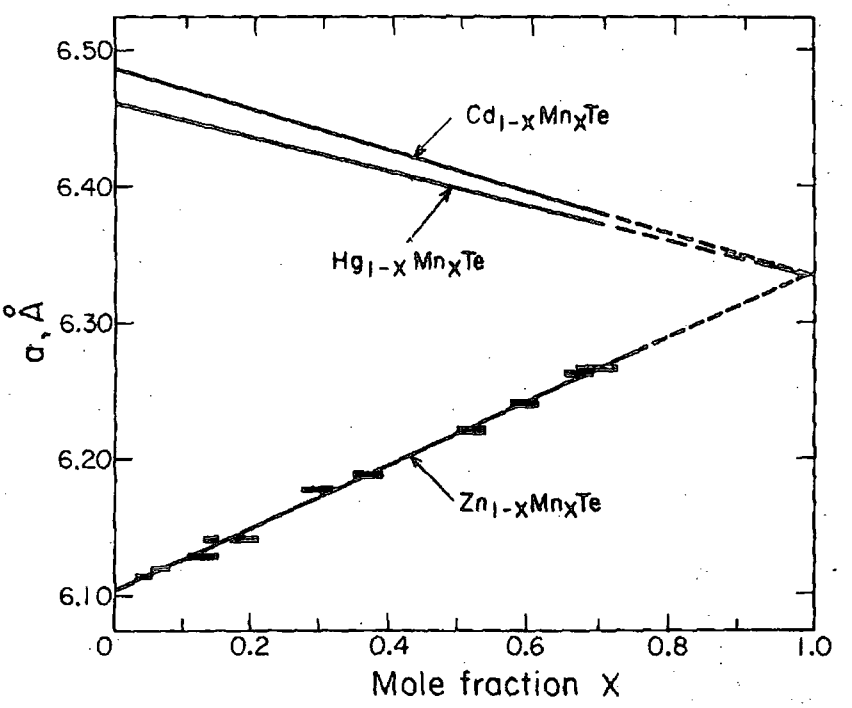

Figure 2.3 - Lattice parameter plotted against manganese fraction, x, for dilute magnetic semiconductors containing Mn and Te. After Furdyna [3].

For $Cd_{1-x}Mn_xTe$ we can express the x dependent lattice parameter with equation 2.1

$$a = (1-x)a_{CdTe} + xa_{MnTe} \qquad \textbf{Equation 2.1}$$

where a_{CdTe} is the lattice parameter of CdTe and a_{MnTe} is the lattice parameter of the hypothetical zinc blende MnTe. It should be noted that for the three compounds shown in figure 2.3 an extrapolation of Vegard's law to x = 1 gives the same value for a_{MnTe}. It has been shown using extended x-ray absorption fine structure (EXAFS) that the Cd-Te and Mn-Te bond lengths for $Cd_{1-x}Mn_xTe$ [4] remain approximately constant as a function of x. These EXAFS results, together with the strict adherence to Vegard's law observed with x-ray diffraction, indicates that the anion and cation sublattices are locally distorted in the vicinity of a Mn ion.

2.2 Basic Theory of Semiconductors

A semiconductor is a material that at T = 0 K has a completely filled valence band, separated from a completely empty conduction band by a region known as the semiconducting band gap (or forbidden gap). This band gap is a region of energy in which there are no electronic states, the gap is formed as a result of the periodicity of the crystal lattice. We can represent the energy bands of a semiconductor by a dispersion (or E-k) diagram which relates electron energy to wavevector, $k = \frac{p}{\hbar}$ an example is shown in below.

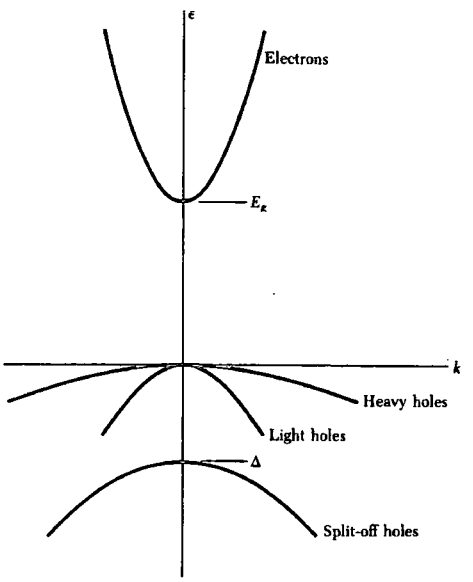

Figure 2.4 - Dispersion (or E-k) diagram for a direct gap semiconducting material.

Figure 2.4 above shows the simplified situation for a direct band gap semiconductor, that is the minimum in the conduction band (CB) energy and the maximum in the valence band (VB) energy coincide at the same point in reciprocal space. The energy of the CB edge with reference to the VB edge is described by,

$$E_c = E_g + \frac{\hbar^2 k^2}{2m_e^*} \qquad \textbf{Equation 2.2}$$

In the CB the energies are similar to the free electron result with the electron mass replaced by an effective mass, m_e^*. This effective mass describes the way in which an electron in a semiconductor responds to an applied electric field, and we define the

effective mass with equation 2.3, so we can see that the curvature of an E-k diagram is related to the effective mass.

$$m_e^* = \hbar^2 \left(\frac{\partial^2 E}{\partial k^2} \right)^{-1}$$ **Equation 2.3**

At finite temperatures conduction occurs via thermal activation of electrons from the VB to the CB across the band gap. The empty electronic state in the VB left behind by an electron is known as a "hole" and in many ways behaves very much like a positively charged carrier contributing to the conduction in a semiconducting material. In general the hole is characterised by its own effective mass given by a similar equation to equation 2.3 above. If the majority of free carriers in a semiconductor are electrons then the material is said to be n-type, conversely if holes dominate the conduction then the material is known as p-type

The size of the band gap is dependent on material properties, for example at room temperature for Si $E_g \sim 1.1$eV and for Ge $E_g \sim 0.75$eV. For $Cd_{1-x}Mn_xTe$ the size of the band gap is dependent on x with an approximately linear relationship, see figure 2.5.

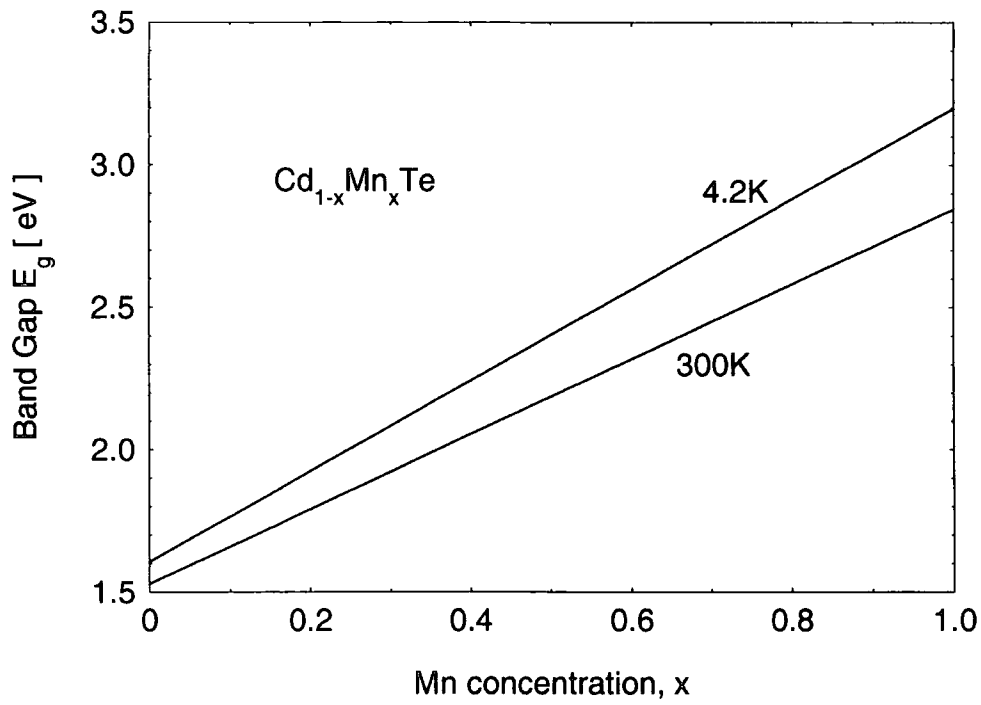

Figure 2.5 – Mn fraction, x, dependence of the semiconducting band gap, E_g, for $Cd_{1-x}Mn_xTe$ shown at 300 K and 4.2 K.

One of the most important parameters of a semiconducting material is the number of free electrons per unit volume in the CB band, n. For an intrinsic material at a temperature T this is given by,

$$n_i = 2\left(\frac{m_e^* k_B T}{2\pi\hbar^2}\right)^{3/2} \exp\left(\frac{-(E_g - E_f)}{k_B T}\right) \qquad \textbf{Equation 2.4}$$

A similar expression can be derived for the number of holes per unit volume in the VB. Most semiconductors that are widely used or studied (including the subject of this thesis work) are not intrinsic, but are in fact termed extrinsic semiconductors. This means that the pure material has had a number of impurities deliberately added in order to change its physical properties. This process of adding small amounts of impurities to semiconductors is known as doping. The result of doping a semiconductor material is to add allowed electronic states to the band gap. By carefully arranging the density and the energy of these impurity states it is possible to control accurately the electronic properties of a material. Indeed, it is due to our ability to carefully control the doping of silicon that a wide range of semiconductor based devices are available today. For the common example of silicon, which has four valence electrons and forms tetrahedral s-p^3 bonds, doping with P which has five valence electrons adds an impurity state just below CB edge. This impurity state can be relatively easily ionised adding an electron to the conduction band and hence increasing the conductivity. An impurity atom adding an electron to the CB is known as a donor impurity, in a similar way an impurity atom can remove an electron from (add a hole to) the VB, such dopants are called acceptors.

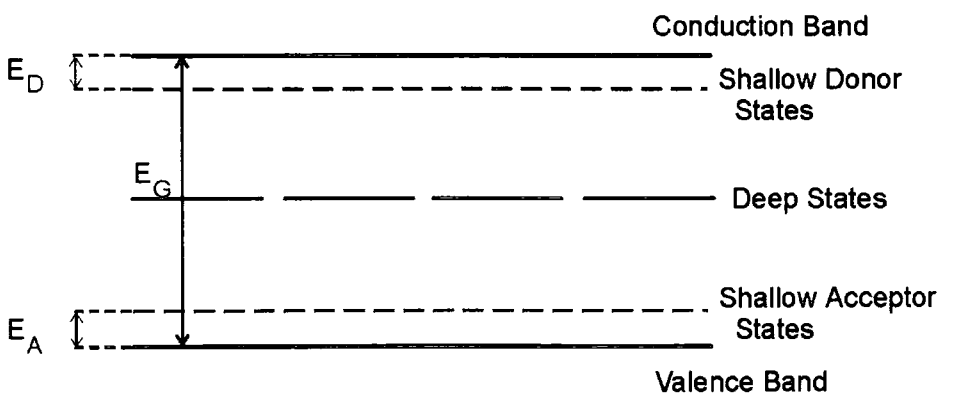

Figure 2.6 - Schematic diagram of a doped semiconductor showing position of donor and acceptor levels within the bandgap.

A schematic diagram showing the positions of deep and shallow impurity states in a doped semiconductor band gap is shown in figure 2.6. A semiconductor that contains

both donor and acceptor dopants is said to be compensated. We can define a dimensionless quantity called the compensation ratio $K = N_A / N_D$, where N_A is the concentration of acceptor atoms and N_D is the concentration of donor atoms.

The position of impurity states within the bandgap is dependent on the choice of dopant atom. Impurity states close to the CB or VB edges are termed shallow impurities, those with energy levels far inside the band gap are called deep states. The situation arising from deep states can be rather complicated (an example of a deep state in a semiconductor is the DX centre discussed in section 2.4) however for shallow impurity states we can estimate the ionization energy using hydrogenic theory. If we consider that the donor impurity atom (electron and positively charged nucleus) approximates to a neutral hydrogen atom then the energy associated with this electron state is calculated by modifying the Bohr theory of a hydrogen atom. The theory is modified to take into account the dielectric constant of the semiconductor material, ε, and the effective mass of the electron, m_e^*, and gives the donor ground state energy as,

$$E_D = \frac{e^4 m_e^*}{2(4\pi\varepsilon\varepsilon_0\hbar)^2} = 13.6\left(\frac{m_e^*}{m\varepsilon^2}\right) \quad \textbf{[eV]} \qquad \textbf{Equation 2.5}$$

and the Bohr radius of the impurity ion as,

$$a_B = \frac{4\pi\varepsilon\varepsilon_0\hbar^2}{m_e^* e^2} = 0.053\left(\frac{m\varepsilon}{m_e^*}\right) \quad \textbf{[nm]} \qquad \textbf{Equation 2.6}$$

To characterise semiconductor materials the most frequently measured physical parameters are the conductivity, σ, and the free carrier density, n (or p for the case of a p-type material). The conductivity can easily be obtained, directly from a resistance measurement given the contact geometry and separation. The carrier density is obtained from a Hall effect measurement.

The conductivity and carrier density of a material are related to each other by,

$$\sigma = ne\mu \qquad \textbf{Equation 2.7}$$

where e is the charge on an electron and μ is the mobility. Thus with a measurement of Hall effect and resistivity we can calculate the mobility, measurements of this type have frequently been made in order to characterise the samples studied in this thesis. The mobility is equal to the magnitude of the drift velocity, v, per unit electric field, E, as shown by equation 2.8.

$$\mu = \frac{|v|}{E}$$ **Equation 2.8**

The carrier mobility is an extremely important parameter in semiconductor physics as it allows us to gain information about the scattering mechanism(s) present in a particular material. In a metal the temperature dependence of the conductivity is largely due to a change in scattering rate with temperature. However in semiconductors, frequently the temperature dependence of the scattering rate can be masked by a much larger change in the carrier density. For this reason it is important to separate the two different temperature dependent contributions to the conductivity (ie due to the carrier density and mobility) in order to gain information about the scattering mechanism.

The well know property of photoconductivity can be understood by considering a modification to equation 2.7. The change due to illumination can be expressed as,

$$(\sigma + \Delta\sigma) = (n + \Delta n)e(\mu + \Delta\mu)$$ **Equation 2.9**

where $\Delta\sigma$, Δn, and $\Delta\mu$ represent the change in conductivity, carrier density and carrier mobility respectively. So we can see that there are two possible mechanisms that will result in photoconductivity. Either the carrier density, mobility, or both are increased. A change in the mobility can occur due to a decrease in the scattering rate. An increase in the carrier density can be understood in terms of a materials band gap by considering figure 2.7 below.

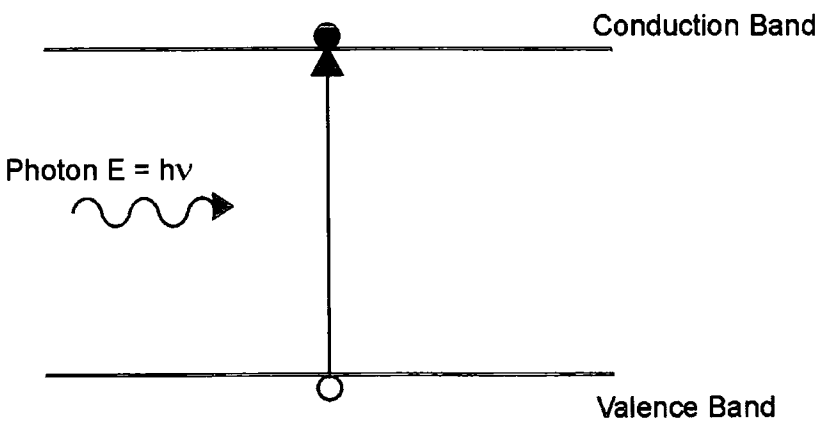

Figure 2.7 - Photoconductivity, electrons excited across the band gap (E_g) by incident photons

A photon incident on the semiconductor has its energy absorbed by an electron in the VB promoting it to the CB thus increasing the free carrier concentration, n, and hence the conductivity is also increased.

A related phenomena called persistent photoconductivity has been observed in a range of different materials including $Cd_{1-x}Mn_xTe$:In. With persistent photoconductivity the increase in conductivity remains even after illumination is removed, provided the material is kept at a low temperatures. Due to the importance of persistent photoconductivity to the work presented in this thesis a full description, along with a brief review of the work carried out on this subject is given in section 2.4.

2.3 Basic Theory of Magnetism

This section is intended to give a brief overview of the magnetism of materials, a more detailed treatment can be found in a number of textbooks [5-7]. Later, in section 3.1 a more specific review of the types of magnetism observed in DMS will be presented. First we shall discuss diamagnetism which is an intrinsic property of all materials, then we move on to describe paramagnetism, ferromagnetism, ferrimagnetism and antiferromagnetism, which may be observed in certain materials. A discussion of the formation of a spin glass phase appears in the next chapter (section 3.1.2) as it is of great importance to both the magnetic and electrical transport properties of materials.

2.3.1 Diamagnetism

The magnetic susceptibility of a material is defined as,

$$\chi = \frac{M}{H} = \frac{\mu_0 M}{B} \qquad \textbf{Equation 2.10}$$

where M is the magnetization (the magnetic moment per unit volume), H is the magnetic field strength, B is the magnetic flux density and μ_0 is the permeability of free space.

If we first consider an atom with all electronic shells filled, it will have zero spin and orbital angular momentum in its ground state. Therefore the only contribution to the magnetic moment of the atom is due to the orbital moment induced by an applied magnetic field. When a magnetic field is applied to this atom the motion of the electron orbit changes such that it opposes the applied field. The opposing magnetic moment can be thought of as arising from an electric current, I, due to the circulating electron and has a magnitude m=IA, where A is the area of the electron orbit. A material composed of a number of such atoms will have a negative magnetization, and hence a negative susceptibility. This is diamagnetism and is present in all materials, the diamagnetic susceptibility can be derived from a semiclassical approach and is given by,

$$\chi_d = -\frac{\mu_0 N Z e^2}{6 m_e} \langle r^2 \rangle \qquad \textbf{Equation 2.11}$$

where N is the number of atoms per unit volume, Z is the number of electrons in each atom, e and m_e are the charge and mass of an electron respectively, and $\langle r^2 \rangle$ is the mean

square radius of the electron orbit. The same result can also be obtained from a relatively simple quantum mechanical treatment.

The value of the diamagnetic susceptibility is in general temperature independent and rather small in most materials, typically the dimensionless volume susceptibility is of the order of 10^{-5}. So although present in all materials, diamagnetism is often masked by a larger paramagnetic susceptibility which is described next in section 2.3.2. An exception to this is seen in the case of materials in a superconducting state, where perfect diamagnetism is exhibited and $\chi = -1$.

2.3.2 Paramagnetism

One form of magnetism that gives rise to a positive contribution to the susceptibility and is found in a wide range of materials is paramagnetism. The magnetic moment of an atom in free space is related to its angular momentum by,

$$\mu = \gamma J = -\frac{g\mu_B J}{\hbar} \qquad \textbf{Equation 2.12}$$

where the constant γ is called the gyromagnetic ratio and is the ratio of the magnetic moment to the angular momentum. The total angular momentum vector, J, (the sum of the spin and orbital angular momenta) of electrons in an atom is quantized in units of $\hbar$. This means that the smallest non zero value of magnetic moment is $\mu_B = e\hbar/2m_e$, it is known as the Bohr magneton and its value is $\sim 9.27\text{x}10^{-24}$ JT^{-1} in SI units. To calculate the total magnetic moment from the total angular momentum we need to know the relative proportions of spin and orbital angular momentum, and this information is contained in the Landé splitting factor, defined by,

$$g = \frac{3J(J+1) + S(S+1) - L(L+1)}{2J(J+1)} \qquad \textbf{Equation 2.13}$$

To determine the ground state of an atom we apply Hund's rules to combine the quantum numbers of the individual electrons. The rules exist as a result of fact that different coupling mechanisms (spin-spin, orbit-orbit, total spin-total orbit) have different energies. The three rules can be summarised as follows :

1. The maximum total atomic spin ($S = \sum s$) is found such that the Pauli exclusion principle is not violated.

2. The total orbital angular momentum is maximised ($L = \sum m$) whilst remaining consistent with rule 1 above.
3. The value of J is equal to | L – S | if the shell is less than half full, and is equal to L + S if the shell is more than half full. If the shell is exactly half full we find that L = 0 so therefore J = S

The energy levels of an atom in a magnetic field are given by,

$$U = -\mu \cdot B \qquad \textbf{Equation 2.14}$$

An atom with angular momentum J has 2J+1 equally spaced energy levels, using equation 2.14 from above and applying Boltzman statistics it is possible to calculate the magnetization,

$$M = NgJ\mu_B B_J(x) \qquad (x \equiv gJ\mu_B B / k_B T) \qquad \textbf{Equation 2.15}$$

where $B_J(x)$ is known as the Brillouin function, and is given by,

$$B_J(x) = \frac{2J+1}{2J}\coth\left(\frac{(2J+1)x}{2J}\right) - \frac{1}{2J}\coth\left(\frac{x}{2J}\right) \qquad \textbf{Equation 2.16}$$

A plot of M vs B will yield a straight line (except at very high fields) with a positive gradient equal to the paramagnetic susceptibility. The paramagnetic susceptibility is given by equation 2.17.

$$\chi_P = \frac{\mu_0 NJ(J+1)g^2\mu_B^2}{3k_B T} = \frac{C}{T} \qquad \textbf{Equation 2.17}$$

2.3.3 Pauli Paramagnetism

In a metal we can consider the behaviour of the conduction electrons to be that of a gas of free electrons which do not interact with the ions. We have already seen that the size of the magnetic moment associated with the spin of the electron is μ_B (see equation 2.12). Pauli showed that by applying Fermi-Dirac statistics to this free electron gas it is possible to obtain a temperature independent positive susceptibility.

If we consider an electron gas at zero temperature, in zero magnetic field the number of electrons with spin pointing in one particular direction will be equal to the number of electrons with their spins pointing in the opposite direction. The electrons will fill all possible energy states up to the Fermi energy, E_F. If we now apply a magnetic field the energy levels of the electrons will be shifted by $\pm \mu_B B$ (as given by equation 2.14) depending on the direction of their spin (shown in figure 2.8). As a result of this it is energetically favourable for some of the electrons with spin parallel to the field to reverse the direction of the their spin and enter the subband of electrons with spins aligned antiparallel to the field. Thus the number of electrons with magnetic moments parallel to the applied field will be increased, conversely the number with their moment antiparallel to the field will be decreased. This results in a net magnetic moment in the direction of the field, and hence a paramagnetic susceptibility.

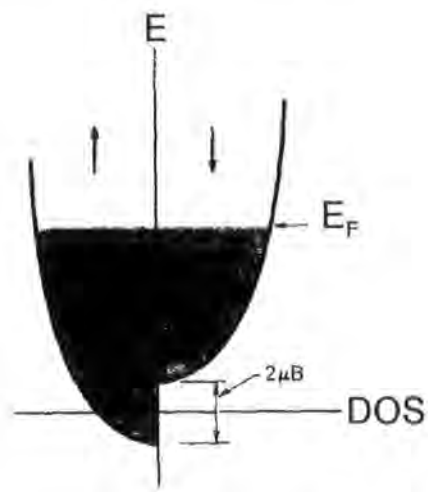

Figure 2.8 –Schematic diagram showing the origin of Pauli paramagnetism. The shaded regions represent occupied states. On the left side of the diagram electrons have their spins antiparallel to the applied magnetic field. Whereas on the right side of the figure the applied field and electron spins are parallel.

2.3.4 Ferromagnetism, Antiferromagnetism and Ferrimagnetism

So far we have assumed that magnetic ions in a material do not interact with one another. We now turn to look at somewhat different magnetic phenomena (ferromagnetism, antiferromagnetism and ferrimagnetism), materials that exhibit these properties can have a finite magnetic moment in zero applied magnetic field below a certain temperature. It is interactions between local moments which can produce the "spontaneous magnetization" observed in some magnetically ordered systems. By considering the so called "molecular field" Pierre Weiss was able to derive the following expression for the susceptibility of a ferromagnet above the temperature at which the spontaneous magnetization vanishes, (known as the Curie point) T_C.

$$\chi_F = \frac{C}{T - T_C} \qquad \textbf{Equation 2.18}$$

Equation 2.18 above is known as the Curie-Weiss law and C is called the Curie constant. The interactions between moments in a magnetic material are known as exchange interactions and are mainly due to the electrostatic interaction between electrons. In reality the exchange interactions are quantum mechanical in nature and have no real classical analogue. The exchange interaction between two spins is described by the Heisenberg spin Hamiltonian,

$$H = -\sum J_{ij} S_i \cdot S_j \qquad \textbf{Equation 2.19}$$

where J_{ij} are known as the exchange coupling constants, and S represents the spin of ith and jth electron.

This interaction is called direct exchange, as it arises from the direct Coulomb interaction between the spins of two electrons. In many cases the magnetic ions are separated by non-magnetic ions, in this situation it is possible for the magnetic ions to have an interaction mediated by the electrons of the non-magnetic ion. Such an interaction is called superexchange and is of importance in insulating materials. There are also other exchange mechanisms that couple magnetic ions via the free carriers in a material.

The difference between ferromagnets, antiferromagnets and ferrimagnets is due to the way in which the ordered moments align themselves with respect to each other, this is shown in figure 2.9 below. In antiferromagnets and ferrimagnets the spins align themselves such that they are antiparallel to their neighbours. If it is energetically

favourable for neighbouring spins to align antiparallel we can see that the exchange integral, J_{ij}, must be negative.

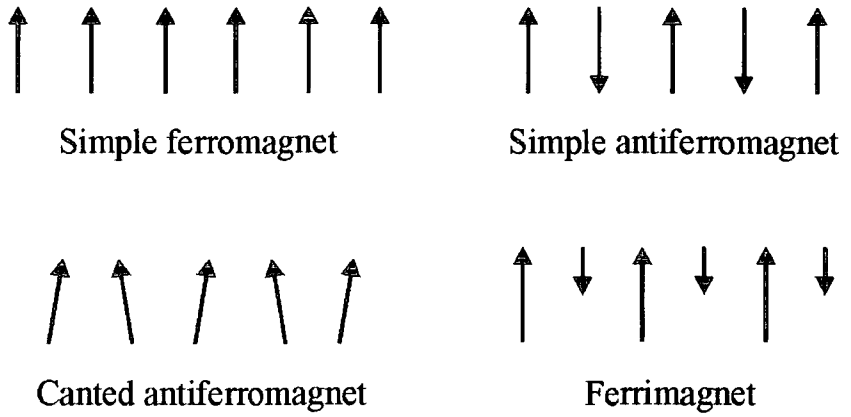

Figure 2.9 – Schematic representations of different possible ordered arrangements of spins.

In addition to the three forms mentioned above figure 2.9 includes a diagram of the spin arrangement in a canted antiferromagnet. It can been seen from the diagram that with the exception of the simple antiferromagnet all these ordered states will result in a net spontaneous magnetization. In an antiferromagnet the temperature below which the spins are ordered is called the Néel temperature, T_N, above this the material is paramagnetic and the susceptibility is described by equation 2.20.

$$\chi_{AF} = \frac{C'}{T+\theta} \qquad \textbf{Equation 2.20}$$

where C' is a constant and the value θ reasonably close to T_N.

2.4 Persistent Photoconductivity

In this section Persistent PhotoConductivity (PPC) is described and a brief review is given of the work to date. Quite generally PPC is the effect shown by some materials whereby irradiation of the material with some wavelength of light produces an increase in conductivity which persists long after the source of illumination has been removed. Often this effect is observed at low temperatures and persists until the temperature is raised to some critical temperature (the quenching temperature) at which the material regains its original conductivity prior to illumination. There exists a wide range of materials that exhibit PPC due to a variety of different mechanisms. We shall focus our attention on PPC related to, so called DX centres, as this is the mechanism for PPC in $Cd_{1-x}Mn_xTe$:In.

Examples of systems that show some form of PPC effect include, II-VI semiconductors eg $Cd_{1-x}Mn_xTe$:In [8] and $Cd_{1-x}Zn_xTe$:In [9], III-V semiconductors eg $Al_xGa_{1-x}As$:Si [10], high T_c superconductors eg oxygen-deficient $YBa_2Cu_3O_x$ thin-films [11] and references therein, colossal magnetoresistance perovskites [12], semiconductor heterostructures, interfaces and quantum wells [13], inhomogeneous semiconductors [14]. This list is not intended to be exhaustive, but rather to indicate to the reader the diverse range of materials showing PPC. It should be noted that in some cases where reference is made to PPC a more accurate description might be long lived photoconductivity, as varying relaxation times are observed. In most materials containing DX centres the photoconductivity is truly persistent and relaxation times of the order of tens of years have been demonstrated.

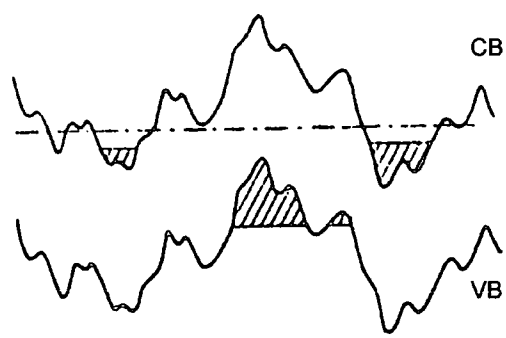

Figure 2.10 - Random fluctuations in conduction band and valence band edges. The shaded regions represent "traps" where electrons and holes may remain spatial separated, thus prevent recombination.

The case of PPC in inhomogeneous semiconductors can be explained if we consider that the edges of the VB and CB can have random fluctuations in potential over some region of the material. After the generation of an electron-hole pair due to an incident photon the charge carriers may drift apart and remain separate because of localized states or "traps" at the band edges. This spatial separation of the electron-hole pair prevents recombination and so the photoconductivity can persist after the illumination ceases. This situation is illustrated schematically in figure 2.10. PPC in homogeneous semiconductors (such as) $Cd_{1-x}Mn_xTe$:In is due to a completely different mechanism which will now be described in the following section.

2.4.1 Persistent Photoconductivity due to DX Centres

As mentioned previously in section 2.2 photoconductivity can arise from an increase in either mobility or carrier density, in the case to be considered here an increase in carrier density, n, is responsible for the observed effect. Plots of n (derived from a Hall measurement) against temperature for both $Al_xGa_{1-x}As$:Si and $Cd_{1-x}Mn_xTe$:In [8] are reproduced in figure 2.11. As can be seen when the sample is initially cooled in dark n decreases as electrons "freeze out" into a deep state. After illumination at low temperatures n is seen to increase. The upper curves corresponding to warming after illumination remain at this high value of n, until at some higher temperature (known as the quenching temperature, T_Q) the two curves meet.

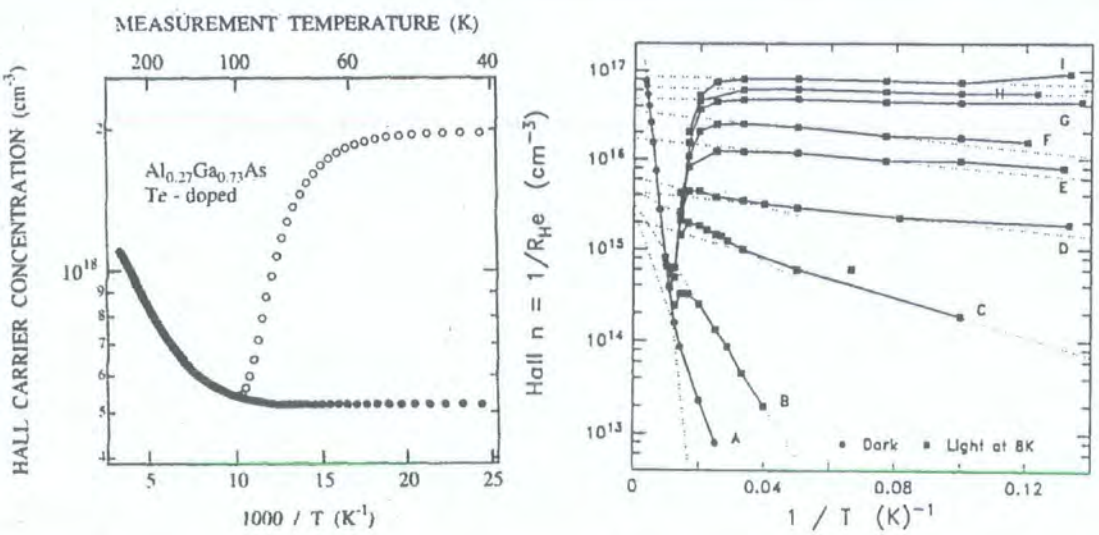

Figure 2.11 – Plots of carrier density against inverse temperature for two different materials which exhibits persistent photoconductivity , (a) AlGaAs:Te for both dark data (closed symbols) and saturation illumination (open symbols) (b) CdMnTe:In where curves labelled A to I are for increasing photogenerated carrier densities.

Early work was carried out by Lang & Logan [15, 16] on PPC in n-$Al_xGa_{1-x}As$ in an attempt to explain the observed experimental results. The defects they were encountering could be characterised by;

(a) A thermal depth much smaller than the optical depth.

(b) A very small, thermally activated, electron capture cross section at low temperatures.

The model that they proposed to account for PPC was due to a large lattice relaxation, they suggested that the origin of the deep state was a complex formed from the substitutional donor atom (D) and an unknown lattice defect (X). Hence the name DX state was used. After the subsequent theoretical work of Chadi & Chang [17, 18] who used *ab initio* pseudopotential calculations to determine the DX centre binding energy and compare it with experimental results. It is now widely accepted that the model describing the DX centre is the "large lattice relaxation negative U model" from a combination of both the above ideas. From this model it is now known that the same donor atom is responsible for the two different observed states.

The key to understanding PPC related to DX centres lies in appreciating the bistable nature of the impurity state. For example in the case of $Al_xGa_{1-x}As$:Si the Si atom can form two different types of impurity state. The first stable state is an ordinary shallow hydrogenic like donor state residing just below the CB edge. In the second stable state (know as the DX^- state) the donor Si ion shifts its position away from a lattice site and at the same time acquires a second electron to become negatively charged. The lattice relaxation associated with the DX^- state means that it is energetically favourable for the impurity ion to be associated with two electrons, the Hubbard correlation energy, U, is negative. It is possible to describe the formation of DX^- state with the charge exchange equation given below,

$$2d^0 \rightarrow d^+ + DX^- \qquad \text{Equation 2.21}$$

where d^0 and d^+ represent neutral and ionized shallow donor states. We can represent the above description using a configuration coordinate diagram, as shown in figure 2.13. In this diagram the total energy of the system is plotted versus a coordinate, which represents the distortion of the lattice close to the dopant Si ion. The two parabolic curves on the left side of the diagram represent the CB, and with a slightly lower energy, the shallow donor state. The parabolic curve on the right side of the figure represents the deep DX^- state. The relevant energies are labelled on the diagram, E_s activation energy of the shallow donor state, and most importantly E_c is the energy barrier that must be overcome if an electron in the shallow donor state is to regain the DX^- state. It is this barrier to recombination that prevents the photoconductivity relaxing at low temperatures. Thus, it can be seen from this diagram that if the sample is cooled in the dark, electrons freeze out into this deep DX state. At low temperatures illuminating with photons of energy greater than E_{opt} excites electrons into the shallow impurity state, and it is in this situation that the barrier to recapture E_c can not be surmounted until the temperature of the system is raised to T_Q. Once again we can write down a charge exchange equation for this process.

$$DX^- \xrightarrow{h\nu} d^+ + 2e^- \qquad \textbf{Equation 2.22}$$

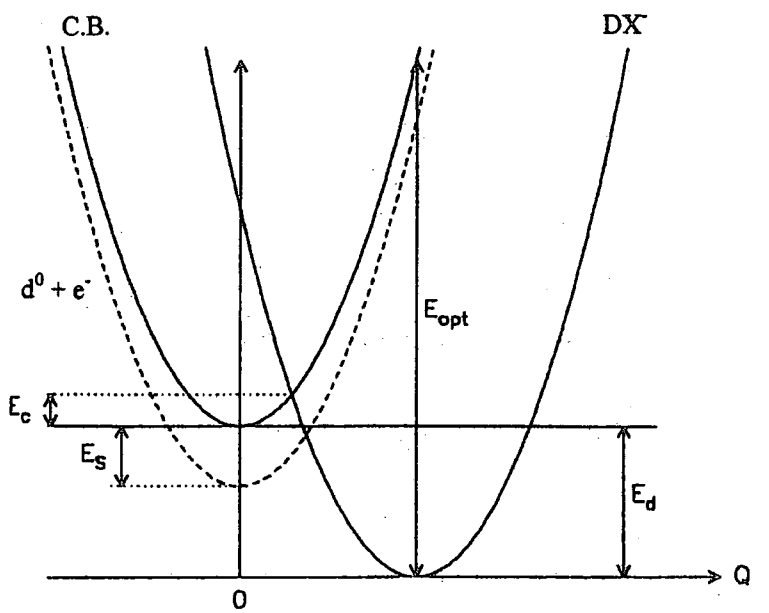

Figure 2.13 - Configuration coordinate diagram illustrating PPC in $Al_xGa_{1-x}As$:Si

PPC in $Cd_{1-x}Mn_xTe$:In is almost exactly analogous to the case described above for $Al_xGa_{1-x}As$:Si. In particular the In donor in $Cd_{1-x}Mn_xTe$:In behaves in the same way as Si in $Al_xGa_{1-x}As$:Si.

It has been suggested recently that materials exhibiting PPC could have important applications as devices to store large amounts of information using holographic techniques [19].

In this study PPC has been used to tune the carrier density of samples of $Cd_{1-x}Mn_xTe$:In allowing properties of the material to be studied as a function of carrier density.

Previously PPC has been used to study the metal insulator phase transition by tuning the carrier density. The very first study of this nature was carried out in a non-magnetic material by Katsumoto *et al* using Si doped AlGaAs. In this work both the behaviour of the conductivity [20] and of the dielectric constant [21] close to the metal insulator transition were examined. Following from this a number of studies were made in the dilute magnetic semicondcutor CdMnTe:In [8, 22, 23]. Experimental data from some of these studies are presented later in a review of the metal insulator transition (see section 3.2).

2.5 References

1. Kolodziejski, L.A., *et al.*, *Two-Dimensional Metastable Magnetic Semiconductor Structures.* Applied Physics Letters, 1986. **48**(21): p. 1482-1484.
2. Giriat, W. and J.K. Furdyna, *Crystal Structure, Composition and Materials Preparation of DMS*, in *Dilute Magnetic Semiconductors*, J.K. Furdyna and J. Kossut, Editors. 1988, Academic Press. p. 1-34.
3. Furdyna, J.K., *Diluted Magnetic Semiconductors.* Journal of Applied Physics, 1988. **64**(4): p. R29-R64.
4. Balzarotti, A., *et al.*, *Local-Structure of Ternary Semiconducting Random Solid-Solutions - Extended X-Ray-Absorption Fine-Structure of* $Cd_{1-x}Mn_xTe$. Physical Review B, 1984. **30**(4): p. 2295-2298.
5. Kittel, C., *Intrduction to Solid State Physics.* 7th ed. 1996: Wiley.
6. Rosenberg, H.M., *The Solid State.* 2nd ed. 1978: Oxford Science Publications.
7. Crangle, J., *Solid State Magnetism.* 1991: Edward Arnold.
8. Terry, I., *et al.*, *Band Tails and the Insulator-Metal Transition in the Persistent Photoconductor* $Cd_{1-x}Mn_xTe:In$. Solid State Communications, 1992. **84**(1-2): p. 235-240.
9. Khachaturyan, K., *et al.*, *Lattice-Relaxation of DX-Like Donors in* $Zn_xCd_{1-x}Te$. Physical Review B, 1989. **40**(9): p. 6304-6310.
10. Theis, T.N., P.M. Mooney, and B.D. Parker, *Bistability of the DX Center in GaAs and* $Al_xGa_{1-x}As$, *and Experimental Tests For Negative-U of the DX Level.* Journal of Electronic Materials, 1991. **20**(1): p. 35-48.
11. Hoffmann, A., *et al.*, *Persistent photoinduced superconductivity.* Journal of Alloys and Compounds, 1997. **251**(1-2): p. 87-93.
12. Gilabert, A., *et al.*, *Photoconductivity in manganites.* Journal of Superconductivity, 2000. **13**(2): p. 285-290.
13. Yang, H.C., T.Y. Lin, and Y.F. Chen, *Persistent photoconductivity in InGaN/GaN multiquantum wells.* Applied Physics Letters, 2001. **78**(3): p. 338-340.
14. Smith, M., J.Y. Lin, and H.X. Jiang, *Disorder and persistent photoconductivity in* $Zn_xCd_{1-x}Se$ *semiconductor alloys.* Physical Review B-Condensed Matter, 1996. **54**(3): p. 1471-1473.

15. Lang, D.V. and R.A. Logan, *Large-Lattice Relaxation Model for Persistent Photoconductivity.* Physical Review Letters, 1977. **39**(10): p. 635.

16. Lang, D.V., *Trapping characteistics and a donor complex (DX) model for the PPC trapping center in Te-doped AlGaAs.* Physical Review B, 1979. **19**(2): p. 1015.

17. Chadi, D.J. and K.J. Chang, *Theory of the Atomic and Electronic-Structure of DX Centers in GaAs and $Al_xGa_{1-x}As$ Alloys.* Physical Review Letters, 1988. **61**(7): p. 873-876.

18. Chadi, D.J., *Tetrahedrally Symmetrical DX-Like States of Substitutional Donors in GaAs and $Al_xGa_{1-x}As$ Alloys.* Physical Review B-Condensed Matter, 1992. **46**(11): p. 6777-6780.

19. Linke, R.A., *et al.*, *Holographic storage media based on optically active bistable defects.* Journal of Applied Physics, 1998. **83**(2): p. 661-673.

20. Katsumoto, S., *The Metal-Insulator Transition in a Persistent Photoconductor*, in *Anderson Localization*, T. Ando and H. Fukuyama, Editors. 1987, Springer-Verlag. p. 45-52.

21. Katsumoto, S., *et al.*, *Dielectric-Constant Measurement Near the Metal-Insulator- Transition in $Al_{0.3}Ga_{0.7}As$.* Journal of the Physical Society of Japan, 1989. **58**(3): p. 791-794.

22. Terry, I., *et al.*, *Magnetic-Field Dependence of the Dielectric-Constant in $Cd_{1-x}Mn_xTe$:In On Approaching the Insulator-to-Metal Transition.* Philosophical Magazine B-Physics of Condensed Matter Statistical Mechanics Electronic Optical and Magnetic Properties, 1992. **65**(6): p. 1245-1254.

23. Leighton, C., I. Terry, and P. Becla, *Metal-insulator transition in the persistent photoconductor $Cd_{1-x}Mn_xTe$:In.* Europhysics Letters, 1998. **42**(1): p. 67-72.

3 Magnetism and Electrical Transport Close to the Metal-Insulator Phase Transition

In this chapter we present previous experimental results and theoretical ideas which are of relevance to the work contained in this thesis. Broadly speaking this chapter is divided into two parts, the first deals with magnetic properties and the second examines electrical transport properties close to the MIT. It is important to appreciate that although presented in separate sections the magnetic and electrical transport properties are intimately linked. In particular as we shall see in this chapter and throughout this thesis, the electrical transport properties of DMS are profoundly affected by the magnetic properties of the material. At the same time many of the interesting phenomena observed in the magnetism of DMS are influenced by the presence of conduction electrons.

3.1 Magnetic Properties of Dilute Magnetic Semiconductors

This section is intended to give an introduction to the magnetic properties specific to DMS, in particular we will focus on the material of interest to this thesis, namely $Cd_{1-x}Mn_xTe$. A variety of magnetic properties can be observed in $Cd_{1-x}Mn_xTe$ at different temperatures and manganese fractions, x. At high temperatures samples show paramagnetic behaviour as described in section 3.1.1. At higher values of x a transition from a paramagnetic phase to a spin glass phase is observed at low temperatures. The spin glass freezing temperature being dependent on x, (see section 3.1.2). For the highest manganese concentrations ($x > 0.7$) it is possible to observe long range ordering, and the magnetic moments align to form an antiferromagnetic phase; details are given in section 3.1.3.

3.1.1 Paramagnetic Phase

At high temperatures the dc susceptibility of $Cd_{1-x}Mn_xTe$ can be approximated by a Curie-Weiss law, equation 3.1

$$\chi = \frac{C}{T-\theta} + \chi_d \qquad \text{Equation 3.1}$$

where θ is the Curie-Weiss temperature, C is the Curie constant, and χ_d is the diamagnetic susceptibility of the host material (CdTe).

The Curie constant C is given by,

$$C = \frac{xN_0(g\mu_B)^2 S(S+1)}{3k_B} \qquad \text{Equation 3.2}$$

where x is the Mn fraction and N_0 is the number of cations per unit volume.
At temperatures below about 50 K deviations from this simple Curie behaviour are observed due to the Mn ions forming interacting clusters. A plot of the inverse susceptibility, χ^{-1}, against temperature, T, is given in figure 3.1. Data are shown for two different Mn containing DMS, CdMnTe and CdMnSe [1].

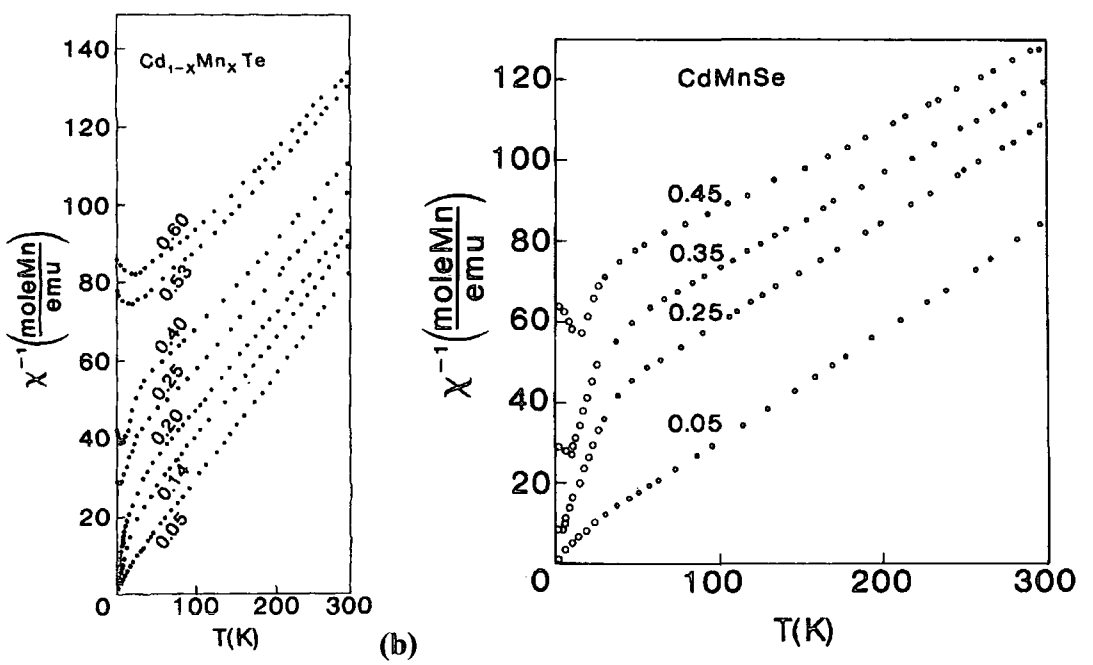

Figure 3.1 - Inverse of magnetic susceptibility plotted against temperature for (a) CdMnTe and (b) CdMnSe after [1].

From fitting the high temperature data it has been shown [2] that the values of θ obtained are negative for all values of x examined. This indicates that the exchange interaction between Mn^{2+} ions is antiferromagnetic. The dependence of θ on the exchange interaction constant is given in equation 3.3, where z is the co-ordination number, k_B is the Boltzman constant and J_n is the nth nearest neighbour exchange constant.

$$\theta = \frac{2S(S+1)x}{3k_B}\sum_n z_n J_n \qquad \textbf{Equation 3.3}$$

This expression can be simplified if we assume that the exchange interaction is short range and involves only nearest neighbour interactions (J_1). Thus for z_1=12 and S=5/2 we have equation 3.4

$$\theta = 70x\frac{J_1}{k_B} \qquad \textbf{Equation 3.4}$$

The value of $J_1/k_B \sim 6 - 8$ K. In actual fact it has been shown that the next nearest neighbour exchange interaction (J_2) is also antiferromagnetic and approximately an order of magnitude weaker.

The physical mechanism which causes the nearest neighbour exchange interaction is nearly entirely due to anion mediated superexchange, with a small amount of indirect coupling of the Bloembergen-Rowland (BR) type.

In the very dilute limit, when the concentration of Mn is less than 1% ($x < 0.01$), the Mn^{2+} spins can be treated as isolated and completely independent. The magnetization is described by the standard Brillouin function. At higher Mn concentrations this function is inadequate to describe the magnetization data, however a phenomenological description of the magnetization is possible if the parameters x and T are replaced by effective values x_{eff} and T_{eff}. [3]. Thus we have equation 3.5 describing the magnetization,

$$M = x_{eff} N_0 5\mu_B B\left(\frac{5\mu_B H}{T_{eff}}\right) \qquad \textbf{Equation 3.5}$$

where B is the Brillouin function, μ_B is the Bohr magneton, H is the magnetic field strength and N_0 is the number of cations per unit volume.

3.1.2 Spin-Glass Phase

In simple terms a spin glass (SG) is a collection of magnetic moments where the low temperature (lowest energy) state is a frozen disordered pattern. This is in contrast to the more commonly found long range magnetically ordered state that we are familiar with for a ferrromagnet or antiferromagnet (AF) phase. To produce such a SG phase a system must fulfil two criteria. Firstly there must be competing interactions between the magnetic moments (this situation is known as magnetic frustration), secondly there must be some random element to these interactions. The mechanism producing magnetic frustration can be understood if we consider three moments positioned at the vertices of an equilateral triangle as depicted in figure 3.2. If we assume that the interaction between these moments is AF and the upper pair of spins are thus aligned antiparallel. This is the lowest energy state for the upper pair. Now we consider the orientation of the third spin, if it aligns antiparallel with one of the upper spins, then it must be parallel to the other. In this arrangement it is thus impossible to satisfy AF coupling between all the nearest neighbours. Although the picture presented above is somewhat idealised it is this situation which is known as magnetic frustration.

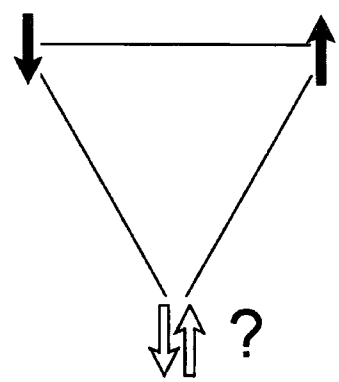

Figure 3.2 - Diagram illustrating frustration in an anteferromagnet.

A spin glass phase with only antiferromagnetic interactions was first predicted for a fcc lattice by DeSeze, Aharony, Villain at the end of the 1970's [4-6].

The transitions from a paramagnetic phase to a spin glass (SG) phase at low temperatures in $Cd_{1-x}Mn_xTe$ was first identified for samples having manganese concentrations above the nearest neighbour percolation limit ($x_c = 0.195$) [7]. It was generally believed at this time that samples with $x < x_c$ remained in the paramagnetic phase at all temperatures. The spin glass freezing temperature (T_g) was defined as the temperature at which the low field susceptibility is a maximum. Figure 3.3 shows the

variation of magnetic susceptibility near T_g for both the field cooled (FC) and zero field cooled (ZFC) condition for a number of different samples with different manganese concentrations $x > x_c$.

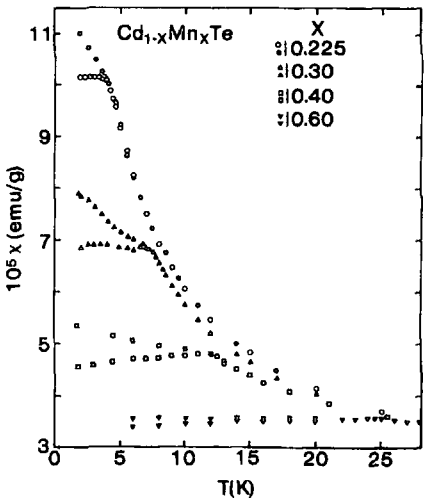

Figure 3.3 Magnetic susecptibility χ(T) near T_g for $x > x_c$ in $Cd_{1-x}Mn_xTe$ after reference [8]. Data as shown for both zero field cooled (open symbols) and field cooled in a 15 Oe field (closed symbols).

In addition to this cusp in the susceptibility other characteristics consistent with the formation of a SG were observed. In particular there was no anomaly present in the specific heat capacity at T_g and the susceptibility below T_g showed a dependence on the samples temperature and field history (ie FC or ZFC). Later work extending the magnetic measurements to lower temperatures [9] showed that a SG phase is observed even for samples with $x < 0.195$. A plot of χ against T for a sample with $x = 0.1$ is shown in figure 3.4.

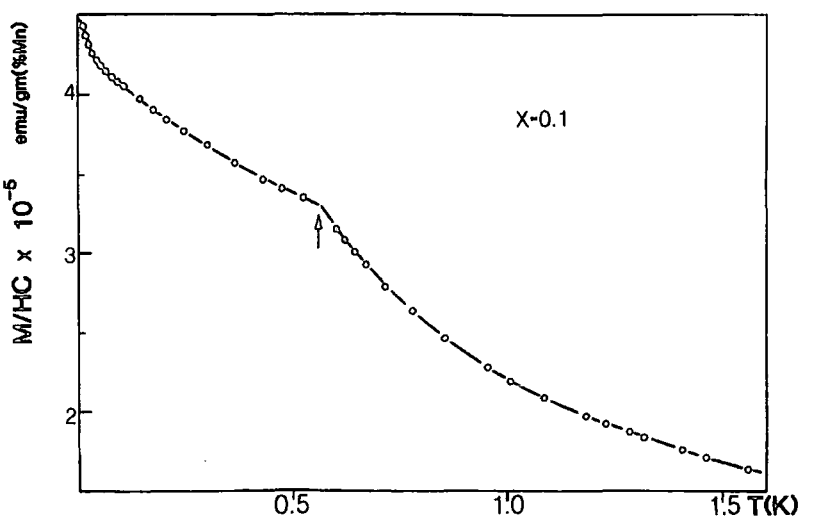

Figure 3.4 Susceptibility as a function of temperature for a sample having a Mn concentration below the nearest neighbour percolation limit. After reference [9].

A new magnetic phase diagram was presented (shown in figure 3.5) and it is now recognised that the SG phase extends all the way down to x = 0 with no paramagnetic behaviour at T =0 K.

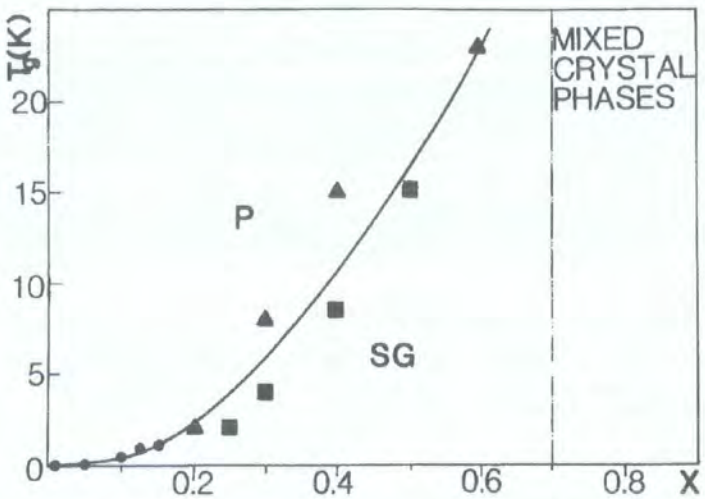

Figure 3.5 Variation of the spin glass freezing temperature T_g on the manganese fraction x, after reference [9].

It should be noted that at concentrations below x_c rather than a cusp in the static susceptibility, a kink (or a discontinuity in $d\chi/dT$) is observed (see figure 3.4). For this reason $\chi(T)$ is seen to diverge as $T \rightarrow 0$ K rather than approach a finite value as observed in more traditional spin glasses.

An explanation of the x dependence of T_g was given by Novak et al in 1985 [9] based on the idea that the SG phase is caused by a mixture of BR exchange and dipolar interactions. However as mentioned above it is now known that the dominant exchange mechanism is superexchange (mediated by the Te anions) rather than the BR type exchange interaction. Recently it has been shown [10] that the shape of the χ vs T curves for samples with $x < x_c$ can be explained by a model which includes contributions to the susceptibility from both the isolated clusters (paramagnetic) and an infinite cluster (spin glass like). For this model to work it is crucial to take into account the weaker exchange interactions between more distant neighbours (ie J_n for $n>1$).

3.1.3 Antiferromagnetic Phase

For the highest concentration of Mn ions (x>0.7) an antiferromagnetically ordered phase is seen at low temperatures. This long range ordering was first confirmed by neutron diffraction studies, where the positions of the peaks means that the it can be identified as antiferromagnetic ordering of type III for an fcc lattice [11]. The antiferromagnetic phase is also inferred from measurements of susceptibility and specific heat.

3.1.4 Bound Magnetic Polarons

At low temperatures entities known as Bound Magnetic Polarons (BMPs) can form in DMS and some other magnetic materials such as the mixed valent perovskites [12]. In II-VI semiconductors BMPs arise as a result of the s-d exchange interaction between a carrier spin and the surrounding localized magnetic ions. For example, in CdMnTe:In, a donor electron polarises the spins of nearby Mn ions, this gives a region of ferromagnetically aligned Mn spins within the donor electron Bohr radius. The situation is shown schematically below. The high temperature situation is depicted in figure 3.6a. The material is in a paramagnetic phase and the Mn ion spins have a random orientation throughout the entire material. When the temperature of the system is reduced (see figure 3.6b) to sufficiently low temperatures the s-d exchange dominates over the thermal fluctuations and the BMPs evolve. As a result of the local polarisation of Mn spins the donor electron energy is reduced (ie it becomes more tightly bound) and its effective Bohr radius shrinks. The remainder of the material outside of the donor localization radius continues to exhibit the expected magnetism for the host material. In the case of CdMnTe:In this will be a paramagnetic or SG phase depending on the Mn fraction and the temperature.

BMPs have been observed experimentally a number of times in different experiments. In DMS spin-flip Raman scattering experiments have shown evidence for a finite spin splitting of electronic levels in zero applied magnetic field which has been attributed to the formation of BMPs. Measurements were made first on n-CdMnSe [13] and also later on n-CdMnTe [14]. Theoretical work describing the observed properties of BMPs has been carried out by Dietl & Spalek [15] and also independently by Heinman, Wolf

& Warnock [16]. By writing an expression for the BMP free energy they were able to calculate various thermodynamic properties of the BMPs.

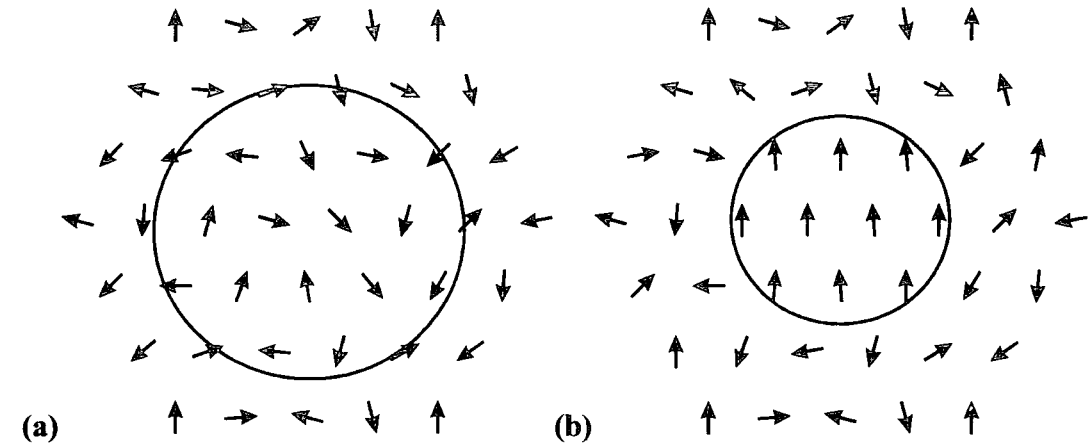

Figure 3.6 - Schematic diagram showing the formation of BMPs in CdMnTe:In.

Evidence for the existence of BMPs is also manifest in electrical transport measurements. Studies of the magnetic semiconductor $Gd_{3-x}V_xS_4$ by von Molnár *et al* [17] have revealed a large negative MR at low temperatures (figure 3.7) and in certain samples a field driven Insulator-Metal Transition both of which can be understood in terms of the formation of BMPs and the destructive effect of an applied magnetic field.

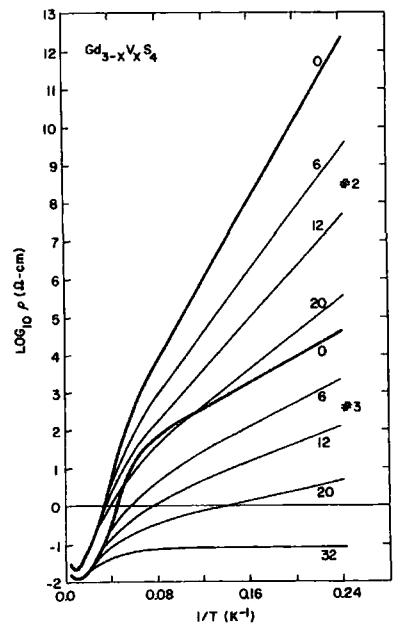

Figure 3.7 - Log of resistivity against inverse temperature for $Gd_{3-x}V_xS_4$ the data show a large negative MR at low temperatures interpreted in terms of BMPs after von Molnár *et al* [17].

Further evidence for magnetic polaron formation in the II-VI diluted magnetic semiconductors can be found in transport measurements of n-CdMnSe carried out by Dietl *et al* [18].

3.1.5 Photomagnetism

Very generally photomagnetism can be described as any change in a materials' magnetism as a result of incident radiation. A number of different material systems have been reported to exhibit this behaviour. Photomagentism has been observed in III-V semiconductor heterostructures by the group led by H Munekata [19], also in II-VI semiconductors with [20] and without [21] magnetic ions.

Figure 3.8 shows the experimental data of Wojtowicz *et al* [20] showing small persistent changes in the magnetization as a result of illumination at low temperatures.

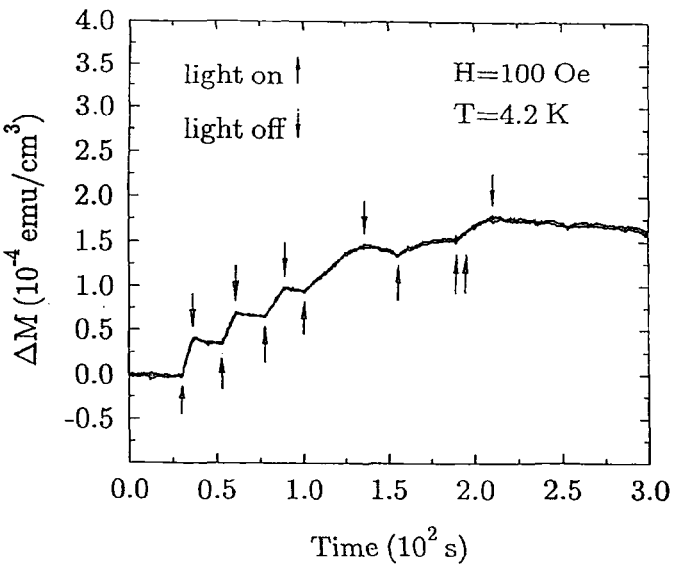

Figure 3.8 – Photo induced change in magnetization plotted as a function of time for a sample of $Cd_{0.9}Mn_{0.1}Te_{0.97}Se_{0.03}$:In. Arrows indicate duration of illumination, after [20]

This effect is due to an increased number of BMPs formed around shallow donor impurities.

In experiments on another member of the II-IV DMS family, CdMnTe, Awschalom *et al* [22] used a rf SQUID to measure the optically induced magnetization when circularly polarized laser light impinges on a sample. The photo induced magnetization may then be measured directly by measuring the flux changes in the pickup loop of the SQUID as a function of incident photon energy. Experimental data from this experiment are reproduced in figure 3.9. At low photon energies the incident radiation is below the band-gap, the material is transparent and no interaction is expected. At energies close to but below the band-gap, the magnetic signal changes rapidly reaching a pronounced maximum and then decreasing again with increasing laser energy. Above band-gap, the

magnetic response appears to be almost independent of photon energy. The peak in the magnetic response near band-gap is attributed to magnetic polaron formation, whereas the higher energy response, is due to the magnetization of the Mn ions produced by spin flip scattering with the conduction electrons and holes.

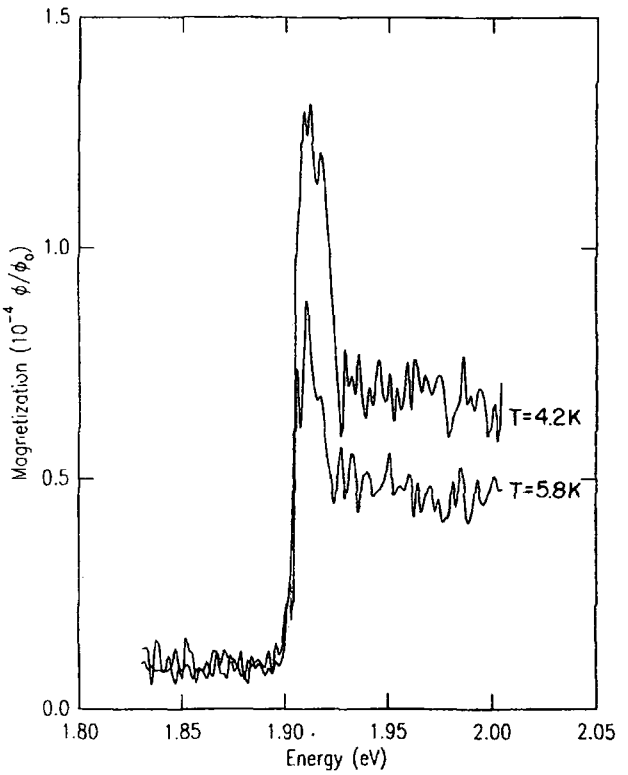

Figure 3.9 – Magnetic spectroscopy of $Cd_{0.8}Mn_{0.2}Te$, after Awschalom *et al* [22]. Measurements are shown for two different sample temperatures with the magnetization plotted as a function of photon energy. Illumination is provided by a constant intesity laser.

3.2 Metal-Insulator Phase Transition in Doped Semiconductors

The original aim of this thesis work was to study the Metal Insulator Transition (MIT) by fine tuning a single sample of the DMS $Cd_{1-x}Mn_xTe$:In. For this reason in the following sections we review past and present work on this subject, both theoretical and experimental. To begin with in section 3.2.1 a brief introduction is given listing in roughly chronological order the major developments of theory and the milestone experiments which have been carried out to test theoretical ideas. These theoretical ideas are then covered in slightly more detail in section 3.2.2. Section 3.2.3 presents a review of the many and varied experimental techniques that have been employed to study MITs. It also lists with references the different material systems that have been studied and the results that have been obtained. This includes some details of previous work on the MIT in $Cd_{1-x}Mn_xTe$:In.

3.2.1 Introduction and History

For over fifty years now the MIT in disordered systems has remained a subject of great interest to physicists, both experimentalists and theorists. In this time our understanding of the problems has increased dramatically, however at the present time it is by no means a completely solved problem.

The earliest work on the subject is attributed initially to Mott [23] and a few years later to Anderson. In 1949 Mott began by considering the problem from the point of view of the role that electron-electron correlation plays in a crystalline array of atoms. Anderson's work started from a very different concept by showing that in a non-interacting system it was possible for diffusion to be absent by introducing a certain (critical) amount of random disorder into the lattice. It should be noted at this point, that it has become apparent, in order to satisfactorily describe real systems we must include in our model both electron-electron interactions and random disorder. A theoretical description of the situation when both are present (particularly when electron-electron interactions are strong) has remained a central unsolved problem.

3.2.2 Theory

Metal-insulator transitions fall into two different categories, the first can be due to a change in a crystal lattice, such as a structural phase transition which leads to initially overlapping energy bands separating and hence a MIT. The second type and the subject of this work is a quantum phase transition that occurs at the absolute zero of temperature. In this strict sense the distinction between a metal and an insulator is properly made only at T = 0 K. As at T > 0 K thermal excitations permit an insulator to carry current. We define a metal as being a material whose dc electrical conductivity, σ, is finite at T = 0 K. Conversely an insulator is a material where $\sigma = 0$ at T = 0 K.

3.2.2.1 Mott Transition

Mott considered a crystalline array of neutral hydrogen atoms (ie one electron per atom) at the absolute zero of temperature. He suggested that this system should exhibit a discontinuous (1^{st} order) transition from a metallic to a non-metallic phase as the spacing between neighbouring atoms is increased. This form of MIT has become known as a "Mott transition". We can easily understand that at large carrier densities (corresponding to small interparticle distances) the system would be a metallic. Conversely it is clear that for large interparticle distances the system will become insulating. Mott suggested that the critical concentration separating metallic and insulating behaviour occurs when the following criterion is satisfied.

$$n_c^{1/3} a_H \approx 0.25 \qquad \textbf{Equation 3.6}$$

Here a_H is the Bohr radius of the isolated atom and n_c is the critical carrier density at the MIT. It has become apparent from the great variety of experimental work (some of which will be reviewed in section 3.2.3) that equation 3.6 (known as the Mott criterion) gives a very useful estimation of the location at which the MIT will occur in different material systems. In figure 3.10 we present experimental data [24] which shows that the Mott criterion approximately describes the experimental results for a remarkably wide variety of system, over many orders of magnitude of n_c. It should however be noted that for specific materials the deviation from this simple relation can be considerably.

A further point relating to the MIT argued by Mott, was the existence of a minimum metallic conductivity σ_{min}. The idea being that at conductivities greater than σ_{min} a

material can still be described as a metal. In three dimension the minimum metallic conductivity is given by,

$$\sigma_{\min} = \frac{Ce^2}{\hbar d_c}$$ **Equation 3.7**

where d_c is the average interatomic spacing at n_c and the constant $C \sim 0.026$.

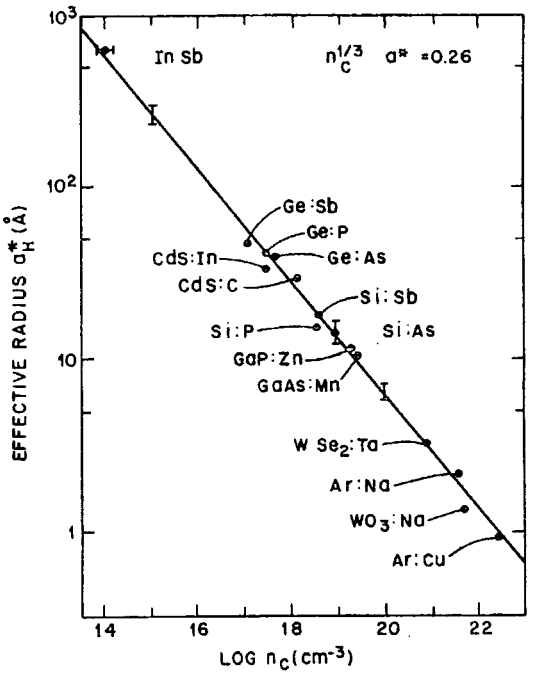

Figure 3.10 - Plot of a_H against n_c from a variety of experimental data, the figure agreement with the Mott criterion after [24].

3.2.2.2 Anderson Localization

The concept of localization was originally described by Anderson in 1958 [25] when he showed that it was possible for diffusion to be absent at T = 0 K in the presence of sufficiently strong disorder. Prior to this the traditional view had been that electron wavefunctions loose phase coherence (due to scattering from random potential fluctuations) over a distance known as the mean free path, l, whilst remaining extended through space. Anderson suggested that when the disorder was strong enough the wavefunction is exponentially localized in space. As described by equation 3.8 below,

$$|\psi(r)| \propto \exp\left(\frac{|r - r_0|}{\xi}\right)$$ **equation 3.8**

where ξ is the localization length. A schematic representation of the two situations described above is given in figure 3.11

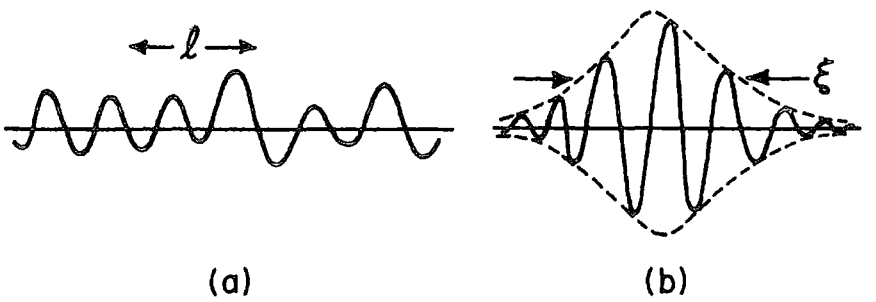

Figure 3.11 - schematic representation of wavefunctions for (a) an extended state (b) a localized state.

The idea of localized states can be understood very easily as we are already familiar with localized electron wavefunctions at traps below the conduction band. The new concept is that we can have a finite and continuous density of states, in which all states are localized. It is clear that localized and extended states cannot coexist at the same energy. If this were the case then the localized state would by necessity mix with the extended one and thus become extended as a result of this mixing. Anderson considered two different arrays of potential wells, shown in figure 3.12. First in the upper section of the figure we have the familiar crystalline array of potential wells. The energy levels of the individual wells broaden to form an energy band. A solution of the Schrödinger equation is in the form of a Bloch wavefunction which is extended throughout space.

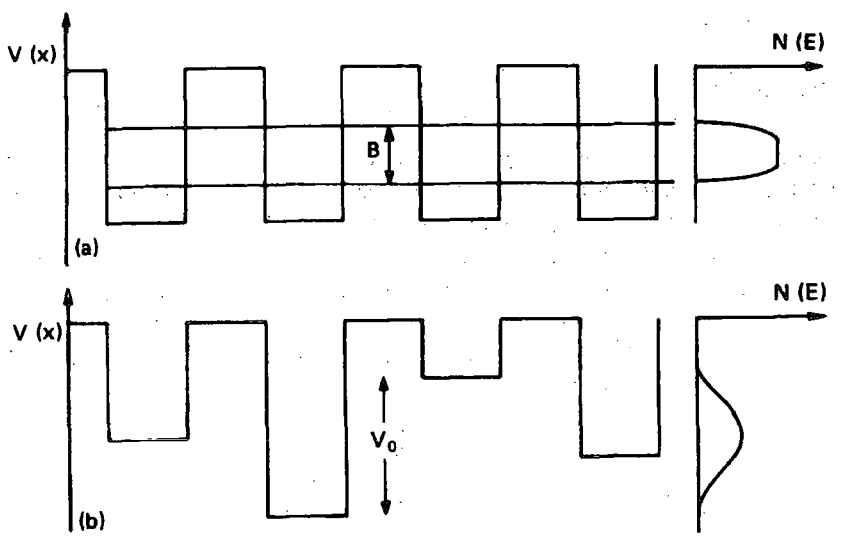

Figure 3.12 – Diagram of potential wells and density of states *N(E)* for (a) a crystalline lattice (b) the Anderson disordered lattice

We can now consider modifying this picture to produce a non-periodic array of potential wells. If the depths of the potential wells are allowed to vary over some energy range V_0 then we have the form shown in the lower half of figure 3.12. Anderson imagined placing an electron in one of the potential wells at a time t=0 and considered what would happen as $t \rightarrow \infty$. He found that if V_0/B was greater than some critical value the probability of finding an electron at some large distance decayed exponentially. In other words there is no diffusion at the absolute zero of temperature and the electron wavefunction is of the form shown in figure 3.11(b). In the other case where V_0/B is less than the critical value the wavefunction is extended through the crystal.

If the criteria for Anderson localization is not fulfilled but we have a moderate level of disorder in the system another situation is possible. It was first shown by Mott in 1966 that states deep in the band tail can be localized while at the same time states near the centre of the band are extended in character. Thus as a function of energy the states change from being localized to being extended. The critical energy separating localized from extended states is called the mobility edge, E_c (see figure 3.13). The name "mobility edge" can be understood by realising that if the Fermi energy, E_F, lies in region of localized states at zero temperature the conductivity is zero and we have an insulator. Conversely if $E_F > E_c$ at T=0K then the system is metallic. If by changing some parameter (eg composition of the material, applying strain or a magnetic field) E_F is made to cross E_c then a transition between a metal and an insulator occurs. This type of MIT is known as an "Anderson transition".

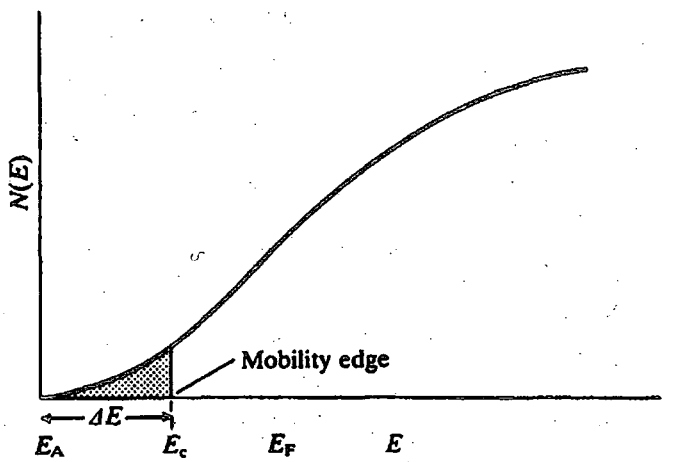

Figure 3.13 - Density of states for a band tail showing the position of the mobility edge, E_c, the shaded area is the region of localized states.

3.2.2.3 Scaling Theory of Electron Localization

The most successful theory to date to describe MITs is scaling theory of localization. In the mid 1970s , based on the work of Anderson discussed above, Thouless considered constructing a sample of size $(2L)^d$ in d dimensions, made up from 2^d smaller samples of size L^d. The eigenstates of the $(2L)^d$ sample are just a linear combination of the eigenstates of the L^d samples. Thouless also suggested that the mixing of the eigenstates of the smaller sample to produce the larger sample depended only on the ratio V/W. Here V is the change in energy of the levels resulting from a change in boundary conditions as a result of putting together the L^d blocks and W is the energy interval between energy levels in the L^d sample.

Thouless also noticed that the conductance of a sample could be expressed as dimensionless quantity defined in equation 3.9 below.

$$g = \frac{\hbar}{e^2} G = \frac{\hbar}{e^2} L^{d-2} \sigma \qquad \textbf{Equation 3.9}$$

It was suggested that g is the only parameter that is required to describe the system as it grows in size from this edge doubling procedure. The other key ingredient in this theory is that g is directly related to the ratio V/W. So we can write equation 3.10,

$$g(L) = \frac{V(L)}{W(L)} \qquad \textbf{Equation 3.10}$$

where the individual terms are as described above.

Wegner added to the development of these scaling ideas in 1976 [26] by writing an equation in the language of general scaling theory of other critical phenomena. He proposed that the MIT should be continuous and described by equation 3.11 for $d \neq 2$.

$$\sigma(T = 0K) = (E - E_c)^{(d-2)\nu} \qquad \textbf{Equation 3.11}$$

Where E_c is the mobility edge defined earlier and ν is called the critical exponent.

Following on from this work, in 1979 the so called "gang of four" (Abrahams, Anderson, Licciardello & Ramakrishnan) [27] developed the scaling ideas by combining them with perturbation theory.

To describe mathematically the way in which the system doubles in size we can write down an equation defining a scaling function (see equation 3.12).

$$\beta = \frac{d \ln g}{d \ln L} \qquad \textbf{Equation 3.12}$$

We can now consider the asymptotic forms of β for large and small values separately.

(i) $g >> g_c$

We start by considering β for large values of g. In this case the amount of disorder is small and the scattering is low. The electron wavefunction is extended throughout space. We have the condition that the mean free path is large compared to the interatomic spacing. Thus conventional Boltzman transport theory, which relies on weak scattering or $(k_F l)^{-1} << 1$ holds and we can write,

$$g(L) = \frac{\hbar}{e^2}\sigma L^{d-2} \qquad \textbf{Equation 3.13}$$

hence,

$$\beta(g) = (d-2) \qquad \textbf{Equation 3.14}$$

(ii) $g << g_c$

Now considering β for the case when g is small. In this case the random potential fluctuations are large and the electron wavefunctions are exponentially localized, as described by the localization length, at T=0K we have insulating behaviour. We can write the dimensionless conductance as,

$$g(L)\alpha \exp\left(-\frac{L}{\xi}\right) \qquad \textbf{Equation 3.15}$$

and thus the scaling function is,

$$\beta(g) = \ln\left(\frac{g}{g_c}\right) \qquad \textbf{Equation 3.16}$$

Abrahams et al were able to construct a plot of β against g by assuming that scaling function is continuous and monotonic between the limiting cases described above. We expect β(g) to be continuous simply because it describes the way that the conductance of a finite system evolves as a function of scale size. A similar plot to that produced by Abrahams et al is shown in figure 3.14.

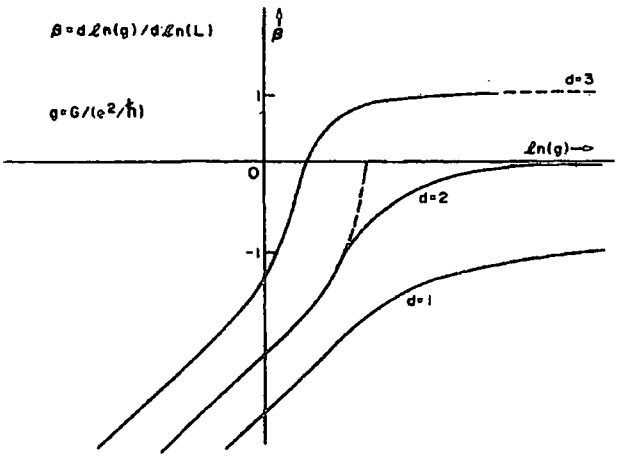

Figure 3.14 - Plot of β(g) against ln(g) for cases of different dimensionality, after [28].

The figure (3.14) above shows the scaling curve constructed for cases of different dimensionality (ie d = 1,2, & 3). We shall now consider the predictions made by scaling theory for each separate dimensionality shown.

(a) d = 1

In the one dimensional case we can see that β is always negative. So if we consider enlarging our system and letting $L \rightarrow \infty$ we quickly arrive at a strongly localized situation. Thus scaling theory clearly predicts that all one dimensional systems are insulating regardless of the amount of disorder.

(b) d = 2

The case of two dimensions is a marginal one and is thus particularly interesting. To briefly describe the predictions of scaling theory we again notice that β is always negative. Although it can be seen that at infinite values of g the β approaches zero. Despite this it is again quite clear that scaling theory predicts that states will always be localized and hence insulating at large enough length scales. Thus scaling theory of electron localization predicts that for a system of non-interctacting electrons in zero magnetic field there can be no truly metallic state. Despite this recently experiments have shown that certain two dimensional systems exhibit metallic type behaviour.

(c) d = 3

The case of three dimensions is, of course, the most relevant to the work presented in this thesis. We can see from figure 3.14 unlike the other two cases described above β

can have both negative and positive values. Thus by necessity β must cross the g axis so there exists a critical value of g we will call g_c. If for example $g > g_c$ the value of β is positive and on increasing the length scale slightly g increases and the value β becomes slightly greater in a positive sense, continuing this to the asymptotic limit of large length scales we reach β = 1 and the system is metallic, electron wavefunctions are extended. Conversely if we start with a situation where $g < g_c$ we have β negative and the value for g decreases as we increase the length scale and the material is an insulator and the electron wavefunction is exponentially localized.

The critical point $g = g_c$ is the point at which a metal-insulator transition occurs, it is an unstable fixed point, this means that if we move slightly in either direction so that β is a small positive or negative number the scaling of the conductance approaches asymptotically one of two qualitatively different regimes.

One of the reasons that scaling theory provides such a useful description of MITs is that using it we can in the same way describe the behaviour of a sample on either side of the transition, (provided that we are sufficiently close to the transition).

$$\sigma = \sigma_0 \left(\frac{n}{n_c} - 1 \right)^{\nu} \qquad \textbf{Equation 3.17}$$

$$\xi = \xi_0 \left(\frac{n_c}{n_c - n} \right)^{\nu} \qquad \textbf{Equation 3.18}$$

The equations above 3.17 and 3.18 describe the scaling behaviour of both the conductivity and the localization length close to the MIT.

3.2.3 Experiment

After discussing the theory associated with the MIT we will now examine the details and results from some of the experimental studies that have been carried out to probe the critical region around the MIT. We shall focus our attention on doped semiconductors, as this is the system studied in the present work, however a great many other systems have been studied.

3.2.3.1 Discretely Doped Samples

Some of the earliest work was carried out by studying the properties of semiconductor samples that had been prepared having different doping levels. Measurements made on Si:P have been performed by Rosenbaum *et al* [29, 30]. We reproduce their experimental data obtained from conductivity measurements on metallic samples in figure 3.15. It can be seen immediately from the figure that the conductivity at T = 0 K drops very sharply at the critical carrier concentration. Despite this three of the samples they measure have values of $\sigma(T = 0\ K)$ below the Mott minimum metallic conductivity, clearly this experimental data suggests that $\sigma(T = 0\ K)$ scales continuously to zero in contrast to the discontinuous transition predicted by Mott. Measurements of the dielectric constant for samples on the insulating side of the transition were also made and it was shown that data on both side of the MIT could be described by scaling theory, they found the critical exponent, $\nu = 0.55 \pm 0.5$.

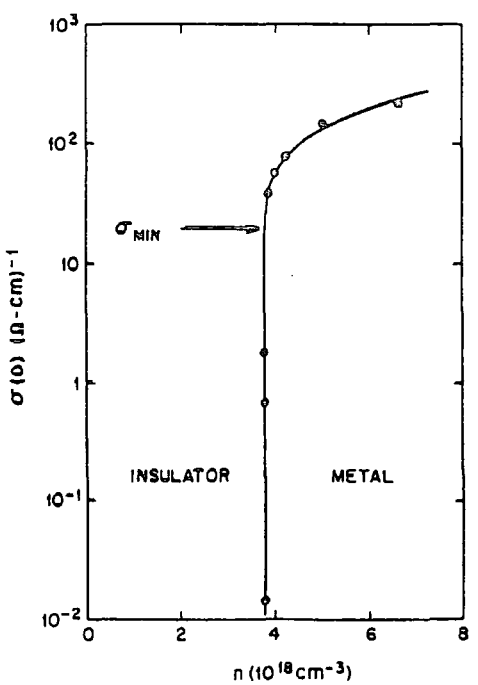

Figure 3.15 - Plot of zero temperature conductivity against donor density for metallic samples of Si:P after [30]. Their calculated value for the Mott minimum metallic conductivity is shown and the solid line is a fit to the data using scaling theory (equation 3.17)

To ensure that the distribution of dopant atoms is random throughout a semiconductor Watanabe *et al* [31] have used a process known as neutron transmutation doping (NTD)

to study samples of ^{70}Ge:Ga. The samples they have studied are nominally uncompensated and their analysis resulted in a value for the critical exponent close to 0.5.

There are two main inherent disadvantages to studying the MIT with discrete doped samples. Firstly effects due to differences in the disorder from one sample to another can never be completely removed. This problem is particularly apparent in compensated semiconductors where the amount of compensation may vary between samples. Secondly a high degree of control over the doping process is required in order to study the region extremely close to the MIT.

One way to overcome these difficulties is to study the MIT by some fine tuning method. We shall now look at three possible ways to fine tune the MIT in a single sample.

3.2.3.2 Stress Tuning

One way to fine tune the MIT is by applying stress to the samples studied. This was first carried out for the case of Si:P by Paalanen *et al* [32, 33]. Data are shown in figure 3.16 for measurements made on both the metallic and the insulating side of the transition.
In experiments of this type the value of n_c is changed via the application of fairly modest stresses. In this way the MIT is tuned as a result of varying n_c in a sample where n remains constant. The critical exponent was determined to be close to 0.5.

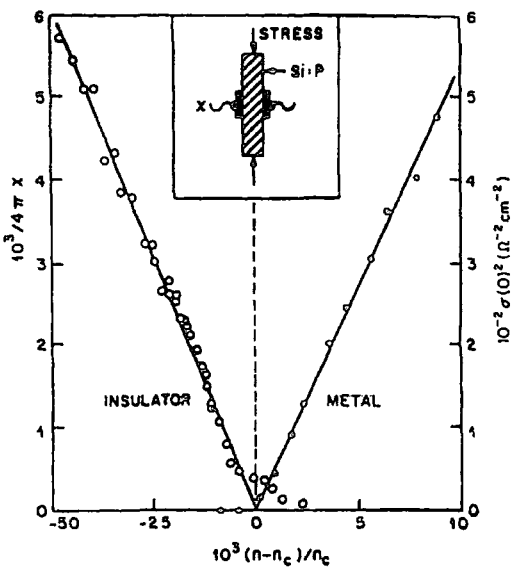

Figure 3.16 - Plot showing the scaling behaviour for samples of Si:P on the metallic and the insulating side of the MIT after [33].

Measurements have been made in a similar way on Si:B [34] and it was found that the value of the critical exponent was different depending on how the transition was studied. They found $\nu = 1.6$ for the stressed tuned study and $\nu = 0.65$ for the doping dependent measurements.

3.2.3.3 Field Tuning

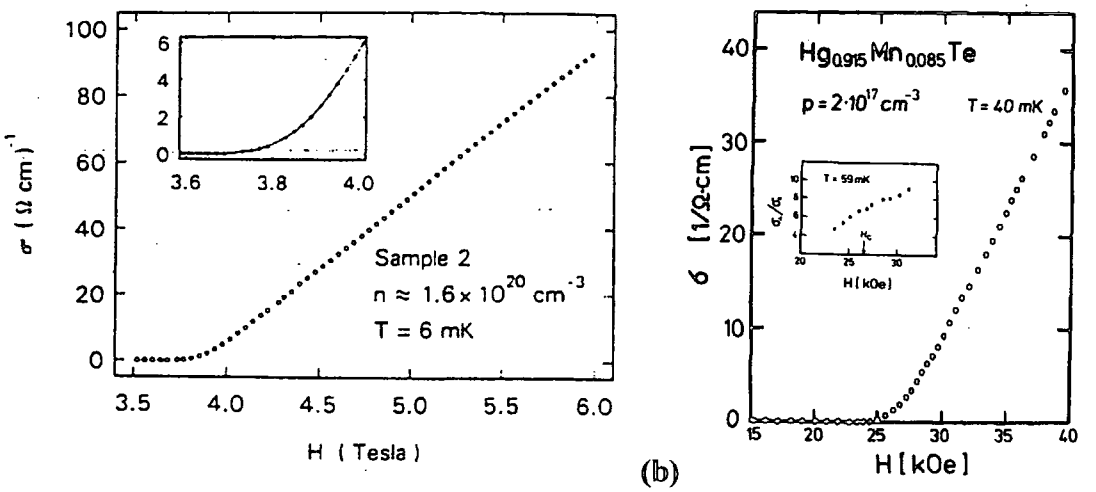

Figure 3.17 - Field tuning the MIT in (a) the magnetic semiconductor $Gd_{3-x}V_xS_4$ after [35] (b) the dilute magnetic semiconductor $Hg_{1-x}Mn_xTe$ after [18]

A field driven MIT has been measured in the magnetic semiconductor $Gd_{3-x}V_xS_4$ by von Molnár *et al* [35] and in the DMS n-CdMnSe and p-HgMnTe by Wojtowicz *et al* [36] (see figure 3.17). It should be noted that the large negative MR and hence the field driven IMT is opposite to the situation observed in a great many other non-magnetic semiconductors. In non-magnetic semiconductors a postive MR is seen resulting from the diamagnetic shrinkage of the donor electron wavefunction, in these materials a MIT can be observed on increasing field.

3.2.3.4 Fine Tuning Using Persistent Photoconductivity

In AlGaAs:Si Katsumoto *et al* [37, 38] investigated the MIT by making use of the PPC effect (already described in section 2.4). They found a critical exponent close to 1 for measurements made both in zero field and in an applied field of 4T (see figure 3.18a). PPC was also used to study the MIT in the DMS CdMnTe:In [39] data from this work are reproduced in figure 3.18b. Again an exponent close to 1 was determined and this represented the first study of a DMS in zero applied magnetic field.

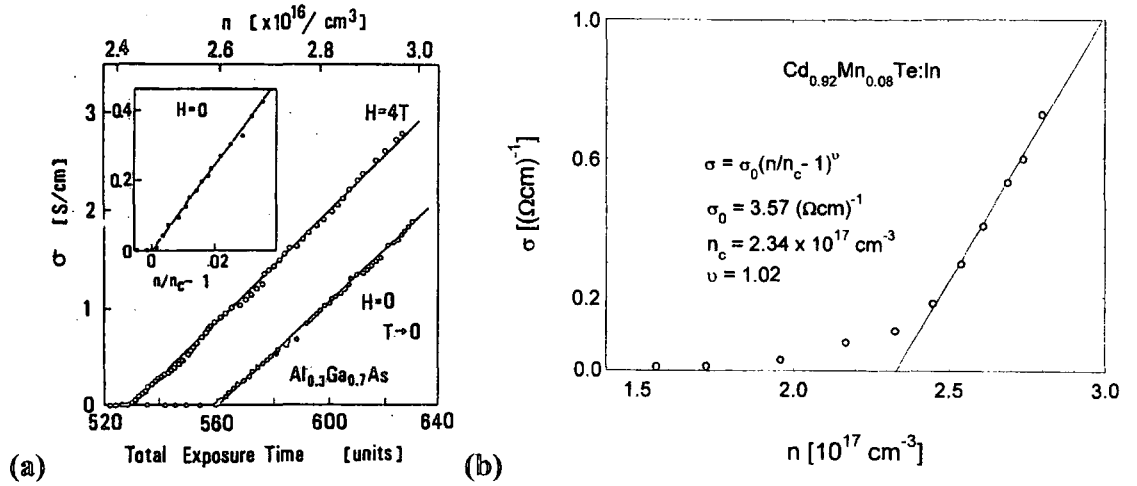

Figure 3.18 - Tuning the MIT using PPC in, (a) $Al_xGa_{1-x}As$:In after [37] (b) the dilute magnetic semiconductor $Cd_{1-x}Mn_xTe$:In after [39]

3.2.3.5 Open Questions

Despite the large body of theoretical and experimental work carried out to study the MIT a number of questions still remain unanswered. One such question concerns the value of the critical exponent. An anomalous value close to ½ has been found experimentally in n type Si, this unexplained result has become known as the "critical exponent puzzle". A great amount of time has been spent trying to understand this, as yet unresolved, problem. One suggestion is that experimental determinations of the critical exponent are extremely sensitive to the region over which the particular study is made. The scaling theory equations are known to only be valid close to the MIT, although it is not exactly clear how far from the transition the critical region extends.

It is now generally accepted that the MIT is continuous, however there remains the suggestion by some authors, such as Mobius *et al* [40], that the idea of a minimum metallic conductivity is still applicable.

3.3 Electrical Properties of Dilute Magnetic Semiconductors

In the following sections we describe the electrical transport properties of relevance dilute magnetic semiconductors close to the metal insulator transition. Section 3.3.1 deals with the insulating side of the MIT and thus concerns electrical transport proceeding via hopping conduction. After a brief general introduction and some details of nearest neighbour hopping (section 3.3.1.1) we examine variable range hopping theory both due to Mott and to Efros & Shklovskii (section 3.3.1.2). Quantum corrections to the conductivity resulting from weak localisation on the metallic side of the MIT are outlined in section 3.3.2. Finally, section 3.3.3 gives details of magnetoresistance relevant to DMS close to the MIT.

3.3.1 The Insulating Side of the Metal Insulator Transition - Hopping Conduction

In a system where the Fermi energy lies below the mobility edge there are two possible ways in which conduction can occur. At finite temperatures conduction in an insulator can either be as a result of activation to energies above the mobility edge or via phonon assisted tunnelling. This phonon assisted tunnelling or hopping conduction occurs when an electron receives energy from (gives energy to) a phonon allowing it to hop to a nearby state with a slightly higher (lower) energy. A requirement for this form of hopping process to take place is that there must be both empty and occupied states close to the Fermi energy for the electrons to tunnel between. In this regime the DC electrical conductivity has the form given below.

$$\sigma(n,\mathrm{T}) = \sigma_1 \exp\left(-\frac{\mathrm{E}_1}{\mathrm{T}}\right) + \sigma_2 \exp\left(-\frac{\mathrm{E}_2}{\mathrm{T}}\right) + \sigma_3 \exp\left(-\frac{\mathrm{E}_3}{\mathrm{T}}\right) + \sigma_{VRH}(n,\mathrm{T})$$

Equation 3.19

In equation 3.19 the three different energies ($E_1 > E_2 > E_3$) correspond to three different processes. Traditionally E_1 denotes activation to the conduction band. E_2 represents activation to the upper Hubbard band. We can think of this process as being related to the motion of electrons over neutral donor impurities. Of greatest interest to us are the final two terms. E_3 is the energy associated with hopping conduction, where an electron

(hole) hops to an unoccupied donor (acceptor) site. If the temperature is low enough the form of the hopping conduction will change from nearest neighbour hopping (NNH) to variable range hopping (VRH). The fourth term (due to VRH) in equation 3.19 will be described in more detail in section 3.3.1.2.

Results of experiments after Fritzsche [41] are shown in figure 3.19. The temperature dependence of the resistivity was measured for p-type Ge:Ga samples prepared by neutron transmutation doping.

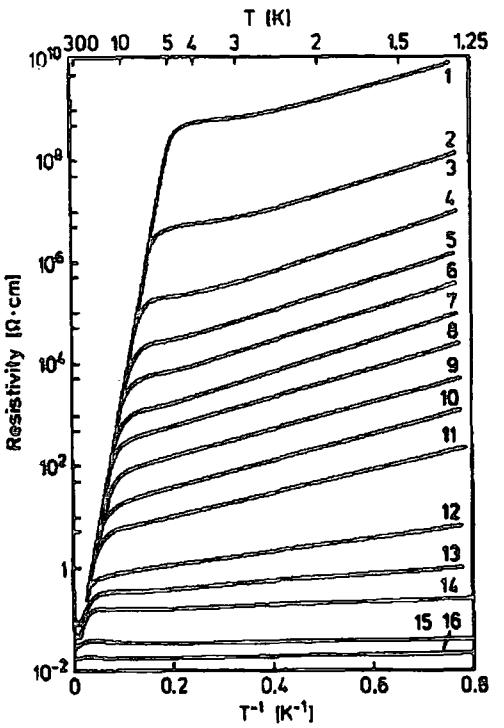

Figure 3.19 - Plot resistivity on a log scale against inverse temperature for samples of Ge:Ga having different doping levels. In the figure the labels 1 to 16 correspond to acceptor densities in the range 7.5×10^{14} cm^{-3} to 1.35×10^{18} cm^{-3}, see Fritzsche *et al* [41].

Of interest to the work in this thesis is the behaviour of the electrical conductivity as the MIT is approached from the insulating side. A review of hopping transport in the critical regime is given by T G Castner [42]. Experimental studies have given information about the carrier density dependence of the three energies mentioned above [43]. E_1 is seen to decrease slightly but remains finite as the MIT is approached (ie as $n \rightarrow n_c$). In the dilute limit $E_2 \sim E_1$, however as $n \rightarrow n_c$ the value of E_2 rapidly decreases to zero. The impurity density dependence of E_3 is given by,

$$E_3 = \frac{0.99e^2 N_D^{1/3}}{\kappa} \qquad \text{Equation 3.20}$$

where κ is the dielectric constant. This simple expression shows that E_3 increases slowly with N_D and has been observed experimentally at low densities, as $n \rightarrow n_c$ E_3 is seen to dramatically decrease towards zero. This decrease can be understood by considering the behaviour of the dielectric constant, which diverges as the MIT is approached. It is also important to appreciate that the values E_1, E_2, E_3 and σ_3 all vary as a function of the compensation ratio, K. Generally observation of E_2 conduction (often over a narrow temperature range) is most likely to occur when the concentration of neutral donors is large and the compensation is low. In the case of a semiconductor which is completely uncompensated hopping conduction cannot occur and E_3 conduction is absent. Adding compensating centres to this system would increase the contribution from E_3 conduction while decreasing the contribution from E_2 conduction. Experimentally the dependence of the activation energy E_3 on compensation was discussed by Mott and Twose [44]. Data for p-type samples having the same doping level, but with different levels of compensation are shown in figure 3.20.

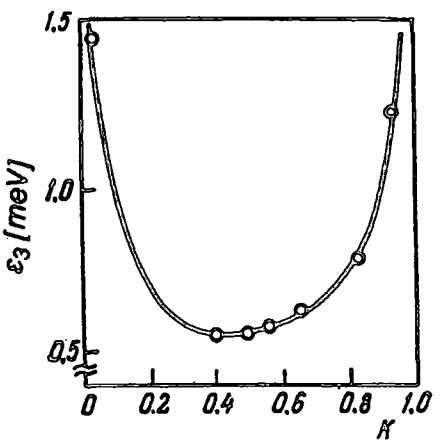

Figure 3.20 - Compensation dependence of the activation energy E_3 for experimental data on p-type samples. After Mott and Twose [44].

3.3.1.1 Nearest Neighbour Hopping (NNH)

The phenomenon of nearest neighbour hopping was first described by Miller and Abrahams [45]. They considered the overlap of the electron wavefunctions of individual donor (acceptor) atoms. Calculating the probability that an electron "hops" between two donors, from state i to state j, emitting or absorbing a phonon. This leads to a resistance R_{ij} between the two states, and thus the problem can be considered in terms of a network of resistors, where the resistance connecting the two sites i and j is given by,

$$R_{ij} = R_{ij}^{0} \exp(\xi_{ij})$$ **Equation 3.21**

If the impurity atom has an electron wavefunction of the form,

$$\psi = (\pi a^3)^{-1/2} \exp\left(-\frac{r}{a}\right)$$ **Equation 3.22**

then we can write,

$$\xi_{ij} = \frac{2r_{ij}}{a} + \frac{\varepsilon_{ij}}{k_B T}$$ **Equation 3.23**

where ε_{ij} is related to the energies ε_i and ε_j of the initial and final sites of the "hop" measured with respect to the Fermi energy. r_{ij} is the spatial separation of the initial and final states, known as the hopping length.

$$\rho = \rho_{03} \exp\left(\frac{\alpha}{N^{1/3}a}\right) \exp\left(\frac{E_3}{kT}\right) = \rho_3 \exp\left(\frac{E_3}{kT}\right)$$ **Equation 3.24**

$$\rho_{03} = \frac{27\pi d v^5 \hbar^4 a^3 \kappa^2 kT}{2e^6 E_{dp}^2 E_3} \left(N^{1/3}a\right)^{0.15} Q(N)$$ **Equation 3.25**

with v the longitudinal velocity of sound, d the density and κ the dielectric constant. The parameter E_{dp} in equation 3.25 above is known as the deformation potential and is a material constant that relates the energy of an electron to compression or dilation of the crystal lattice.

where $Q(N) = \left[1 + \left(\frac{\eta_2 E_3 a}{2\hbar v}\right)^2\right]^4$ with η_2 a numerical constant of order unity.

3.3.1.2 Variable Range Hopping (VRH)

At very low temperatures it can become energetically favourable for electrons to tunnel further than a nearest neighbour impurity. As a result of hopping over a larger distance the initial and final states can be much closer in energy. In this VRH regime the temperature dependence of the resistivity depends strongly on the energy dependence of the density of states close to the Fermi energy (E_F). Following on from the work of Miller and Abrahams, Mott in 1968 [46] obtained,

$$\sigma(T) = \sigma_0 \left(\frac{1}{T}\right)^s \exp\left[-\left(\frac{T_0}{T}\right)^p\right]$$ **Equation 3.26**

where the exponent, p = 1/(d+1), here d is the dimensionality of the system, thus p = ¼ in 3 dimensions. The results of Mott are based on a constant (or at least slowly varying) density of states close to E_F. Mott derived expressions for the characteristic temperature T_0, in addition to the mean hopping length and the mean hopping energy. These are given below [42].

$$T_0 = \frac{\beta}{k_B N(E_F) a^3(n)}$$ **Equation 3.27**

$$\overline{R}_{hop}(T) \approx \frac{3}{8} a^3 \left(\frac{T_0}{T}\right)^{1/4}$$ **Equation 3.28**

$$\overline{\Delta}_{hop}(T) \approx \frac{1}{4} k_B T^{1/4} T_0^{1/4}$$ **Equation 3.29**

Later Efros and Shklovskii (ES) [47] showed that as a result of electron-electron interaction the density of states is reduced to zero at the Fermi energy. Close to the Fermi energy the single particle density of states has a parabolic energy dependence. This behaviour is commonly referred to as a soft Coulomb gap, in contrast to a hard gap where the DOS is zero over a finite range of energies. ES showed that the temperature dependence of the resistivity could be given by,

$$\sigma(T) = \sigma_0 \left(\frac{1}{T}\right)^s \exp\left[-\left(\frac{T_0'}{T}\right)^p\right]$$ **Equation 3.30**

this is the same as equation 3.26 except that the characteristic temperature is now denoted by T_0', which is given by,

$$T_0' = \frac{2.8e^2}{\kappa(n) k_B \xi(n)}$$ **Equation 3.31**

where κ is the dielectric constant and ξ is the localization length. In the ES case the exponent p = ½ regardless of the dimensionality of the system. Once again we give the

expressions for the mean hopping length and the mean hopping energy that result from their calculations,

$$\overline{R'}_{hop}(T) \approx \frac{1}{4} a(n) \left(\frac{T_0'}{T} \right)^{1/2} \qquad \text{Equation 3.32}$$

$$\overline{\Delta'}_{hop}(T) \approx \frac{1}{2} k_B T^{1/2} T_0'^{1/2} \qquad \text{Equation 3.33}$$

As described above we expect that on reduction of the temperature the form of conduction will change from NNH to VRH. The critical temperature (T_c) at which this crossover occurs has been estimated by a number of different authors. We can write,

$$T_c = C \frac{E_3 N^{1/3} a}{k_B} \qquad \text{Equation 3.34}$$

Where C is a numerical constant. ES suggested that $C = 0.53$ [48]. While Pollak found the value to be an order of magnitude larger, $C = 5.3$ [49]. The level of doping is also of relevance to the form of hopping conduction observed, experimental data suggests [50] that when $(N_D^{1/3}a)^{-1}$ is greater than 5 NNH is only seen over a limited temperature range. For values of $(N_D^{1/3}a)^{-1}$ less than 5 only VRH is observed and there is no NNH

The theoretical ideas outlined above have been observed experimentally in a variety of different semiconducting and amorphous systems (see for example [50]).

3.3.2 The Metallic Side of the Metal Insulator Transition – Quantum Corrections to the Conductivity

In weakly disordered metals at low temperatures the quantum mechanical nature of electrons must be considered in order to accurately describe the electrical transport properties. In this regime the temperature dependence of the conductivity can be described by two separate quantum corrections to the Boltzmann conductivity. For a review see reference [28], we can write,

$$\sigma(T) = \sigma(0) + mT^{1/2} + BT^{p/2} \qquad \text{Equation 3.35}$$

On the right side of equation 3.23 the second term is due to electron-electron interaction [51] and the final term is a correction which comes from the effect of weak localization [52]. The term $\sigma(0)$ gives the value of the conductivity at T = 0 K.

At low temperatures it is possible that the mean free path of the electron is smaller than the phase coherence length. In this regime the effects of interference must be taken into account in order to explain the properties observed experimentally.

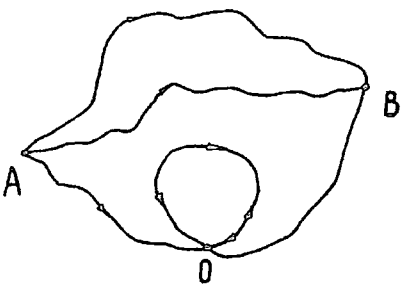

Figure 3.21 - Self interacting path between point A and point B intersecting at point O.

Figure 3.21 shows schematically a number of different possible paths that could be taken by a particle propagating from point A to point B. The probability of a particle passing from point A to B is obtained by summing the probabilities of all the different possible paths. In general (as for the upper two paths shown in figure 3.21) the effect of interference is unimportant because the path lengths and hence the wavefunction phases vary. As a result of summing over all paths the interference term averages to be zero. For certain self interacting paths (the low path shown in figure 3.21 intersects at a point labelled O) the effect of interference is not negligible. In the case of the self interacting path the loop can be traversed in either direction. This provides two different paths in which the phase coherence remains. Calculating the effect of this interference for time reversed paths yields an increased probability of the particle being backscattered, and hence localized. It is this weak localization that gives rise to the $BT^{p/2}$ term in equation 3.23 above. The exponent p describes the temperature dependence of the scattering rate for the dominant dephasing mechanism. $\tau_\phi^{-1} \propto T^p$ [52].

As the temperature is increased the weak localization effect is reduced rapidly. In addition the application of a relatively small magnetic field suppresses the effect, this is due to the fact that a magnetic field destroys the phase coherence required for weak localization.

We now consider the other quantum correction which is due to electron-electron interaction. The $mT^{1/2}$ term was calculated by Alshuler and Aronov from considerations of the influence of electron-electron interaction on the density of states. For a review see reference [53] or [28]. The value of m is given by,

$$m = \alpha\left[\frac{4}{3} - \frac{3}{2}\gamma F_\sigma\right] \qquad \text{Equation 3.36}$$

where,

$$\alpha = \frac{1.3e^2}{4\pi^2\hbar}\left(\frac{k_B}{2\hbar D}\right)^{\frac{1}{2}} \qquad \text{Equation 3.37}$$

D is the diffusion constant, and F_σ is related to the Fermi liquid parameter in a way that is dependent on the dimensionality of the system [28].

3.3.3 Magnetoresistance in Dilute Magnetic Semiconductors

In this section we introduce some of the possible mechanisms that can cause magnetoresistance (MR) in materials. In particular we shall focus on the effects observed in DMS as these are of prime interest to us and they can also be quite different from the more ordinary forms of MR seen in other non-magnetic materials. Prior to describing the magnetoresistive properties of DMS we shall briefly introduce the mechanisms at work in non-magnetic materials. Quite generally MR refers to any change in the resistivity of a material when a magnetic field is applied. This change in resistivity, $\Delta\rho$, can be positive or negative depending on the mechanism at work. It is quite common to observe positive MR in an ordinary material such as a metal or some semiconductors, this form of MR is due to the Lorentz force experienced by a charge carrier in a magnetic field. This can be understood in a similar fashion to the classical description of the Hall effect. The observed effect gives an increase in resistance which has a quadratic dependence on applied magnetic field.

$$\frac{\Delta\rho}{\rho} \propto B^2 \qquad \text{Equation 3.38}$$

This effect is normally found to be rather small, and is often swamped by larger contributions to the MR, some of which will now be briefly described in the subsequent sections.

3.3.3.1 Magnetoresistance in the Hopping Regime

In the insulating phase of some materials a positive MR (PMR) has been observed. On going to higher applied magnetic fields negative MR (NMR) has been observed. The PMR can be understood in terms of the diamagnetic shrinking of the electron wavefunction. If we consider the case of an impurity band in a doped semiconductor in a regime where the transport proceeds via some form of hopping conduction, the resistivity of the material is determined, in part, by the amount of overlap between electron wavefunctions. The shrinking of the electron wavefunctions in an applied field results in a reduction of this overlap, thus a decreased hopping probability. This results in the observed PMR which has a strong temperature dependence. For the case of VRH conduction and weak magnetic fields the PMR can be expressed as [42],

$$\ln\frac{\rho(H)}{\rho(0)} = t\left(\frac{a_B}{\lambda}\right)^4\left(\frac{T_0}{T}\right)^y \qquad \textbf{Equation 3.39}$$

here a_B is the Bohr radius and λ is the magnetic length given by,

$$\lambda = \left(\frac{c\hbar}{eH}\right)^{1/2} \qquad \textbf{Equation 3.40}$$

Equation 3.39 can be used for both the Mott's law and the ES form of VRH. In the Mott's law (ie constant DOS close to E_F) the exponent $y = 3/4$ and the numerical constant $t = 0.0025$. For low field PMR in the ES VRH regime (ie parabolic DOS at E_F) $y = 3/2$ and $t = 0.0015$.

Thus at a constant temperature this form of PMR has a field dependence described by equation 3.41.

$$\frac{\Delta\rho}{\rho} \propto \exp\left(B^2\right) \qquad \textbf{Equation 3.41}$$

For a fixed magnetic field $\frac{\Delta\rho}{\rho} \propto \exp\left(T^{-1/4}\right)$ for a system without electron-electron interactions and $\frac{\Delta\rho}{\rho} \propto \exp\left(T^{-1/2}\right)$ if interactions are important.

3.3.3.2 Magnetoresistance in the Weakly Localized Regime

When a material is just on the metallic side of the MIT (ie when n is slightly greater than n_c) it is said to be in the Weakly Localized Regime (WLR). This is a regime where the effects of electron-electron interactions and interference are of great importance. As described above the localization of electrons is due to the destructive interference of the electron wavefunction. In certain circumstances this interference leads to a reduction in the probability that the electron motion is diffusive. In this way the electron is effectively backscattered and hence localized In the WLR a negative MR is often observed.

$$\frac{\Delta\rho}{\rho} \propto B^{1/2} \qquad \text{Equation 3.42}$$

This negative MR arises due to the fact that that the magnetic field destroys the phase coherence required to produce the weak localizing effect.

3.3.3.3 Magnetoresistance of Dilute Magnetic Semiconductors

The two forms of MR that have been described in the sections above can be present in non-magnetic materials. Both these effects are observed in measurements of n-CdSe, as have been carried out by Dietl *et al* [54], we reproduce their data in figure 3.22. We can see from the figure that as the electron concentration is decreased the MR changes from being all negative, to negative MR at low fields followed by positive MR at higher fields. Dietl *et al* linked this change in the form of the MR with the carrier concentrations passing through the critical carrier density n_c. They attributed the positive MR to reduced hopping conduction as a result of diamagnetic shrinkage of the electron wavefunction. A similar conclusion was drawn, also from measurements on n-CdSe by Finlayson *et al* [55]. For the negative MR seen in the WLR Sawicki *et al* [56] carried out a quantative analysis which contained two components, firstly the effect of a magnetic field on the coherent backscattering responsible for weak localization (see above) and secondly an effect relating to electron-electron interaction.

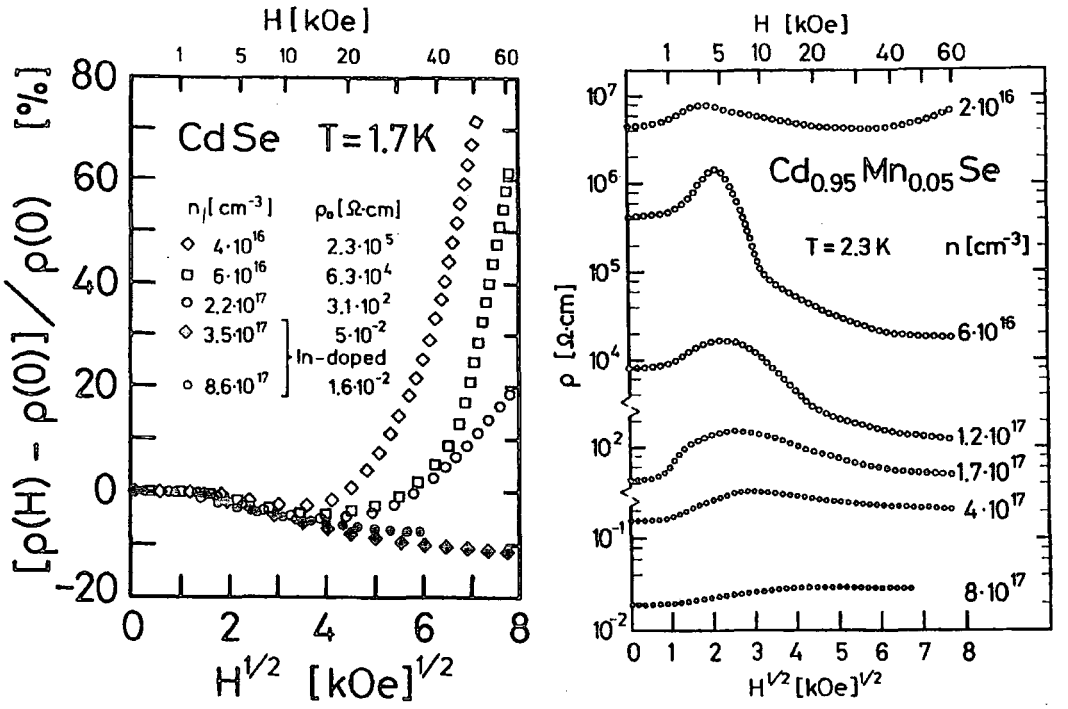

Figure 3.22 - Magnetoresistance of n-CdSe plotted as a function of square root of applied magnetic field at a temperature T = 1.7 K. Data are presented for five different electron concentrations after [54]

Dietl *et al* also measured the MR of n-CdMnSe, their results are shown in figure 3.23 for two samples having different electron concentrations. We can immediately see that adding a small amount of magnetic ions to this system causes very different and much larger MR. Their data shows MR which is positive at low fields reaches maximum and then decreases as negative MR at high fields.

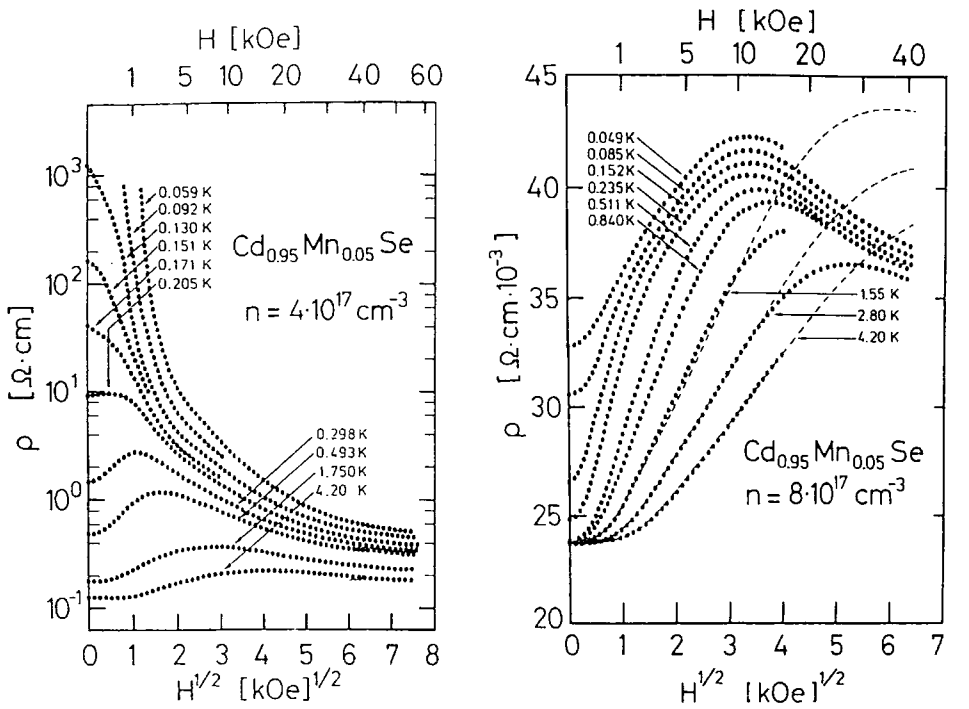

Figure 3.23 - Magnetoresistance of n-CdMnSe plotted at various temperatures against square root of applied magnetic field. Data are presented for two different samples having electron concentrations (a) n = 4x10^{17} cm^{-3} (b) n = 8x10^{17} cm^{-3} after [54]

In a magnetic material the charge carriers can be scattered by their interaction with localized randomly aligned magnetic moments. These localized moments may be localized electrons or the moments associated with magnetic ions within the material. The scattering rate for this spin disorder scattering can be greatly reduced when the localized moments are aligned in an applied magnetic field, this leads to negative MR. It has been shown that the formation of BMPs can greatly enhance the spin disorder scattering rate [56, 57]. The destructive effect of a magnetic field on BMPs can in a similar fashion produce a negative MR.

In DMS the total spin splitting is given by,

$$h\omega_s = g^* \mu_B H + \frac{\alpha}{g\mu_B} M_0(T,H) \qquad \textbf{Equation 3.43}$$

where M_0 is the macroscopic magnetization, α is the s-d exchange integral and g^* is the Lande splitting factor for the electrons. The first term on the right side of equation 3.43 describes the ordinary Zeeman splitting of the conduction band and the second term gives the exchange induced spin splitting. Typically in a DMS at low temperatures this second term can be many hundreds of times larger than the Zeeman term.

One effect that the large spin-splitting has is to cause a redistribution of carriers between two polarized spin subbands. The redistribution of electrons results in a shift in the Fermi energy relative to the mobility edge. As the mobility of electrons is a function of their energy this can lead to another mechanism for MR.

3.4 References

1. Oseroff, S.B., *Magnetic-Susceptibility and Electron-Paramagnetic-Res Measurements in Concentrated Spin-Glasses - $Cd_{1-x}Mn_xTe$ and $Cd_{1-x}Mn_xSe$.* Physical Review B-Condensed Matter, 1982. **25**(11): p. 6584-6594.
2. Oseroff, S. and P.H. Keesom, *Magnetic Properties: Macroscopic Studies*, in *Semiconductors and Semimetals*, J.K. Furdyna and J. Kossut, Editors. 1988, Academic Press. p. 73.
3. Gaj, J.A., R. Planel, and G. Fishman, *Relation of Magneto-optical Properties of Free Excitons to Spin Alignment of Mn^{2+} Ions in $Cd_{1-x}Mn_xTe$.* Solid State Comm, 1979. **29**: p. 435-438.
4. Villain, J., *Insulating Spin-Glasses.* Zeitschrift Fur Physik B-Condensed Matter, 1979. **33**(1): p. 31-42.
5. Aharony, A., *Low-Temperature Phase-Diagram and Critical Properties of a Dilute Spin Glass.* Journal of Physics C-Solid State Physics, 1978. **11**(11): p. L457-L463.
6. Deseze, L., *Antiferromagnetic Dilute Bond Ising-Model Exhibiting a Spin- Glass Phase-Transition.* Journal of Physics C-Solid State Physics, 1977. **10**(12): p. L353-L356.
7. Oseroff, S. and F. Acker, *Magnetic-Susceptibility On Semimagnetic Semiconductors.* Solid State Communications, 1981. **37**(1): p. 19-23.
8. Oseroff, S. and F.G. Gandra, *Time, Temperature, and Field-Dependence of the Remanent Magnetization in $Cd_{1-x}Mn_xTe$.* Journal of Applied Physics, 1985. **57**(8): p. 3421-3423.
9. Novak, M.A., *et al.*, *Spin-Glass Behavior of $Cd_{1-x}Mn_xTe$ Below the Nearest-Neighbor Percolation Limit.* Journal of Applied Physics, 1985. **57**(8): p. 3418-3420.
10. Karaoulanis, D., J.P. Xanthakis, and C. Papatriantafillou, *The nature of the magnetic phase of diluted magnetic semiconductors below the nearest-neighbour percolation threshold.* Journal of Magnetism and Magnetic Materials, 1996. **161**: p. 231-234.
11. Furdyna, J.K., *Diluted Magnetic Semiconductors.* Journal of Applied Physics, 1988. **64**(4): p. R29-R64.

12. Coey, J.M.D., M. Viret, and S. von Molnar, *Mixed-valence manganites.* Advances in Physics, 1999. **48**(2): p. 167-293.

13. Nawrocki, M., *et al.*, *Exchange-Induced Spin-Flip Raman-Scattering in a Semimagnetic Semiconductor.* Physical Review Letters, 1981. **46**(11): p. 735-738.

14. Peterson, D.L., *et al.*, *Spin-Flip Raman-Scattering in Normal-Type Diluted Magnetic Semiconductors.* Physical Review B-Condensed Matter, 1985. **32**(1): p. 323-340.

15. Dietl, T. and J. Spalek, *Effect of Fluctuations of Magnetization On the Bound Magnetic Polaron - Comparison With Experiment.* Physical Review Letters, 1982. **48**(5): p. 355-358.

16. Heiman, D., P.A. Wolff, and J. Warnock, *Spin-Flip Raman-Scattering, Bound Magnetic Polaron, and Fluctuations in (Cd,Mn)Se.* Physical Review B-Condensed Matter, 1983. **27**(8): p. 4848-4860.

17. von Molnar, S., *et al.*, *Local Magnetization and Magnetotransport in Magnetic Semiconductors.* Physica B, 1994. **197**(1-4): p. 151-157.

18. Dietl, T., *et al.*, *Interaction Effects Near the Metal-Insulator Transition in Semimagnetic Semiconductors*, in *Anderson Localization*, T. Ando and H. Fukuyama, Editors. 1987, Springer-Verlag. p. 58.

19. Koshihara, S., *et al.*, *Photocarrier induced ferromagnetic order in III-V-based magnetic semiconductor heterostructures of (In,Mn)As/GaSb.* Physica E, 1998. **2**(1-4): p. 417-420.

20. Wojtowicz, T., *et al.*, *Magnetization of Bound Magnetic Polarons - Direct Determination Via Photomemory Effect.* Physical Review Letters, 1993. **70**(15): p. 2317-2320.

21. Enichlmair, H., *et al.*, *Light-Induced Magnetization in* $Hg_{1-x}Cd_xTe$. Journal of Crystal Growth, 1992. **117**(1-4): p. 844-849.

22. Awschalom, D.D., J. Warnock, and S. Vonmolnar, *Low-Temperature Magnetic Spectroscopy of a Dilute Magnetic Semiconductor.* Physical Review Letters, 1987. **58**(8): p. 812-815.

23. Mott, N.F., *The Basis of the Electron Theory of Metals, with Special Reference to the Transition Metals.* Proceedings of the Royal Society A, 1949. **62**: p. 416-422.

24. Edwards, P.P. and M.J. Sienko, *Universality Aspects of Metal-Nonmetal Transition in Condensed Media.* Physical Review B, 1978. **17**(6): p. 2575-2581.

25. Anderson, P.W., *Absence of Diffusion in Certain Random Lattices.* Physical review B, 1958. **109**(5): p. 1492-1505.
26. Wegner, C., Z. Phys., 1976. **B25**: p. 327.
27. Abrahams, E., *et al.*, *Scaling Theroy of Localization: Absence of Quantum Diffusion in Two Dimensions.* Physical Review Letters, 1979. **42**(10): p. 673-676.
28. Lee, P.A. and T.V. Ramakrishnan, *Disordered Electronic Systems.* Reviews of Modern Physics, 1985. **57**(2): p. 287-337.
29. Rosenbaum, T.F., *et al.*, *Metal-Insulator-Transition in a Doped Semiconductor.* Physical Review B-Condensed Matter, 1983. **27**(12): p. 7509-7523.
30. Rosenbaum, T.F., *et al.*, *Sharp Metal-Insulator Transition in a Random Solid.* Physical Review Letters, 1980. **45**(21): p. 1723–1726.
31. Watanabe, M., *et al.*, *Metal-insulator transition of isotopically enriched neutron- transmutation-doped Ge-70 : Ga in magnetic fields.* Physical Review B-Condensed Matter, 1999. **60**(23): p. 15817-15823.
32. Paalanen, M.A., *et al.*, *Stress Tuning of the Metal-Insulator-Transition At Millikelvin Temperatures.* Physical Review Letters, 1982. **48**(18): p. 1284-1287.
33. Paalanen, M.A., *et al.*, *Critical Scaling of the Conductance in a Disordered Insulator.* Physical Review Letters, 1983. **51**(20): p. 1896-1899.
34. Bogdanovich, S., M.P. Sarachik, and R.N. Bhatt, *Conductivity of metallic Si : B near the metal-insulator transition: Comparison between unstressed and uniaxially stressed samples.* Physical Review B-Condensed Matter, 1999. **60**(4): p. 2292-2298.
35. von Molnar, S., *et al.*, *Electron Localization in a Magnetic Semiconductor - $Gd_{3-x}v_xS4$.* Physical Review Letters, 1983. **51**(8): p. 706-709.
36. Wojtowicz, T., *et al.*, *Metal-Insulator-Transition in Semimagnetic Semiconductors.* Physical Review Letters, 1986. **56**(22): p. 2419-2422.
37. Katsumoto, S., *The Metal-Insulator Transition in a Persistent Photoconductor*, in *Anderson Localization*, T. Ando and H. Fukuyama, Editors. 1987, Springer-Verlag. p. 45-52.
38. Katsumoto, S., *et al.*, *Fine Tuning of Metal-Insulator-Transition in $Al_{0.3}Ga_{0.7}As$ Using Persistent Photoconductivity.* Journal of the Physical Society of Japan, 1987. **56**(7): p. 2259-2262.
39. Leighton, C., I. Terry, and P. Becla, *Metal-insulator transition in the persistent photoconductor $Cd_{1-x}Mn_xTe:In$.* Europhysics Letters, 1998. **42**(1): p. 67-72.

40. Mobius, A., *et al.*, *Metal-insulator transition in amorphous $Si_{1-x}Ni_x$: Evidence for Mott's minimum metallic conductivity.* Physical Review B-Condensed Matter, 1999. **60**(20): p. 14209-14223.
41. Fritzsche, H. and M. Cuevas, *Impurity conduction in transmutation-doped p-type germainium.* Physical Review, 1960. **119**: p. 1238.
42. Castner, T.G., *Hopping conduction near the metal insulator transition*, in *Hopping Transport in Solids*, M. Pollak and B.I. Shklovskii, Editors. 1991, Elsevier: Amsterdam. p. 2.
43. Davis, E.A. and W.D. Compton, Physical Review, 1965. **140**: p. A2813.
44. Mott, N.F. and W.D. Twose, *The theory of impurity conduction.* Adv. Phys., 1961. **10**: p. 707.
45. Miller, A. and E. Abrahams, Phys Rev, 1960. **120**: p. 745.
46. Mott, N.F., J. Non-Cryst. Solids, 1968. **1**: p. 1.
47. Efros, A.L. and B.I. Shklovskii, J. Phys. C, 1975. **8**: p. L49.
48. Shklovskii, B.I. and A.L. Efros, *Electronic Properties of Doped Semiconductors*. 1984, Berlin: Springer-Verlag.
49. Pollak, M., Philos. Mag. B, 1980. **42**: p. 781.
50. Mansfield, R., *Hopping conduction in III-V compounds*, in *Hopping transport in solids*, M. Pollak and B.I. Shklovskii, Editors. 1991, Elsevier: Amsterdam. p. 350.
51. Altshuler, B.L. and A.G. Aronov, *Fermi-Liquid Theory of the Electron-Electron Interaction Effects in Disordered Metals.* Solid State Communications, 1983. **46**(6): p. 429-435.
52. Gorkov, L.P., A.I. Larkin, and D. Khmelnitskii, JETP Lett., 1979. **30**: p. 228.
53. Altshuler, B.L. and A.G. Aronov, *Electron-Electron Interaction in Disordered Conductors*, in *Electron-Electron Interactions in Disordered Systems*. 1985.
54. Dietl, T., *et al.*, *Remarks On Localization in Semimagnetic Semiconductors.* Physica Scripta, 1986. **T14**: p. 29-36.
55. Finlayson, D.M., J. Irvine, and L.S. Peterkin, *Electrical Conduction in CdSe Near the Metal Insulator Transition.* Philosophical Magazine B, 1979. **39**(3): p. 253-266.
56. Sawicki, M., *et al.*, *Influence of s-d Exchange Interaction On the Conductivity of $Cd_{1-x}Mn_xSe$:In in the Weakly Localized Regime.* Physical Review Letters, 1986. **56**(5): p. 508-511.

57. Leighton, C., I. Terry, and P. Becla, *Metallic conductivity near the metal-insulator transition in* $Cd_{1-x}Mn_xTe$. Physical Review B, 1998. **58**(15): p. 9773-9782.

4 Experimental Details

This chapter outlines the details of sample selection and preparation techniques along with the experimental procedures used in this study. The first section (4.1) describes the samples' growth and the preparations for their measurement. In section 4.2 the compositional analysis of the samples is described. The experimental apparatus and techniques used for both the electrical and magnetic measurements are detailed in sections 4.3 and 4.4 respectively.

4.1 Sample Growth and Preparation

The samples used in this study are bulk single crystals of $Cd_{1-x}Mn_xTe$:In or $Cd_{1-x}Mn_xTe$:In,Al, typically having 10^{17}-10^{18} dopant atoms cm^{-3}. The samples were grown using the vertical bridgman technique by P. Becla at Massachusetts Institute of Technology. As grown material is usually found to be p-type, due to the presence of Cd vacancies. The samples used for our study have all been post growth annealed in a Cd atmosphere at temperatures in the range 900-1100K, thereby strongly reducing the number of vacancies, and thus increasing the room temperature electron concentration. Like CdTe, crystals of $Cd_{1-x}Mn_xTe$ frequently exhibit twinning, so as is outlined below it is important to assure crystal quality before making measurements, (particularly important in the case of electrical transport measurements). The samples used for electrical and magnetic measurements were typically 1-2 mm thick and up to approximately 5 mm on a side. Samples were obtained from the ingots by cutting disc shaped sections, these were then subdivided and examined using infra-red microscopy (IRM). To facilitate this an optical microscope was used in transmission mode, in conjunction with an edge filter (cut off wavelength 850 nm) and a CCD detector array in the form of a digital camera or video camera. Only samples which appeared uniform using IRM were selected for electrical measurements. It was often found that samples cut from the very edge of the ingots were of poorer quality than those cut from the centre.

Prior to making magnetic measurements samples were cleaned with toluene to remove any organic contaminants. Before electrical measurements could be made a procedure to place electrical contacts on the samples was undertaken. Initially the samples were polished to a finish of typically a few microns. The samples were then etched using a

3% solution of bromine in methanol, for up to 200 seconds. The purpose of the etch is to remove any oxide layer that may have formed on the surface of the samples. After etching, samples were cleaned, rinsed and then stored under pure methanol until just before contacting when they were dried at room temperature. Ohmic electrical contacts were then produced by placing high purity indium (99.9999 %) metal on the sample surface with a soldering iron. The Ohmic nature of contacts produced was verified by measuring the I-V characteristic. A typical example of an I-V measurement is shown in figure 4.1, it can be seen that up to the highest current used (in this case 5mA) the response is extremely linear. Four contacts were placed at the perimeter of the sample to allow measurements to be made using the van der Pauw technique outlined in section 4.3.1

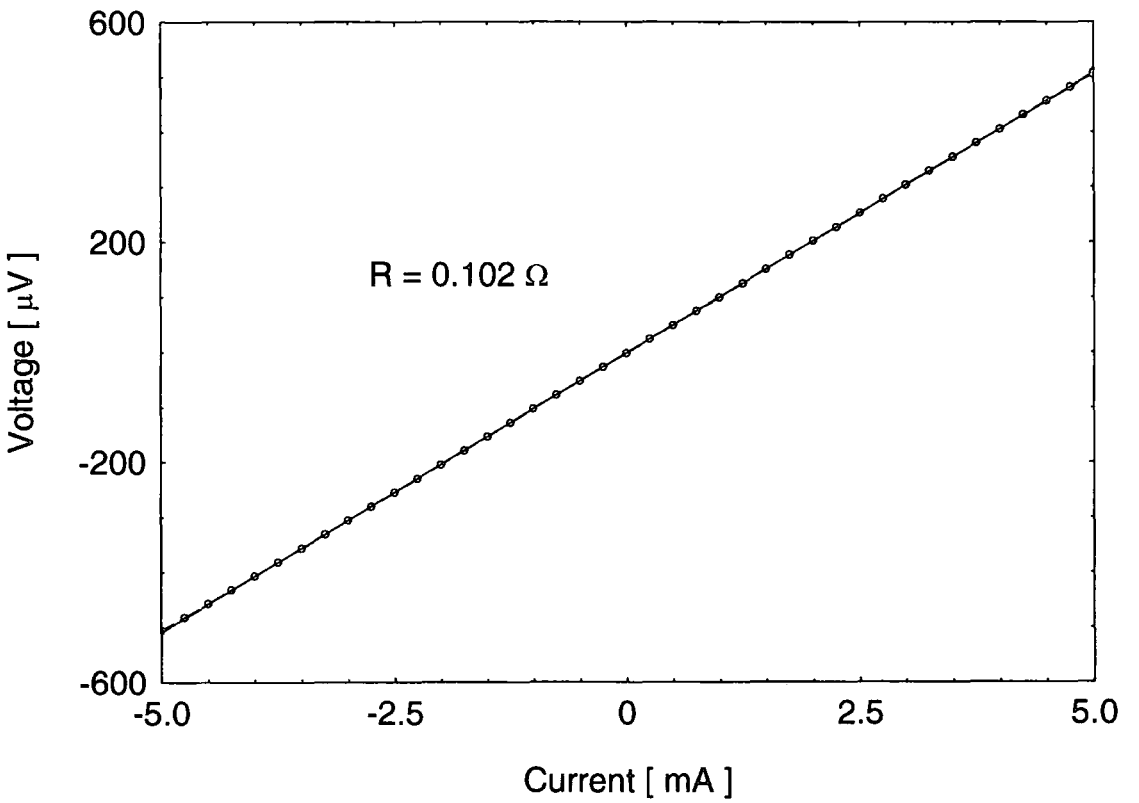

Figure 4.1 - A typical example of an I-V characteristic measured at T = 4.2 K showing an extremely linear response indicative of good quality Ohmic contacts.

4.2 Compositional Analysis of Samples Studied

The composition of the samples studied has been determined using two different analytical techniques. The first method used was Energy Dispersive Analysis of X-rays (EDAX), and this analysis was carried out on all samples studied, EDAX is sometimes also known as electron microprobe analysis. The second technique, a combination of Inductively Coupled Plasma Mass Spectroscopy (ICPMS) and Inductively Coupled Plasma Atomic Emission Spectroscopy (ICPAES) was used on only 3 of the samples examined.

EDAX is carried out using a Scanning Electron Microscope (SEM) in conjunction with a cryogenically cooled solid state x-ray detector head. This technique works by analysing the characteristic x-rays emitted from a particular element in the material when an electron beam is incident on the surface of the sample. A typical example of an EDAX spectrum for a sample of $Cd_{1-x}Mn_xTe$:In is shown in figure 4.2.

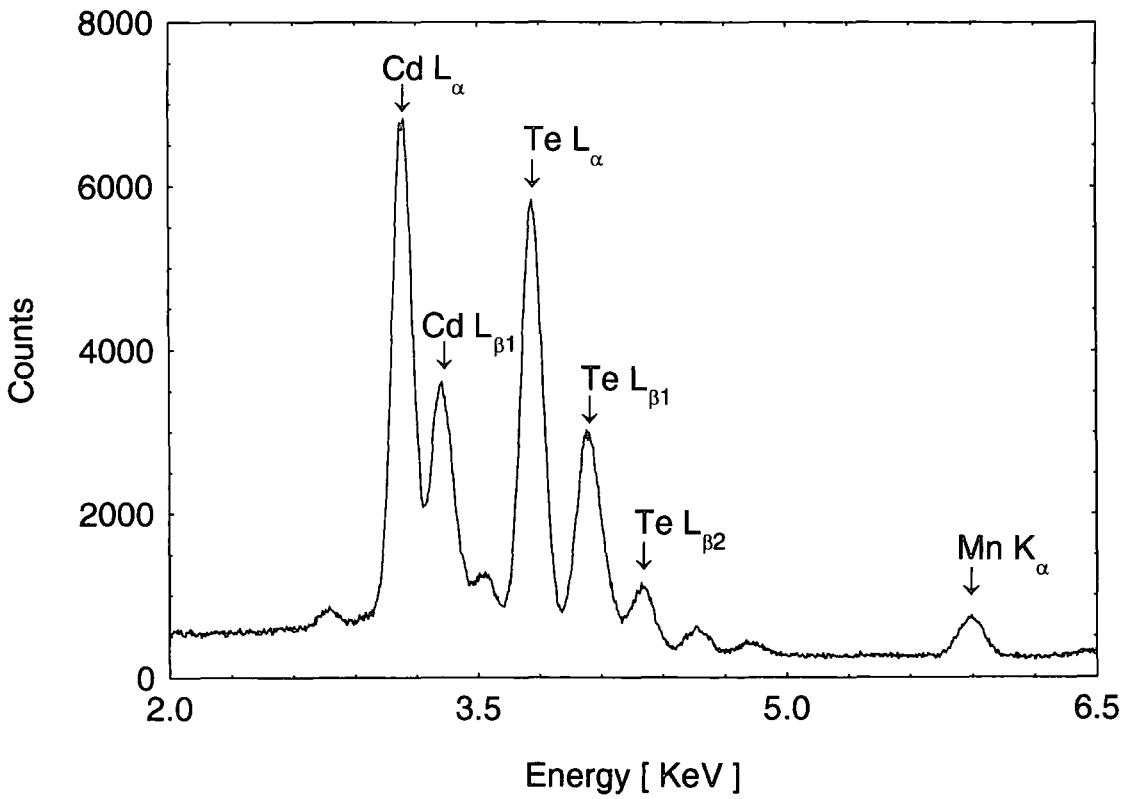

Figure 4.2 - A typical EDAX spectrum obtained from a sample of $Cd_{1-x}Mn_xTe$:In.

Accurate quantitative compositional analysis is normally only possible using this method if the x-ray peak intensities are compared to those obtained from measuring a set of elemental reference standards. In addition to this process of comparison with

standards it is important that the instrumental measurement conditions (for example electron beam accelerating voltage, beam current, spot size and incidence angle) remain constant throughout the measurements. Electrons entering the sample from the beam lose energy at a rate that depends partly on the mean atomic number of the material, thus electrons are affected differently by the sample and by the standard. This factor needs to be corrected for if accurate quantitative analysis is to be made. Corrections must also be made to allow for the fact that x-rays produced from atoms within the sample may be re-absorbed before leaving the material and reaching the detector. Also secondary x-rays may be produced (x-ray fluorescence) within the sample. These three corrections are commonly carried out by making use of the ZAF method.

In our case EDAX measurements were carried out only to determine the manganese concentration. Analysis made in Durham used a Princeton Gamma Tech thin window detector in a JEOL JSM-IC848 scanning electron microscope. This could be done rather more easily by simply measuring the ratio of the peak heights due to Cd and Mn then comparing them to the peak height ratios obtained when measuring a number of samples whose compositions had been previously determined accurately.

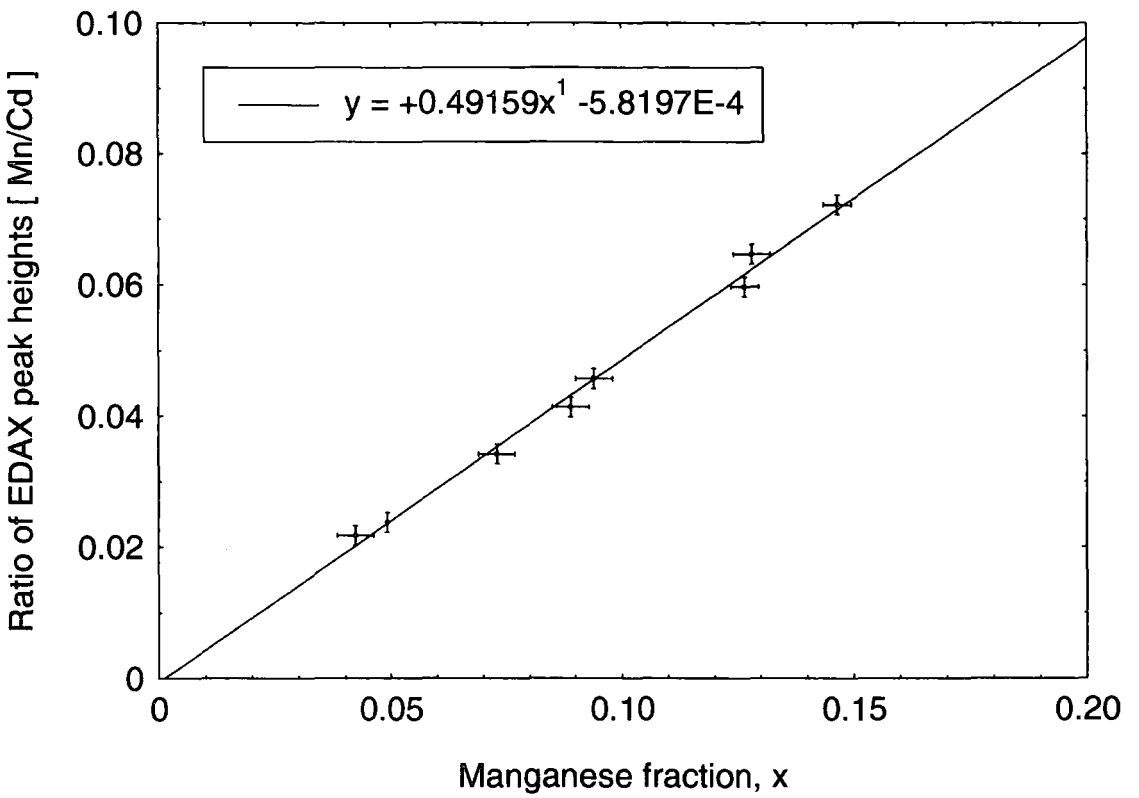

Figure 4.3 - The calibration curve which has been employed to determine the Mn concentrations of the samples of $Cd_{1-x}Mn_xTe$:In used in this study.

Shown in figure 4.3 is the calibration curve used to determine the manganese concentration of samples from the EDAX measured ratio of peak heights. Of the 8 samples used for this calibration, the manganese fraction of 3 of the samples was obtained from ICPAES and the remaining 5 samples had their compositions previously determined by EDAX making use of the necessary reference standards and taking into account the relevant corrections.

The manganese fraction calculated using this calibration is given by equation 4.1 below:

$$x = \left(\frac{\frac{I_{Mn}}{I_{Cd}} + 5.8197 \times 10^{-4}}{0.49159} \right) \qquad \textbf{Equation 4.1}$$

Whilst using EDAX in this way allows us to determine accurately the concentrations of Cd, Mn and Te, it is not however a sufficiently sensitive technique in order to obtain information about the doping level (either with In or with both In and Al). To measure the very low levels of dopant atoms present it was necessary to make use of ICPMS which has the sensitivity to detect certain elements at the level of 1 part in 10^9. For this reason ICPMS was performed on 3 samples, the results of these measurements are given in section 5.2.

4.3 Electrical Measurements

The temperature dependent conductivity measurements were made using a number of different systems at temperatures down to as low as 40mK. For the temperature range 40mK < T < 600mK a dilution refrigerator was employed, this will be described in section 4.3.2 For temperatures, T > 300mK a helium-3 refrigerator was available, however this system was predominantly used in conjunction with the SQUID system, and its operation will be discussed in section 4.4.2. At the highest temperatures (T > 4.2K) two different systems utilising liquid helium-4 have been used and these will be described briefly in section 4.3.4.

4.3.1 Experimental Details of Electrical Measurements

Firstly it is worth noting that some thought should be given to the choice of material used to construct the sample holder, for our work where the lowest temperature used

was T ~ 40mK copper is a perfectly acceptable material (silver is normally used at lower temperatures). In all cases the sample and thermometer were mounted very close to each other and both were well thermally anchored to the copper sample holder. At temperatures T > 300 mK the samples were mounted on sapphire to provide electrical insulation from the cryostat. For the experiments to lower temperatures, in the dilution refrigerator, extra care had to be taken. The sample holders used were constructed from copper and subsequently annealed (at T ~ 800 K) and quench cooled in ethanol to improve the thermal conductivity at the lowest temperatures. In addition to this the samples were no longer mounted on sapphire, but instead were glued directly with GE varnish and a layer of Rizla paper to provide electrical insulation.

All electrical measurements were made with contacts in the van der Pauw configuration, allowing both Hall effect and resistivity measurements to be made on the same sample with just 4 Ohmic contacts. If a singly connected sample of uniform thickness, t, has four contacts placed at its perimeter, as shown in figure 4.4 then it is possible to compute the resistivity of the material regardless of the sample shape.

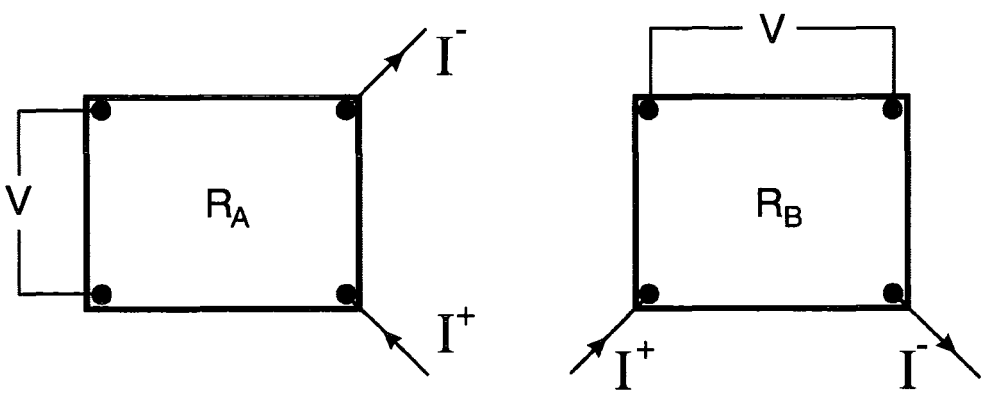

Figure 4.4 - The van der Pauw technique. The diagram shows the current and voltage connections to the sample for both resistance configurations allowing determination of the sample resistivity.

Measuring both resistance configurations labelled R_A and R_B then the resistivity is given by,

$$\rho = \frac{\pi t}{\ln 2}\gamma\left(\frac{R_A + R_B}{2}\right) \qquad \textbf{Equation 4.2}$$

Where γ is a function that is dependent only on the ratio of the two resistance configurations R_A and R_B (see figure 4.5). For samples which are isotropic and approximately square in shape then the ratio R_A/R_B is close to 1. If R_A/R_B is equal to unity then the van der Pauw factor $\gamma = 1$, if R_A/R_B increases to as much as 5 then $\gamma \sim 0.8$.

The importance of making measurements in the van der Pauw configuration, and hence observing changes in the sample anisotropy will be commented upon in later chapters.

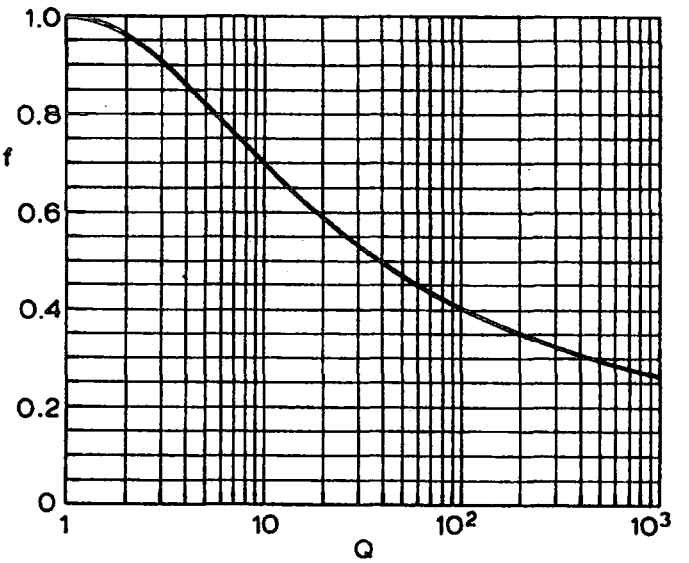

Figure 4.5 - Plot of the van der Pauw factor, γ (labelled f in the figure), as a function of the ratio of the resistance configurations, R_A/R_B (labelled Q in the figure).

Using the van der Pauw configuration [1] we can also make a measurement of the Hall carrier density. This is carried out by passing the current through two opposite contacts and measuring the voltage developed across the other two contacts as a function of applied magnetic field. In practice it is of vital importance to make measurements of the Hall voltage V_H for both forward and reverse current direction and also for both positive and negative applied magnetic fields. It is necessary to reverse the current direction in order to cancel out any thermal voltages that may be present due to a temperature gradient across the sample. Reversing the field direction is important to take account of the fact that the measured Hall voltage at zero applied field is non-zero. This is caused by a non ideal van der Pauw geometry where there is a slight misalignment of the voltage contacts, meaning that at zero field a voltage is present due to the resistance of the material. It is important to note that this resistance and therefore voltage may be field and temperature dependent. In fact at low temperatures where the magnetoresistance may be large, and thus dominating the field dependence in this configuration, it can become impossible to make a Hall effect measurement.

The Hall carrier density, n, may be determined from V_H and is given by equation 4.3,

$$n = \frac{BI}{V_H et} \qquad \textbf{Equation 4.3}$$

Where B is the applied magnetic field, I is the sensing current, t is the sample thickness and e is the charge on an electron.

In reality contacts are somewhat different from the Van der Pauw ideal of infinitely small point contacts at the sample perimeter. We can gain some insight into the approximate error on a resistivity measurement by considering a perfectly circular sample [2]. Figure 4.6 shows such a sample (of diameter D) : in (a) finite sized contacts are shown to extend a distance d around the circumference and in (b) contacts are displaced by a distance d from the sample perimeter.

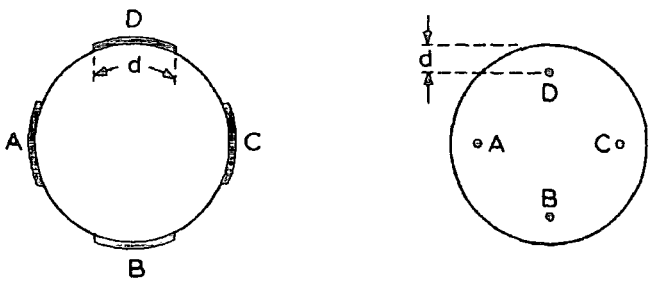

Figure 4.6 - Non ideal Van der Pauw contact configurations.

For case (a) the error is given by,

$$\frac{\Delta\rho}{\rho} \approx -\frac{d^2}{16D^2 \ln 2}$$ **Equation 4.4**

and for (b) we have,

$$\frac{\Delta\rho}{\rho} \approx -\frac{d^2}{2D^2 \ln 2}$$ **Equation 4.5**

Throughout all of the electrical transport measurements extreme care was taken to ensure that the sample temperature was not raised above that of the thermometer due to Ohmic heating caused by the excitation current. This was achieved by regularly checking with an excitation dependent measurement made at a fixed temperature. At temperatures below 100mK where the power levels required to heat the sample are extremely small, a great degree of caution had to be exercised. Also at these temperatures the thermal time constants are rather long due to the low thermal conductivity of most materials (including those used in the sample and sample holder), thus adequate time between measurements at different temperatures must be allowed. In

this temperature regime power levels of the order of a few picowatts could be used without adversely effecting the SNR by opting for a low frequency ac technique.

4.3.2 Details of Bayreuth Dilution Refrigerator

The lowest temperature measurements have been carried out at the University of Bayreuth, Germany. The cryostat used is based around a commercial dilution unit from Oxford Instruments, to which a copper nuclear adiabatic demagnetisation stage and associated superconducting magnets have been added. The nuclear stage gives access to temperatures below 5mK not required for our work, where the lowest temperature is limited by the measurement of resistance of the sample.

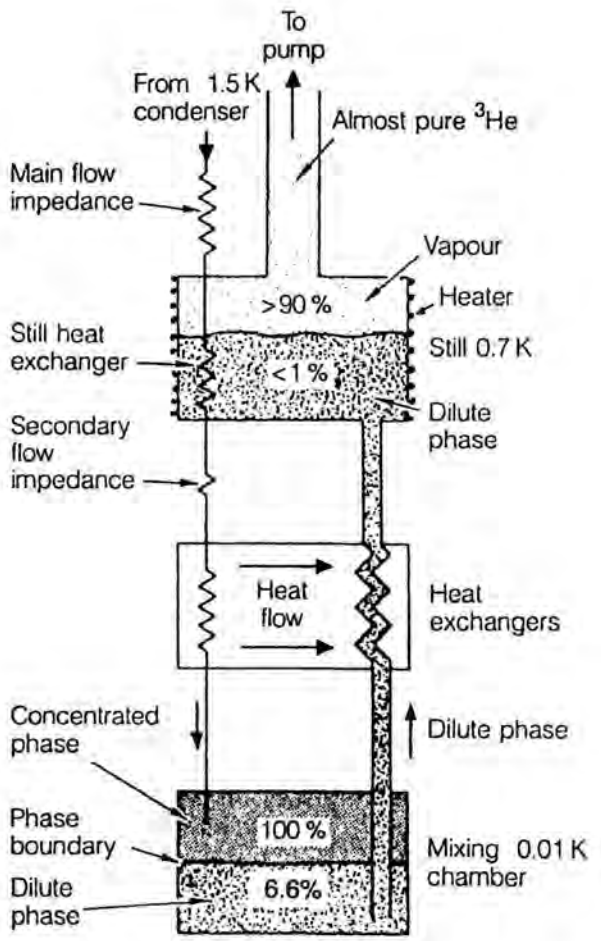

Figure 4.7 – Schematic of a ^{3}He-^{4}He dilution refrigerator after [3].

A ^{3}He-^{4}He dilution refrigerator provides a continuous method of cooling samples to temperatures of the order of 5mK and works by making use of the enthalpy of mixing of the two isotopes of helium. An idealised schematic plan of a dilution refrigerator is

shown in figure 4.7. Cooling occurs when ^{3}He atoms in the mixing chamber are transferred from the pure ^{3}He phase to a phase diluted with, and mostly containing ^{4}He. At a higher temperature than the mixing chamber is the still. It is here that, by pumping on the dilute phase, almost pure ^{3}He is removed due to its higher vapour pressure at this temperature (T ~ 700 mK). Room temperature sealed pumps are used to circulate the ^{3}He which is returned to the cryostat and pre-cooled to 4.2 K using the main ^{4}He bath. After this a flow impedance in the line is used to raise the pressure sufficiently that the ^{3}He will condense giving up its latent heat at 1.5 K. The only other important component in the design of a dilution refrigerator are the heat exchangers, these utilise the dilute mixture passing form the mixing chamber to the still in order to pre-cool the ^{3}He returning to the mixing chamber.

Measurements were carried out at different times with the samples mounted in two different positions, these are shown on a schematic diagram of the cryostat in figure 4.8. In the first position the samples were mounted in nominally zero field and were very closely thermally connected to a calibrated thermometer. The thermometer used was known as 'RH' and was constructed by modifying a Speer 220Ω ¼ Watt carbon resistor [4]. It was calibrated originally against a Co-60:Ni Nuclear orientation thermometer in 1984 and cross checked in 1993 against a ^{3}He melting pressure thermometer. Using this RH resistance thermometer allowed a calibration of a RuO_2 thermometer, as well as a measurement of the temperature dependence of the sample's electrical resistance in nominally zero magnetic field. Secondly the samples and RuO_2 thermometer were moved to a new position below the nuclear demagnetisation stage. This position allowed the field dependence of the samples' resistance to be measured in fields of up to 6T, using a superconducting solenoid. In this position the sample's temperature could be measured using the newly calibrated RuO_2 thermometer. The sample's resistance was measured using an RV Elektroniikka AVS-47 ac resistance bridge operating at a frequency of 12.5Hz. Measurements of the thermometer's resistance were made in a similar way using an RV Elektroniikka AVS-46 bridge. Temperature control was achieved using a Linear Research (LR130) temperature controller, using the RH thermometer as the sensor and with heating power being supplied to a wire wound resistance heater mounted next to the thermometer on the mixing chamber.

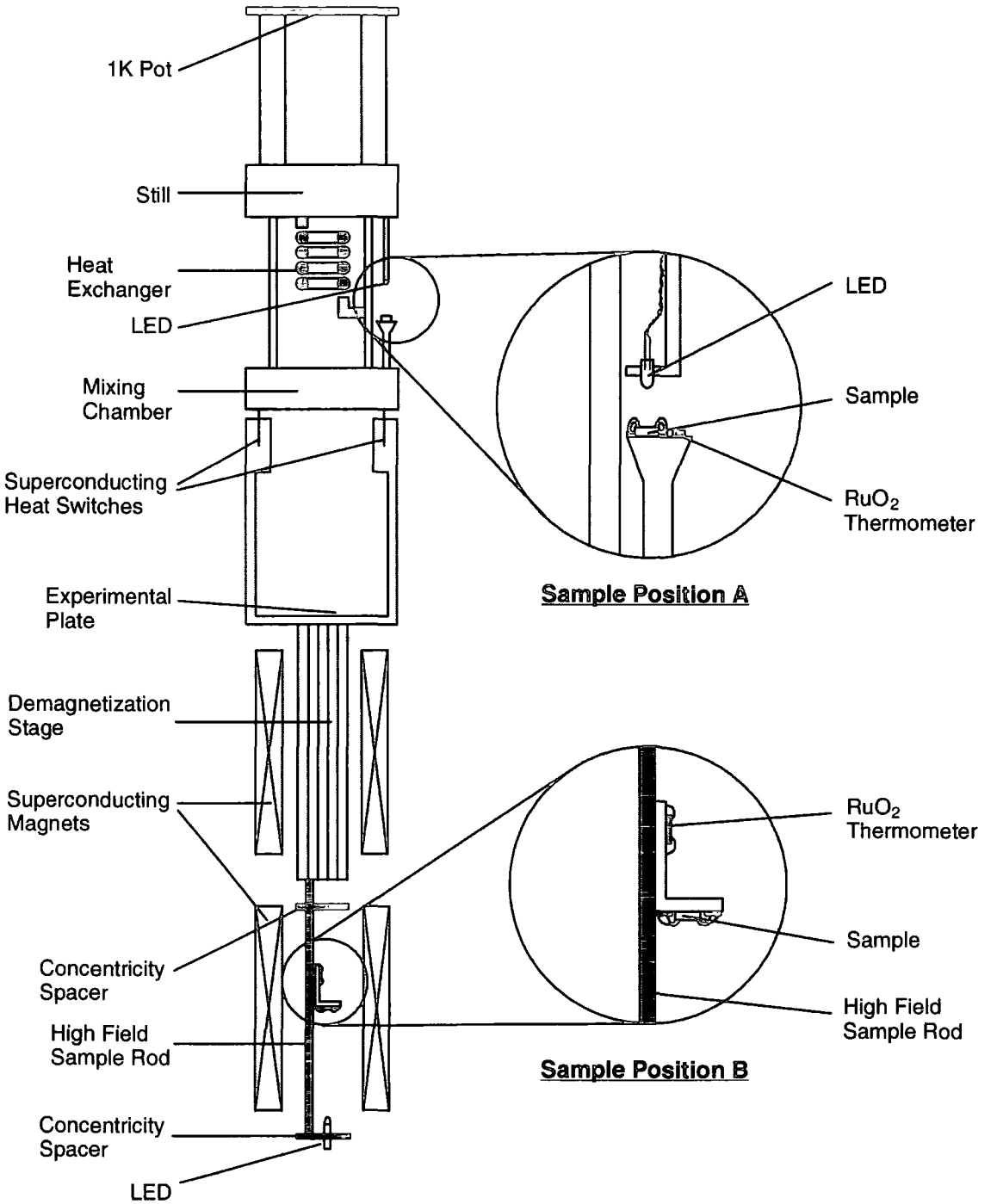

Figure 4.8 - The Bayreuth dilution refrigerator, a schematic diagram showing the two different mounting positions of samples for low temperature electrical transport measurements.

To allow the samples to be illuminated at low temperatures with sub-bandgap IR radiation a Kodenshi GaAs LED was also mounted inside the cryostat and was found to operate without problems down to the lowest temperatures used. A very simple circuit based around a NE555 timer IC was constructed and used to pulse the current through the LED in order to reduce the heat load, the values of the mark and space could be set independently. The LED had a peak output at 933nm and a FWHM of 27nm at 300K

and a small shift in the wavelength of the peak output (33 nm decrease) was previously observed on cooling to 90 K [5]. Decreasing the temperature further resulted in a weakening of the temperature dependence of the wavelength of light emitted. After illuminating the sample at low temperatures adequate time was allowed for the temperature of the cryostat to re-stabilise and to ensure that the sample and thermometer were once again in thermal equilibrium.

4.3.3 Effect of Strain on Samples During Cooldown

It should be noted that we have attempted to make very low temperature measurements (ie using the Bayreuth dilution refrigerator) on two additional samples of CdMnTe:In not reported in this thesis. The samples in question had both previously been examined at T > 300 mK and were found to be high quality samples. However on cooling with the dilution refrigerator both samples showed evidence of unusual behaviour inconsistent with previous measurements. When removing these samples from the refrigerator one had suffered macroscopic physical damage. As this was completely atypical of our usual measurements we should attempt to offer some reasoned explanation at this point. The only major difference when making measurements in the dilution refrigerator (except for the lowest temperature studied) was the method of sample mounting. As already mentioned in section 4.3.1, for measurements at T > 300 mK the samples were mounted on a thin (0.5 mm) sapphire wafer before installing in the cryostat, for measurements in the dilution refrigerator samples were glued directly (utilising GE varnish and Rizla paper) to the copper sample holder. In figure 4.9 we plot the temperature dependence of the coefficient of thermal expansion for materials of interest, these are copper, sapphire and CdTe. The data have been obtained from the references listed in the figure caption.

We can see from figure 4.9 that at high temperatures the contraction of copper on cooling is much larger than that of CdTe. Data above 100 K shows that the contraction of sapphire used to mount samples is much closer to that of CdTe. It is suggested that mounting a sample on a sapphire substrate (rather than gluing directly to the copper sample holder) may reduce the strain experienced by a sample when cooling in the cryostat. It is thus possible that mounting samples directly on the copper sample holder may result in an increased risk of damage occurring during the cooldown procedure. This may explain the inconsistent measurements and macroscopic damage experienced in previously studied samples, which will not be reported further in this thesis.

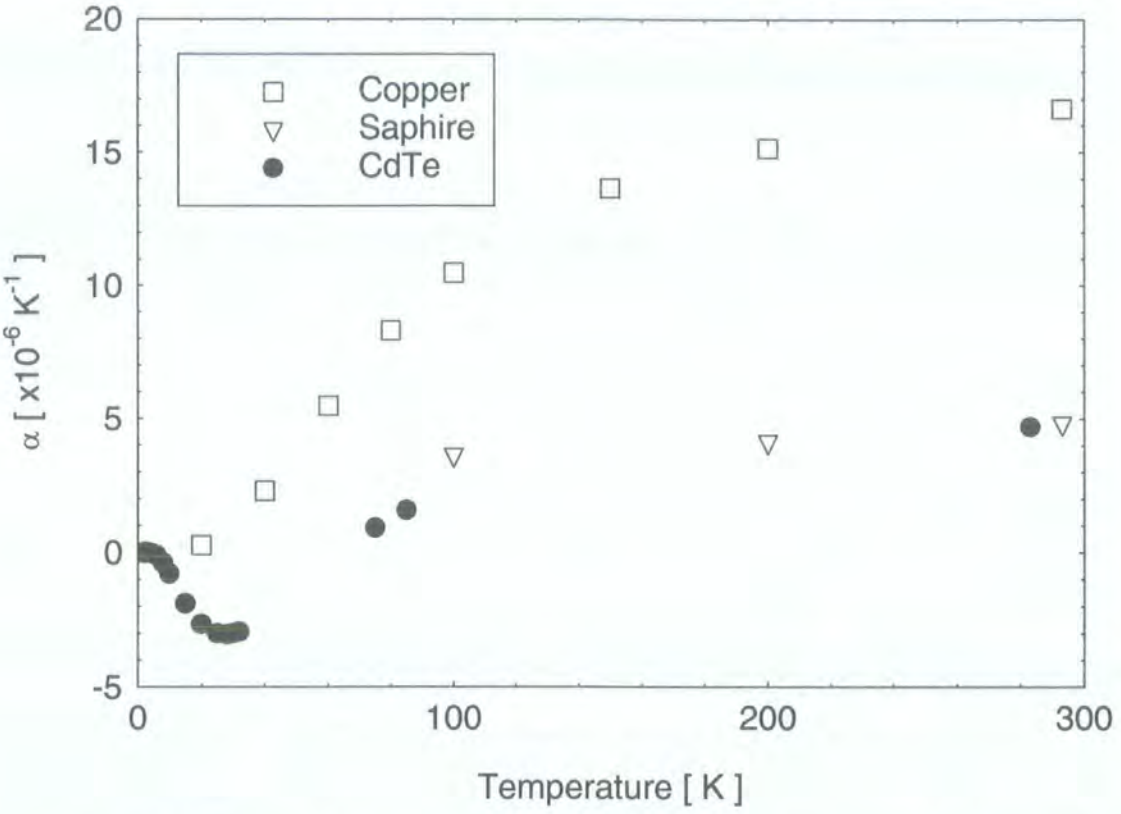

Figure 4.9 – Temperature dependence of coefficient of thermal expansion for Copper [6], sapphire [7] and CdTe [8].

4.3.4 Helium-4 Measurement Systems

In addition to the low temperature measurement system already described, two pieces of equipment were available to enable fast general electrical characterisation of a large number of samples. The first of these is a small lightweight probe that consists of a copper sample holder and associated wiring, along with a well thermally coupled RhFe thermometer. By inserting this probe inside an ordinary helium transport dewar it is possible to make zero field resistivity measurements by slowly varying the height of the sample above the level of the helium liquid. A schematic diagram of this probe is shown in figure 4.10(c). The temperature was read out using an Oxford Instruments ITC4, the sample resistance with a Keithley 199 DVM, measurements of sample temperature and resistance were recorded using a PC.

To obtain field dependent data a second system was used. This consisted of a continuous flow cryostat (Oxford Instruments CF1200) mounted between the pole pieces of a copper wound electromagnet (Newport Instruments 8" type D) capable of producing fields of up to 0.75 T at 18 A. The system works by connecting the cryostat,

via a vacuum shielded transfer siphon, to a helium transport dewar. Liquid (or cold gas) is taken from the dewar and circulated through the cryostat heat exchanger using a diaphragm pump, the cooling power of this liquid is balanced by the heat supplied to a 40Ω resistance heater mounted on the heat exchanger and in close proximity to a AuFe - chromel thermocouple. Again an Oxford Instruments ITC4 was used to control the temperature at a constant value during measurements. The AuFe - chromel thermocouple is chosen due to its small magnetic field dependence. The actual measurement of sample's temperature is made in zero field using a calibrated RhFe thermometer mounted directly on the copper sample holder of the probe. A schematic diagram of the experimental arrangement is shown in figures 4.10 (a) and (b).

In both the systems described above it is also possible to illuminate the sample with IR radiation from a Kodenshi LED of the sort described in section 4.3.2.

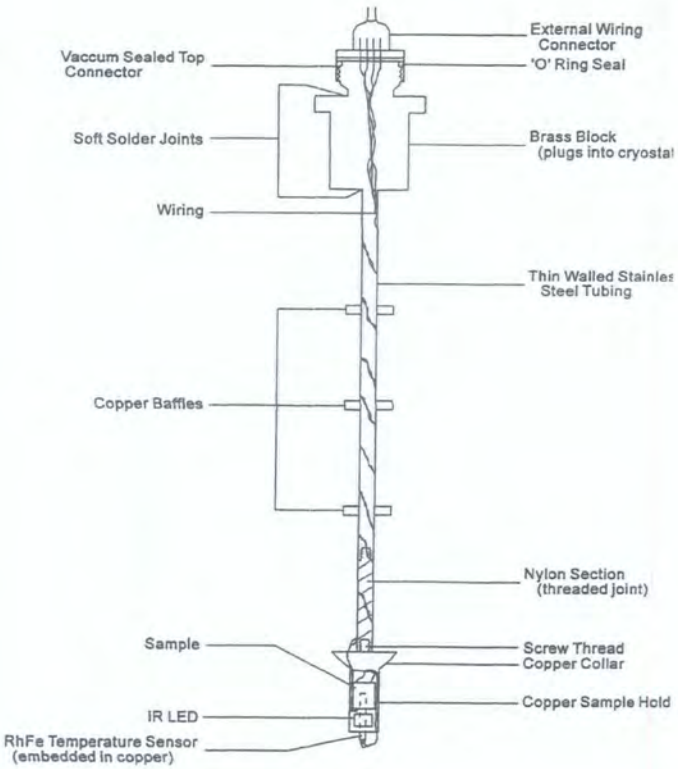
External Wiring Connector
Vaccum Sealed Top Connector
'O' Ring Seal
Soft Solder Joints
Brass Block (plugs into cryostat
Wiring
Thin Walled Stainles Steel Tubing
Copper Baffles
Nylon Section (threaded joint)
Sample
Screw Thread
Copper Collar
IR LED
Copper Sample Hold
RhFe Temperature Sensor (embedded in copper)

(a)

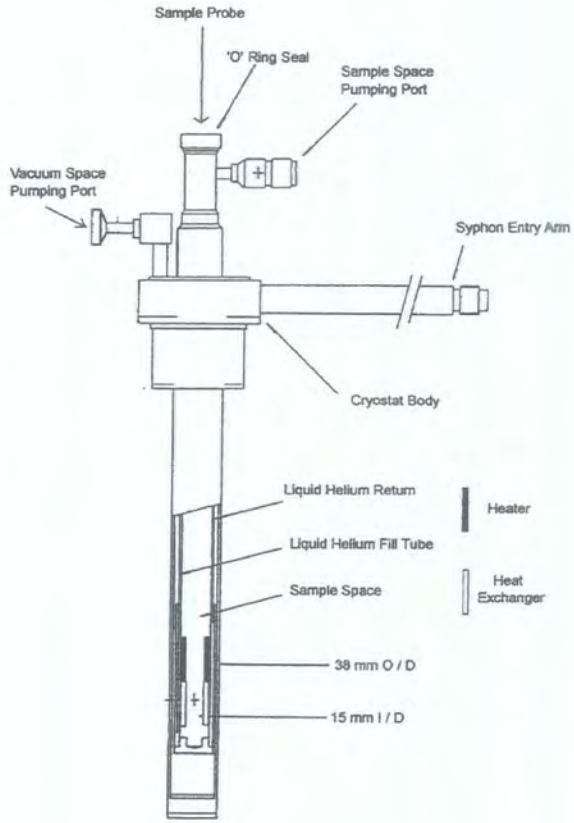
Sample Probe
'O' Ring Seal
Sample Space Pumping Port
Vacuum Space Pumping Port
Syphon Entry Arm
Cryostat Body
Liquid Helium Return
Liquid Helium Fill Tube
Sample Space
38 mm O / D
15 mm I / D
Heater
Heat Exchanger

(b)

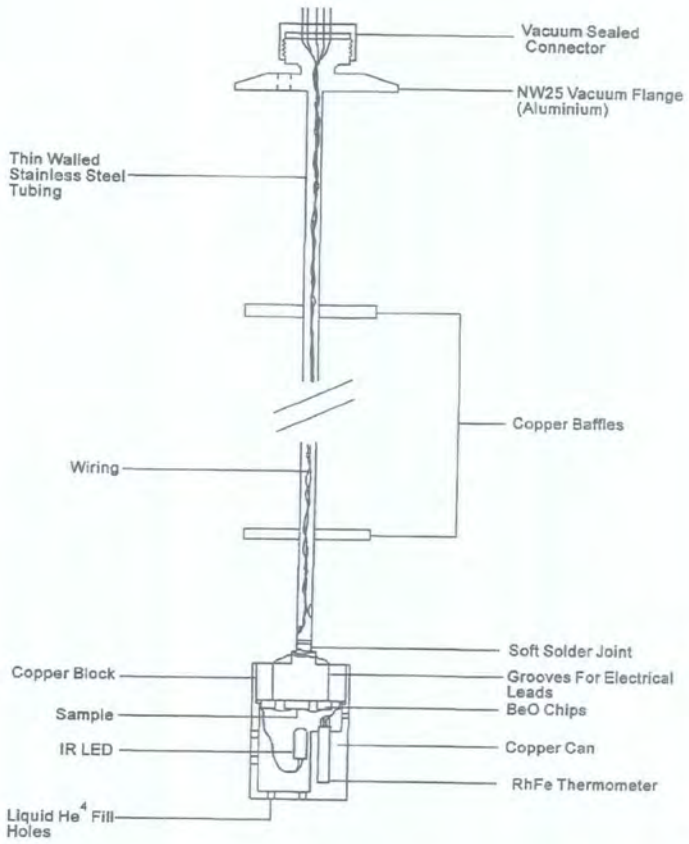
Vacuum Sealed Connector
NW25 Vacuum Flange (Aluminium)
Thin Walled Stainless Steel Tubing
Copper Baffles
Wiring
Soft Solder Joint
Copper Block
Grooves For Electrical Leads
Sample
BeO Chips
IR LED
Copper Can
RhFe Thermometer
Liquid He4 Fill Holes

(c)

Figure 4.10 (Previous page) – Schematic diagrams of the ^{4}He measurement systems used. (a) Sample holder and associated wiring for continuous flow cryostat (b) Continuous flow cryostat (c) Zero field 4.2 K measurement probe. After Leighton [5].

4.4 Magnetic Measurements

A Superconducting QUantum Interference Device (SQUID) offers a method of making magnetic measurements with unrivalled sensitivity. Commercial magnetometers that can resolve changes in magnetic moment as small as $1x10^{-11}$ JT^{-1} are freely available. Such systems can be used to resolve very small weakly magnetic samples or to observe tiny changes in the magnetic moment of materials. For this study measurements have been made using two different SQUID systems over two different temperature ranges as detailed below, and in addition to these some less sensitive measurements have been made using a Vibrating Sample Magnetometer (VSM).

4.4.1 Basic Principle of Operation of a SQUID

Most simplistically a SQUID can be considered to be a ring of superconducting material interrupted by superconducting weak links (two weak links are present in the case of a dc SQUID, one for a rf SQUID). Application of magnetic flux to the SQUID ring produces an output parameter that is a periodic function of the flux threading the ring. For a dc SQUID this output parameter is a dc voltage, for a rf SQUID the output parameter is the rf impedance of the device. The first SQUID produced in 1964 was of the dc variety, shortly after work on dc SQUIDs was largely abandoned with the advent of the more easily fabricated rf SQUID. More recently dc SQUIDs have again received greater attention due their superior sensitivity along with simpler and cheaper readout electronics. The operation of these two different types of SQUID will now be outlined in the following sections.

4.4.1.1 dc SQUID

As mentioned above a dc SQUID is constructed from a ring of superconducting material interrupted by two weak links known as Josephson junctions. A schematic diagram along with a plot of the current-voltage characteristic for a dc SQUID is shown in figure 4.11 below. The I-V characteristic of the device is dependent on the magnetic flux applied to the SQUID ring, with the critical current of the SQUID oscillating as a

function of applied flux. By applying a constant bias current to the SQUID we can measure a voltage which is a periodic function of the applied flux, the period being one flux quantum ϕ_0=h/2e. In practice, SQUIDs are almost always used in conjunction with a piece of room temperature electronics known as a flux-locked loop. Quite simply an ac magnetic flux with a frequency typically of the order of 100 kHz and a peak-to-peak amplitude of $\phi_0/2$ is applied to the SQUID ring. The output voltage from the SQUID then undergoes phase sensitive detection at the modulation frequency, f. If the average flux applied to the SQUID is exactly equal to $n\phi_0$ (where n is an integer) then the SQUID output signal at frequency, f, is zero, however if the flux is increased or decreased slightly from this value then a voltage at f appears on the SQUID output. The phase of this signal is dependent on the sign of the flux change, in this way the output from the lockin can be fed back via a resistor to a coil coupled to the SQUID. This feedback current produces a flux that is equal to, and opposes the original change in flux. Measuring the voltage across the feedback resistor gives a value which is proportional to the flux applied to the SQUID, hence this gives a linear response to applied flux with a very large dynamic range.

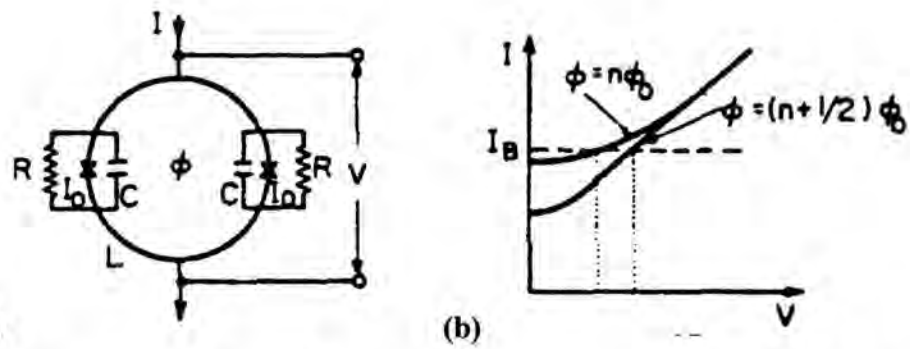

Figure 4.11 - (a) Schematic diagram of a dc SQUID (b) I-V characteristic of a dc SQUID for two applied flux values $\phi=n\phi_0$ and $\phi=(n+½)\phi_0$.

Although in principle it would be possible to use a SQUID in this way to measure magnetic field applied directly to the SQUID ring, due to the upper limit on the size of a SQUID ring being relatively small, more often a superconducting flux transformer is used to couple flux into the device. The flux transformer consists of an entirely superconducting loop of wire with a large sensing coil that couples flux into a smaller secondary coil having the same size as, and being inductively coupled to, the SQUID ring. The primary coil of the flux transformer is often not just a single simple coil, but an arrangement of coils. For example by making the primary from two identical

oppositely wound coils (see figure 4.12) one can create a device that is only sensitive to field gradient and is not affected by changes in a spatially uniform external field. More complex primary coil designs are available to detect higher order spatial derivatives of magnetic field changes.

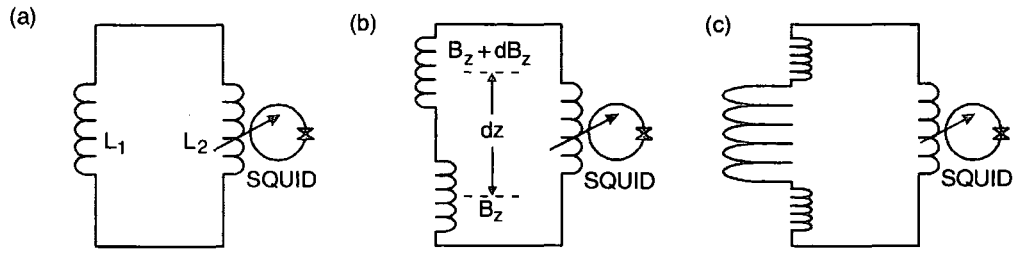

Figure 4.12 – Schematic diagram of three different flux transformers.

4.4.1.2 rf SQUID

A rf SQUID consists of a superconducting ring interrupted by just one Josephson junction (see schematic figure 4.13(a)). The SQUID ring is inductively coupled to the inductor of a resonant LC circuit excited by an RF current. This circuit has a resonant frequency of typically 20MHz to 10GHz. In this case the RF V-I characteristic is dependent on the value of the flux threading the SQUID ring (see figure 4.13(b)). At certain values of I_{RF} then V_{RF} oscillates as a function of applied flux with period ϕ_0. In a similar manner to that described in section 4.4.1.1 for a dc SQUID, a rf SQUID can be operated in a flux locked mode. By using exactly the same principles to design a flux transformer we can produce a device that gives a voltage proportional to the change in magnetic flux applied to a primary pickup coil.

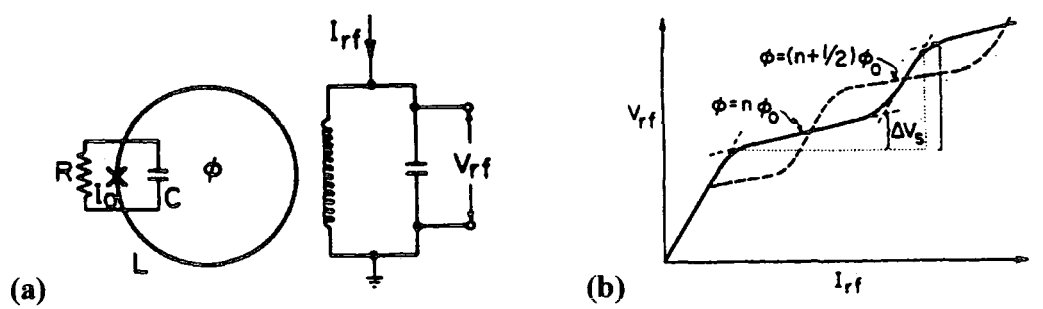

Figure 4.13 – (a) Schematic diagram of a rf SQUID ring (b) V-I characteristic for a rf SQUID.

4.4.2 Low Temperature SQUID Measurements

The lowest temperature magnetic measurements were made in a system constructed in Durham by combining an Oxford Instruments Heliox Probe sorption pumped He^3 refrigerator (this system has also been used for electrical transport measurements, T > 300mK) with a Quantum Design Model 5000 dc SQUID sensor. The SQUID sensor itself is constructed from a thin film of niobium (T_c = 9.26 K).

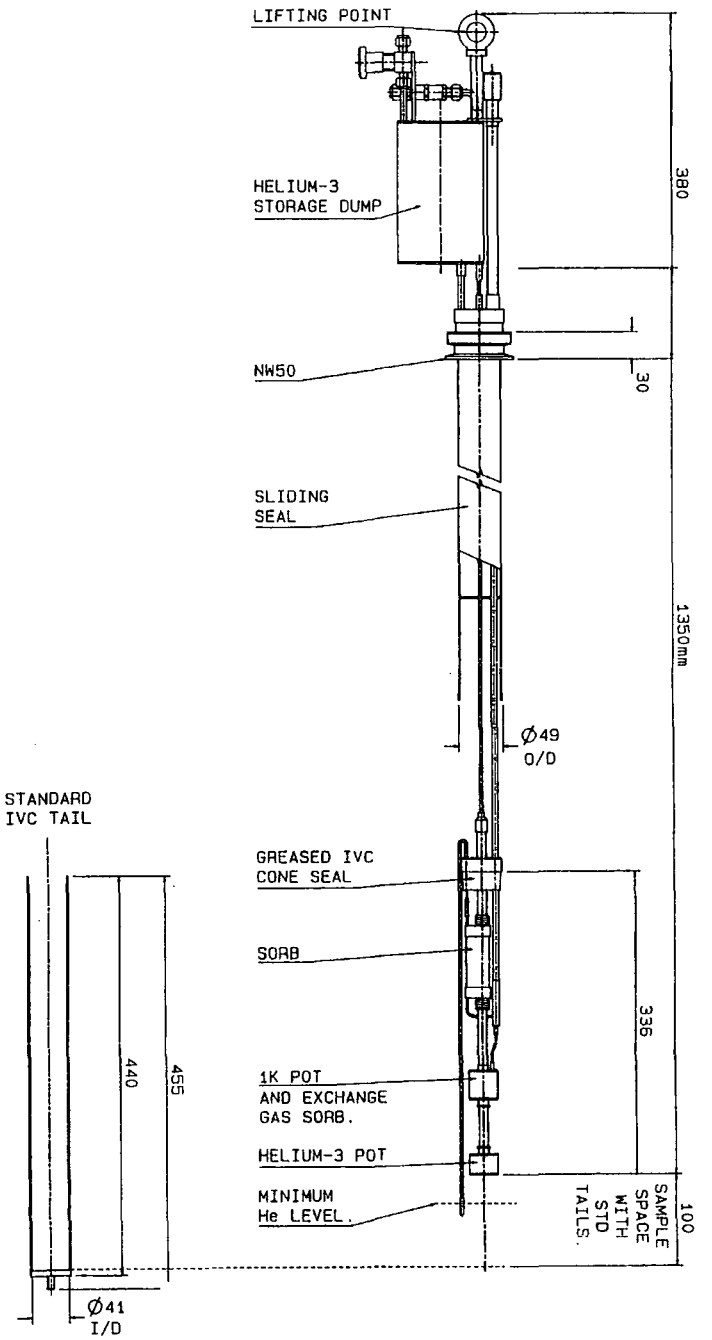

Figure 4.14 – Schematic diagram of Heliox probe He^3 refrigerator, dimensions in mm.

Figure 4.14 shows a schematic diagram of the ^{3}He cryostat which is designed to have an overall diameter less than 50mm thus the entire refrigerator can be lowered into an ordinary 120 litre liquid helium transport dewar. This mode of operation allows for a very fast and efficient cooldown coupled with a relatively quick turnaround time to change the sample being measured.

The operation of the refrigerator is very simple to understand and will now be described. Initially the system is cooled from room temperature by lowering it slowly into the dewar, at this point ^{4}He exchange gas is present inside the IVC so the sample holder and SQUID assembly are cooled easily to 10K. At temperatures below approximately 10K the IVC is pumped by an activated charcoal sorbtion pump. When the temperature of the probe has reached 4.2K the 1K pot is filled with liquid ^{4}He from the dewar, via a small vacuum insulated pickup tube. The pressure above the liquid in the 1K pot is then lowered by the operation of a room temperature rotary vacuum pump. This reduces the temperature of the ^{4}He to approximately 1.4K which is low enough to condense the ^{3}He from the sealed dump vessel, ($T_{boiling}$ ^{3}He = 3.19 K at atmospheric pressure). After complete condensation of ^{3}He, the pressure and hence temperature of the ^{3}He liquid can be lowered by the operation of a second activated charcoal sorbtion pump. In the range 300mK < T < 1.4K the temperature of the sample can be adjusted and controlled by altering the pumping speed of the ^{3}He sorb pump, this is realised by controlling the temperature of the sorb. For temperatures higher than 1.4K the ^{3}He pot is heated directly by applying a voltage to a resistance heater mounted on it.

A schematic diagram showing the arrangement of the SQUID and sample is given in figure 4.15. The copper block is in good thermal contact with the inside of the brass IVC which is partially immersed in the ^{4}He bath. The copper block acts as a heat sink and keeps the temperature of the SQUID and coil sets at a constant temperature of 4.2K. A flux transformer is connected to the input terminals of the SQUID sensor, this is constructed from NbTi single filament superconducting wire and is wound on a MACOR (a machinable glass ceramic material) former in the arrangement of a first order gradiometer. Using a pickup coil set of this geometry is intended to cancel the effects caused by fluctuation in the background magnetic flux, thus the signal we measure is only due to changes in the samples moment, caused by changing the applied magnetic field or temperature. In actual fact using this gradiometer set-up we measure the first derivative of flux with respect to position, it has become apparent that magnetic

objects close to the refrigerator (or parts of the refrigerator itself) can cause a contribution to the background signal. The size of this background is dependent on temperature and is shown in figure 4.16 measured in the Earth's magnetic field. It can be see that at low temperatures (T < 4 K) the background signal is rather small.

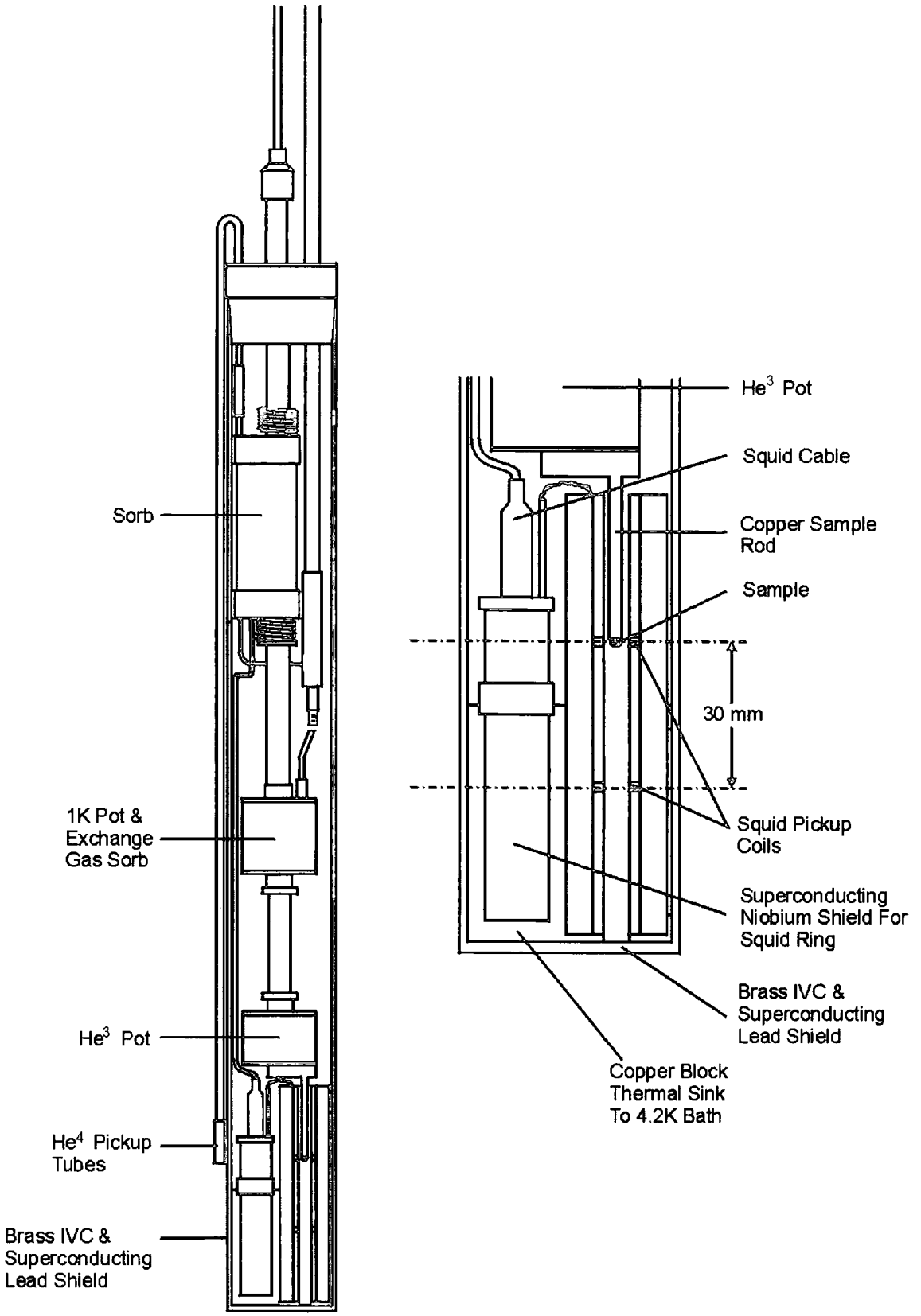

Figure 4.15 – Schematic diagram of the Durham SQUID arrangement.

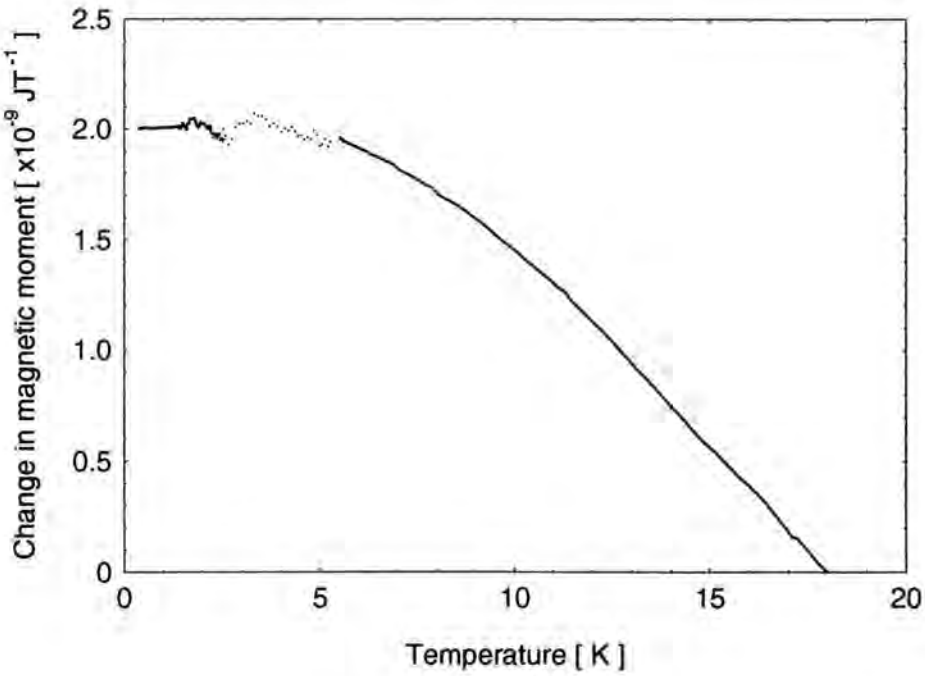

Figure 4.16 – Durham SQUID background signal as a function of temperature. Data are plotted as the change in magnetic moment normalised at some arbitrary high temperature.

In an attempt to screen out external fluctuations in the field gradient the brass IVC is covered with a thin layer (~ 0.5mm) of lead to act as a superconducting shield at 4.2K. It was shown that the superconducting shield successfully screened out changes in field gradient due to high magnetic fields produced in nearby laboratories. In addition to this, certain high frequency peaks in the noise spectrum were attenuated as the shield cooled through its superconducting transition temperature. The source of the high frequency noise had previously been found to be network communication cables in the vicinity of the SQUID apparatus.

The sample is directly mounted on a copper rod by gluing with GE varnish, this copper sample rod is bolted to the underside of the ^{3}He pot and arranged in such a way that the sample sits directly at the centre of the upper loop of the gradiometer coil set. It can be shown [9] that the highest sensitivity to flux is obtained from a dc SQUID when the primary and the secondary coil of the flux transformer have equal inductances. For this reason the primary coil of the flux transformer was designed to have an inductance equal to that of the SQUID input coil (1.9μH) [10].

A superconducting magnet was also designed and constructed, however it was shown that the application of even small currents to this magnet produced an unphysical SQUID signal due to unlocking of the flux locked loop. For this reason all the lowest temperature SQUID measurements presented in this thesis were carried out using the Earth's magnetic field as the measuring field. This was possible due to the high sensitivity obtained from this device. The noise was measured to be $\sim 5x10^{-3}\ \phi_0$ at low frequencies, and this means that the smallest resolvable change in moment is $\sim 1x10^{-12}\ JT^{-1}$.

4.4.3 High Temperature SQUID Measurements

Magnetic measurements have also been made in a commercial rf SQUID magnetometer at the University of Bayreuth, Germany. The instrument used was a Cryogenic Consultants S600. This system was able to resolve magnetic moments down to $m \sim 1x10^{-9}JT^{-1}$ and could be operated over two different temperature ranges using two different modes of operation. Firstly measurements could be made from 4.5K up to room temperature by passing cold helium gas from the main liquid bath via a resistive heater through the variable temperature insert (VTI) containing the sample. In the second mode of operation the lower section of the VTI and sample space could be filled with liquid helium, then by adjusting the pressure using a rotary pump and needle valve the temperature could be reduced and controlled to allow measurements to be made down to $T \sim 1.4K$. In both cases the temperature was monitored using two resistance thermometers one mounted above and one mounted below the sample, this allowed an accurate determination of the sample temperature. The sample was then moved repeatedly over a distance of 60mm through the second order gradiometer coils. The SQUID voltage as a function of sample position recorded during this movement of the sample was then fitted by a function describing the ideal response of a moment moving through the coil set (shown in figure 4.17) thus allowing the moment to be calculated. A superconducting solenoid provided a measuring field of known value.

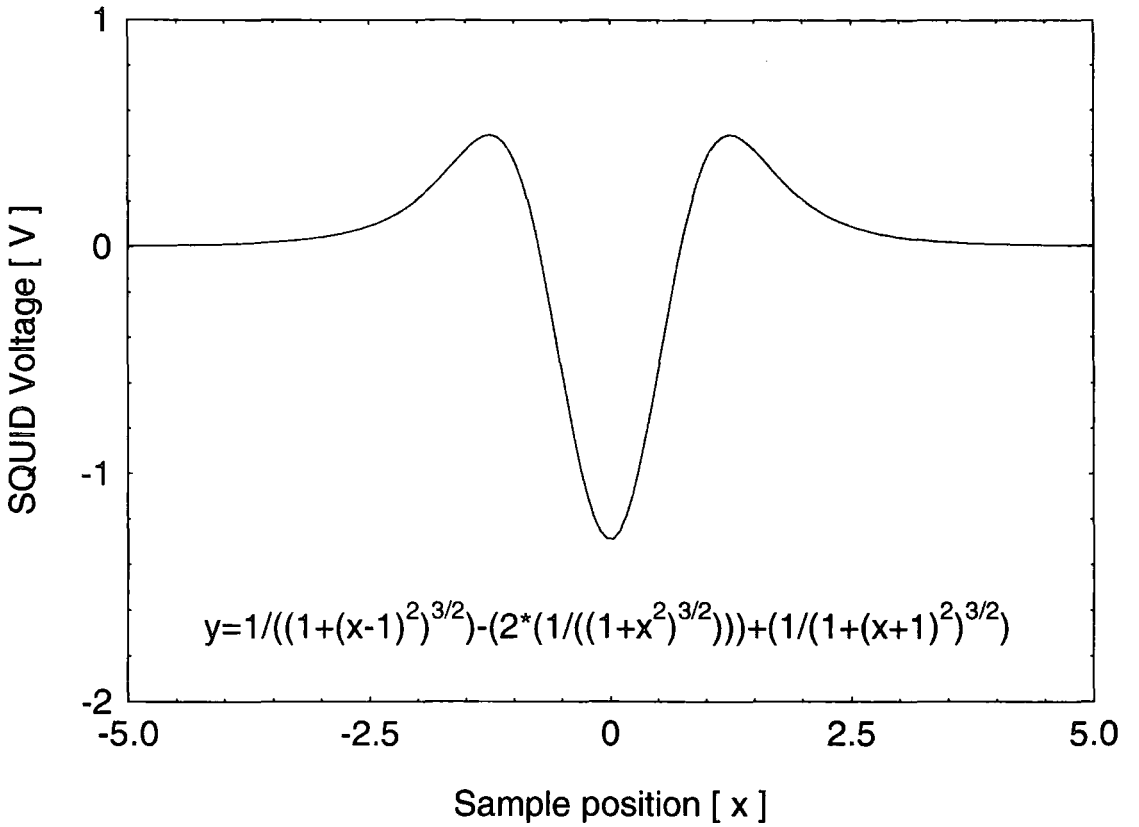

Figure 4.17 – Plot showing the ideal SQUID response expected when using a second order gradiometer coil.

4.4.4 Vibrating Sample Magnetometer Measurements

In addition to the high sensitivity measurements made using the SQUID susceptometers described above, a number of measurements were also undertaken in Durham using a VSM. The system was previously constructed in Durham and is capable of making measurements with a sensitivity of $m \sim 1x10^{-7}\ JT^{-1}$ at fields of up to 0.75T and temperatures down to 4.2K. The temperature and magnetic field environment for the sample is provided by means of a copper wound electromagnet and continuous flow cryostat, as previously described for the high temperature electrical transport measurements in section 4.3.4.

A VSM works by vibrating a magnetic moment (the sample to be measured) at a known frequency, f, inside a set of pick-up coils. When the moment is vibrated the flux linking the pickup coils oscillates at the same frequency as the moving magnetic moment, this changing flux in the pick-up coils induces a voltage and this can be measured using a lockin amplifier. The voltage measured across the coil set is proportional to the size of the moment, m, moving in the coils set and is given by equation 4.6 [11].

$$E = mGA2\pi f \cos 2\pi ft \qquad \text{Equation 4.6}$$

Here A is the (small) amplitude of the moment's oscillation and G is a constant that depends on the geometry of the pickup coils [12].

The main use of the VSM for our work was to calibrate the Durham SQUID susceptometer, this calibration was achieved by making a small loop of copper wire and then passing a known and constant current through this loop to produce a dipole moment that could be measured on both systems. A calibration of the VSM signal voltage was then made using standard samples of known masses. Both nickel foil (ferromagnetic) and palladium rod (paramagnetic) have been used as calibration standards and these data are shown in figure 4.18. The magnetic field at the sample position is measured by passing a constant current through an FW Bell Hall chip and measuring the resulting Hall voltage with a Keithley 196 DVM. The lockin amplifier used to make a phase sensitive measurement of the pickup coil voltage was an EG&G 7220.

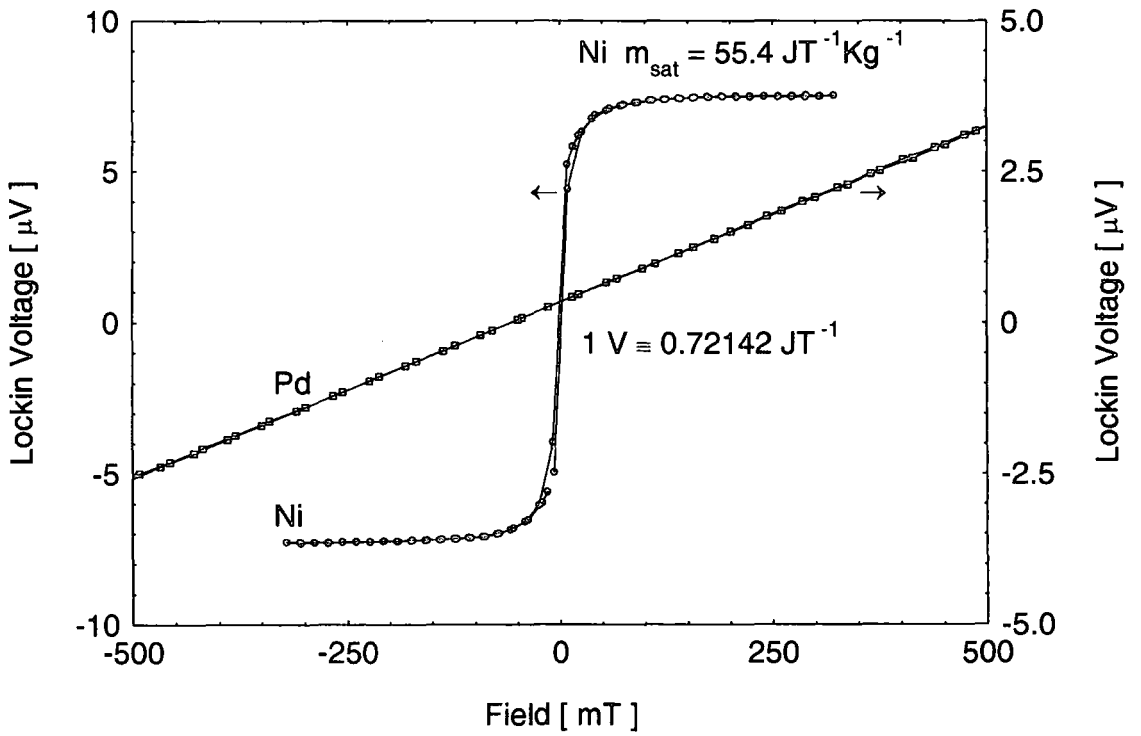

Figure 4.18 Calibration measurements of VSM using Ni and Pd standard samples.

4.5 References

1. van der Pauw, L.J., *A Method of Measuring Specific Resistivity and Hall Effect of Discs.* Philips Research Reports, 1958. **13**(1).
2. Blood, P. and J.W. Orton, *The Electrical Characterization of Semiconductors: Majority Carriers and Electron States*. 1992: Academic Press.
3. Pobell, F., *Matter and Methods at Low Temperatures*. 1995: Springer.
4. Eska, G. and K. Neumaier, *A Carbon Resistance Thermometer With Fast Response Below 10mK.* Cryogenics, 1983. **23**(2): p. 84-86.
5. Leighton, C., *Persistent Photoconductivity and the Metal-Insulator Transition in* $Cd_{1-x}Mn_xTe:In$, in *Physics*. 1997, University of Durham.
6. Novikova, S.I., Sov. Phys. Solid State, 1960. **2**: p. 2087.
7. Clark, A.F., *Materials at Low Temperatures*, in *Materials at Low Temperatures*, R.P. Reed and A.F. Clark, Editors. 1983, AMS: Ohio. p. 120.
8. Barnes, T.H.K., Adv. Phys., 1980(29): p. 609.
9. Gallop, J., *SQUIDs, the Josephson Effects and Superconducting Electronics*. 1991: Adam Hilger.
10. Quantum-Design, *SQUID Model 5000 Users Manual*. 2000.
11. Foner, S., *The vibrating sample magnetometer: Experiences of a volunteer.* Journal of Applied Physics, 1996. **79**(8): p. 4740-4745.
12. Zieba, A. and S. Foner, *Detection Coil, Sensitivity Function, and Sample Geometry- Effects For Vibrating Sample Magnetometers.* Review of Scientific Instruments, 1982. **53**(9): p. 1344-1354.

5 Results of Magnetic Measurements

5.1 Introduction

This chapter presents the results of magnetic measurements made on seven different samples of $Cd_{1-x}Mn_xTe$:In and on three samples of $Cd_{1-x}Mn_xTe$:In,Al. Measurements have been made in two different temperature regimes using the two different SQUID systems described previously in section 4.4. From high temperature susceptibility measurements it has been possible to extract the Curie constant and Curie-Weiss temperature. The dependence of these parameters on manganese fraction has previously only been determined for nominally undoped samples. The results presented in this thesis represent measurements made on heavily doped samples. At low temperatures we have observed samples that undergo a transition from a paramagnetic phase to a spin glass-like phase. The variation of the spin glass freezing temperature with manganese concentration will be discussed in section 5.4.1. In addition to this, small changes in the low temperature susceptibility have been seen when the free electron density of samples has been increased after illumination. Some brief comments are made about the samples studied in terms of their electrical properties.

5.2 Electrical Characterisation and Compositional Analysis of Samples Used for Magnetic Measurements

The samples used in the magnetic measurements are listed in table 5.1. In the first column of the table we give each sample studied an identifying label (a letter followed by a number). Samples having a label beginning with the letter 'A' or 'B' are doped only with indium. Samples that have been doped with both indium and aluminium have a label beginning with the letter 'I'. The second column of table 5.1 gives a value for the manganese concentration of each sample. These values have been determined from EDAX or ICPAES as labelled in the table. In columns three and four we indicate for each sample the temperature range over which measurements have been made. "High T" and "Low T" refer to measurements made above and below 1.5 K respectively. Given in column five are measured values of the room temperature resistivity. Finally, the last two columns give the Hall carrier density and Hall mobility, determined from

electrical transport measurements. The majority of the electrical transport measurements presented in this chapter were previously carried out by C Leighton [1].

Sample	Mn fraction	High T data	Low T data	ρ(300K)‡ Ωcm	n(300K)‡ $x10^{17}cm^{-3}$	μ(300K)‡ $cm^2V^{-1}s^{-1}$
A1	0.0492 ± 0.0003 *	✓	✓	0.046	3.9	453
A2	0.046 ± 0.005	✓	✓	0.052	1.4	858
A6	0.126 ± 0.003 *	✓	✓	1.17	0.26	206
A7	0.146 ± 0.003*	✓	✓	2.94	0.11	193
A9	0.197 ± 0.005	✓	✗	-	-	-
B5	0.093 ± 0.005	✗	✓	0.41	0.67	228
B6	0.133 ± 0.005	✗	✓	1.34	0.16	292
I1	0.188 ± 0.005	✓	✗	0.11	3.4	166
I3	0.148 ± 0.005	✓	✗	0.071	5.0	175
I4	0.044 †	✓	✓	0.24	4.0	64.4

Table 5.1 – Details of samples used for magnetic measurements. Parameters listed are the Mn fraction, the room temperature resistivity, carrier density and Hall mobility. * denotes a value determined by atomic emission spectroscopy. † sample I4 showed an anomoulously inhomogeneous manganese concentration. ‡ Electrical transport data after C Leighton [1]

In addition to the other analytical techniques employed we have used ICPMS to determine the In dopant atom concentration for three of the samples studied. The results are given in table 5.2. Using the dopant concentration in combination with the room temperature carrier concentration we can compute the dimensionless compensation ratio, this value is also given in table 5.2 for sample A7.

Sample	Mn fraction	In concentration [$x10^{18}$ cm^{-3}]	Compensation ratio $K = N_A/N_D$
A1	0.0492	0.374	
A6	0.126	6.61	
A7	0.146	0.209	0.47‡

Table 5.2 – Results of ICPMS carried out on three samples in order to determine the Indium dopant atom concentration. ‡ The compensation ratio for sample A7 has been previously calculated by Leighton *et al.* The value is obtained from fitting to the temperature dependence of the Hall carrier density, full details can be found in reference [2].

5.3 High Temperature Magnetic Measurements

In this section results of magnetic susceptibility measurements made in the higher temperature range are presented. The measurements have been made using the commercial SQUID magnetometer described in section 4.4.3. Measurements have been made for eight of the samples listed in table 5.1 above. For all of the high temperature measurements made in this way the measuring field was fixed at a value between 15 - 100 mT. Some samples were measured using a number of different measuring fields within this range, in all cases the susceptibility was found to be independent of the measuring field used. The figures below show plots of the mass susceptibility [m^3kg^{-1}] or the inverse mass susceptibility [kgm^{-3}] as a function of temperature. In all cases the diamagnetic contribution from the host lattice, CdTe, has been subtracted. The temperature independent value used for this subtraction is $\chi_d = -3.9x10^{-9}$ m^3Kg^{-1} [3].

Figure 5.1 shows the temperature dependence of the inverse susceptibility (χ^{-1}) for four samples having different manganese concentrations. More samples have been measured (see appendix A), however for the purpose of clarity only four are shown on this plot. Other samples measured showed similar behaviour.

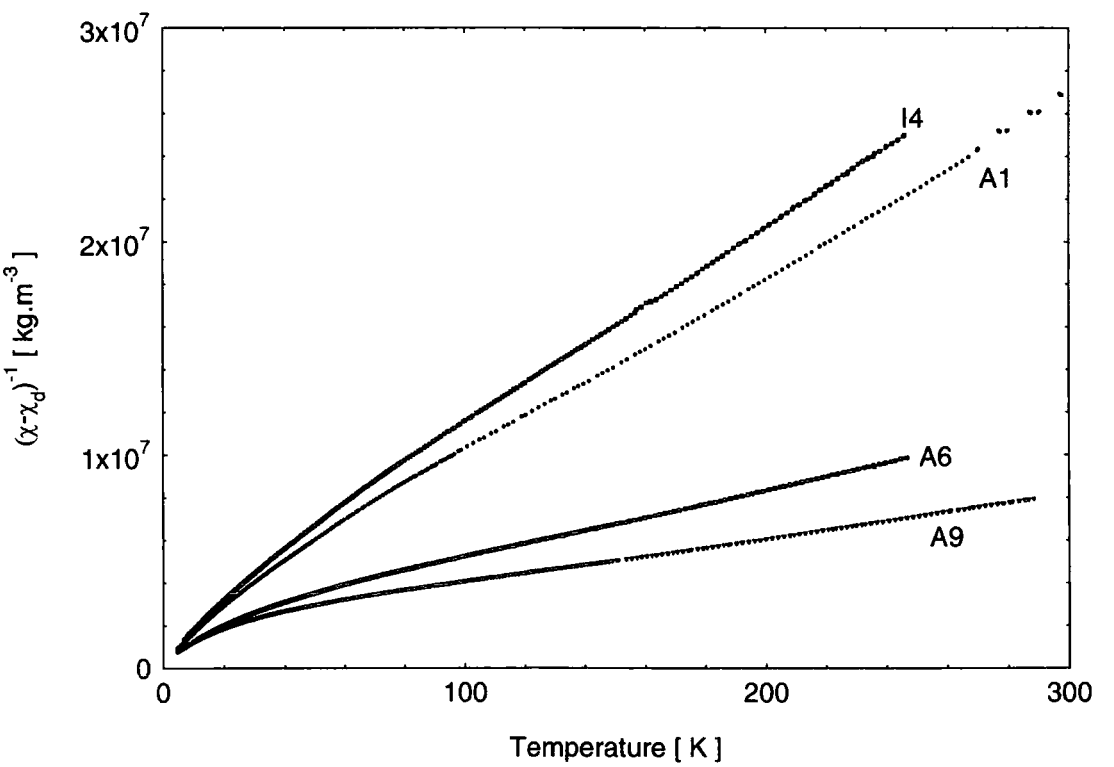

Figure 5.1 – Inverse of magnetic susceptibility as a function of temperature. Data are presented for four different samples having different Mn concentrations.

As expected at the highest temperatures measured all the samples show Curie-Weiss like behaviour indicated by the linearity of χ^{-1} plotted against temperature. At lower temperatures $T \sim 40 - 60$ K deviations from this simple Curie-Weiss behaviour are observed in the form of a downturn in the plot of χ^{-1} against temperature. This behaviour has previously been observed in nominally undoped samples of $Cd_{1-x}Mn_xTe$ [4]. Similar behaviour has also been observed for other DMS systems, such as HgMnTe [5] and CdMnSe [4]. In general the deviations observed are strongest for those samples having the larger Mn fraction. Previous measurements on undoped samples over a larger range of Mn concentrations have suggested that deviations from the Curie-Weiss behaviour are seen to begin at higher temperatures for those samples with higher Mn fractions. For the samples that we have studied this trend is not so obviously apparent.

The observed downturn of χ^{-1} against T can be understood within the spin-cluster model. The basic idea is that if Mn ions are distributed at random on the crystal lattice, there is some finite probability of finding a certain sized cluster of Mn ions. The probability of finding different types and sizes of clusters can be calculated [6]. However the problem becomes mathematically complicated for clusters larger than three Mn ions. Within a cluster Mn spins can interact, the model neglects interaction between clusters. The total susceptibility of the material is then just the sum of contributions from all the different types and sizes of clusters, the coefficients being the probabilities of the various cluster types and sizes. A similar model has been used to quantitatively explain the high field magnetization in II-VI DMS containing Mn ions [7].

For our purposes we shall quantitatively analyse only the high temperature susceptibility data. By fitting a straight line to the high temperature sections of the data it is possible to obtain an estimate for the Curie constant, C, and for the Curie-Weiss temperature, θ. Appendix A contains plots of χ and χ^{-1} as a function of temperature for each of the eight samples measured in the high temperature region. In addition to the experimental data these figures contain the fits and the values of C and θ extracted from the fitting procedure. The values obtained from this curve fitting procedure are tabulated in table 5.4. The table also indicates the temperature range over which measurements were made and the approximate temperature below which strong deviations from a Curie-Weiss law are observed. For some of the samples measured data obtained is limited to relatively low temperatures, so we can expect a larger error in the values of C and θ determined for these samples. For all the samples examined here θ is found to be

negative indicative of an antiferromagnetic exchange interaction, this has been observed in previous measurements on nominally undoped samples.

Figure 5.2 shows the variation of the Curie constant, C, with Mn concentration, x, for the samples measured. The dashed line in the figure is obtained from equation 5.1 (see section 3.1.1),

$$C = xC_0 = \frac{xN_0(g\mu_B)^2 S(S+1)}{3k_B} \qquad \text{Equation 5.1}$$

with S = 5/2, x is the Mn fraction and N_0 is the number of cations per unit volume. It can be seen from the figure that our experimental values of C are in reasonable agreement with the values obtained from equation 5.1.

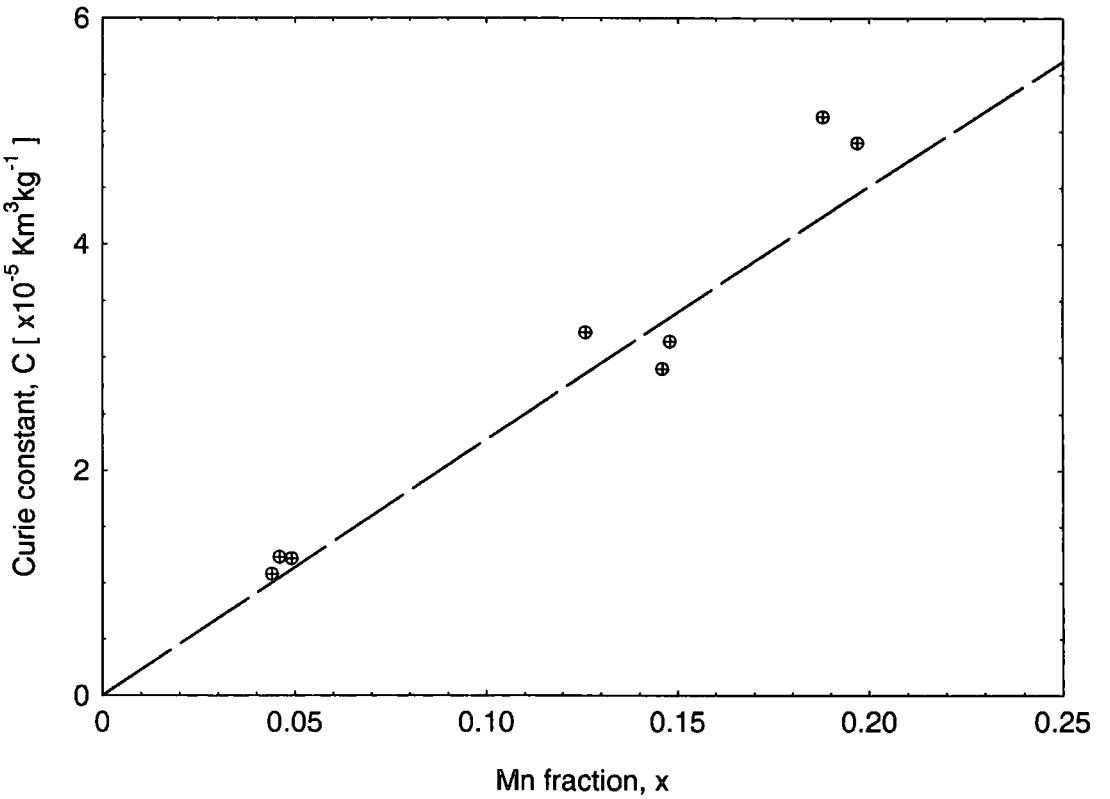

Figure 5.2 - Variation of Curie constant, C, with Mn concentration, x. Data points are obtained from fitting to our high temperature measurements of magnetic susceptibility (see appendix A). The dashed line on the graph shows the x dependence of C, calcuated from equation 5.1.

In a similar way figure 5.3 shows the variation of the Curie-Weiss temperature with Mn fraction, x. Equation 5.2 (see section 3.1.1) gives the relation between Curie-Weiss temperature, Mn fraction and the nearest neighbour exchange constant, J_{NN}.

$$\theta = \frac{70 x J_{NN}}{k_B}$$ **Equation 5.2**

The upper and lower dotted lines in figure 5.3 are plots of equation 5.2 where the value of $-J_{NN}/k_B$ has been set to 10K and 6K respectively. These values for the nearest neighbour exchange energy represent the extremes of the range of values previously reported for $Cd_{1-x}Mn_xTe$. A review of the values for the nearest neighbour exchange energy taken from the literature is given in table 5.3. In addition to the value of $-J_{NN}/k_B$ the method used for its determination and a reference are also listed in the table.

In the table column headed "Method", the word "Susceptibility" refers to a value of $-J_{NN}/k_B$ obtained directly from a measurement of susceptibility (as we have carried out in our study). The label "Step" indicates that a value of $-J_{NN}/k_B$ that was determined from measuring the position of the first step in the high field magnetization, and "Neutron" implies that a result was taken from neutron diffraction measurements.

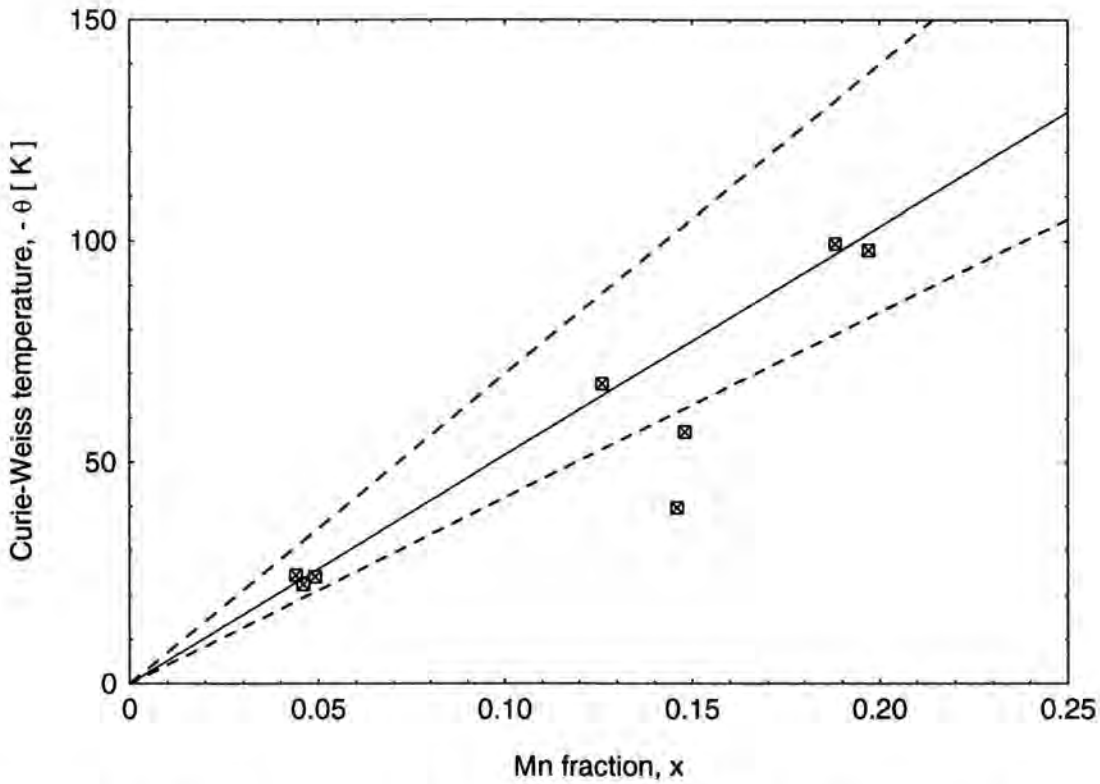

Figure 5.3 - Variation of Curie-Weiss temperature, θ, with Mn fraction, x. Data points are obtained from fitting to our high temperature measurements of magnetic susceptibility (see appendix A). The upper and lower dotted lines on the graph show the x dependence of θ, caluated from equation 5.2 with the value of $-J_{NN}/k_B$ set to 10 K and 6 K respectively. The solid line represents a fit to our experimental data points (excluding samples A7 and I3) and gives a value of $-J_{NN}/k_B$ = 7.5 K.

$-J_{NN} / k_B$ [K]	Method	Reference
~ 7	Susceptibility	Oseroff [8]
7.7 ± 0.3	Step	Aggarwal *et al*[9]
~ 10	Step	Shapira *et al* [7]
6.3 ± 0.3	Step	Larson *et al* [10]
6.1 ± 0.3	Step	Shapira & Oliveira [11]
6.2 ± 0.2	Step	Foner *et al* [12]
7.5	Neutron	Giebultowicz *et al* [13]
6.7	Neutron	Giebultowicz *et al* [14]
6.9 ± 0.15	Susceptibility	Spalek *et al* [15]
7.7 ± 0.3	Step	Galazka *et al* [16]
6.1 ± 0.2	Step	Isaacs *et al* [17]

Table 5.3 – Values for the antiferromagnetic nearest neighbour exchange energies, $-J_{NN}/k_B$. The values listed are obtained from the available literature. The method used to determine $-J_{NN}/k_B$ and the reference are also listed.

It can be seen from figure 5.3, that in general, the values of -θ determined from measurements lie within the region described by equation 5.2 and using the extreme value of $-J_{NN}/k_B$ obtained from reviewing the literature. Notable exceptions to this are samples I3 and A7 which have values of -θ that are smaller than expected. This disagreement can be easily explained if we recall the rather limited temperature range ($T < 75$ K) over which measurements of samples I3 and A7 have been made. As a result the fits used to extract θ and C for these samples are only made over a very narrow temperature range and thus are likely to be inaccurate. If we assume that at $T < 75$ K the susceptibility has already started to deviate from a Curie-Weiss law behaviour (ie we are fitting to a region on the "down turn" of the curve) it would seem likely that we would produce values of θ and C that are lower than the true values for these samples. The fit for sample A7 is made at a slightly lower temperature than that for sample I3, thus if the above explanation is correct we would expect the values of θ and C to be further from the expected values. This is indeed what we observe in figure 5.3. By neglecting the data for samples A7 and I3 we can fit to the remaining points on the graph shown in figure 5.3, carrying out this procedure results in a value of $-J_{NN}/k_B = 7.5$ from our high temperature susceptibility data. This value is in excellent agreement with

a number of previous measurements made using different methods as described above in table 5.3.

Sample	Mn fraction	C [$x10^{-5}$ Km^3kg^{-1}]	-θ [K]	Deviation temperature [K]	Temperature range of measurements [K]
A1	0.0492	1.22	24.1	35	1.5 – 300
A2	0.046	1.23	22.3	-	1.5 – 100
A6	0.126	3.22	67.8	55	10 – 250
A7	0.146	2.90	39.7	-	10 – 60
A9	0.197	4.90	98.0	50	4 – 300
I1	0.188	5.13	99.5	50	4 – 275
I3	0.148	3.14	56.9	-	10 – 75
I4	0.044	1.08	24.4	45	1.5 – 250

Table 5.4 – For samples having different Mn concentrations the parameters obtained from fitting a Curie-Weiss law to the high temperature magnetic susceptibility measurements are given. The deviation temperature gives an indication of the temperature below which a strong departure from the Curie-Weiss behaviour is observed. The range of temperatures over which high temperature magnetic measurements have been made is listed in the final column of the table.

Figure 5.4 shows high temperature susceptibility data for two samples A9 and I1 having similar Mn concentrations. The difference between these two samples is that A9 is doped with In only, however in contrast I1 is doped with both In and Al. Data are presented for the temperature range 4 K < T < 300 K and it can be seen from the figure that both samples show qualitatively similar behaviour. Thus it would appear from simply comparing these two samples that the dopant atom does not drastically affect the observed behaviour of the high temperature magnetic susceptibility.

Although this result is not completely unexpected, it was thought possible that the difference in dopant atom could effect the sample's magnetism. The obvious difference between the two atoms used to dope our samples is their ionic radii (these are 155pm for In and 125 pm for Al, from reference [18]). This difference almost certainly leads to local distortions of the crystal lattice around the dopant atom. The dominant exchange mechanism in these samples is superexchange, mediated by the tellurium anions. The mechanism of superexchange is known to depend on the Mn-Te-Mn bond angle, and thus any change in this angle would affect the strength of the interaction. The absence of any dopant dependent differences in the parameters obtained from high temperature

susceptibility measurements is consistent with measurements made on the other six samples described above.

We should also note at this point, that for a more rigorous comparison of the effect different dopant atoms may have, it would be useful to compare magnetic data for two samples having identical Mn concentrations.

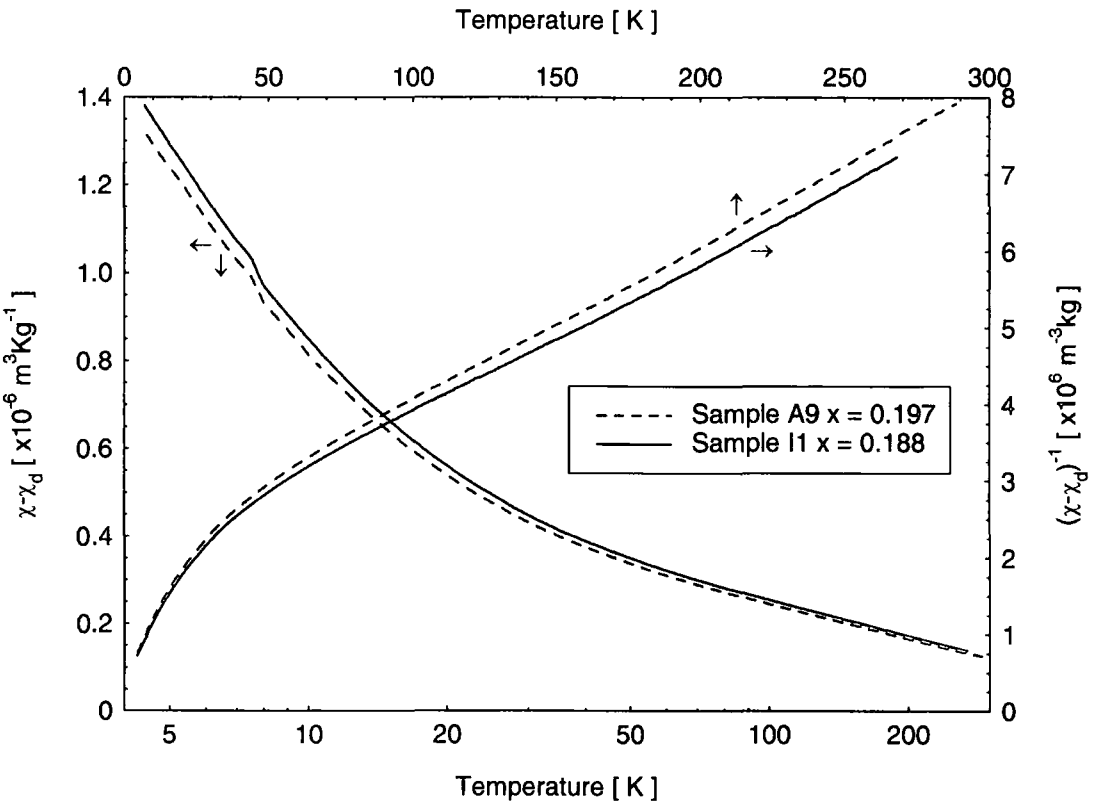

Figure 5.4 – Magnetic susceptibility (left axis) and its inverse (right axis) plotted as a function of temperature. Data are presented for two samples having similar Mn concentrations, but different dopant ions

It should be noted (see figure 5.4) that a small feature in the susceptibility is observed at a temperature of approximately 7.5 K. It was found to occur at an identical temperature in all samples measured and is thought to be an artefact of the commercial SQUID magnetometer used for the measurements

On further careful examination of the high temperature susceptibility data another interesting feature is observed. In figure 5.5 we plot inverse susceptibility as a function of temperature for sample A1. In addition to this we have computed the derivative with respect to temperature and this is shown on the right axis of the same figure (note that this axis has been reversed for clarity). It is seen that the value of the derivative has a minimum at a temperature of approximately 110 K. One immediately obvious

possibility is that this minimum is in some way linked to the persistent photoconductivity effect that is seen in these samples and is measured to have a quenching temperature of slightly greater than 100 K.

A similar feature can be observed by examining the derivative curves obtained from measurements on other samples having low manganese concentrations. For samples having higher Mn concentrations this minimum in the derivative curve was not obviously apparent. One conclusion that could be drawn is that this small effect (possibly related to PPC as suggested above) is masked by the larger effect of the local moments present in samples with higher Mn concentrations.

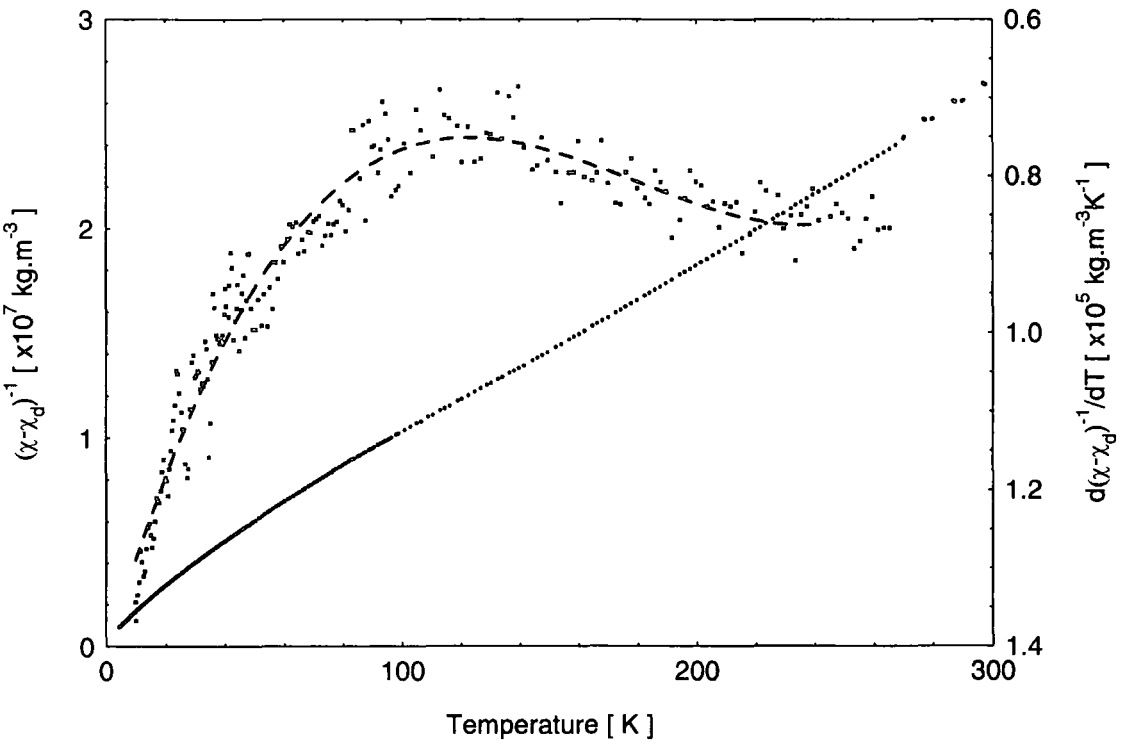

Figure 5.5 - Inverse susceptibility (left axis) and its derivative (right axis, note axis inverted for clarity) as a function of temperature. Data are presented for sample A1, having Mn fraction x = 0.0492. The dashed line serves as a guide to the eye for the derivative curve.

5.4 Low Temperature Magnetic Measurements

In addition to the data presented in the previous section seven of the samples, (namely A1, A2, A6, A7, B5, B6 and I4) have been studied using a different SQUID system (see section 4.4.2) to allow measurements to be extended to temperatures below 1.5K. Sample I4 has also been measured in the commercial SQUID magnetometer, in the temperature range 1.5 K < T < 4 K and these results show an interesting and somewhat unexpected feature which will be described later.

In figure 5.6 we plot the change in magnetic moment per unit mass for three samples which all have Mn fractions close to x = 0.05 (see table 5.1 for exact x values). For the purpose of clarity the value at T= 1.5 K for each sample has been arbitrarily chosen such that the curves are offset from one another. All samples show similar behaviour, however close examination of the figure reveals that the exact temperature dependence of the susceptibility varies slightly for each sample. The differences observed are likely to be due to slightly different sample compositions, in particular small differences in the Mn fraction of the samples are likely to affect the temperature dependence of the susceptibility at low temperatures.

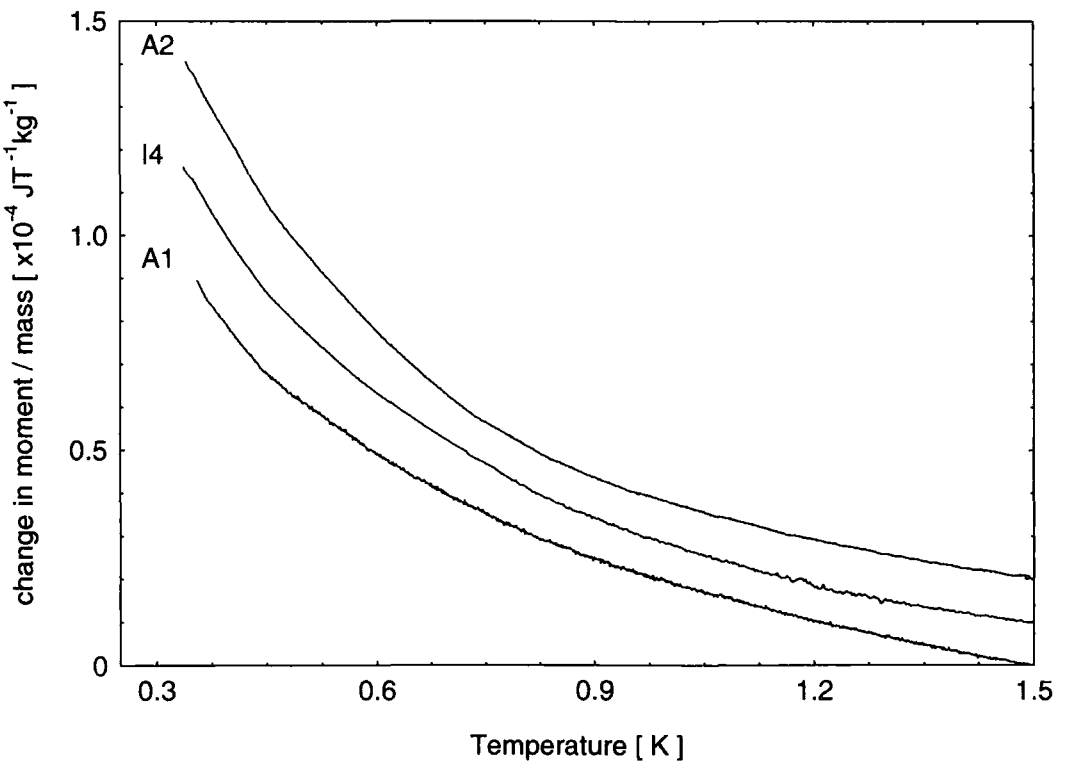

Figure 5.6 - Plot of change in magnetic moment per unit mass as a function of temperature for three samples of CdMnTe:In. All samples have manganese fractions close to x = 0.05. Curves have been offset by 1x10^{-5} JT^{-1}kg^{-1} for the purpose of clarity.

5.4.1 Spin Glass Phase Transition

We will now move on to consider low temperature magnetic measurements made on a number of samples having slightly higher concentrations of Mn. It is known from previous measurements [19, 20] on undoped samples of $Cd_{1-x}Mn_xTe$ that a transition from a paramagnetic to a spin glass phase occurs at low temperatures. This is true even of samples having x values below the nearest-neighbour percolation threshold. A plot of χ against T for a sample of $Cd_{1-x}Mn_xTe$ having x = 0.1, after Novak et al is shown in figure 5.7. The arrow denotes the point in temperature below which the sample enters a spin glass phase.

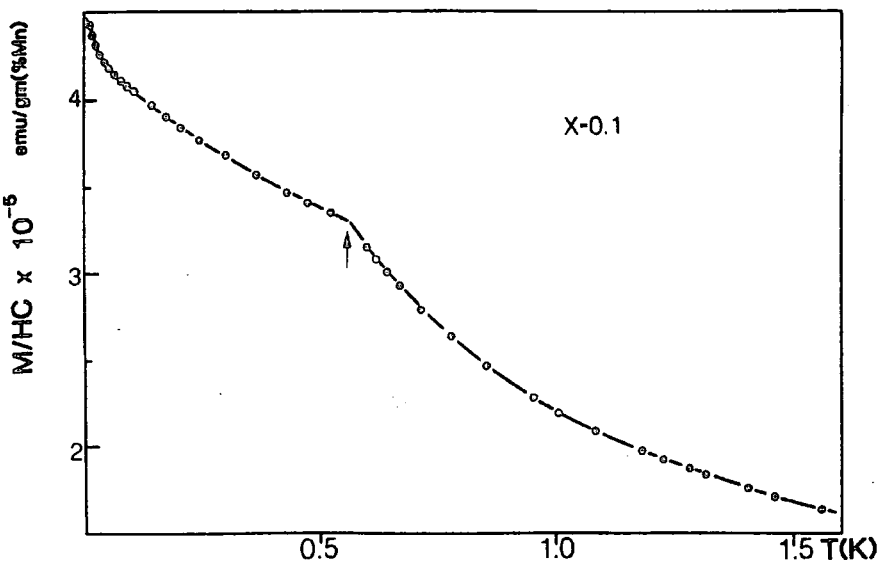

Figure 5.7 - Spin glass freezing in $Cd_{0.9}Mn_{0.1}Te$ after Novak *et al* [20], the arrow indicates the spin glass freezing temperature.

Three of the samples we have studied show similar features in their magnetic susceptibility in the temperature range 300 mK < T < 1.5 K indicative of the formation of a SG phase. Experimental data for samples A6, B6 and A7 are shown in figure 5.8. We have plotted change in magnetic moment (set to zero at 1.5 K) divided by the sample's mass as a function of temperature. In this case an absolute calibration of the y-axis in terms of susceptibility is unimportant as we are primarily concerned with identifying the SG freezing temperature. Also shown inset are the same data plotted on a log-log scale in order to emphasise the SG freezing temperature.

Due to problems with the SQUID superconducting solenoid (already mentioned in section 4.4.2) all measurements were made in the Earth's magnetic field. (A

measurement of the ambient field in the lab in the direction that the measurement were made gives B ~ 40 μT). Thus all curves shown represent the zero field cooled condition.

Although for a canonical spin-glass (such as the much studied AuFe or CuMn) one normally observes a cusp in the dc susceptibility [21], similar behaviour to that seen here has previously been observed in undoped $Cd_{1-x}Mn_xTe$ as shown in figure 5.7.

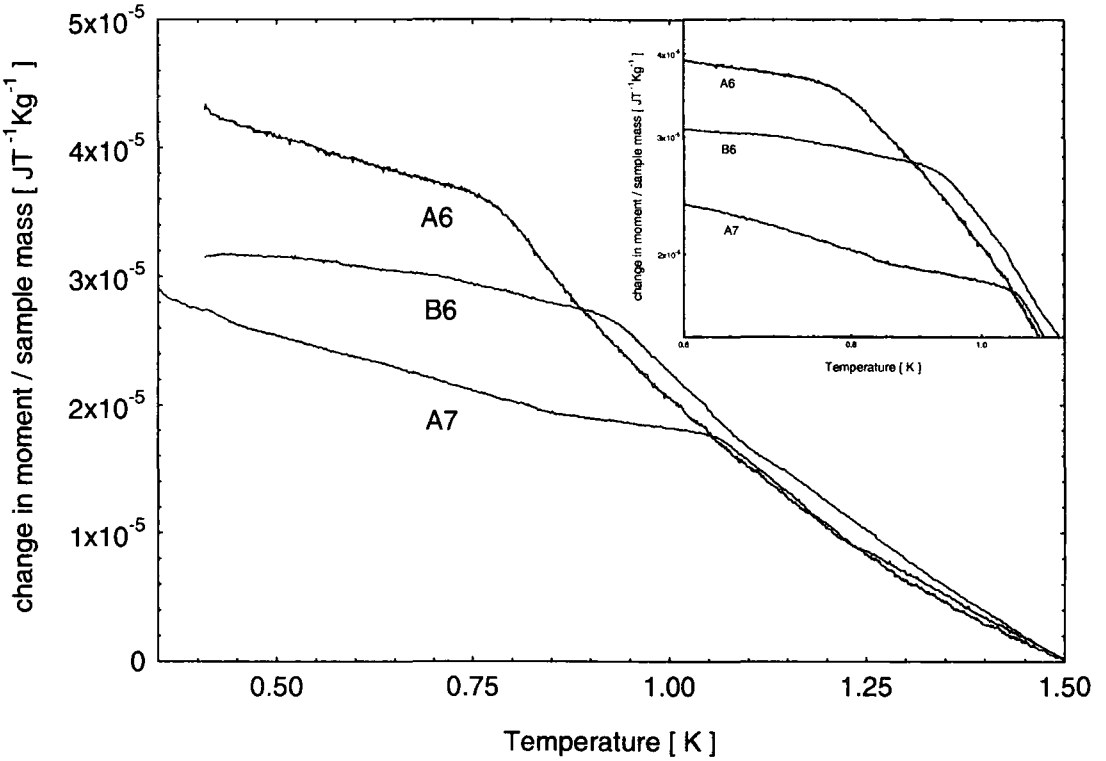

Figure 5.8 - Plot of change in magnetic moment per unit mass as a function of temperature for three samples of $Cd_{1-x}Mn_xTe$:In. Each sample has a different manganese concentration, and shows a spin glass phase transtion at a different temperture, T_g < 1.5K (inset the same data is plotted on a log-log scale).

As we have no cusp in χ it is more complicated to determine exactly the spin-glass freezing temperature. In an attempt to define some criteria for measuring T_g the first derivative of χ with respect to temperature has been determined for each sample measured (see figure 5.9). We can clearly see from the figure that there is a discontinuity in the derivative of susceptibility, this coincides with and is due to the 'kink' in the susceptibility data, observed at the SG freezing temperature. From the plot of $d\chi/dT$ we can determined T_g and also gain some information regarding the broadness of the transition.

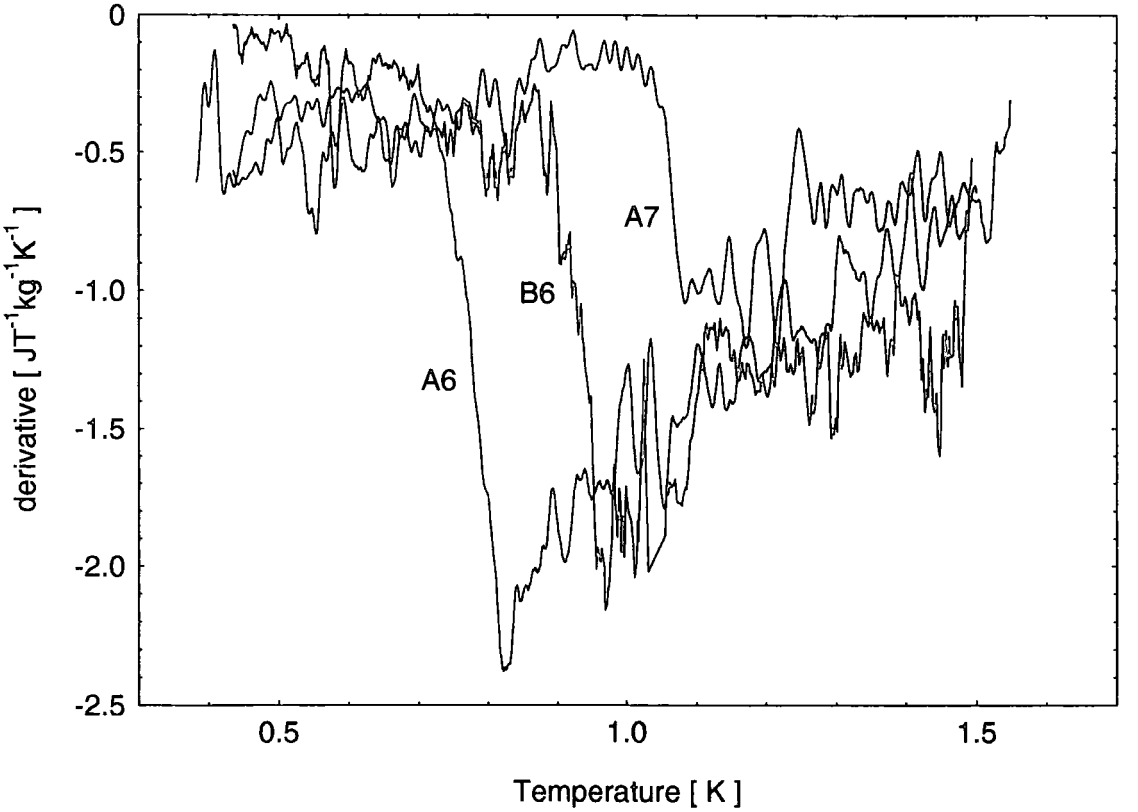

Figure – 5.9 Derivative with respect to temperature of data presented in figure 5.8 plotted against temperature for three different samples showing a spin-glass phase transition

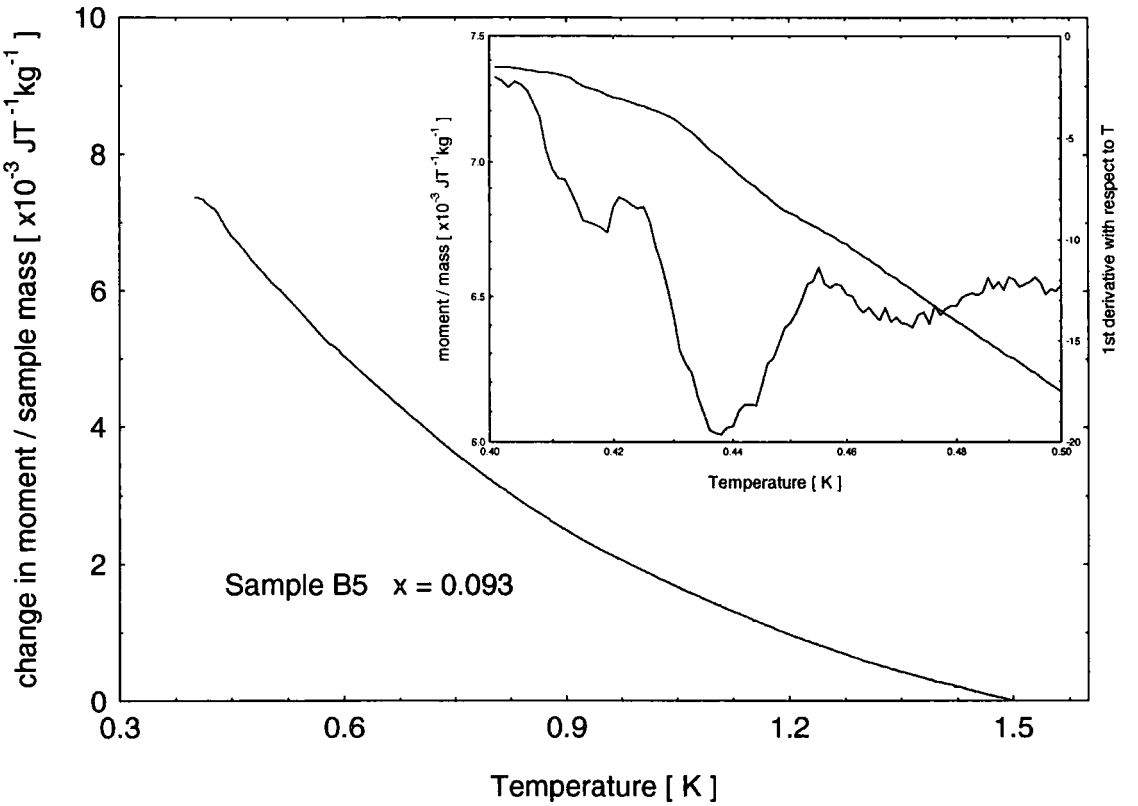

Figure 5.10 - Plot of change in magnetic moment per unit mass as a function of temperature for sample B5, with Mn fraction x = 0.093. Inset the low temperature data are plotted along with the derivative of the susceptibility with respect to temperature. The data are shown plotted on a log-log scale to indicate the SG freezing temperature.

In addition to the three samples for which data are shown in figure 5.9, a fourth sample, B5 (with x = 0.093) has been measured at temperatures down to 425 mK. Data obtained for sample B5 are shown in figure 5.10. At first sight it would appear that this sample shows similar behaviour to those in the paramagnetic phase discussed above, however on closer examination of the low temperature region of the curve we can see that the susceptibility starts to flatten, indicating the onset of SG freezing.

The inset of figure 5.10 shows a close up of the region around the SG freezing temperature. In addition we again plot the first derivative of χ with respect to temperature. We can see that the derivative calculated for sample B5 has the same form as those shown in figure 5.9 for the other three samples measured.

In figure 5.11 we plot the variation of T_g with the sample's Mn concentration, determined from EDAX. The figure contains four data points corresponding to the four samples for which we have measured T_g. Also we have included data after Novak *et al* [20]. Their interpretation was that SG freezing was due to Bloembergen-Rowland exchange interactions at high Mn concentrations. And for low Mn concentrations ($x < x_c$) they suggested that long range dipolar interactions were responsible for the SG freezing. By assuming that T_g is proportional to the mean effective field at each Mn ion site they were able to obtain an expression for the x dependence of T_g. A good fit to the experimental data could be obtained with two free parameters, this fit and their data is shown in figure 5.11 in addition to four data points from our experimental results at $T < 1.5$ K. Although agreement with the experimental data for the x dependence of T_g is reasonable, this model doesn't offer any satisfactory explanation for the shape of the χ vs T curves. Also later theoretical work of Larson *et al* [22] showed that superexchange, and not Bloembergen-Rowland interaction, is the dominant exchange mechanism.

Recently theoretical work has been carried out by Karaoulanis *et al* [23, 24] which seems to be able to describe (at least qualitatively) the experimental data. In their model the kink in χ vs T is attributed to the formation of a cluster glass. The basic idea is that for all Mn concentrations there are two contributions to the susceptibility. One contribution is an ordinary "Curie-Weiss-like" 1/T dependence due to isolated non-interacting clusters. The second contribution is from an infinite cluster (ie of the order of the sample size) and gives the traditional cusp in χ for a spin glass. The measured susceptibility is just a combination of these two contributions.

For this spin glass-like phase transition to occur there must be an infinite cluster. In order for an infinite percolative cluster to exist below the nearest neighbour percolation threshold ($x_c = 0.19$) it is necessary to consider nearest neighbour interactions of higher rank. For example if we include second nearest neighbour interactions the critical concentration becomes $x_{c2} = 0.13$, for third nearest neighbour interactions $x_{c3} = 0.06$ and so on.

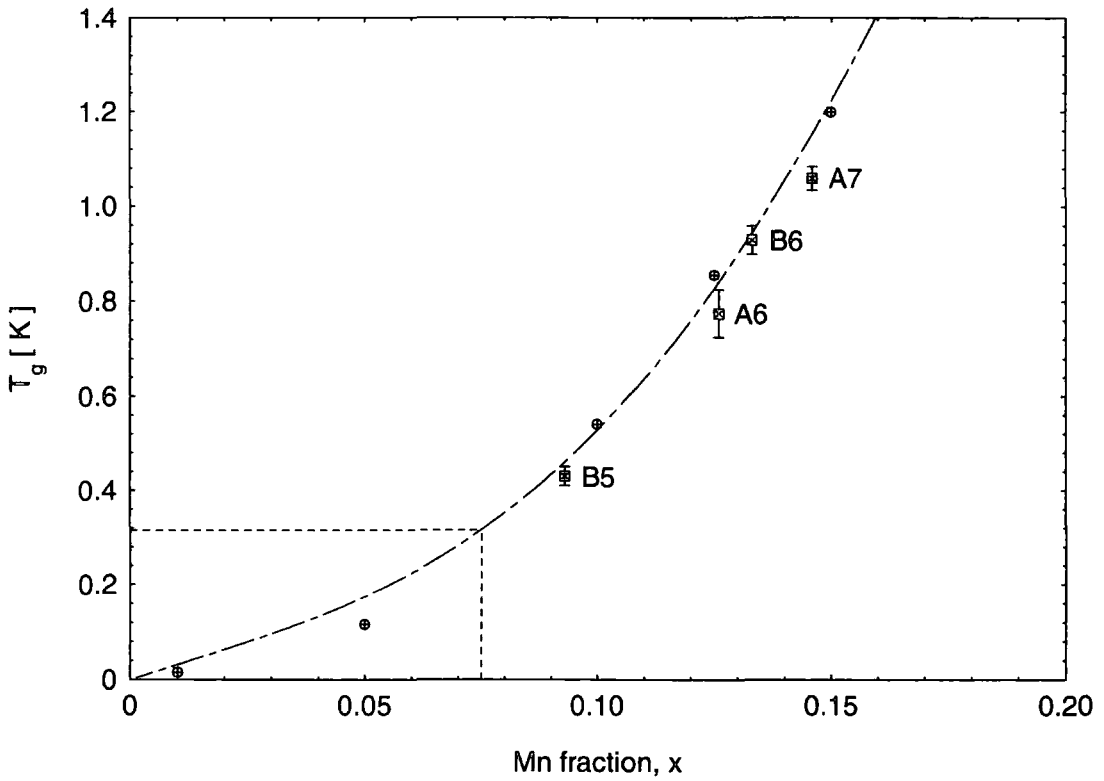

Figure – 5.11 Plot of spin glass freezing temperature (T_g) against manganese fraction (x) for our CdMnTe:In samples. Included in the figure are data points for the undoped CdMnTe samples measured by Novak et al [20]. The dashed curve represents an expression for the temperature dependence of Tg also after Novak et al [20]. The area enclosed by dotted lines in the bottom left corner of the figure indicates a region at temperatures below the lowest possible measuring temperature of our SQUID system.

Turning now to examine sample I4 at slightly higher temperatures ($T > 1.5$ K) we observe somewhat unexpected behaviour, see figure 5.12. If we initially look at just the zero field cooled (ZFC) data, we see a kink, not unlike those seen in figure 5.8 at lower temperatures. The data for the ZFC case were obtained after performing a zero field oscillation of the superconducting magnet. This oscillation of the magnet about zero field with reducing amplitude is intended to remove any remnant field due to trapped flux in the superconducting magnet. Many layers of high permeability material surround the SQUID cryostat serving to reduce the size of the Earth's magnetic field at the sample position. In addition to this kink, we also observe hysteresis between the FC and

ZFC data, this behaviour is characteristic of a SG phase. It should however be noted that this is a rather unexpected result. From both the high temperature susceptibility data and the EDAX measurement of this sample it would appear to indicate a Mn concentration of the order of 5%. If this were the case then the expected value of the SG freezing temperature would be approximately 150 mK. In fact to reconcile the measured T_g would require that the sample had a Mn concentration slightly greater than 20%.

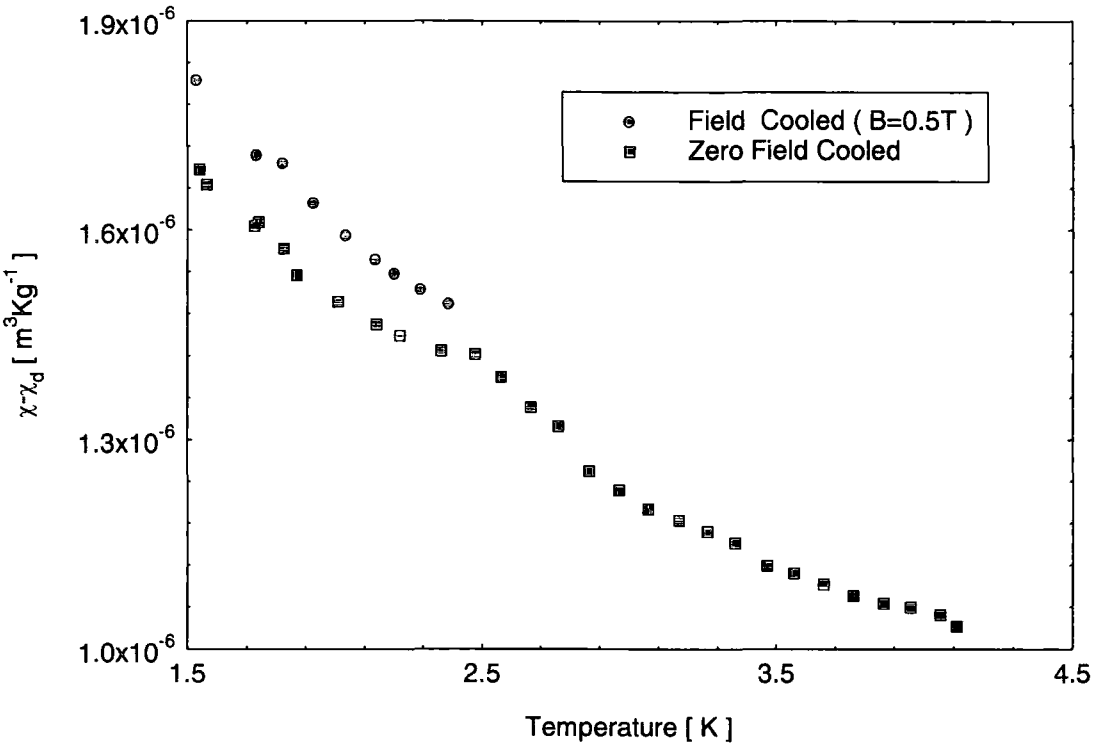

Figure – 5.12 Magnetic susceptibility against temperature for sample I4 (x = 0.045) showing an apparent spin-glass phase transition at T~2.5K

Susceptibility measurements made in the Durham SQUID system on a different piece of I4 (ie another sample cut from the same ingot) have not shown a kink at any temperature measured down to T ~ 335mK. One possibility is that for this particular crystal there exists some spatial inhomogeneity in the Mn concentration. Repeating EDAX measurements on other sections of the same crystal have produced a larger range of values for x than we have normally come to expect from these samples. (For sample I4 $\Delta x \sim 0.1$) Despite this it seems unlikely that we could encounter fluctuations in Mn concentration providing regions with 5% Mn and others with Mn concentrations in excess of 20%. However previous measurements of Leighton *et al* [25] reported a Mn concentration close to 18% for another sample of I4 cut from the same original crystal.

5.4.2 Photo-Induced Changes in Magnetism

Of the seven samples measured at temperatures below 1.5 K, two have been studied both before and after illumination. As described in section 2.4 utilising PPC is this way enables us to change the free electron concentration of the material. More importantly here, we are also changing the concentration of electrons localized at (neutral) shallow donor impurity sites. Figure 5.13 shows the results from two temperature dependent susceptibility measurements made on the same sample at different persistently photogenerated carrier densities. Unlike other photomagnetic measurements made using continual illumination, we can immediately rule out sample heating as the cause of any observed changes in magnetism. If illumination is required throughout a measurement great caution must be exercised in order to ensure that the power levels used do not raise the temperature of the sample. Conversely for our measurements of a persistent photoconductor (measurements being made after illumination ceases) we are able to use relatively high power levels to illuminate the sample. The illumination procedure was carried out at temperatures close to 1.5 K. After the LED is switched off and before measurements are started an adequate amount of time must be allowed for the sample to relax to a stable condition. During this waiting period (typically of the order of 30 minutes) the refrigerator was cooled to its base temperature. All the magnetic data presented in this thesis was obtained by recording the SQUID signal whilst slowly increasing the sample temperature.

When the sample was illuminated using a low power level from the LED we were able to observe changes in the sample's moment as a function of illumination time. In this way we can directly correlate the changes in the sample's magnetism with the effect of illumination. Data obtained in this way are not presented in this thesis for two reasons. Firstly, as mentioned above, the situation is complicated somewhat by the possibility of effects due to heating (either the sample or the LED). Although these effects can be minimised by using low LED power levels. Secondly, during illumination we frequently observed "flux jumps" in the SQUID signal as a result of switching the current through the LED. This meant that although we were able to observe a magnetic moment change coincident with illumination, it was impossible to measure the absolute magnitude of this change for a given illumination time. For these reasons we will compare the temperature dependence of the susceptibility, before and after illumination.

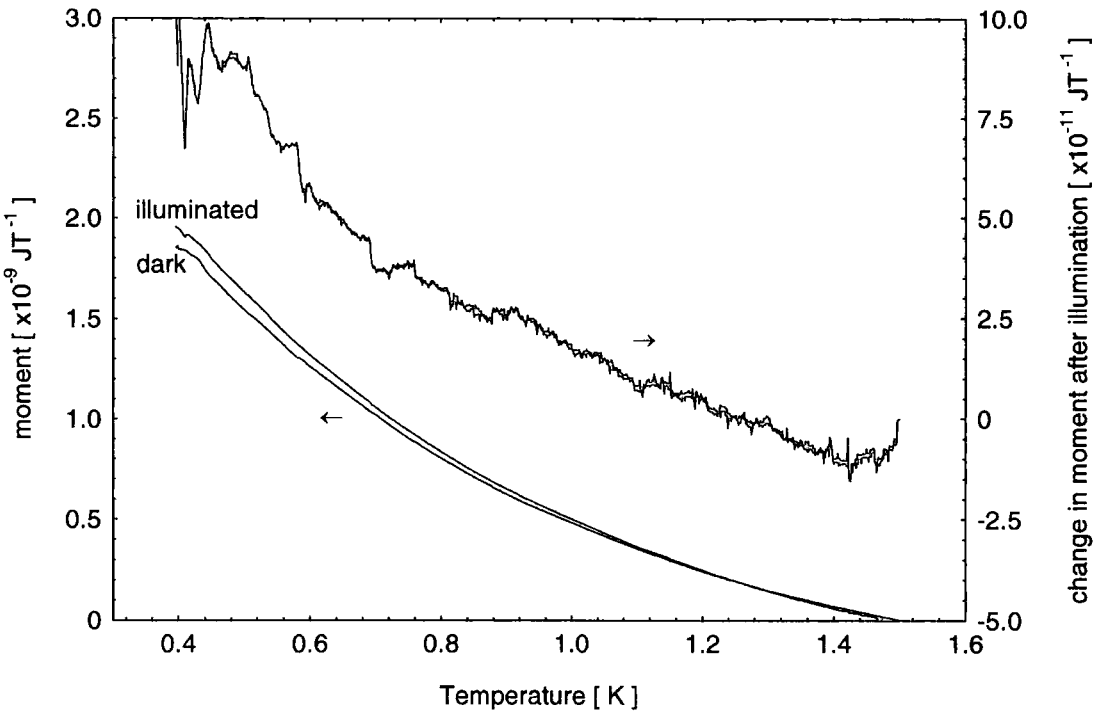

Figure 5.13 - (Left axis) change in magnetic moment as a function of temperature for sample B5 (x = 0.092). Curves are shown for both dark and saturation illumination. (Right axis) photo-induced change in magnetism, ie the measured difference between dark and illuminated curves.

Figure 5.13 shows just such a measurement for sample B5. Two different experimental data curves are presented, these correspond to measurements made before and after illumination. If we study figure 5.13 we can see a small change in the temperature dependence of the susceptibility for sample B5 after illumination. Although the observed change is rather small, it is much larger than the smallest resolvable moment of the system. This is clearly apparent from close examination of the graph where it can easily be seen that the observed change is larger than the noise. As a check, measurements were reproduced under identical sample conditions and the agreement was found to be excellent.

Due to the nature of SQUID measurements made with a static sample at a constant applied magnetic field we have no absolute calibrated measurement of susceptibility for this sample. For this reason in figure 5.13 above we are plotting change in magnetic moment, Δm, as a function of temperature. This value will be proportional to susceptibility as the sample mass and measuring field are unchanged for the duration of the measurement. We have arbitrarily chosen to set Δm to be zero at a temperature of 1.5 K, for both the dark and the saturation illumination curves. Also, on the plot in figure 5.13 we show on the right hand axis the difference in magnetic moment between the two curves measured at different free electron densities. This is the photomagnetic

contribution to the magnetic susceptibility. A similar effect has been observed previously in $Cd_{1-x}Mn_xTe_{1-y}Se$:In by Wojtowicz *et al* [26] at slightly higher temperatures (2 K < T < 4.5 K). In their case the enhanced magnetic susceptibility was attributed to an increased number of bound magnetic polarons formed around localized s electrons. As described in section 3.1.5 when we illuminate the sample at low temperatures we are photoexciting electrons from the deep DX centre, a number of the electrons become localized at shallow donor impurity sites. It is around these localized electrons that BMPs can form. A theoretical model describing the observed properties of BMPs has been proposed by Dietl & Spalek [27] and also independently by Heinman, Wolf & Warnock [28]. Although the exact details of these models vary slightly the results are essentially the same. Wojtowicz *et al* were able to fit to their temperature and field dependent magnetic measurements using BMP theory. Despite the limited extent of their experimental data they claim good agreement with the theory using only one fitting parameter, the change in concentration of shallow donors ΔN_d. They suggest that the number of BMPs prior to illumination is zero, it should be noted that this is very unlikely to be the case. From transport measurements activated conduction from a shallow impurity state is observed at low temperatures. This indicates that electrons freeze out into shallow states around which BMPs can form. Thus even before illumination a finite number of BMPs will exist. In a heavily doped sample this polaronic contribution to the susceptibility may not be negligible. Also, the somewhat simplistic suggestion that ΔN_d is equal to the change in carrier density determined from Hall measurements may not reflect accurately what is happening in a real system.

Similar measurements have also been carried out by Stankiewicz & Palacio on CdMnTe:Ga [29]. In their work the field dependence of the photo-induced change in magnetisation was measured. In contrast to the work of Wojtowicz *et al*, Stankiewicz & Palacio measured the magnetic field dependence up to higher field values and observed a saturation on the BMP magnetization.

A second sample, A7, which showed a SG phase transition at $T_g^{dark} = 1.06K$ has also been measured before and after illumination. The data for this sample are shown in figure 5.14 where we plot both the dark and illuminated susceptibilities as a function of temperature on the left axis. In addition we have again plotted the difference between these two curves on the right axis.

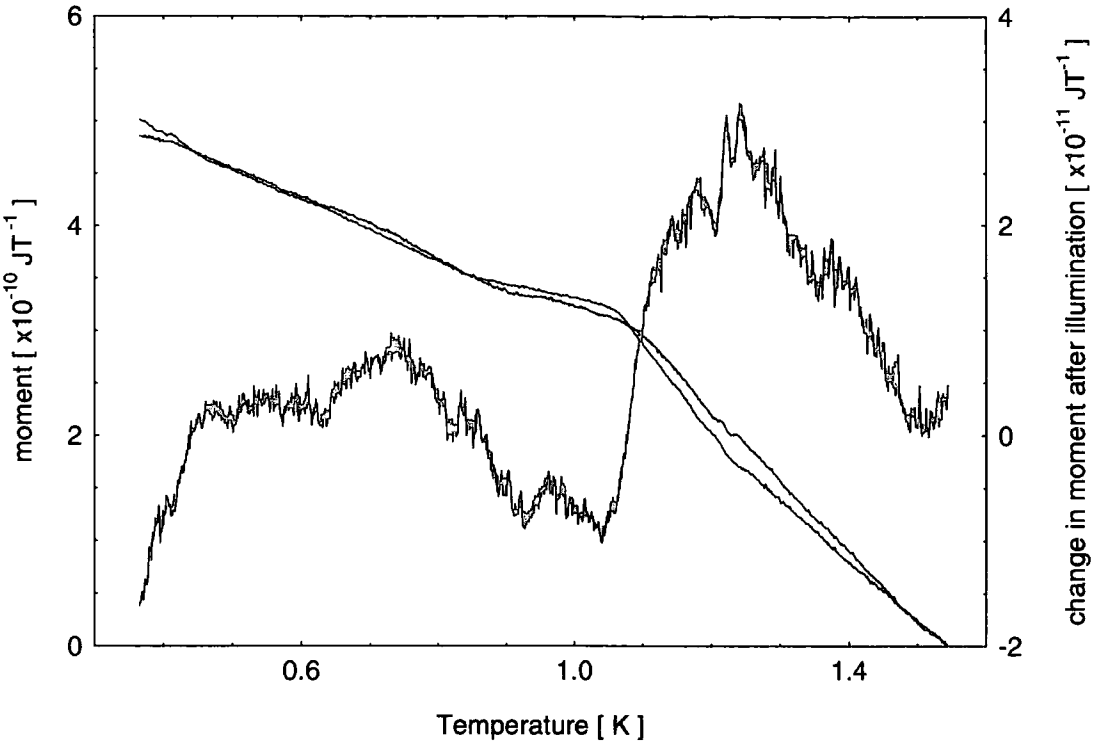

Figure – 5.14 Left axis: change in magnetic moment as a function of temperature for sample A7 (x = 0.146) showing the spin-glass phase transition, both for dark and saturation illumination. Right axis: difference between dark and illuminated curves.

The measured photomagnetic contribution to the susceptibility for sample A7 is quite different to that shown previously for sample B5. At high temperatures (above T_g) the behaviour is qualitatively similar, that is both samples show an increase as the temperature is reduced. For sample A7 we see that at $T \sim 1.25$ K the photoinduced susceptibility peaks and is then seen to drop very rapidly in the region of the SG freezing temperature. At temperatures below T_g the behaviour is more complicated, however in general we can see that the temperature dependence is weaker than we observed in the paramagnetic phase.

We can see quite clearly from the figure that the effect of illumination changes the sample's magnetism. After illumination to saturation the SG phase transition is shifted to a slightly higher temperature (ie $T_g^{ill} = 1.10\text{K}$, compared with $T_g^{dark} = 1.06\text{K}$). Also we see that after illumination the SG transition is considerably broadened, this can be more easily appreciated by examining the derivative $d\chi/dT$ which is shown in figure 5.15.

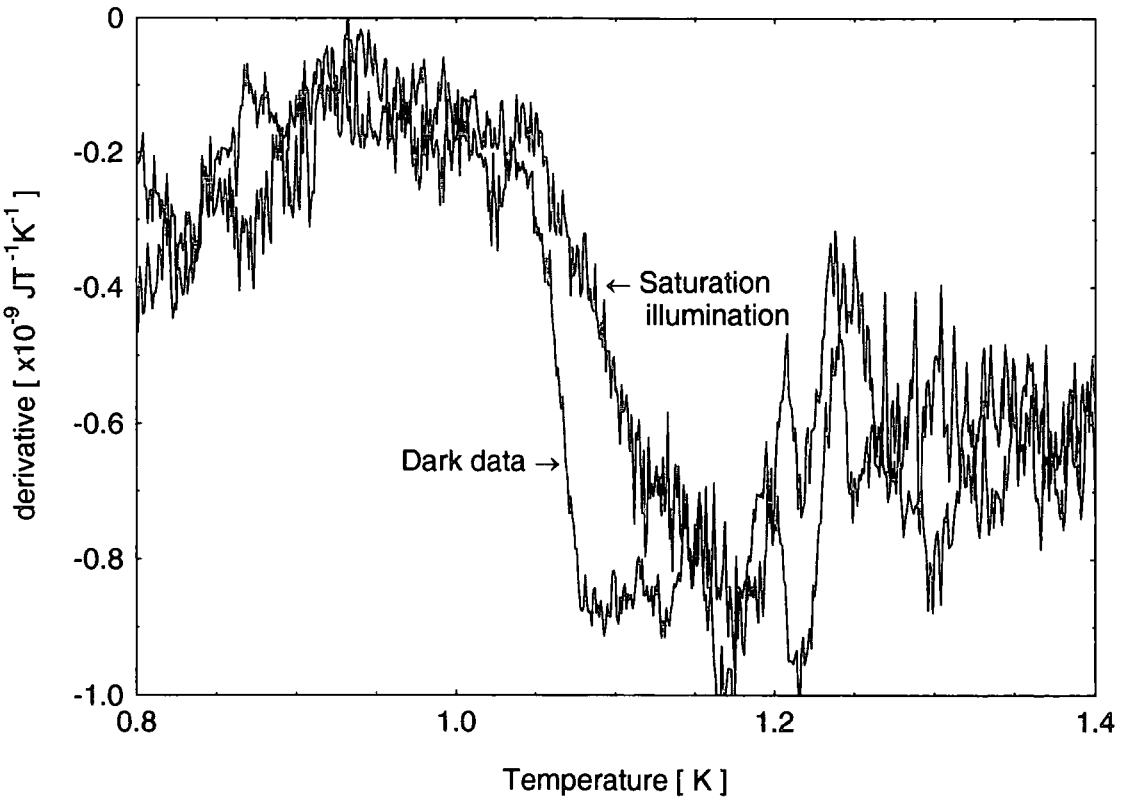

Figure – 5.15 Derivative with respect to temperature for sample A7 data shown above in figure 5.14 for both dark and saturation illumination measurements.

The exact mechanism behind the observed effect on the SG freezing is not immediately clear, however there are two possibilities that could be tentatively suggested. As we have already seen for sample B5 above, an increase in the number of shallow donors after illumination at low temperatures leads to an increased magnetic contribution due to the formation of bound magnetic polarons. If the increase in the concentration of BMPs is sufficiently high then these small ferromagnetic entities will almost certainly have some affect on the SG freezing.

The second possibility is that a RKKY exchange interaction plays a role in the magnetism of these samples. Normally for wide bandgap materials such as $Cd_{1-x}Mn_xTe$ the RKKY exchange interaction is negligible. However our samples are heavily doped and the free electron concentration is increased after illumination. So this itinerant electron exchange mechanism may influence the SG freezing process in our samples.

In order to examine our experimental data in terms of the theory of BMPs it is necessary that we obtain the temperature dependence of the magnetic susceptibility before and after illumination. As mentioned previously, due to the nature of the low temperature SQUID system used, we have so far presented data in terms of changes in magnetic

moment measured in the Earth's field. We can now go on to use our susceptibility measurements made on the same samples at higher temperatures in order to calibrate our low temperature measurements. We have fitted the lowest temperature data from the Bayreuth SQUID using a modified Brillouin function first proposed by Gaj *et al* [30]. This leads to a form for the low field susceptibility given by,

$$\chi = \frac{A}{T + T_0} \qquad \textbf{Equation 5.3}$$

The values of T_0 obtained from this fitting are listed in table 5.5.

Sample	Mn fraction X	T_g [K]	T_0 [K]	Measuring field, B [μT]
A1	0.0492	< 0.355	2.24	81
A2	0.046	< 0.340	2.47	76
A6	0.126	0.78	2.59	58
A7	0.146	1.06	2.79	82
I4	0.044	< 0.335	1.86	70
B5	0.093	0.43	-	-
B6	0.133	0.93	-	-

Table 5.5 – Details of the samples measured at low temperatures using the the Durham SQUID. In the second and third columns we give values for the Mn fraction and SG freezing temperature respectively. Fitting to the high temperature susceptibility data using a modified Brilloiun function results in a parameter T_0 listed in column four. This has allowed an extrapolation to lower temperatures and an estimate of the measuring field is given in column five.

We can then extrapolate to slightly lower temperatures and use this fit to put our low temperature Durham SQUID data on an absolute scale. The values of the measuring fields obtained from this procedure are listed in table 5.5. At this stage we should make some comment about the values of the measuring fields calculated in this way. We can see from the table that these values are not exactly identical from one run to the next. This is not completely unexpected as variations in the background field measured have been observed. It is likely that these are due to sources of magnetic fields which may be either within or external to our own laboratory. It should be stressed that due to the use of a superconducting shield around our SQUID system the measuring field remains constant for the duration of a measurement on any one particular sample. This field

value is simply the background field in the laboratory, and is "frozen" as the superconducting shield is cooled through its superconducting transition temperature.

Following the theory of Dietl & Spalek [31] we can write an expression (see equation 5.4) for the magnetic susceptibility of the BMPs as a function of both temperature and magnetic field. This result is obtained by taking the second partial derivative with respect to magnetic field of the magnetic polaron contribution to the free energy of the system.

$$\chi_P = \frac{N_D \mu_B^2}{4k_B T}\left[g^* + \frac{\alpha\chi(H,T)}{g\mu_B^2}\right]^2\left[\left(1+\frac{\varepsilon_p}{3k_B T}\right)\left(1+\frac{\varepsilon_p}{k_B T}\right)^{-1}\right]$$

Equation 5.4

Where the magnetic polaron energy, ε_P, is given by,

$$\varepsilon_P = \frac{\alpha^2 \chi(H,T)}{32\pi a_B^3 (g\mu_B^2)^2}$$

Equation 5.5

In the equations above, N_D is the concentration of shallow donors, around which the BMPs form and χ(H,T) is the bulk magnetic susceptibility of the material which is dependent on both temperature and magnetic field. The value α is the s-d exchange energy, g and g^* are the Landé splitting factors for the Mn spins and the donor electron respectively. In our fitting we use the value of the Landé splitting factor g^*(CdTe) = -0.75. We can calculate a_B assuming a shallow hydrogenic donor (see equation 2.6), again using parameters for CdTe, we have the dielectric constant ε_r(CdTe) = 10.2 and the electron effective mass m_e^*(CdTe) = 0.1m_e [32]. We take the value of $N_0\alpha$ = 0.22 eV [30], where N_0 is the number of unit cells per unit volume, and can be calculated from the lattice parameter.

In figure 5.16 we show the results obtained for sample A7 along with the fit made using the theory described above. We have adjusted the parameter N_D to obtain the best fit at high temperatures. The value used in this case is $N_D = 2.2 \times 10^{16}$ cm^{-3}, it is interesting to note that this value is in approximate agreement with the change in electron density, $\Delta n = 1 \times 10^{16}$ cm^{-3}, determined from low temperature Hall measurements [2]

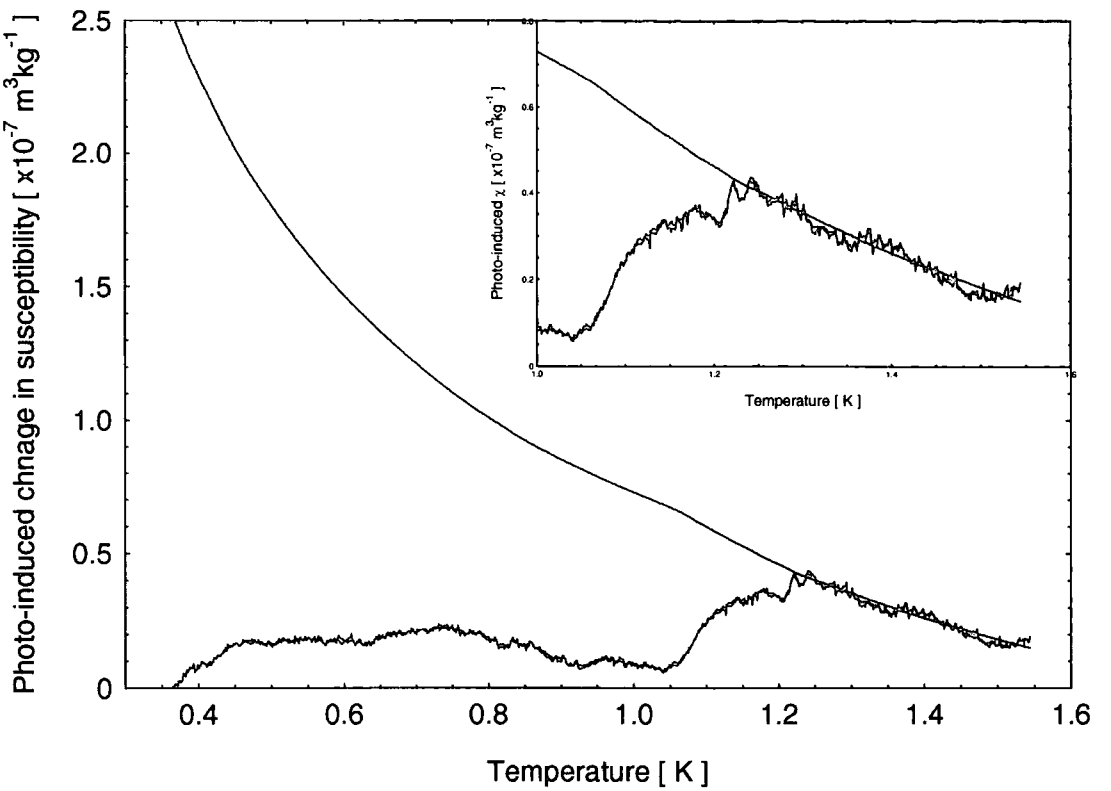

Figure 5.16 - Plot of the photo-induced change in susceptibility as a function of temperature for sample A7. The graph shows both the experimental data obtained and a curve calculated from theory. Shown inset is an enlargement of the region in which the fit has been made using the model of Dietl & Spalek as detailed in the text.

Figure 5.17 shows the data that have been obtained for sample B5. Again we have made a fit using the BMP theory. In this case we have to set $N_D = 5 \times 10^{15}$ cm^{-3} in order to obtain agreement with the experimental data. This result is a little surprising as electrical transport measurements have shown $\Delta n = 2 \times 10^{16}$ cm^{-3} [1].

One interesting difference to note about the two samples measured is the effect of SG freezing. Sample B5 is in a paramagnetic phase over almost the entire temperature range measured. This sample shows a photo-induced contribution to the susceptibility which increases with decreasing temperature. In contrast to this sample A7 undergoes a transition from a paramagnetic phase to a SG phase and we see a corresponding decrease followed by a weakening of the temperature dependence of the photo-induced change in susceptibility.

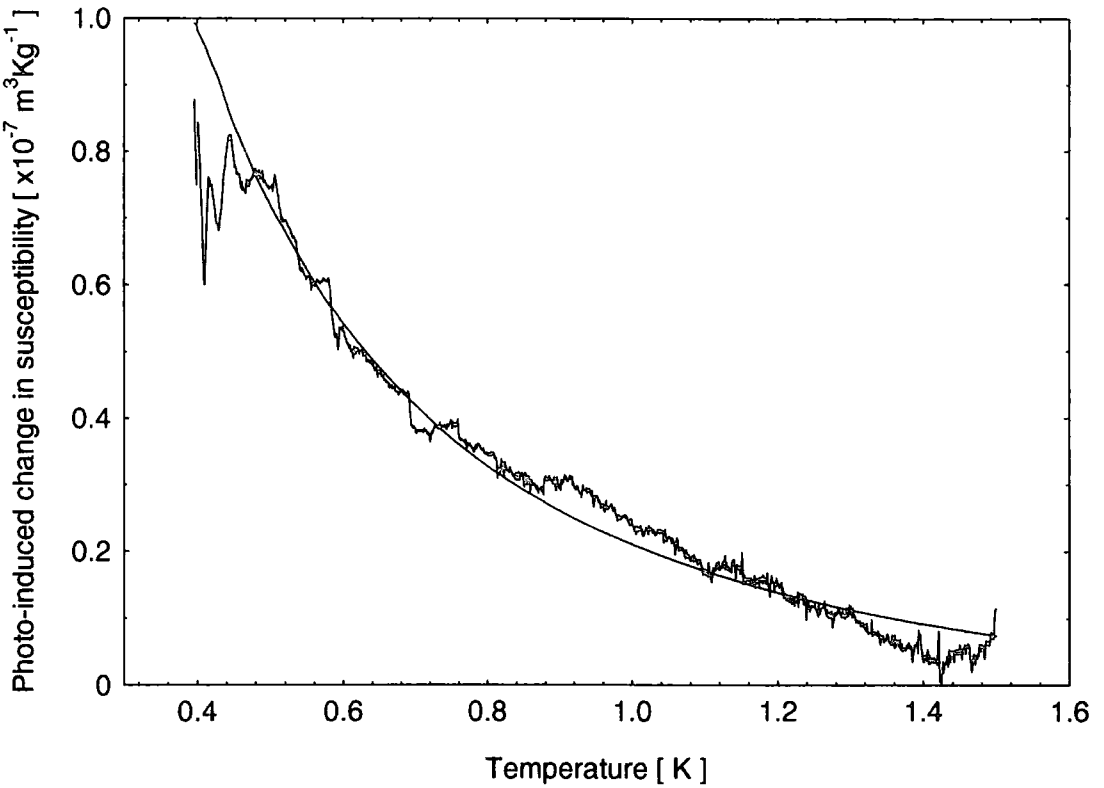

Figure 5.17 - Plot of photo-induced susceptibility as a function of temperature for sample B5. The graph shows both the experimental data obtained and a curve calculated from the theoretical model of Dietl & Spalek as detailed in the text

A recent theoretical work by Chudnovskiy *et al* attempts to describe the properties of magnetic polarons in the presence of spin glass order [33]. It is illuminating to examine the results of our measurements with reference to their work. They conclude that the onset of SG order changes the temperature dependence of the magnetic polaron binding energy. To be specific they suggest a plateaulike flattening in the temperature dependence of the polaron energy close to T_g. This result would seem to be consistent with our magnetic measurements of the polaron susceptibility described above. That is, we see a weak temperature dependence for the polaron susceptibility in the SG phase compared to the much stronger temperature dependence observed in the paramagnetic phase.

5.5 Summary and Conclusions

We have seen that the results of magnetic measurements made at high temperatures ($T > 4.2$ K) and presented above in section 5.3 are in good agreement with previous measurements for nominally undoped samples of $Cd_{1-x}Mn_xTe$. At lower temperatures some of the samples measured (ie those having higher x values) show a transition from a paramagnetic to a SG phase. The dependence of the SG freezing temperature on Mn fraction has been shown to be in reasonable agreement with earlier measurements.

At low temperatures two different samples have shown photo-induced changes in magnetism. These have been measured both in the paramagnetic phase and in the SG phase. The observed photo-induced changes have been attributed to the formation of bound magnetic polarons around quasi-localized s electron spins.

The measured contribution to the magnetic susceptibility of the sample from bound magnetic polarons shows a qualitative difference in the spin glass phase compared to that seen in the paramagnetic phase. The much weaker temperature dependence of the susceptibility in the spin glass phase is consistent with theoretical work which suggests that the magnetic polaron energy is effectively independent of temperature below the spin glass freezing temperature.

By illuminating at low temperatures, hence increasing the free electron density and the number of neutral shallow donors, we have seen an increase in the SG freezing temperature. In addition at higher carrier densities the transition is shown to have been somewhat broadened.

5.6 References

1. Leighton, C., *Persistent Photoconductivity and the Metal-Insulator Transition in $Cd_{1-x}Mn_xTe:In$*, in *Physics*. 1997, University of Durham.
2. Leighton, C., T. Terry, and P. Becla, *Nearest neighbor hopping in $Cd_{0.83}Mn_{0.17}Te:In$, controlled by persistent photoconductivity.* Solid State Communications, 1999. **110**(10): p. 531-536.
3. Candea, R.M., S.J. Hudgens, and M. Kastner, *Ionicity trends in the diamagnetism and its temperature dependence in average-valence-four semiconductors.* Physical Review B, 1978. **18**(6): p. 2733–2738.
4. Oseroff, S.B., *Magnetic-Susceptibility and Electron-Paramagnetic-Resonance Measurements in Concentrated Spin-Glasses - $Cd_{1-x}Mn_xTe$ and $Cd_{1-x}Mn_xSe$.* Physical Review B-Condensed Matter, 1982. **25**(11): p. 6584-6594.
5. Nagata, S., *et al.*, *Magnetic susceptibility, specific heat, and the spin-glass transition in $Hg_{1-x}Mn_xTe$.* Physical Review B, 1980. **22**(7): p. 3331–3343.
6. Kreitman, M.M., *et al.*, *Magnetic Susceptibility of Mn^{2+} in CdS and Effects of Antiferromagnetic Exchange.* The Physical Review, 1966. **144**(2): p. 367-372.
7. Shapira, Y., *et al.*, *Technical Saturation and Magnetization Steps in Diluted Magnetic Semiconductors - Predictions and Observations.* Physical Review B-Condensed Matter, 1984. **30**(7): p. 4021-4023.
8. Furdyna, J.K., *Diluted Magnetic Semiconductors.* Journal of Applied Physics, 1988. **64**(4): p. R29-R64.
9. Aggarwal, R.L., *et al.*, *Optical Determination of the Antiferromagnetic Exchange Constant Between Nearest-Neighbor Mn^{2+} Ions in $Cd_{0.95}Mn_{0.05}Te$.* Physical Review B-Condensed Matter, 1985. **32**(8): p. 5132-5137.
10. Larson, B.E., K.C. Hass, and R.L. Aggarwal, *Effects of Internal Exchange Fields On Magnetization Steps in Diluted Magnetic Semiconductors.* Physical Review B-Condensed Matter, 1986. **33**(3): p. 1789-1796.
11. Shapira, Y. and N.F. Oliveira, *High-Field Magnetization Steps and the Nearest-Neighbor Exchange Constant in $Cd_{1-x}Mn_xS$, $Cd_{1-x}Mn_xTe$, and $Zn_{1-x}Mn_xSe$.* Physical Review B-Condensed Matter, 1987. **35**(13): p. 6888-6893.
12. Foner, S., *et al.*, *Magnetization Steps in Dilute Magnetic Semiconductors to 55-T - Mn^{2+} Pair Saturation in $Cd_{1-x}Mn_xTe$ and Steps in $Zn_{1-x}Mn_xSe$,$Zn_{1-x}Mn_xTe$, and*

$Cd_{1-x}Mn_xSe$. Physical Review B-Condensed Matter, 1989. **39**(16): p. 11793-11799.

13. Giebultowicz, T., *et al.*, *Neutron-Scattering Studies of $Cd_{1-x}Mn_xTe$.* Journal of Applied Physics, 1984. **55**(6): p. 2305-2309.
14. Giebultowicz, T.M., *et al.*, *Harmonic Magnons in $Cd_{1-x}Mn_xTe$ and $Zn_{1-x}Mn_xTe$.* Physical Review B-Condensed Matter, 1989. **39**(10): p. 6857-6870.
15. Spalek, J., *et al.*, *Magnetic-Susceptibility of Semimagnetic Semiconductors - the High-Temperature Regime and the Role of Superexchange.* Physical Review B-Condensed Matter, 1986. **33**(5): p. 3407-3418.
16. Galazka, R.R., S. Nagata, and P.H. Keesom, *Paramagnetic—spin-glass—antiferromagnetic phase transitions in $Cd_{1-x}Mn_xTe$ from specific heat and magnetic susceptibility measurements.* Physical Review B, 1980. **22**(7): p. 3344–3355.
17. Isaacs, E.D., *et al.*, *Magnetic-Ion-Pair Interaction in (Cd,Mn)Te and (Cd,Mn)Se Using Spin-Flip Raman-Scattering and Magnetization.* Physical Review B-Condensed Matter, 1988. **38**(12): p. 8412-8418.
18. Slater, J.C., J. Chem. Phys., 1964. **39**: p. 3199.
19. Novak, M.A., *et al.*, *Spin Freezing Below the Nearest-Neighbor Percolation Concentration in $Cd_{1-x}Mn_xTe$ and $Cd_{1-x}Mn_xSe$.* Physical Review B-Condensed Matter, 1986. **33**(9): p. 6391-6394.
20. Novak, M.A., *et al.*, *Spin-Glass Behavior of $Cd_{1-x}Mn_xTe$ Below the Nearest-Neighbor Percolation Limit.* Journal of Applied Physics, 1985. **57**(8): p. 3418-3420.
21. Mydosh, J.A., *Spin Glasses : An Experimental Introduction.* 1993: Taylor & Francis.
22. Larson, B.E., *et al.*, *Theory of Exchange Interactions and Chemical Trends in Diluted Magnetic Semiconductors.* Physical Review B-Condensed Matter, 1988. **37**(8): p. 4137-4154.
23. Karaoulanis, D., J.P. Xanthakis, and C. Papatriantafillou, *The nature of the magnetic phase of diluted magnetic semiconductors below the nearest-neighbour percolation threshold.* Journal of Magnetism and Magnetic Materials, 1996. **161**: p. 231-234.
24. Karaoulanis, D., J.P. Xanthakis, and N.C. Bacalis, *Interpretation of the spin glass behaviour of diluted magnetic semiconductors below the nearest-*

neighbour percolation threshold via realistic Monte Carlo simulations. Journal of Magnetism and Magnetic Materials, 2000. **221**(3): p. 407-413.

25. Leighton, C., I. Terry, and P. Becla, *Metal-insulator transition in the persistent photoconductor $Cd_{1-x}Mn_xTe:In$.* Europhysics Letters, 1998. **42**(1): p. 67-72.
26. Wojtowicz, T., *et al.*, *Application of Photomemory Effect in $Cd_{1-x}Mn_xTe_{1-y}Se_y:In$ For Direct Measurements of Magnetization of Bound Magnetic Polarons.* Acta Physica Polonica a, 1992. **82**(4): p. 637-640.
27. Dietl, T. and J. Spalek, *Effect of Fluctuations of Magnetization On the Bound Magnetic Polaron - Comparison With Experiment.* Physical Review Letters, 1982. **48**(5): p. 355-358.
28. Heiman, D., P.A. Wolff, and J. Warnock, *Spin-Flip Raman-Scattering, Bound Magnetic Polaron, and Fluctuations in (Cd,Mn)Se.* Physical Review B-Condensed Matter, 1983. **27**(8): p. 4848-4860.
29. Stankiewicz, J. and F. Palacio, *Magnetization of bound magnetic polarons in Ga-doped $Cd_{1-x}Mn_xTe$.* Physical Review B-Condensed Matter, 1997. **56**(19): p. 12077-12079.
30. Gaj, J.A., R. Planel, and G. Fishman, *Relation of Magneto-optical Properties of Free Excitons to Spin Alignment of Mn^{2+} Ions in $Cd_{1-x}Mn_xTe$.* Solid State Comm, 1979. **29**: p. 435-438.
31. Dietl, T. and J. Spalek, *Effect of Thermodynamic Fluctuations of Magnetization On the Bound Magnetic Polaron in Dilute Magnetic Semiconductors.* Physical Review B-Condensed Matter, 1983. **28**(3): p. 1548-1563.
32. Zanio, K., *Cadmium Telluride.* Semiconductors and Semimetals, ed. W. Beer. Vol. 13. 1978: Academic Press.
33. Chudnovskiy, A.L., *et al.*, *Effect of spin-glass order on magnetic polarons in semimagnetic semiconductors.* Physical Review B-Condensed Matter, 1997. **55**(16): p. 10519-10527.

6 Results of Electrical Measurements Close to the Metal-Insulator Transition

6.1 Introduction

This chapter presents the results of extensive electrical transport measurements made at very low temperatures ($T > 40$ mK). These measurements have been carried out on a number of samples of $Cd_{1-x}Mn_xTe$:In which have all been cut from the same ingot (denoted by the label A1) and were found to have very similar properties. Using ICPAES we have determined the manganese fraction to be $x = 0.0492 \pm 0.0003$ for one sample cut from the ingot. Using EDAX we have found that all the pieces studied have manganese concentrations close to this value ($\pm$ 0.005).

Electrical measurements have been made in a variety of different cryostats using slightly different techniques, as has been previously described in section 4.3. The results of these measurements will be presented in the following chapter. The subsequent sections of this chapter are set out as described below. First in section 6.2 we present the results of electrical transport measurements made at the highest temperatures. These measurements clearly show PPC in our samples and have been used to characterise the material. In sections 6.3 and 6.4 we go on to examine the extension of electrical transport measurements to lower temperatures. We will present data for sample A1 prior to illumination and also at higher photogenerated carrier densities. We will make comments about the samples behaviour with reference to its proximity to the metal insulator transition. In addition, it is possible to drive this sample from an insulating to a metallic phase, by application of a magnetic field. The analysis of this observed IMT will be presented in section 6.4. Throughout our measurements on two of the samples taken from the ingot labelled A1 we have observed a strong temperature dependence of the anisotropy in the resistivity at very low temperatures ($T < 200$ mK). In section 6.5 we will present our experimental data and make some comments about the likely cause of this unusual effect. Finally in section 6.6 we report on the low temperature magnetoresistance that has been measured in this sample. Of the MR data presented those measurements made at relatively high temperatures show forms of MR which have been previously observed by other authors. At very low temperatures we observe a large low field negative MR not previously reported. Some concluding remarks about the results of these electrical measurements are made in section 6.7.

6.2 High Temperature Measurements

In this section we present the results of electrical measurements of sample A1 made at relatively high temperatures (T > 4.2 K). A number of different pieces cut from the same crystal have been measured at high temperatures and all showed similar behaviour. We will present results for one sample of crystal A1 which is representative of those studied.

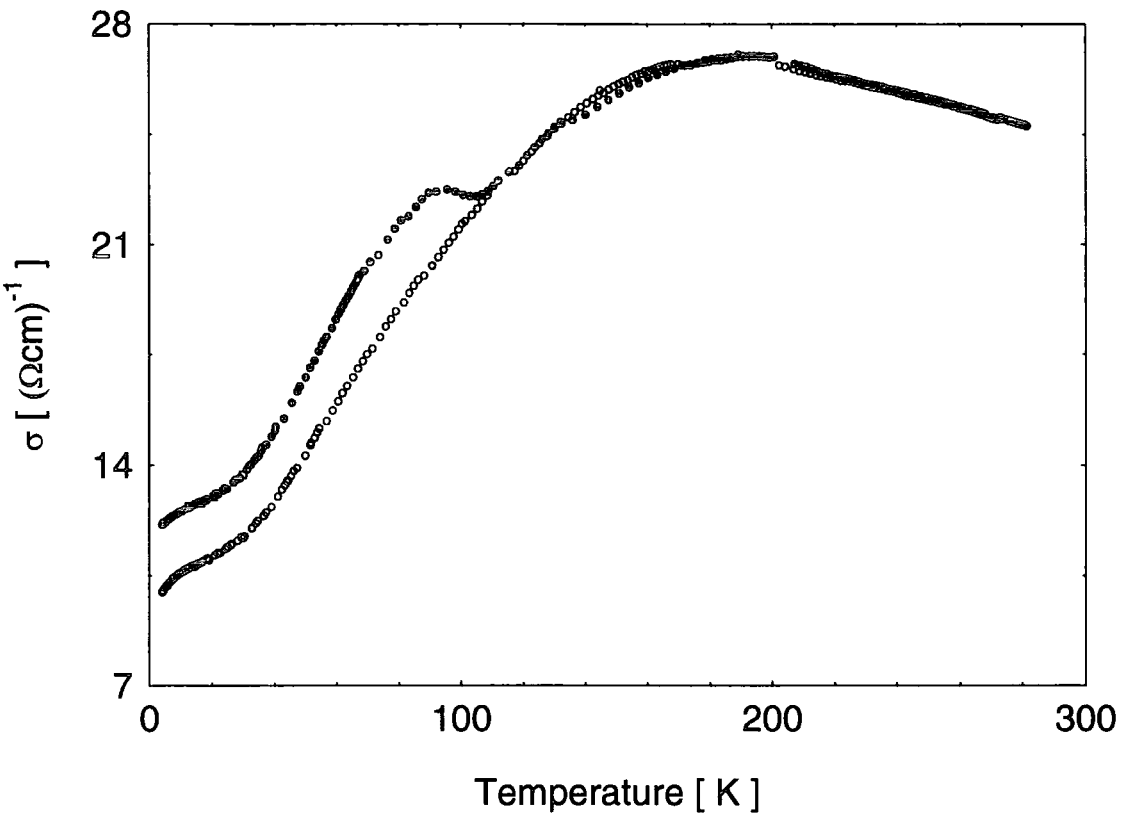

Figure 6.1 - Plot of conductivity against temperature measured from 300 K down to 4.2 K for sample A1. Data are shown for two photogenerated carrier densities, these correspond to measurements made after cooling in the dark (open symbols) and after illumination to saturation (closed symbols).

In figure 6.1 the conductivity of sample A1 is shown plotted as a function of temperature. In this figure data are presented for two different carrier densities. Initially the sample was measured in the dark, following this the sample was cooled again to 4.2 K where the carrier density was increased by illuminating. After which the conductivity was again measured as a function of temperature while warming the sample. The increase in effective free electron density is brought about using the PPC effect which has already been described in section 2.4.

At room temperature the carrier density was determined from Hall measurements and found to be, $n \sim 4x10^{17}$ cm^{-3}. At T ~ 12 K we have measured n both before and after illumination. Prior to illumination we found $n \sim 3.3x10^{17}$ cm^{-3}, the carrier density then increased by a factor of approximately 1.14 on illuminating to saturation. Figure 6.2 shows a plot of the variation of the Hall carrier density with temperature. The effect of illumination on carrier concentration at low temperatures is apparent from this plot.

After illumination as the sample temperature is increased we observe that the PPC starts to relax as the temperature approaches the so called "quenching temperature", T_Q. This occurs as the energy an electron requires to overcome the energy barrier to recombination is reached (that is $k_BT \sim E_C$). Electrons which overcome this barrier can once again occupy the deep DX$^-$ state. We simply define T_Q as the temperature at which the illuminated resistivity curve rejoins the dark curve. From the conductivity data in figure 6.1 we can see that $T_Q \sim 105$ K, although it has been shown that the quenching temperature determined by experiment is rather sensitive to the warming rate. This can be understood by considering the temperature dependence of the PPC relaxation rate [1].

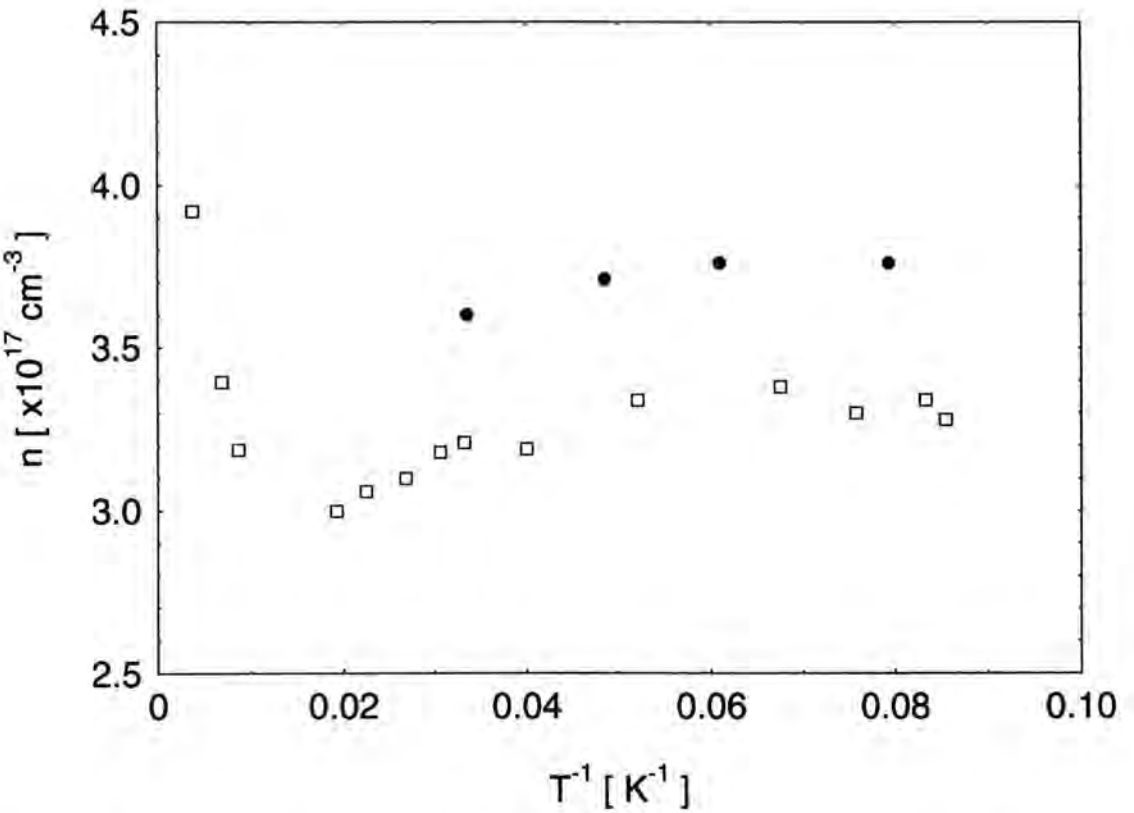

Figure 6.2 - Plot of Hall carrier density, n, against inverse temperature from room temperature down to T ~ 12 K for sample A1. Data are shown for 2 photogenerated carrier densities, these correspond to measurements made after cooling in the dark (open symbols) and after illumination to saturation (closed symbols).

The high temperature electrical measurements presented above are in good agreement with those made previously on similar samples [2]. The behaviour is qualitatively the same and the magnitudes of the carrier density are of course dependent on the exact details of the doping, which can vary between different samples. One particular feature that is worthy of note is the apparent minimum in the Hall carrier density at temperatures in the region of 65 K. Again this was previously observed and attributed to a change in the conduction mechanism. It was proposed that at high temperatures conduction proceeds via activation of electrons from shallow impurity levels to the conduction band, while at low temperatures there is conduction of a metallic nature taking place within an impurity band. This suggestion is backed up by the fact that in the region of the dip a slight nonlinearity in the Hall effect has previously been observed [3]. This nonlinearity of the Hall effect is expected in the temperature range where such a crossover between conduction mechanisms occurs.

Due to the size and nature of the low temperature magnetoresistance observed in these samples an accurate Hall effect measurement is almost impossible at temperatures below T ~ 10 K. It can, however, be seen from figure 6.2 that at low temperatures the carrier density is only very weakly temperature dependent. Thus for this reason it seems acceptable to take the values of n measured at 10 K to be representative of the values at lower temperatures. To illustrate the difficulties encountered we present data for an attempted Hall measurement on sample A1 at temperature of 8 K. In figure 6.3 we plot the variation of the sample's resistance measured in the Hall configuration, it can clearly be seen that the large MR prevents a determination of the Hall number at this temperature. It should also be realised that this effect presents a greater problem when measuring conductive samples, rather than the case of more insulating samples. This is simply due to the fact that a sample with a large carrier density has a small Hall voltage.

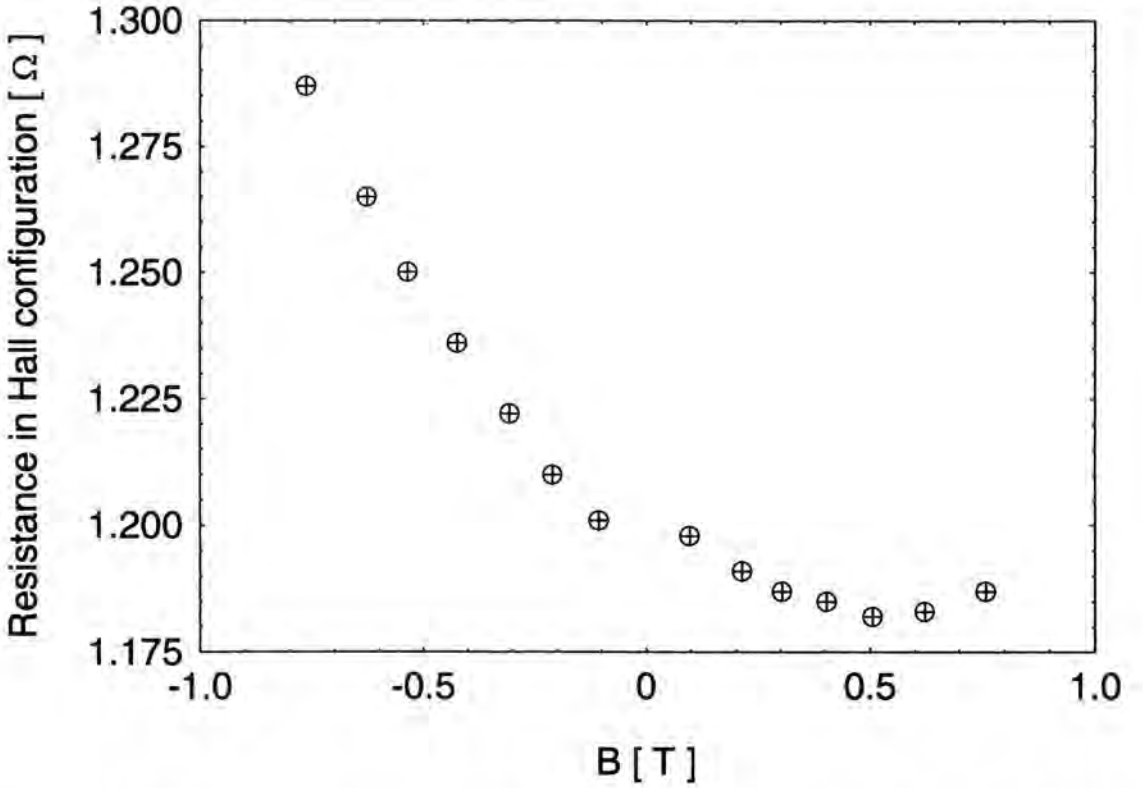

Figure 6.3 - Attempt made to measure the Hall number for sample A1 at T = 8 K. The plot highlights the large contribution due to the positive MR seen in at this temperature.

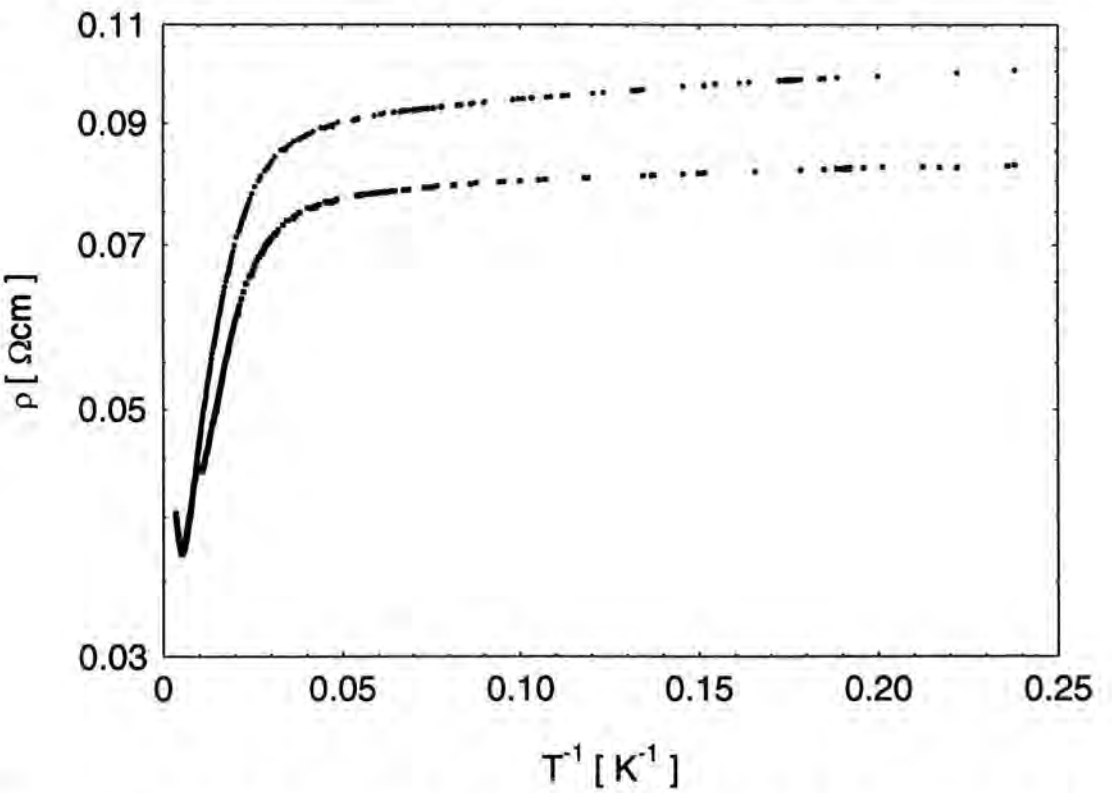

Figure 6.4 - Plot of log resistivity against inverse temperature for sample A1 in the temperature range 4.2 K < T < 300 K. Data shown are measured warming the sample after (a) cooling in the dark (circles) (b) illuminating to saturation at 4.2 K (squares).

In figure 6.4 we plot the inverse temperature dependence of the resistivity on a log scale. If we assume that the conduction is of an activated form then analysis of the data gives the following activation energies listed below, along with the temperature range over which the data were fitted.

$E_D = 3.7$ meV. For $T > 50$ K.
(dark) $E_s \sim 0.04$ meV. (saturation illumination) $E_s \sim 0.02$ meV. For $T < 25$ K.

These values were obtained by fitting to linear regions of the resistivity (figure 6.4), or more accurately Hall effect data (figure 6.2) as resistivity measurements also contain temperature dependence of mobility. Thus it is more accurate to determine activation energies from Hall effect measurements rather than resistivity. The values listed above are clearly unphysical and thus it is necessary to analyse the data of figures 6.2 and 6.4 assuming the sample is degenerate (or weakly degenerate) in the temperature range of interest.

From independent measurements of the resistivity and the Hall effect, as have been described above, it is possible to calculate the Hall mobility. This has been carried out and the results are plotted as a function of temperature in figure 6.5. The temperature dependence of the mobility allows us to gain some insight into the dominant scattering mechanisms at work over the different temperature regimes examined.
Previous results were obtained from measurements made on a similar sample [2] and the temperature dependence of the mobility was attributed to scattering from ionized impurities. We observed that upon illuminating the sample at low temperatures the Hall mobility is increased. If we consider this observation in terms of the effect that it will have on the ionized impurity scattering rate we can see that there will be two different contributions. Firstly on illumination there may be some change in the number of ionized impurities present, thus the number of scattering centres will be changed. It is unlikely that this will be a large effect, because both the deep DX state and the ionized shallow impurity state of the In donor have a charge of magnitude e. The second effect of illumination is likely to be more important. When the free electron concentration is increased there will be a greater screening of the impurity ions and hence the scattering rate will be reduced.

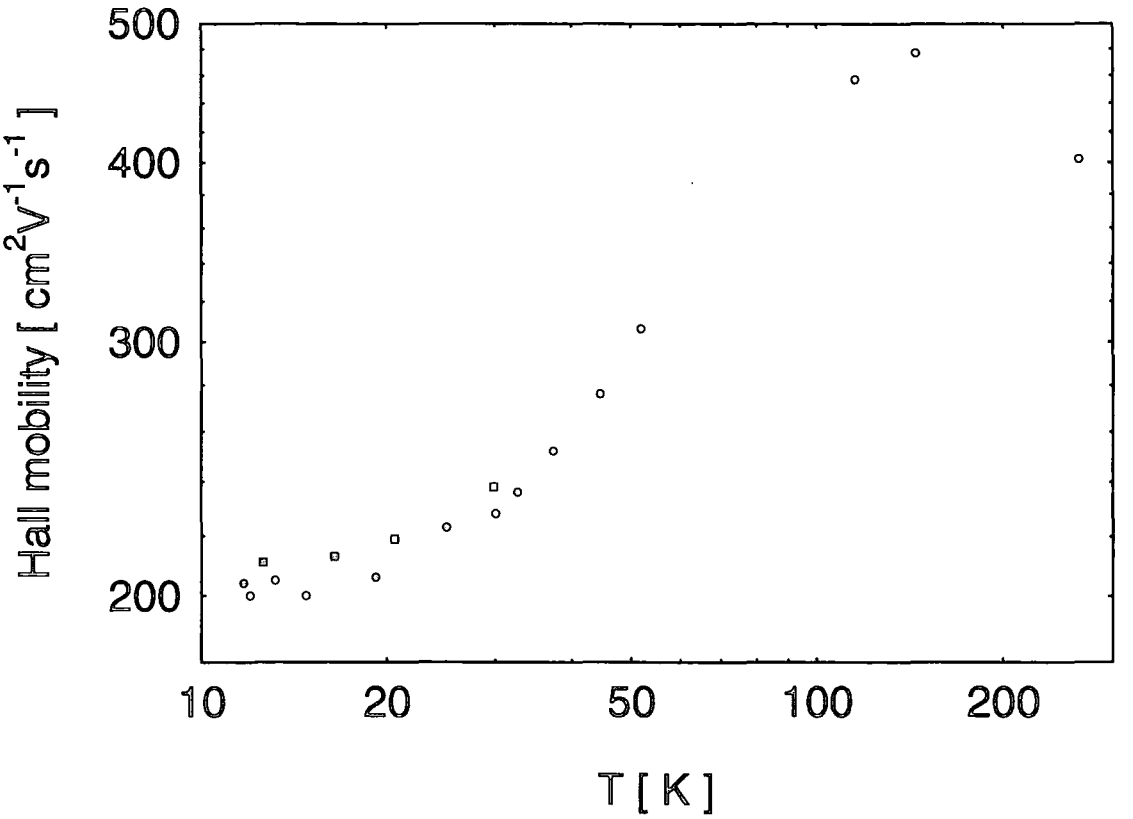

Figure 6.5 - Plot of Hall mobility against temperature from room temperature down to 4.2 K for sample A1. Data are shown for both dark (circles) and saturation illumination (squares).

Although ionized impurity scattering may play a role in the electrical transport of sample A1 at low temperatures, from our data it would appear that the mobility has a weaker temperature dependence than $T^{3/2}$ normally expected from this scattering mechanism.

We can now explore alternative scattering mechanisms that may be relevant to sample A1. The temperature dependence of the mobility for a number of different scattering mechanisms is summarised in reference [4]. At temperatures below approximately 30 K the mobility is only very weakly dependent on temperature.

In contrast to ionized impurity scattering, the effect of neutral impurities is predicted to be essentially independent of temperature [5]. Another possible cause of a temperature independent mobility is some combination of temperature dependent scattering rates competing to give a temperature independent result.

In an alloy (such as $Cd_{1-x}Mn_xTe$) an electron can be influenced, and hence scattered by, local changes in the potential resulting from fluctuations in the composition. It can be shown (eg see [4]) that this alloy scattering gives rise to a temperature dependent mobility where, $\mu \propto T^{-1/2}$. Combining this scattering mechanism with dipolar scattering,

which has $\mu \propto T^{1/2}$ could (if both effects had similar magnitudes) result in an almost temperature independent mobility. Dipolar scattering could also be present as a result of pairs of positively and negatively charged impurities. It seems likely that this situation could arise in a heavily doped semiconducting material, such as we have examined here. Thus a combination alloy scattering and dipolar scattering would result in a low temperature mobility that is independent of (or very weakly dependent on) temperature.

Having examined in some detail the electrical transport properties of sample A1 at, and above liquid helium temperatures, we shall now move on to discuss the results of lower temperature measurements made in the millikelvin regime.

6.3 Low Temperature Electrical Measurements as a Function of Illumination

Once again we shall begin by examining previous measurements made on the same sample [2] and then move on to more recent results extending the measurement range to lower temperatures.

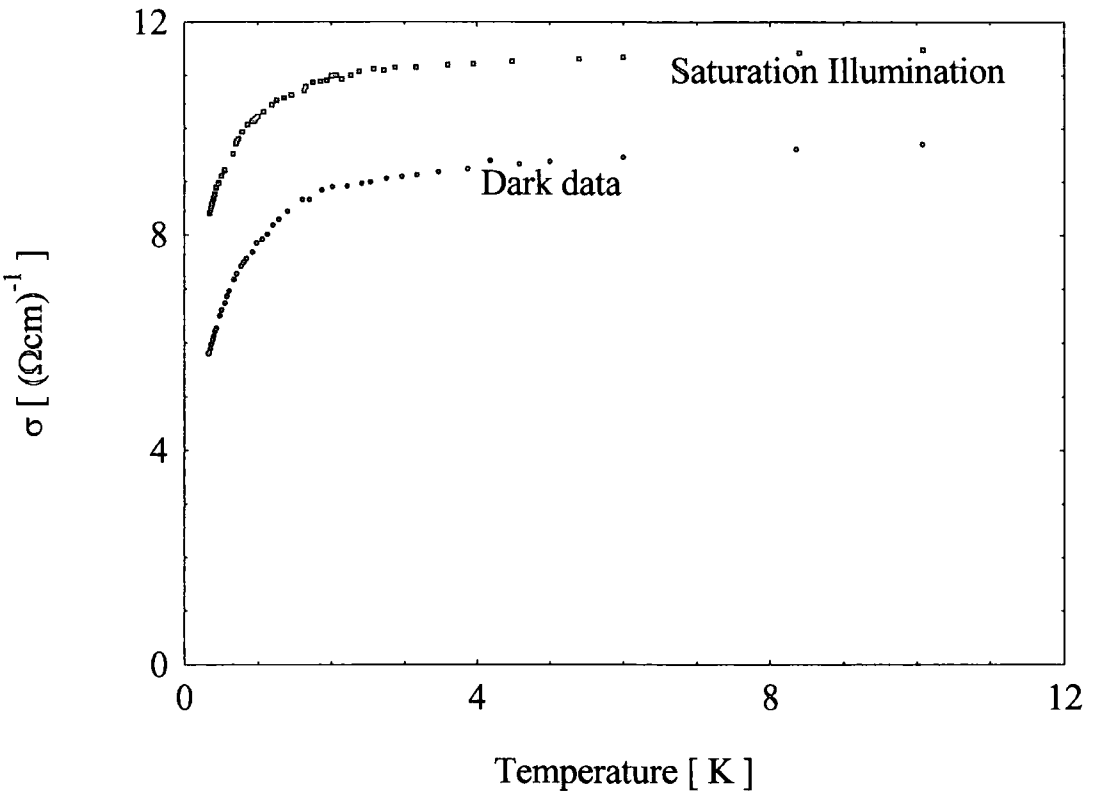

Figure 6.6 - Plot of conductivity against temperature down to 300 mK for sample A1. These measurements presented here were previously carried out by C Leighton [3].

Figure 6.6 shows the conductivity measured down to He^3 temperatures (T > 300 mK) after Leighton *et al* [3]. At high temperatures the conductivity is rather weakly temperature dependent. As the temperature is reduced below T ~ 2K the conductivity begins to fall off more quickly, below T ~ 800 mK the decrease is very rapid indeed. This sudden and very dramatic drop in the conductivity was attributed to an enhanced spin disorder scattering rate due to the formation of BMPs. A similar effect had previously been observed in CdMnSe (albeit at a lower temperature T ~ 300 mK) by Dietl *et al* [6]. It was suggested by Leighton *et al* that this difference in the temperature at which the rapid downturn in the conductivity begins, could be simply explained by considering the different material parameters characterising samples of CdMnTe compared with those of CdMnSe. We shall make more comments on the comparison between our work and that of Dietl *et al* later in this chapter.

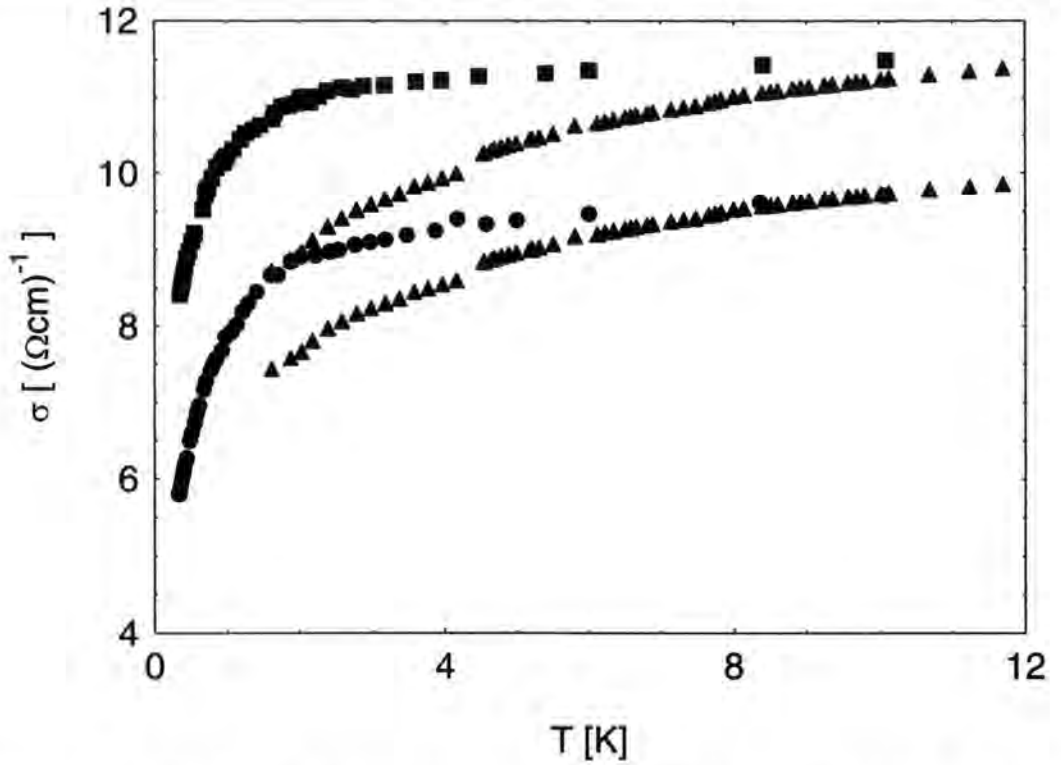

Figure 6.7 - Conductivity against temperature down to 300 mK for sample A1. Curves are shown for both dark data (circles) and saturation illumination (squares). In addition an attempted fit to the data based on a model of Sawicki *et al.* is shown (open triangles).

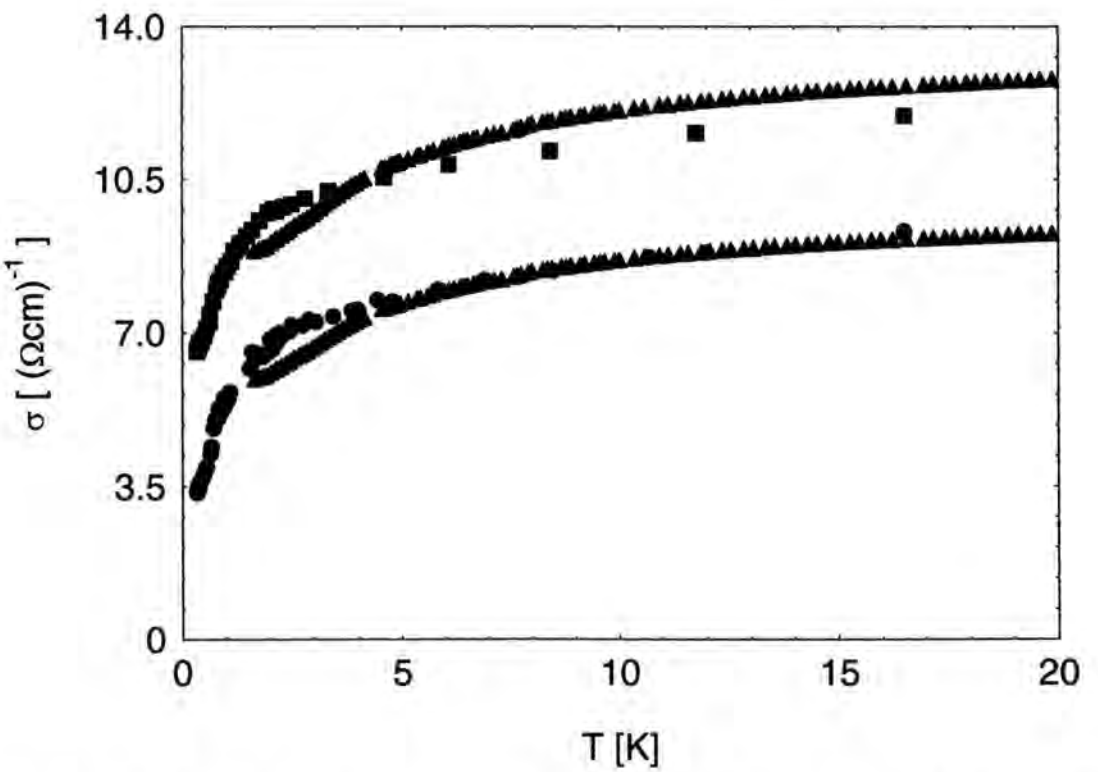

Figure 6.8 - Conductivity against temperature down to 300 mK for sample A2. Curves are shown for both dark data (circles) and saturation illumination (squares), from reference [7]. In addition an attempted fit to the data based on a model of Sawicki *et al.* is shown (open triangles).

Leighton *et al* [3] were able to use an approximate model based on the work of Sawicki *et al* [8] in order to model the observed temperature dependence of the conductivity at low temperatures. This model gave good agreement with the measured conductivity when the functional form for the low temperature magnetic susceptibility was assumed to be,

$$\chi = aT^{-b} \qquad \text{Equation 6.1}$$

with a and b used as fitting parameters. Our measurements of the low field magnetic susceptibility at low temperatures suggest that this model is in fact insufficient to describe accurately the observed experimental data for the conductivity [7]. In figures 6.7 and 6.8 the results of electrical conductivity measurements [3] made on two samples A1 and A2 respectively are presented. In addition to the experimental data we present our attempted fits using the model described by Sawicki *et al* [8] and our measurements of the magnetic susceptibility for these samples.

The other adjustable parameters which contribute to this fitting are the donor electron Bohr radius and the value of σ_0 from scaling theory (equation 3.17). Prior to our measurement of the magnetic susceptibility a fit to the conductivity data produced a value for the donor Bohr radius (BMP radius at high temperatures) of the order of 100 Å [3], which is somewhat larger than we might expect. Using equation 2.6 for a simple hydrogenic donor in CdTe we obtain $a_B \sim 50$ Å. Although it should be noted that the exact determination of the relevant radius for a sample close to the MIT is rather more complicated.

Using our measured susceptibility and fixing the polaron radius at high temperatures close to 50 Å results in a good fit to the conductivity data with σ_0 as a fitting parameter. In this case we obtain $\sigma_0 \sim 8\ (\Omega\text{cm})^{-1}$ which is higher than the values obtained from experimental measurements on these samples. From this we can conclude that whilst this model seems to describe approximately the basics of the observed decrease in conductivity, it is not however capable of a fully quantitative description of our experimental data.

At this stage it may be useful to make some comments about this sample in terms of its proximity to the MIT. From the Mott criterion (equation 3.6) given in section 3.2.2.1 we can estimate the critical carrier density at which we might expect the MIT to take place. Using the material parameters for CdTe to calculate the Bohr radius, and making use of the Mott criterion we can estimate $n_c = 1.1\text{x}10^{17}\ \text{cm}^{-3}$. Of course in reality for

CdMnTe:In we would expect a higher value of n_c, due to the inherent disorder added when substituting Mn for Cd ions. A previous study of the MIT by Leighton *et al* [9] found $n_c = 2.34 \times 10^{17}$ cm^{-3} for a sample of CdMnTe:In having a Mn concentration of x = 0.08. From electrical transport measurements made at relatively high temperatures Shapira *et al* estimated that $n_c = 2 \times 10^{17}$ cm^{-3} for CdMnTe samples having x = 0.05 [10]. By examining the scaling behaviour of dielectric constant and the localization length for samples on the insulating side of the MIT Terry *et al* suggested that $n_c = 2.3 \times 10^{17}$ cm^{-3} [11] for a CdMnTe sample having x = 0.09.

Thus for sample A1 having x ~ 0.05 and n (dark) = 3.3×10^{17} cm^{-3} it would seem logical to assume that this sample is on the metallic side of the MIT, even prior to any illumination. Measurements presented thus far, for T > 300 mK would appear to add weight to this suggestion. If we examine again figure 6.6, then we can see that despite the rapid decrease in conductivity at low temperatures an extrapolation to T = 0 K would suggest a finite conductivity, thus indicating the expected metallic behaviour. We shall now see that measurements below 300 mK result in a somewhat different conclusion.

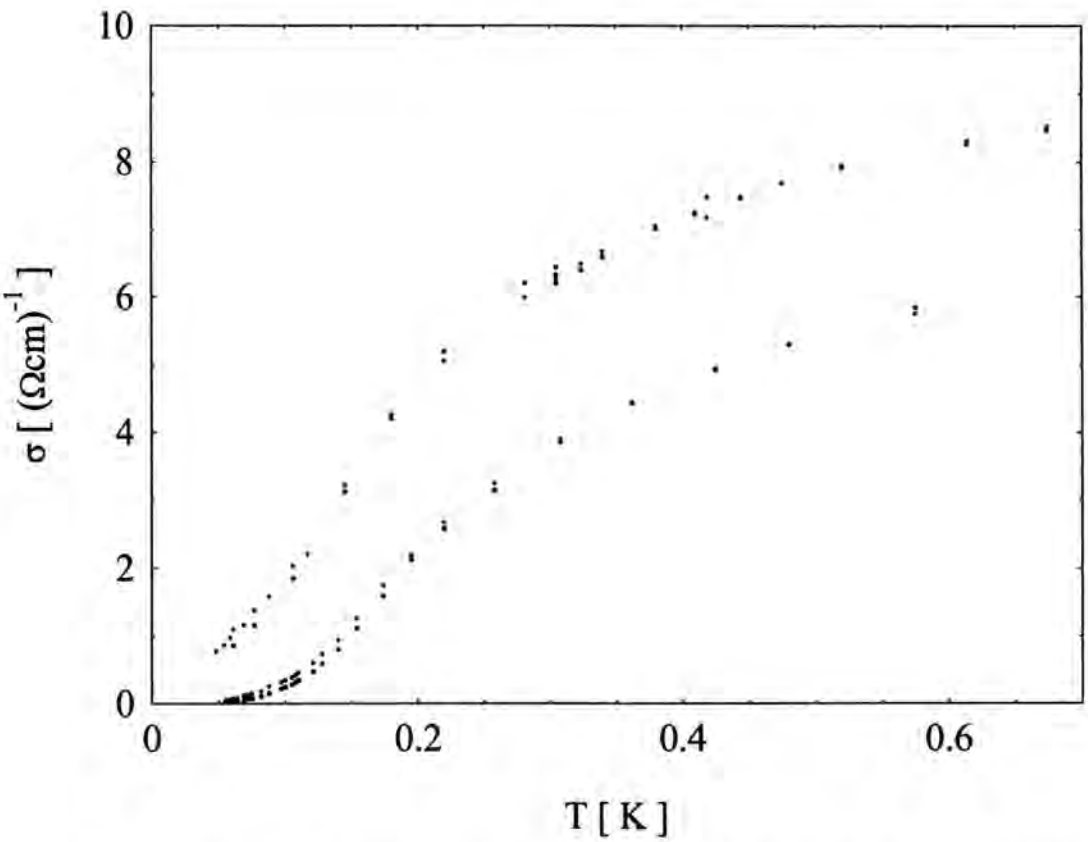

Figure 6.9 - Plot of conductivity against temperature down to 45 mK for sample A1. Data are presented for two different photogenerated carrier concentrations. Dark data n = 3.3×10^{17} cm^{-3}, saturation illumination n = 3.8×10^{17} cm^{-3}.

Figure 6.9 presents data from such measurements. The curves shown represent measurements made at two different photogenerated carrier densities. These correspond to dark data ($n = 3.3x10^{17}$ cm^{-3}) and the saturation illumination level ($n = 3.8x10^{17}$ cm^{-3}). It should be noted that in each case we now plot two curves which correspond to the two different van der Pauw configurations (ie two different measurements made with the current direction perpendicular to each other). The reason that we plot both these conductivities is due to the fact that we have measured a temperature dependent anisotropy ratio, K, at temperatures below T ~ 200 mK. (Where K is the ratio of the two measured resistances R_A and R_B, see section 4.3.1). We would normally expect this ratio to be independent of temperature, as indeed it is at high temperatures (T > 200 mK). We will return to discuss the nature of the temperature dependence of the anisotropy, K, in section 6.5, however for now we shall plot both the high (R_A) and the low (R_B) resistivity configuration wherever possible. In order to calculate the two different van der Pauw configuration values of the resistivity or conductivity we take simply the shape anisotropy ratio (ie K for T > 200 mK) and calculate the resistivity from the measured sample resistance. It should be noted that the behaviour of both resistivity configurations is qualitatively the same in most circumstances, and we shall draw attention to any differences observed.

Contrary to the high temperature results presented it would seem that these measurements (for T > 40 mK) indicate that the sample is an insulator both before and after illumination. An extrapolation of the conductivity to T = 0 K very clearly indicates a conductivity equal to zero. In the case of saturation illumination the sample is very close to being critical. This result is rather surprising when we consider the sample's behaviour at higher temperatures, and also the values of n compared to n_c described above. It seems that we are observing some form of temperature dependent localization. One way in which we could describe the situation in this sample is that we are observing a temperature driven MIT. Previously this terminology has been applied to systems where a structural phase transition occurs at a finite temperature. In CdMnTe:In there is no structural phase transition at these low temperature. However if the interpretation of Leighton *et al*, following Dietl *et al*, is correct and the decrease in conductivity at low temperatures is due to the enhanced spin disorder scattering from BMPs, then it is possible that these BMPs could be responsible for the increasing localization as temperature is reduced.

Of course in the strict sense the MIT is a zero temperature quantum phase transition and quite clearly this sample is an insulator both before and after illumination.

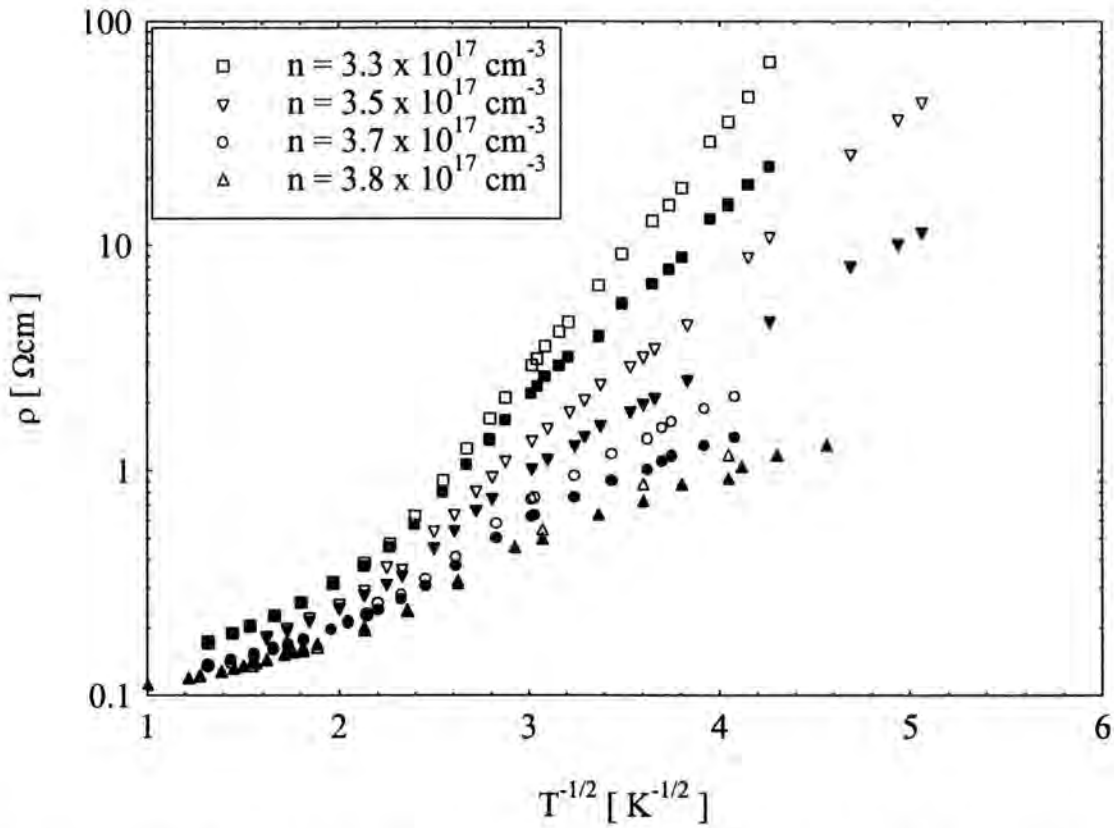

Figure 6.10 - Plot of resistivity on a log scale against $T^{-1/2}$ for sample A1a in nominally zero field. Data are presented for four different photogenerated carrier concentrations (see graph legend) and for both resistivity configuration (represented by open and solid symbols).

In order to gain some information about the nature of the insulating phase in this sample we have plotted in figure 6.10 the resistivity data from figure 6.9 along with two intermediate carrier densities. Data are presented with resistivity plotted on a log scale as a function of $T^{-1/2}$. We can see that at low temperatures ($T < 140$ mK) the curves are linear. This temperature dependence of the resistivity is consistent with VRH as described by Efros and Shklovskii where the effects of electron-electron interaction are taken into account (see section 3.3).

$$\rho = \rho_0 \exp\left(\frac{T_0}{T}\right)^{\frac{1}{2}} \qquad \textbf{Equation 6.2}$$

From our experimental data we can calculate the values of T_0 using equation 6.2. These are given in table 6.1.

	T_0 for R_A [K]	T_0 for R_B [K]	Carrier density [cm^{-3}]
Dark data	3.61	5.90	3.3×10^{17}
1st illumination level	1.49	2.92	3.5×10^{17} *
2nd illumination level	0.67	1.32	3.7×10^{17} *
Saturation illumination	0.43	0.82	3.8×10^{17}

Table 6.1 - Parameter associated with hopping transport obtained for sample A1b at four different illumination levels. The carrier densities given for the dark data and the saturation illumination data were measured at T ~ 10 K. For the intermediate carrier densities (denoted by *) the values of n have been estimated from the scaling theory equation.

The parameter $T_0 = 2.8e^2/k_B\kappa\xi$. As the MIT is approached both the dielectric constant and the localization length diverge. Thus we would expect that as the carrier density is increased the value of T_0 should decrease. This is exactly as we observe in our experimental data.

Although the analysis presented above seems to make sense for this insulating sample which is rather close to the MIT, we should point out that some caution should be exercised as the number of data points within the low temperature hopping regime is slightly limited. In fact it is possible to obtain a reasonable fit to the dark data presented above when an activated form for the conductivity is used. At higher carrier densities however the conduction is certainly not activated and thus ES VRH seems to be the most logical conclusion.

In an attempt to improve our analysis for the lowest carrier concentration we have made more detailed low temperature measurements on a second piece of sample A1. Data for sample A1b in zero field and also in an applied magnetic field of 50 mT are shown in figure 6.11 plotted as a function of 1/T. We can see from the figure that the zero field data fits very well to this simple activated form for the conduction at temperatures below approximately 120 mK. Shown on the figure 6.12 we plot the same data as a function of $T^{-1/2}$, an attempt here to fit a straight line to the zero field data clearly fails suggesting that the sample is not in a ES VRH regime.

From the activated form for the conduction we calculate the characteristic temperature to be 0.43 K, this corresponds to an energy gap of approximately 3.7×10^{-5} eV. An interesting observation is made if we now examine the temperature dependence of the same sample in a small applied magnetic field, B = 50 mT, see figure 6.11 and

figure 6.12. Measurements were made cooling the sample in this small applied magnetic field.

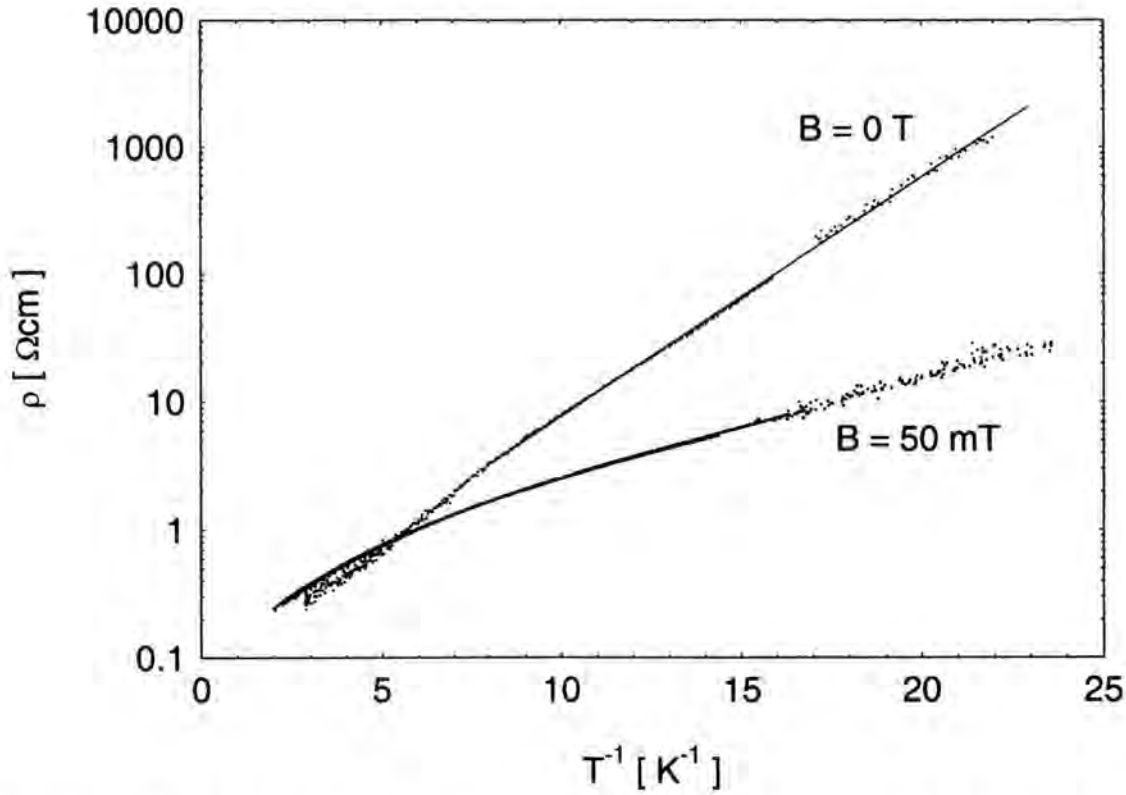

Figure 6.11 - Plot of resistivity on a log scale against inverse temperature for sample A1b in zero field and in an applied field of 50 mT. The solid line is a straight line fit to the zero field data yielding the activation energy given in the text.

We can now see that with the application of a 50 mT magnetic field the simple activated form of the resistivity is suppressed and we see ES VRH once again present at the lowest temperatures. In this case for the R_A resistance configuration the value of T_0 is found to be 1.75 K. This value is in reasonable agreement with the values obtained for sample A1a at the first illumination level (see table 6.1).

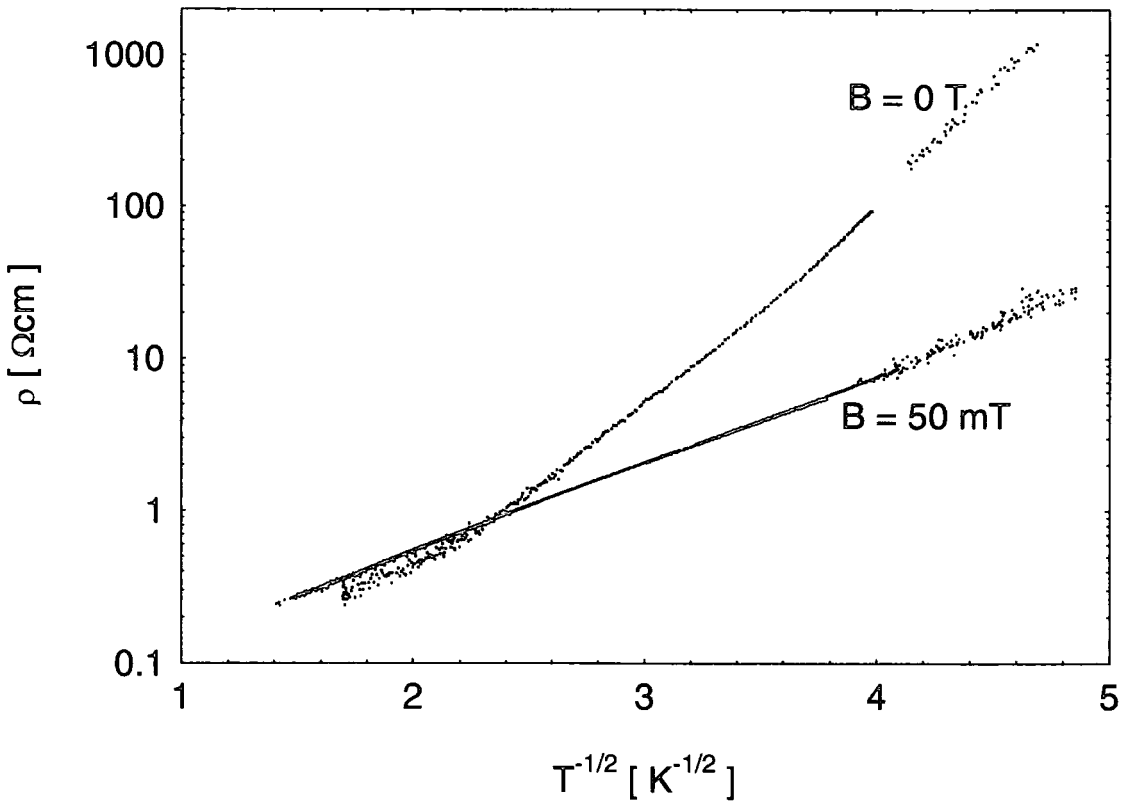

Figure 6.12 - Plot of resistivity on a log scale against $T^{-1/2}$ for sample A1b in an applied magnetic field (B = 50 mT). The solid line is a straight line fit to the data giving a value of T_0 = 1.75 K. The zero field data is shown plotted on the same scale.

It is immediately tempting to interpret the activated behaviour described above for the dark data, in terms of the formation of a hard gap in the DOS states which has a magnetic origin. This was previously seen in CdMnTe:In by Terry *et al* [12]. In their work Terry *et al* observed a crossover from ES VRH to activated behaviour as the temperature was reduced (T < 1 K), with $E_H \sim 2$ K. Thus, the crossover to activated behaviour was found to occur at higher temperatures than we have measured here in sample A1. In addition to this there are some other differences between our current measurements and those in reference [12]. Most notably Terry *et al* were able to describe all of their experimental data using a scaling form for the resistivity given by,

$$\rho = \rho_0 \exp\left[\frac{T_0}{T} + \frac{E_H^2}{T^2}\right]^{1/2} = \rho_0 \exp[A(t_0)F(t)] \qquad \textbf{Equation 6.3}$$

Trying to carry out a similar analysis with our current experimental data, it proved impossible to obtain a single curve describing all of our data.

Also for our sample (A1b) the crossover from activated to ES VRH occurs in extremely small applied magnetic field (B ~ 50 mT) and the size of the energy gap E_H is much smaller than found by Terry *et al.* Although it should be noted that we are making measurements down to approximately one order of magnitude lower temperatures, thus we may expect to be able to observe the effects of form of the DOS on much smaller energy scales. Finally the proximity of the samples to the IMT is likely to be of great importance, data of reference [12] are for an insulating sample having 9% Mn, whereas sample A1b has <5% Mn and is extremely close to the IMT.

Also, Dai *et al* reported a similar observation in their experiments on insulating Si:B [13]. At low temperatures (T < 100 mK) they saw an activated form for the resistivity measured in zero field. Applying a magnetic field B < 1 T changed the form of the low temperature resistivity to that consistent with ES VRH. They attributed the observed effects to some form of hard gap in the density of states having a magnetic origin. It should be noted that the exact mechanism for the formation of a hard gap in the non magnetic semiconductor Si:B is unclear. It is however highly unlikely that this effect has exactly the same origin as that seen by Terry *et al* in the dilute magnetic semiconductor CdMnTe:In. Measurements made by Yakimov *et al* [14] on certain samples of a-SiMn have also shown a cross over from ES VRH to simple activated behaviour at low temperatures. The theoretical work by Oppermann & Rosenow [15] has shown that a gap in the DOS could form as a result of the low temperature SG phase. They suggest that this could lead to a SG based MIT. It is also noted in their work that there are two different origins of the localized magnetic moments in the various experimental systems studied. In systems such as Si:B localized impurity spins are the source of magnetic behaviour, however in CdMnTe:In and a-SiMn the situation is more complicated as carrier spins interact with the magnetic ions and form BMPs. It is interesting to note that the expected value of the SG freezing temperature for sample A1 is T_g ~ 150 mK, and that we are observing the crossover to an activated form for the conductivity at T ~ 120 mK. Although it should be remembered that this value for T_g is just an estimate based on the previous work of Novak *et al* [16] where measurements were made on nominally undoped samples of CdMnTe. In our measurements on highly doped samples we have observed values of T_g close to those obtained by Novak *et al* (see figure 5.11). As already described, the lowest temperature at which we could make magnetic measurements was close to 300 mK, thus a direct determination of T_g for sample A1 was impossible. In addition it should be remembered that for a sample, such

as A1, having $x < x_c$ (ie below the nearest neighbour percolation threshold) a cluster glass model is more appropriate to describe the spin freezing process. For this reason it may be more accurate to think of the sample having some relatively narrow distribution of freezing temperatures rather than the sharper transition that we are familiar with in a canonical spin glass.

6.4 Field Tuning the Metal-Insulator Transition

We shall now examine the behaviour of the resistivity when we apply a larger magnetic field perpendicular to the plane of the sample. In this section we shall discuss the data in terms of field tuning the MIT. Later in section 6.6 some more general comments are made about the magnetoresistance observed in these DMS materials. Initially we shall present measurements made on the sample prior to illumination. After this we will examine the differences that are seen when the sample has been illuminated to saturation in order to produce the highest free electron density.

6.4.1 Dark Data

Figure 6.13 shows the temperature dependence of the conductivity for sample A1b at a number of different applied field values, again data are presented for both van der Pauw resistivity configurations.

We can see that at a field of B = 1 T the sample shows insulating behaviour, with a value of the conductivity equal to zero at the absolute zero of temperature. Temperature dependent data obtained at lower field values also shows insulating behaviour, with the resistivity having a much stronger temperature dependence. Conversely the data obtained in a field of B = 3 T indicates a very different situation. Plotting the conductivity against $T^{1/2}$ we obtain a straight line over the entire temperature range studied. From these data an extrapolation to T = 0 K gives a finite value for the conductivity, $\sigma(T = 0\ K) \sim 0.45\ (\Omega cm)^{-1}$. From this information it is clear that we are observing a field driven insulator-metal transition. A similar transition has been studied in the magnetic semiconductor $Gd_{3-x}V_xS_4$ by von Molnár *et al* [17] and in the DMS n-CdMnSe and p-HgMnTe by Wojtowicz *et al* [18]. Also a field driven IMT has been studied in amorphous-Gd_xSi_{1-x} by Teizer *et al* [19]. It should be noted that the large negative MR and hence the field driven IMT is opposite to the situation observed in a great many other non-magnetic semiconductors where a MIT is observed on increasing magnetic field. Clearly, from figure 6.13 the case of the measurement made with B = 2 T is a critical one with an extrapolation of the conductivity to T = 0 K having a value extremely close to zero.

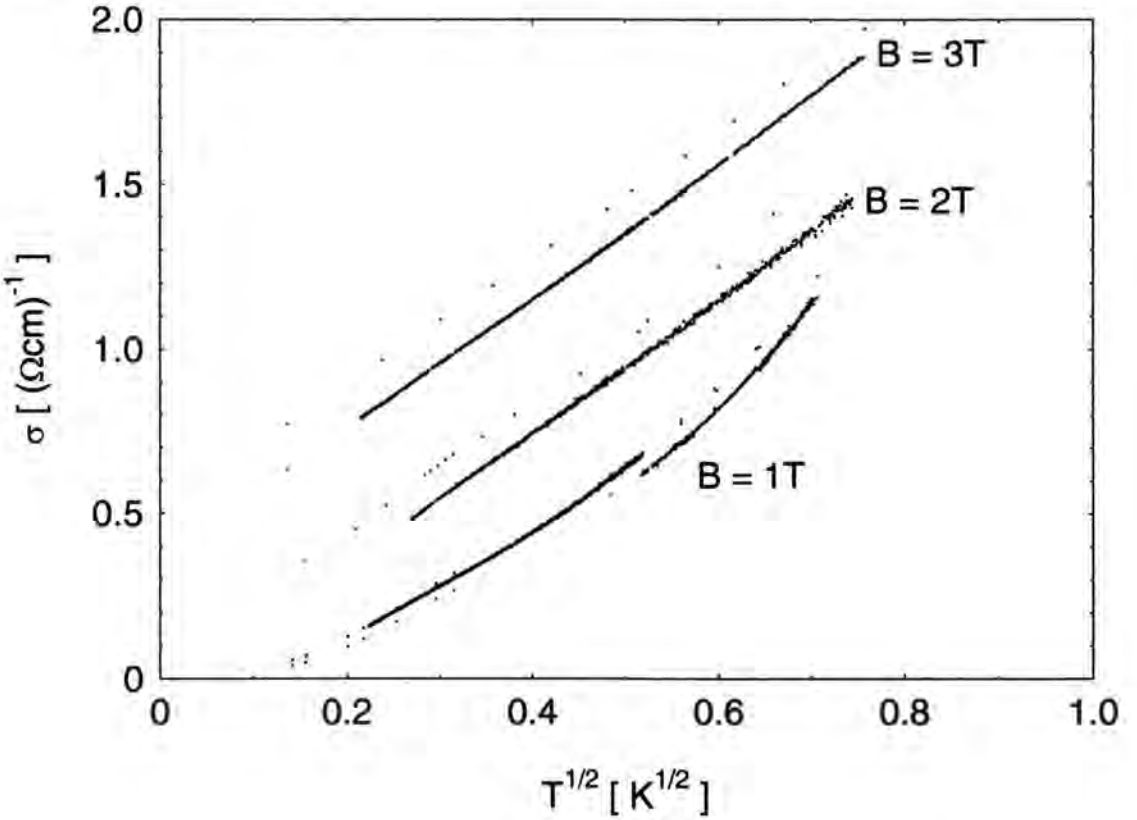

Figure 6.13 - Plot of conductivity as a function of $T^{1/2}$ at a number of different applied magnetic fields for sample A1 before illumination.

Previously the conductivity in the metallic regime has been described by equation 6.4 (see section 3.3.2) which describes the quantum corrections to the zero temperature conductivity.

$$\sigma(T) = \sigma(0) + mT^{1/2} + BT^{p/2} \qquad \textbf{Equation 6.4}$$

The first term is the conductivity at T = 0 K, the second term is due to electron-electron interaction and the final term is due to weak localization. When a magnetic field is applied it suppresses the weak localization and the $BT^{p/2}$ term tends to zero. Thus in our case we shall fit to the experimental data with just the first two terms on the right side of equation 6.4. The parameters obtained from fitting the experimental data shown in figure 6.13 are given in table 6.2. This procedure was carried out only for those samples which are metallic, that is for samples where an extrapolation to T = 0 K resulted in a finite value of σ(0). Excellent fits to the data can be achieved over the entire temperature range measured, typically 40 mK < T < 600 mK.

Magnetic Field [T]	m(B) R_B [$(\Omega cmK^{1/2})^{-1}$]	$\sigma(0)$ R_B [$(\Omega cm)^{-1}$]	m(B) R_A [$(\Omega cmK^{1/2})^{-1}$]	$\sigma(0)$ R_A [$(\Omega cm)^{-1}$]
2	2.02	0.035	2.02	-0.066
3	1.93	0.503	2.01	0.352
4	1.75	0.935	2.01	0.682
5	1.73	1.161	1.91	0.891

Table 6.2 - Parameters obtained by fitting to temperature dependent conductivity data using equation 6.3. These data were obtained for sample A1b prior to illumination.

The first thing to be noted from table 6.2 is that in all cases the values of m are found to be positive. The expression for m is given in equation 3.36 after Altsuler *et al* [20]. The sign of m is likely to determine the sign of the gradient of conductivity against temperature at temperatures approaching T = 0 K. It is also interesting to examine the field dependence of m, we can see that as the sample is driven further into the metallic region (as the field is increased) the value of m decreases slightly. Figure 6.14 shows the values of m obtained from our measurements, plotted as a function of B/B_c. Included on this figure for the purpose of comparison are data from previous studies of the MIT in a number of different material systems. For MITs driven by application of a magnetic field we plot m against B/B_c data are given for a-GdSi, GdvS, CdMnSe and our present work on CdMnTe:In. For studies of the MIT as a result of changing carrier density we plot m against n/n_c for Si:B, AlGaAs:Si and the previous zero field study of CdMnTe:In. References to work carried out by others are given in the caption of figure 6.14. Firstly we note that the values for m determined from our measurements are in good agreement with those previously measured. We see that the general trend in the collected data, is that for almost all the studies included in the figure the value of m decreases as x/x_c is increased. The value of m is only very weakly dependent on x/x_c in the case of CdMnSe, GdSi and our study of CdMnTe:In. In the remaining systems m is seen to depend much more strongly on x/x_c. The case of Si:B is rather interesting, here with no applied magnetic field the value of m is seen to change sign from negative to positive as the MIT is approached from the metallic side. A similar change of sign of m has also been observed in other systems. When the same samples of Si:B were examined in an applied magnetic field of 7.5 T the value of m was always found to be positive. For the previous study of CdMnTe:In made in zero field the values of m were always determined to be negative. Although in this case the measurement closest to the

MIT is made at $n = 1.115n_c$ so it is possible that a change of sign would be observed closer to the transition as is the case for Si:B in zero field.

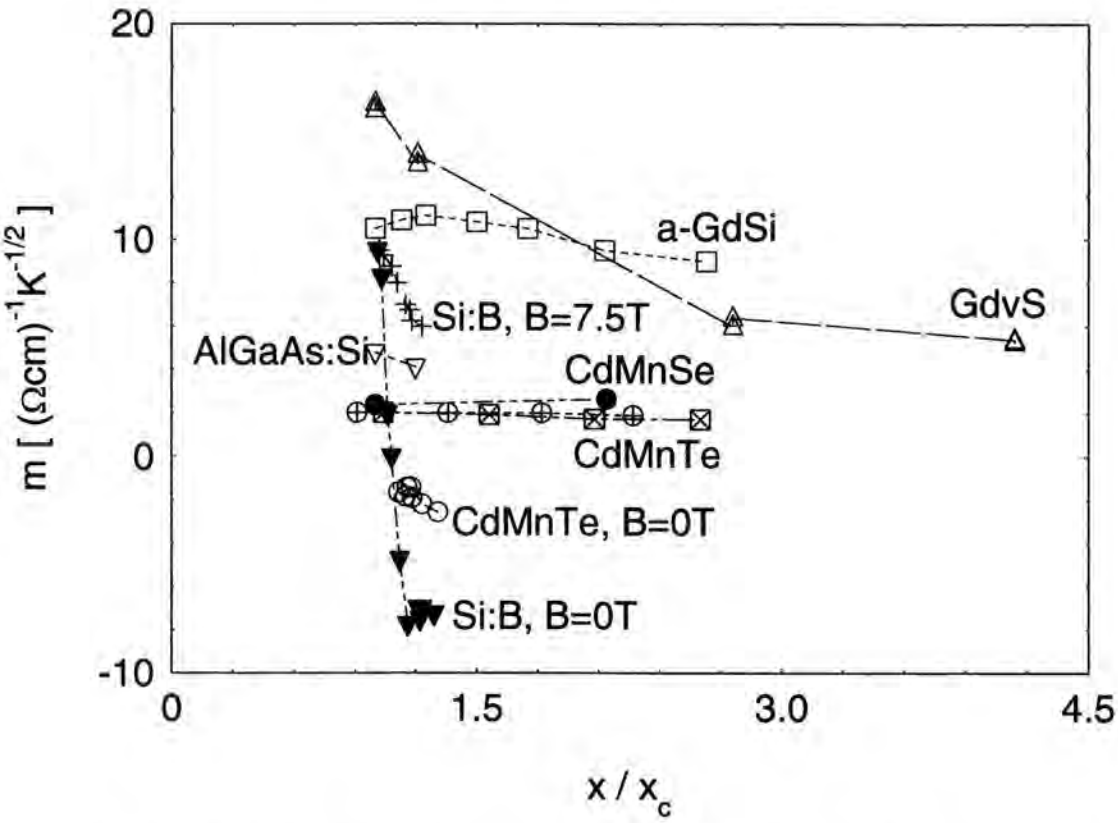

Figure 6.14 - Plot of m against x/x_c for a number of different material systems including data from our study field tuning the MIT in CdMnTe. The value x denotes the parameter that has been used to tune the MIT which occurs a critical value of $x = x_c$. Data are obtained from the following references, a-GdSi [19], GdvS [21], CdMnTe B = 0 T [9], CdMnSe [18], Si:B [22], AlGaAs:Si [23].

In an attempt to examine the transition in more detail we have measured the conductivity as a function of applied magnetic field at a fixed low temperature (T = 53 mK). The results of this measurement are shown in figure 6.15. It should be noted that the lowest field value plotted on this figure is of the order of 50 mT, at truly zero magnetic field the conductivity of the sample is much smaller, this is due to a rather large negative MR which has been observed at low temperatures and we will go on to describe and examine this MR more closely in section 6.6. A clear IMT has been seen on increasing magnetic field, similar behaviour has previously been observed in other magnetic systems. Once again we shall compare our work to that of others, in particular we shall focus our attention on studies made previously of magnetic and dilute magnetic semiconductors.

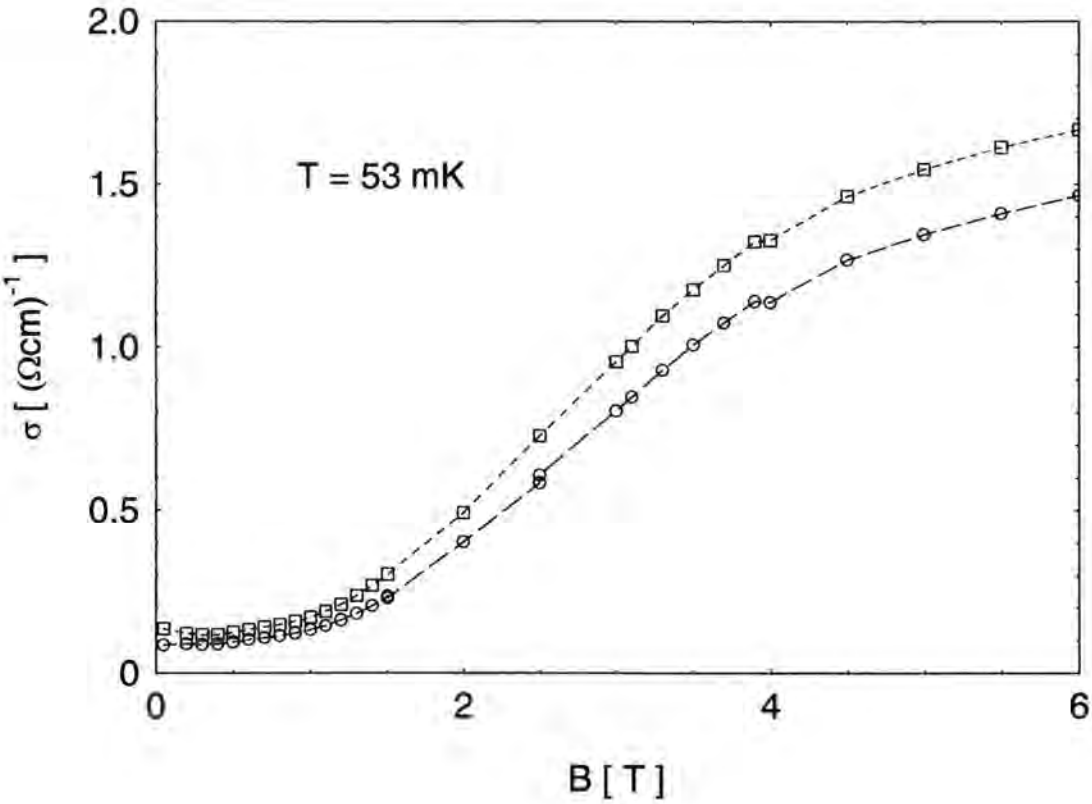

Figure 6.15 - Plot of conductivity at low temperature (T = 53 mK) against applied magnetic field for sample A1 prior to illumination (n = 3.3x10^{17} cm^{-3}). The two different curves on this plot represent the high and low resistivity configurations R_A and R_B.

From simply examining figure 6.15 it would appear that $B_c \sim 1$ T. For the work Dietl *et al* [6, 24] similar measurements made on p-HgMnTe at T = 40 mK give $B_c \sim 2.5$ T and data for n-CdMnSe suggests that $B_c \sim 0.25$ T. In the case of Dietl *et al* measurements of p-HgMnTe the temperature dependence of the conductivity at low temperatures is relatively weak. This means that a conductivity measurement made as a function of magnetic field at low temperatures approximate rather well to the behaviour of the zero temperature conductivity. Conversely for CdMnSe and our study of CdMnTe the conductivity varies more strongly with temperature, thus to determine accurately the critical field an extrapolation must be made in order to calculate the zero temperature conductivity. When this was carried out by Dietl *et al* they found that for CdMnSe the critical field ($B_c = 1.33$ T) is much higher than would be inferred from a finite temperature measurement.

Another difference apparent when comparing our work to that of others is the large amount of rounding close to the transition. Previous measurements on HgMnTe [6] and Gd_vS [25] have shown some rounding close to the transition. In the case of Gd_vS it was suggested that alloy broadening as a result of an inhomogeneous distribution of vacancies was likely to be the dominant cause of the observed rounding. This

conclusion was reached after thermal rounding was shown to have only a small contribution to the observed effect. Although our measurements are likely to be subject to a certain amount of alloy broadening it is believed to be unlikely to result in such a large effect. It is interesting to note that a lesser degree of rounding was observed in the previous study of CdMnTe using PPC which was carried out at temperatures, T > 300 mK [9]. The proximity of a sample to the MIT in its initial insulating state is an important factor. The sample that we have measured is extremely close to the MIT, thus it is expected that a sharp but continuous transition will only be observed by extending measurements to a much lower temperature. Alternatively this effect may in some way be related to the magnetism of the sample, in our case we are studying a field driven metal insulator transition occurring within a spin-glass phase.

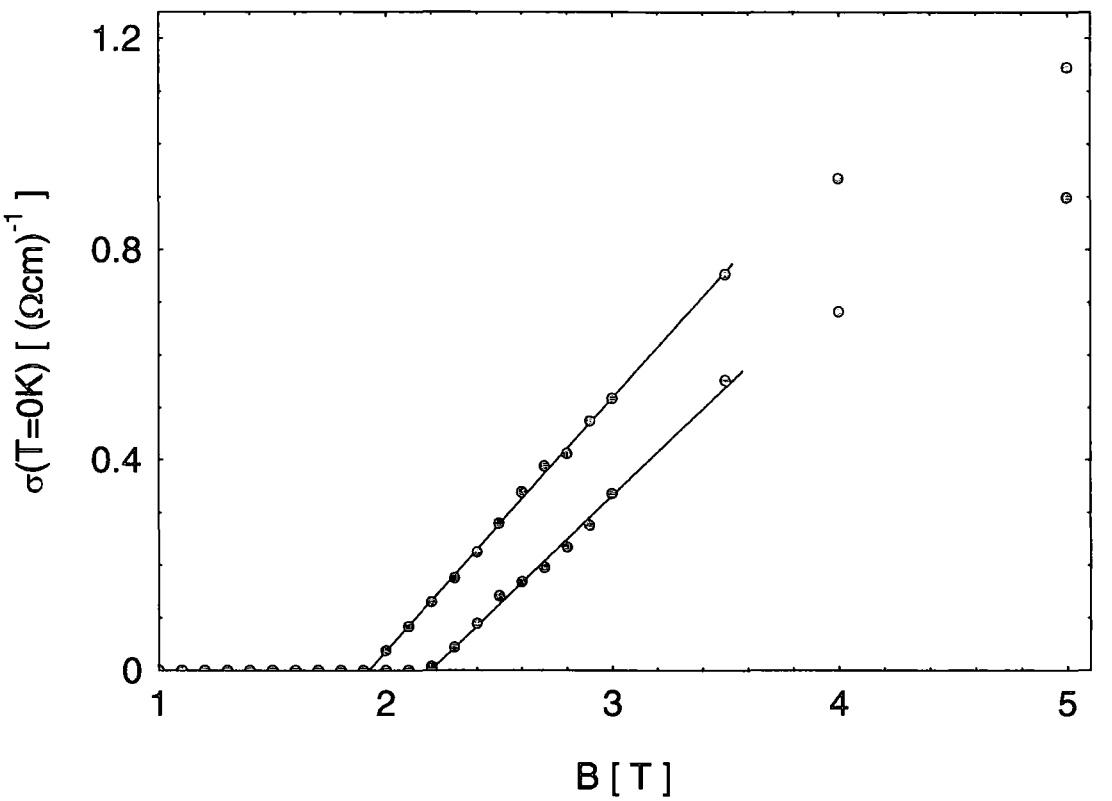

Figure 6.16 - Plot of conductivity at zero temperature against applied magnetic field for sample A1. The two different curves on this plot represent the high and low resistivity configurations R_A and R_B. The solid black lines represent fits to the data using scaling theory as described in the text.

The field driven IMT in magnetic semiconductors has been attributed to the destruction of BMPs and the giant Zeeman splitting of the impurity band (with the MIT occurring in a spin subband), the transition occurring when $E_c = E_F$. Taking the critical field to be $B_c \approx 2$ T (see figure 6.16) the values of $\sigma(T = 0\ K)$ have been obtained by extrapolations

to zero temperature, made in a similar way to those described above for the curves shown in figure 6.13. This figure shows a much sharper IMT. As seen above in the data of figure 6.16 the conductivity starts to saturate at the highest fields. The reason that we see this saturation of the conductivity is because of the saturation in the BMP mechanism driving the transition. Rough calculation based on experimental magnetic data gives the spin splitting at T = 0.5 K of the order 44meV for an applied field of 1 T. This is approximately 380 times larger than the ordinary Zeeman splitting term.

It is quite clear from the data that have been presented above, that we are observing a continuous MIT. Throughout our measurements we have seen no evidence to support the existence of Mott's minimum metallic conductivity. We can make a fit to our data using the scaling theory equation.

$$\sigma(T=0K)=\sigma_0\left(B/B_c-1\right)^{\upsilon} \qquad \text{Equation 6.5}$$

From this the critical field is found to be B_c = 1.92 T and B_c = 2.20 T when determined for the two resistivity configurations. The critical exponent at low fields close to the MIT appears to be of the order of unity as expected for a compensated semiconductor. As often seems to be the case, both in our current study and in the previous experimental work of others, the value that is obtained for ν will be slightly sensitive to the field range over which the fitting is carried out. Of course the region over which scaling theory is valid is not precisely determined and is still a hotly debated topic.

The parameters obtained from this fitting procedure are listed in table 6.2. We shall examine the value of σ_0 that has been determined from this analysis in comparison with those determined from previous measurements by others in the next section, where we consider the effect of illumination.

6.4.2 Saturation Illumination

After illuminating to saturation and hence increasing the sample's free electron concentration we can again make similar magnetic field dependent measurements. The results of temperature dependent measurements made in zero field and also applied fields of 2 T and 4 T are shown for saturation illumination ($n = 3.8 \times 10^{17}$ cm^{-3}) in figure 6.17. It can be seen that in contrast to the previous field dependent measurements

made at a lower carrier density, it would appear that the critical field is much smaller. In figure 6.17 the B ~ 2 T curve is clearly metallic with an extrapolated $\sigma(T = 0\ K) \sim 0.5\ (\Omega cm)^{-1}$, whereas for the dark data the curve at B ~ 2 T was critical. As for the case of the dark data we again see that the conductivity is linear when plotted as a function of $T^{1/2}$. Again, fitting to the data using equation 6.4 gives the parameters shown in table 6.3. On comparison with the dark data we see that the values of m are only slightly reduced after illumination.

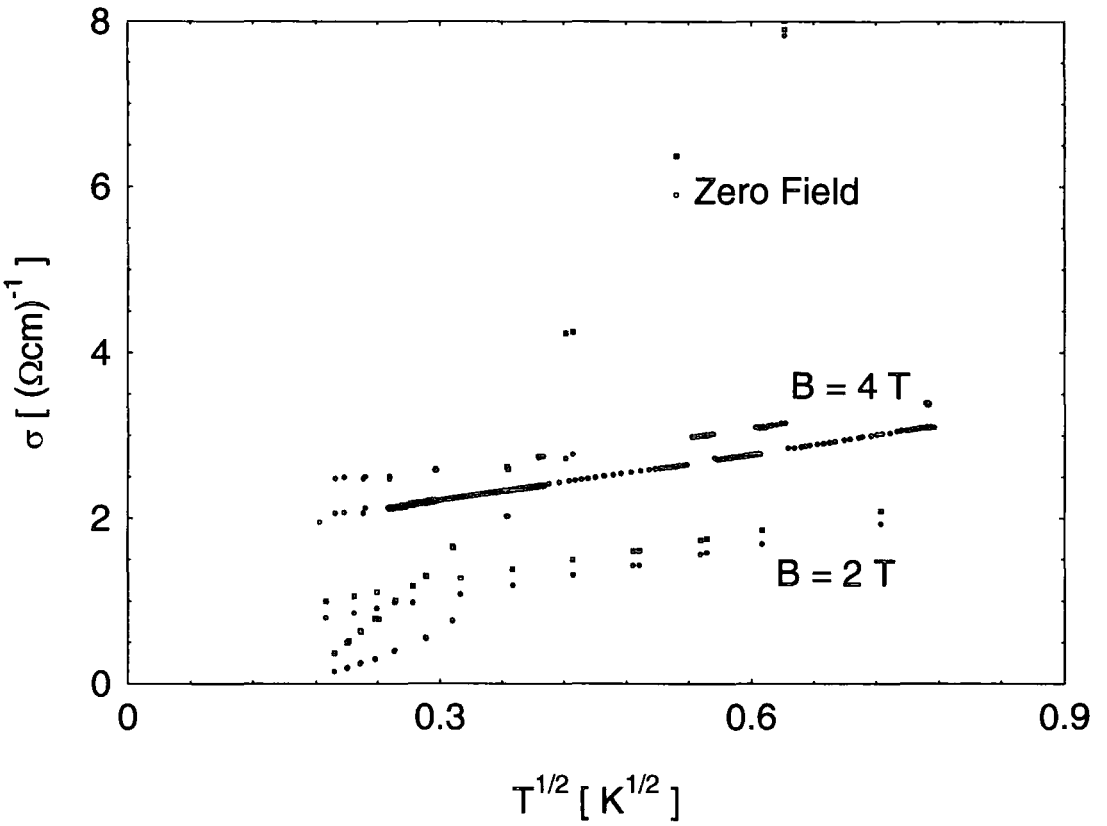

Figure 6.17 - Plot of conductivity as a function of $T^{1/2}$ at a number of different applied magnetic fields for sample A1 after illumination to saturation (n = 3.8x10^{17} cm^{-3}).

Magnetic Field [T]	m(B) R_A [$(\Omega cmK^{1/2})^{-1}$]	$\sigma(0)$ R_A [$(\Omega cm)^{-1}$]	m(B) R_B [$(\Omega cmK^{1/2})^{-1}$]	$\sigma(0)$ R_B [$(\Omega cm)^{-1}$]
2	2.02	0.622	2.10	0.403
4	1.71	2.06	1.86	1.65

Table 6.3 - Parameters obtained by fitting to temperature dependent conductivity data using equation 6.4. These data were obtained for sample A1b after illuminating to the saturation level.

We have measured the low temperature conductivity as a function of applied magnetic field for sample A1b at the saturation illumination level. These data are shown in figure 6.17 along with extrapolations to zero temperature from the curves measured at B = 2 T and B = 4 T. Qualitatively the data after illumination appears similar to that measured prior to illumination. We will now go on to look more closely at the parameters obtained from analysing the data using scaling theory. A summary of these parameters obtained from measurements before and after illumination is given in table 6.4. At saturation illumination the critical field is found to be $B_c = 1.14$ T and $B_c = 1.36$ T when determined for the two resistivity configurations. These critical field values have been decreased by almost 1 T as a result of increasing the free electron concentration.

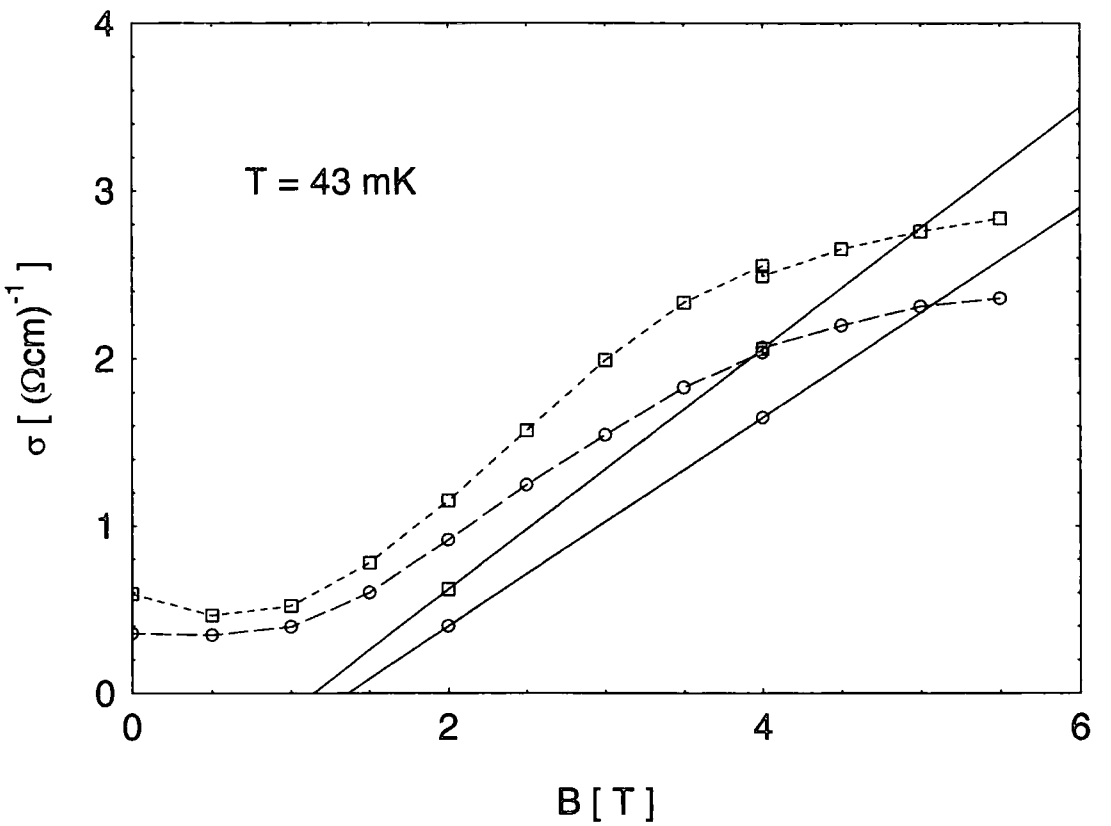

Figure 6.18 - Plot of conductivity at low temperature (T = 43 mK) against applied magnetic field for sample A1 after illumination to saturation (n = 3.8x10^{17} cm^{-3}). The two different curves on this plot represent the high and low resistivity configurations R_A and R_B. Also shown are the extrapolated values of the conductivity at T = 0 K.

If we think of the MIT as occurring when the mobility edge is lowered through the Fermi energy, then we can see that there are two possible ways to tune the transition in this sample. Application of a magnetic field reduces the mobility edge, and can cause an IMT as we have seen above. In addition to this, the illumination increases the carrier

concentration, and thus has the result of increasing the Fermi level in the material. As has been seen it has not been possible to drive the sample into a metallic state by the effect of illumination alone, resulting in the consequence that we always observe insulating behaviour in zero field.

	σ_0 [$(\Omega cm)^{-1}$]	B_c [T]	ν
R_A (dark)	0.91	1.94	0.97
R_B (dark)	0.92	2.11	1.17
R_A (light)	0.85	1.14	1*
R_B (light)	0.82	1.36	1*

Table 6.4 - Parameters obtained by fitting to data in figures 6.16 and 6.18 using scaling theory (equation 6.5).* denotes a value of ν fixed at unity instead of a free fitting parameter.

Table 6.4 shows the values of various parameters obtained from fitting to the experimental data shown in figures 6.16 and 6.18. It should be noted that for the light case (ie saturation illumination), due to the limited data it was not possible to obtain the value of ν (the critical exponent) from a fitting procedure. In this case the critical exponent was fixed at a value, $\nu = 1$, as denoted by * in the final column of the table. It is clear from measurements made before illumination that a critical exponent close to 1 describes the field driven IMT observed in these samples. Now consider the parameter σ_0 obtained from our scaling analysis. We see from table 6.4 that on increasing n, the value of σ_0 decreases. We can compare our result with those obtained from previous measurements. In particular the work of Leighton *et al* on CdMnTe:In in zero field [2], found $\sigma_0 = 0.55\ (\Omega cm)^{-1}$ and $\sigma_0 = 3.75\ (\Omega cm)^{-1}$ for two different samples studied. The reason for the difference between the two measurements made on samples which were nominally the same is at present unknown. We can see that our values for σ_0 are in agreement with the lower value of σ_0 obtained by Leighton *et al* and also the value measured by Dietl *et al* for CdMnSe [6].

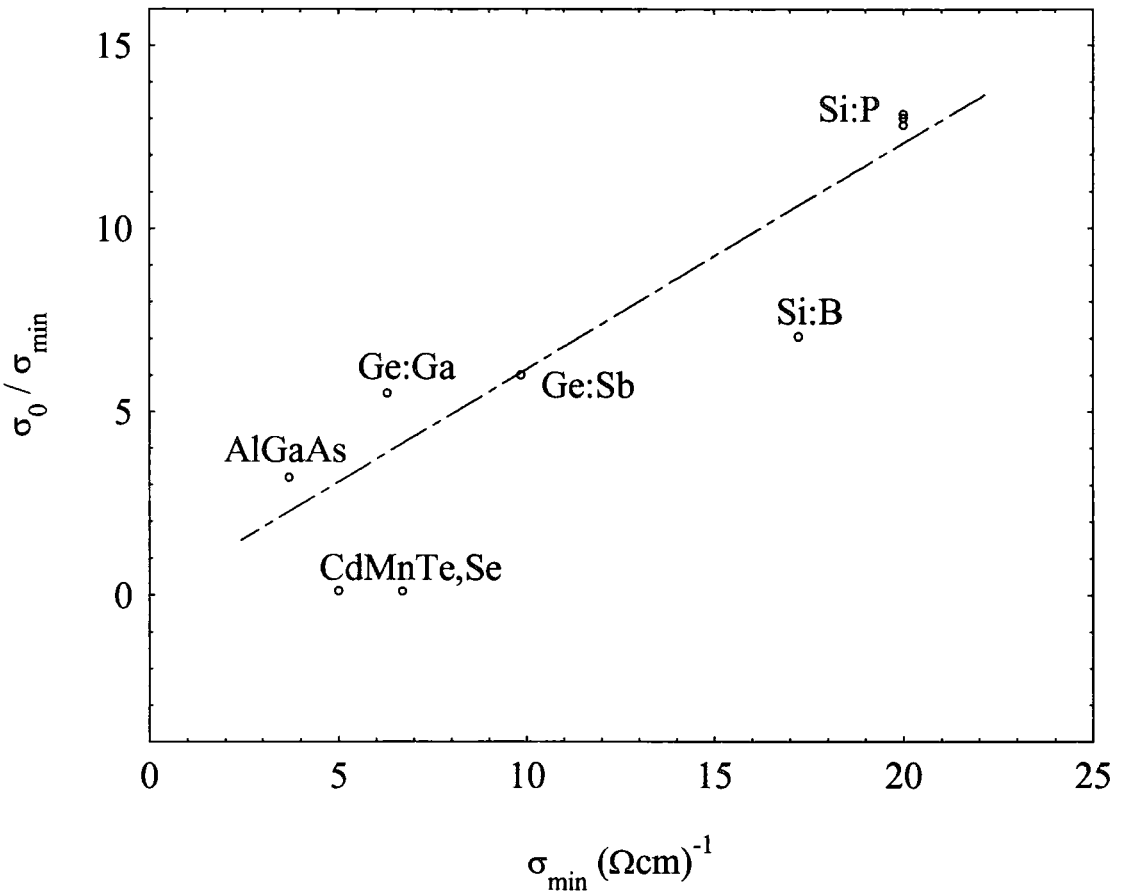

Figure 6.19 - Plot of the ratio σ_0/σ_{min} against σ_{min} for different material systems, after [2].

It has been suggested [3] that the ratio of the conductivity prefactor to the minimum metallic conductivity, σ_0/σ_{min}, is an interesting material dependent parameter that can be used to compare different systems in which MITs have been observed (see figure 6.19).

6.5 Temperature Dependence of Low Temperature Anisotropy Ratio

As discussed in section 4.3 electrical transport measurements have been made using a sample with contacts in the van der Pauw configuration. In the previous sections of this chapter we have presented results from such measurements for both resistance configurations. In the present section the reason for presenting the data in this way will become apparent as we discuss the change in anisotropy ratio at low temperatures. Essentially we see a well behaved isotropic sample from 300 K all the way down to 200 mK. At $T < 200$ mK we observe a dramatic change in the anisotropy ratio with decreasing temperature. Previously a large number of samples have been studied at relatively high temperatures ($T > 4.2$ K), in a small number of cases a temperature dependent anisotropy ratio has been observed, and was attributed to a few poor quality samples. However, it should be noted that the temperature dependent anisotropy observed here is quite unlike the situation seen in a poor quality crystal. Normally for the case of a poor quality sample we observed a very gradual change in K, beginning at much higher temperatures (typically 50 – 100 K). In addition to this IRM (which is sensitive to fluctuations in composition) often reveals that such samples are inhomogeneous, again this is not the case for sample A1. Images of sample A1 acquired via IRM showed it to be extremely uniform.

Figures 6.20 and 6.21 show the temperature dependence of the anisotropy ratio K. Data are presented both for different carrier densities (figure 6.20) and also for different applied magnetic fields (figure 6.21). On both of these figures we show inset the same data plotted with temperature on a logarithmic scale to highlight the temperature range in which the anisotropy ratio is rapidly changing.

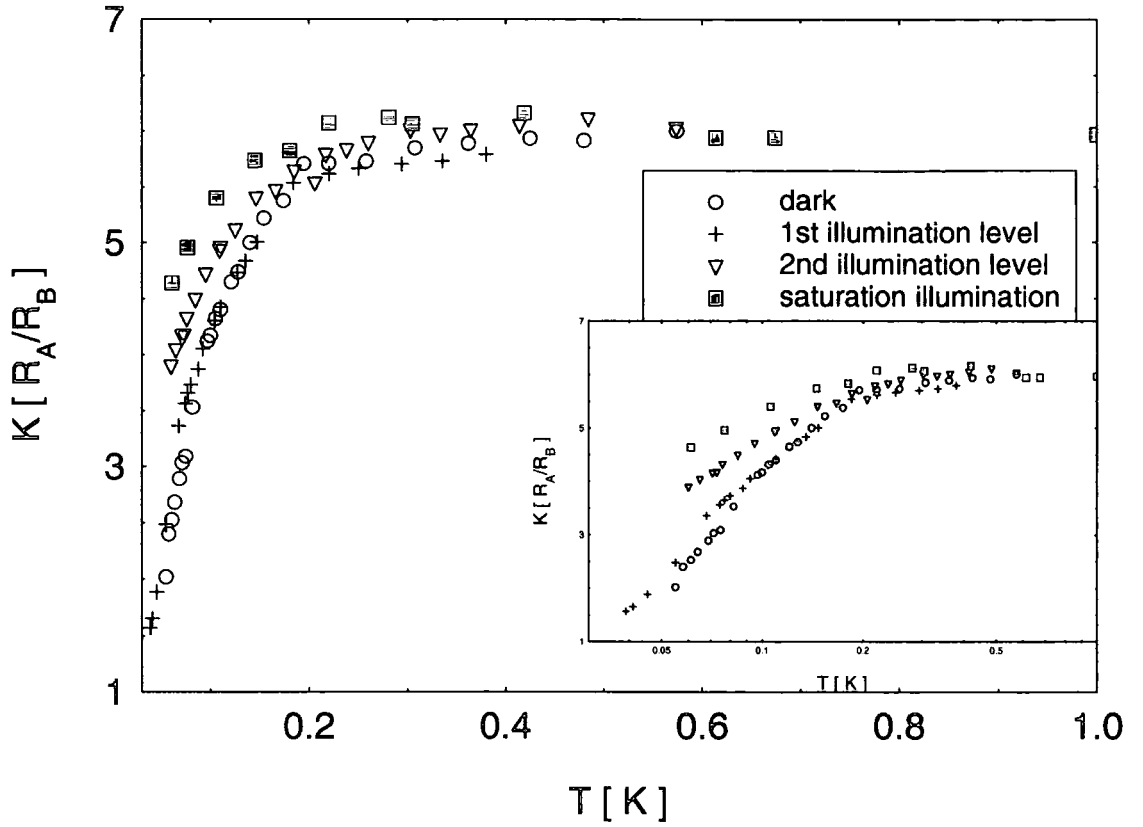

Figure 6.20 - Temperature dependence of anisotropy ratio, K, for sample A1a at very low temperatures. Data curves shown are for different illumination levels, inset the same data is plotted with temperature on a log scale.

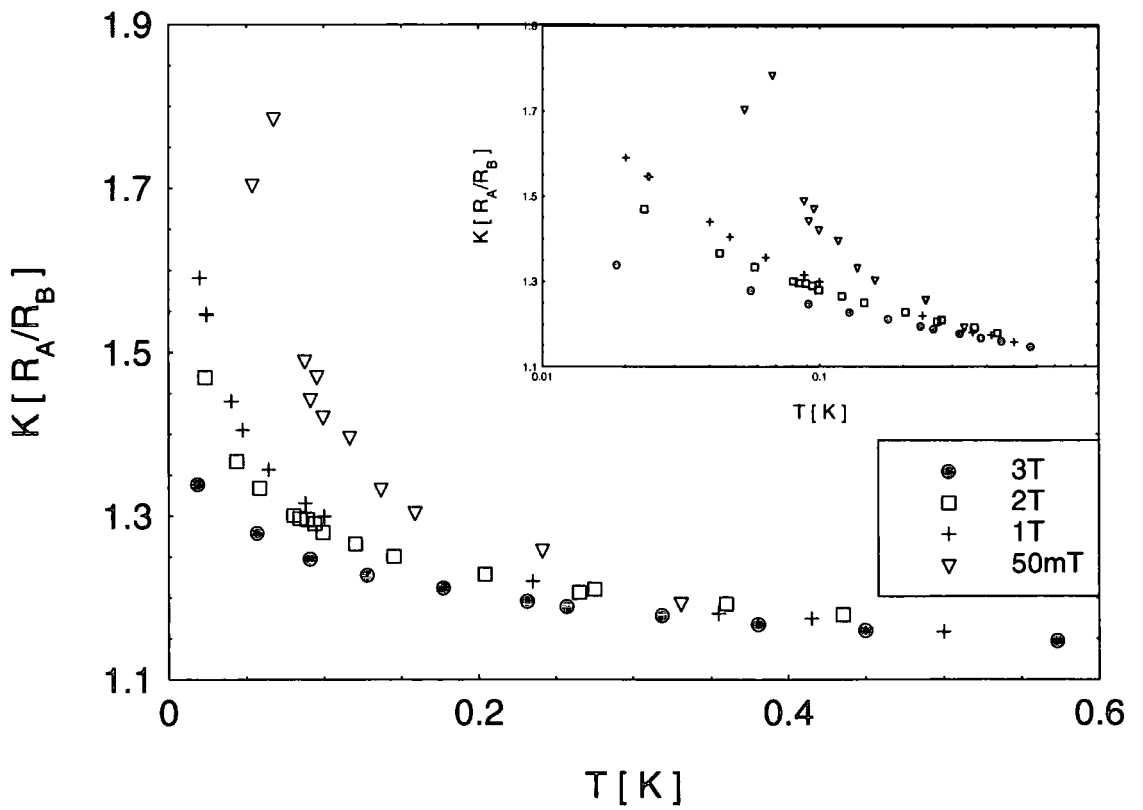

Figure 6.21 - Temperature dependence of anisotropy ratio, K, for sample A1b at very low temperatures. Data curves shown are for different values of applied magnetic fields, inset the same data is plotted with temperature on a log scale.

It is quite clear from the data shown that at low temperatures (T < 200 mK) we see a dramatic change in the anisotropy ratio, K. Alternatively we can think in terms of measuring a slightly different temperature dependence of the resistivity for the two different current directions. We shall now turn to examine two possible causes for these data. Firstly we should consider the effect that spatial variations in the impurity concentration (ie slightly inhomogeneous doping) may have on the measured transport properties. Secondly it has been noted that observed effect occurs at temperatures below a value which is close to the SG freezing temperature in this sample ($T_g \sim 150$ mK). It should be noted that this value is estimated from the previous work of Novak et al [16] where measurements were made on nominally undoped samples. We are unable to determine an exact value for T_g of sample A1 as our magnetic measurements were limited to temperatures greater than 300 mK. As the change in anisotropy begins at a temperature close to the expected value of T_g it could be suggested that in some way this observed effect is intimately related to the transition from paramagnetic to SG phase. We shall now try to examine these two possibilities in a little more detail.

Considering first the possibility of spatial variations in impurity concentration, it is useful for us to determine the effect that this may have of the different mechanisms for electrical transport observed in this sample.

In the case of a metallic sample we have been able to describe our experimental data with equation 3.35. Without considering a term due to weak localisation we have,

$$\sigma(T) = \sigma(0) + mT^{1/2} \qquad \textbf{Equation 6.6}$$

If we assume that due to spatial variations in the DOS both the zero temperature conductivity, $\sigma(0)$ and the value of m are dependent on the direction of the current through the crystal, thus we could write the anisotropy ratio as,

$$K = \frac{\sigma_A(0) + m_A T^{1/2}}{\sigma_B(0) + m_B T^{1/2}} \qquad \textbf{Equation 6.7}$$

At high temperatures the $T^{1/2}$ term is likely to dominate so we would have $K = m_A/m_B$ as the temperature approaches absolute zero the $T^{1/2}$ term tends to zero and the value for the anisotropy ratio would become $K = \sigma_A(0)/\sigma_B(0)$. Thus on going to low temperatures a change in the ratio K would be observed. It is unlikely that this mechanism could

produce such a dramatic change as we see in the insulating curves, however we see from figure 6.21 that the more metallic curves (ie those measured in higher applied magnetic fields) show a weaker temperature dependence of the anisotropy.

If we now turn to consider a sample in the HC regime from the point of view of a spatially inhomogeneous doping level. We may expect that again from differences in the DOS the probability of an electron hop may depend on the impurity concentration at the initial and final sites of the electron tunnelling event. For Mott VRH this could easily lead to a difference in the characteristic temperature T_0 for different current direction. In the case of our samples we observe ES VRH and the situation is more complicated. According to theory [26] the width of the Coulomb gap is dependent of the DOS close to the Fermi energy. Thus we could expect to have Coulomb gaps of differing sizes relevant to the two different resistivity configurations. This would suggest that the temperature at which we observe ES VRH would also be different for the two resistivity configurations. This is not observed in our experimental data (see for example figure 6.10).

Anisotropy in electrical transport measurements could also be connected with the formation of a SG phase. As has previously been discussed spin disorder scattering is an important scattering mechanism in these materials, thus it would seem likely that the details of the localized spin system (ie the Mn ions) would play an important role in the transport properties. CdMnTe is known to undergo a transition from a paramagnetic phase to a SG phase at low temperatures dependent on x. However, at low Mn concentrations (such as is the case for sample A1, $x = 0.047$) a "cluster-glass" forms with a characteristic freezing temperature. Experimental data from magnetic measurements presented in the previous chapter are in good agreement with previous studies of "cluster-glass" materials. Thus we may expect that our measurements will show transport phenomena that are very different from those of a canonical SG.

From the magnetic results (chapter 5) we see that at lower temperatures the SG phase transition is broader. Thus if for sample A1 we have $T_g \sim 150$ mK then we might expect to see effects of spin glass at higher temperatures (ie 180 mK) just due to broadening transition. Also magnetic data for sample A7 shows that onset of SG freezing begins at a temperature $T > T_g$. Also we have seen that the SG phase transition is broadened by increasing n, therefore we may see a more broadened change in K at higher illumination

levels. We observe in our data that the dramatic change in K is somehow suppressed or broadened both on increasing illumination level, and also on increasing field, thus adding weight to this interpretation for a magnetic origin to the anisotropy.

In order to firmly link the observed anisotropy with the SG phase we have attempted to examine any possible time dependencies close to T_g. To be explicit, we may expect to see a dependence of the samples' resistance on time in the SG phase. However it proved impossible to observe any such effects. Difficulties arose due to the long time constants below T_g. It was also extremely difficult to separate any possible time dependent effects relating to the SG phase from those due to small thermal relaxation or to decay of the remnant field in the superconducting magnet.

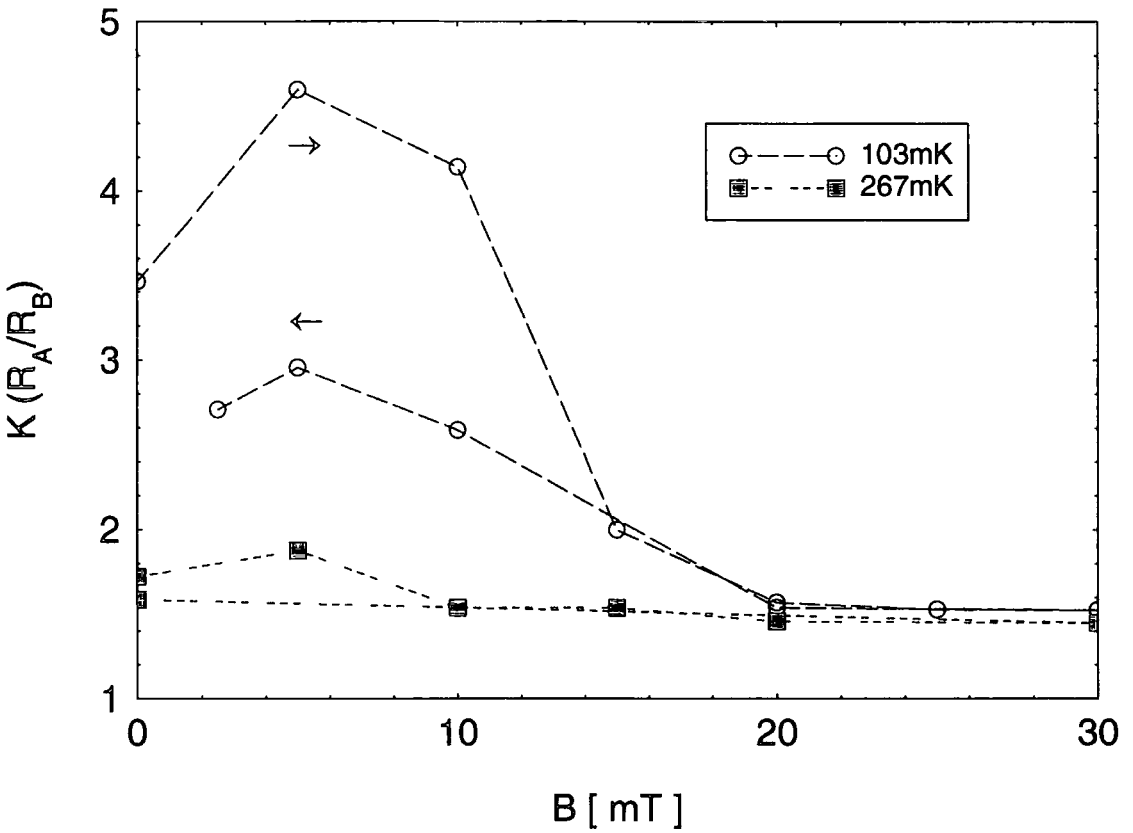

Figure 6.22 - Magnetic field dependence of anisotropy ratio, K, for sample A1 at very low temperatures. Data curves shown are for two different temperatures (above and below T_g) indicated in the figure legend.

Although we have observed no evidence for time dependent effects below T_g, low field magnetoresistance measurements have shown evidence for hysteresis. Data obtained at two different temperatures (above and below the expected value for T_g) are plotted in figure 6.22. Quite clearly at the lowest fields measured and for $T < T_g$ we see hysteresis

present in the anisotropy ratio. These data support the suggestion that the likely origin of the anisotropy is linked to the magnetism of the sample, and in particular the process of spin glass freezing

It should be noted that this anisotropy could have been observed in other systems where a SG phase transition is observed, however the van der Pauw technique is very seldom used. More precisely many workers in this field check for anisotropy in samples at one or at best two temperatures. Frequently, full temperature dependent resistivity measurements are made having samples patterned as Hall bars. In this way a measurement is unable to determine the temperature dependence of the anisotropy, and valuable information relating to the SG phase may be overlooked.

6.6 Magnetoresistance

In this section we shall examine the field dependence of the resistivity at low temperatures for sample A1. Measurements have been made over different field and temperature regions in order to examine in detail the different forms of MR observed in this material.

6.6.1 Magnetoresistance Close to the Metal Insulator Phase Transition

The low field MR of sample A1 at relatively high temperatures ($T > 4.2$ K) has previously been measured by C Leighton [2], we present these data in figure 6.23. It can be seen from the figure that at a temperature of 14 K the resistivity is only weakly dependent on magnetic field up to $B \sim 0.75$ T. This result is in fact generally true for temperatures greater than 14 K, and also for samples having higher Mn concentrations. At lower temperatures a positive MR is observed, the magnitude of which increases with decreasing temperature.

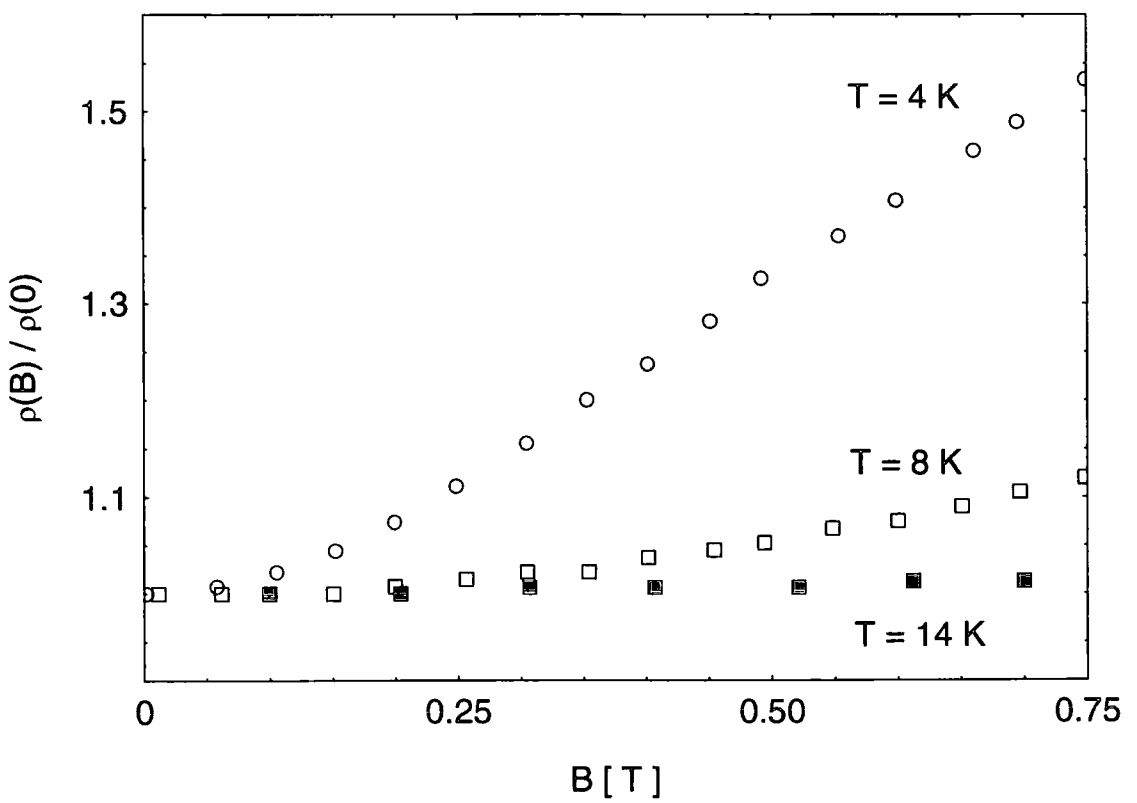

Figure 6.23 - Magnetoresistance of sample A1 at a number of different relatively high temperatures. These measurements presented here were previously carried out by C Leighton [2].

Similar behaviour at low magnetic fields was previously observed by Terry *et al* [27] for an insulating sample of $Cd_{1-x}Mn_xTe$:In having x = 0.1. They were able to obtain quantitative agreement with their experimental data using a model that described the effect of an applied magnetic field on BMPs.

We now turn to examine the data from MR measurements made at lower temperatures and higher magnetic fields.

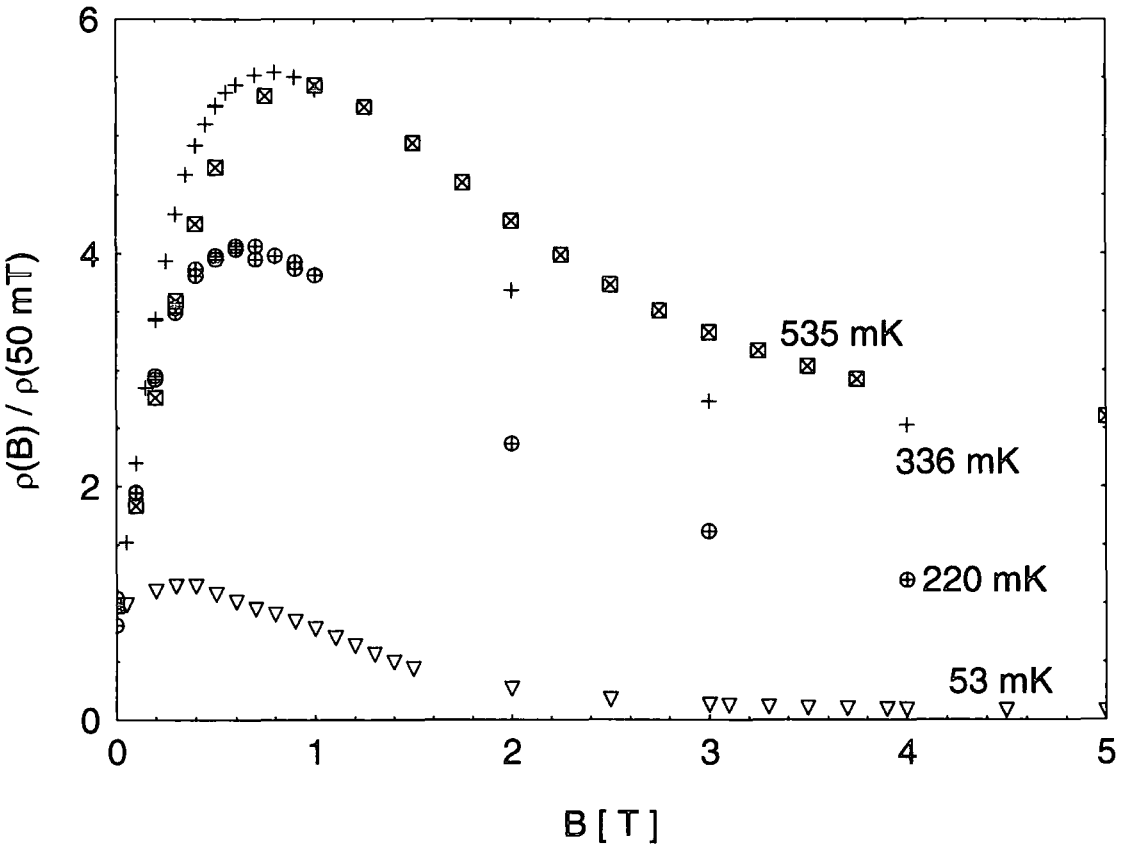

Figure 6.24 - Magnetoresistance of sample A1b at a number of different low temperatures.

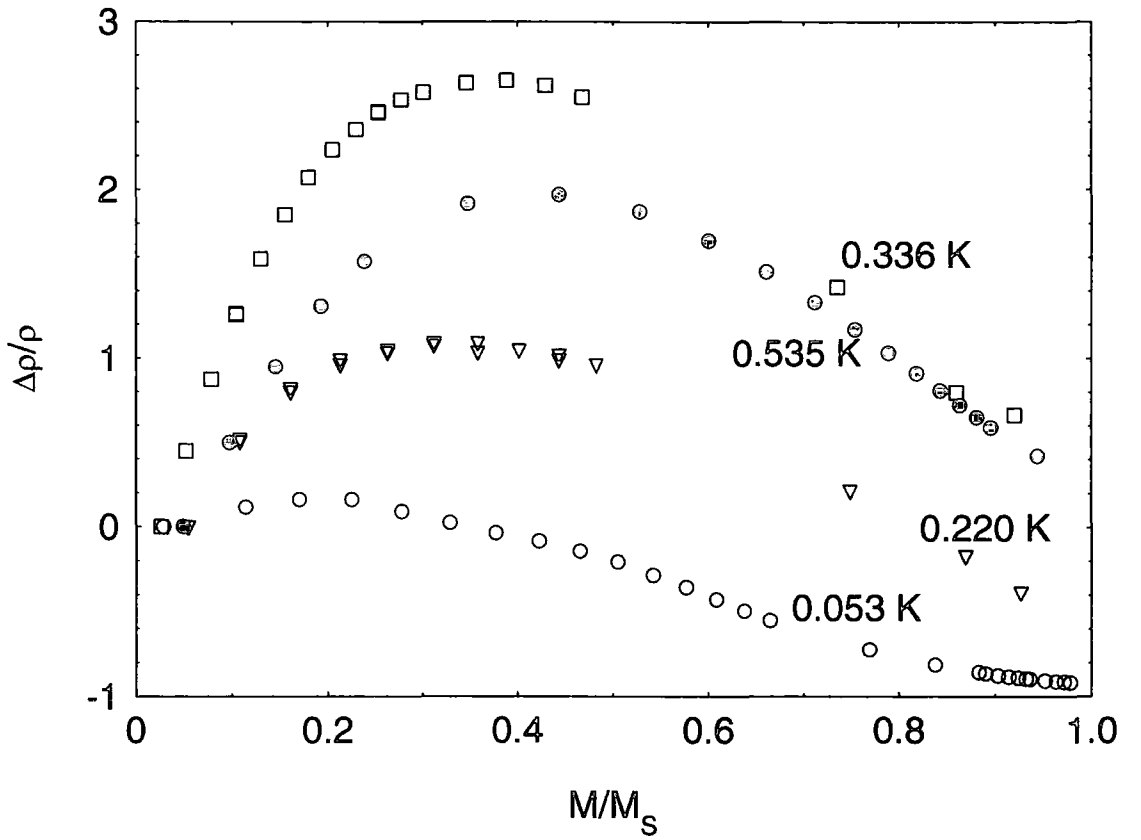

Figure 6.25 - Magnetoresistance of sample A1b at a number of different low temperatures. Data are shown plotted as a function of the magnetization.

Figure 6.24 shows the MR observed at lower temperatures (down to 53 mK) and in higher magnetic fields, up to 5 T. Initially we see an increase in resistivity as the applied magnetic field is increased, with the resistivity reaching a maximum and then decreasing at higher field values. At $T \sim 0.5$ K this maximum occurs at $B \sim 1$ T, on going to lower temperatures the position of this maximum moves to lower fields. Qualitatively similar behaviour has been observed previously by a number of authors, Shapira *et al* in CdMnSe [28-30] and CdMnTe [10]. Dietl *et al* have examined CdMnSe [8, 31] making measurements to temperatures as low as $T \sim 50$ mK. Also measurements on insulating samples of CdMnTe:In by Terry *et al* [27, 32] have shown similar features.

Shapira *et al* [30] found that MR plotted against magnetization resulted in all the curves peaking at approximately the same value of the magnetization. This is not the case for our samples when we use a modified Brillouin function fitted to our experimental susceptibility data ($T > 1.5$ K) to calculate the magnetization (see figure 6.25). From the figure it is clear from our data that the peak in the MR shifts in magnetization as a

function of temperature. With further careful examination of the data from reference [30] a similar shift in the peak of the MR can be observed. Previous work by both von Molnár *et al* [33] and later by Leighton [2] showed similar results from slightly higher temperature measurements made on more insulating samples. In the work of reference [33] an elegant experiment enabled both the magnetoresistance and magnetisation of the sample to be measured simultaneously in the same sample for different illumination levels. This allowed a plot of the MR against the actual measured magnetisation to be obtained. As already noted above they found that the peak in the MR did not fall at the same value of M/M_S for measurements made at different temperatures. It was found that by adjusting the values of M/M_S using a modified Brillouin function (see equation 5.3 section 5.4.2) the peaks in the MR would align, however the values of T_0 determined were lower than those predicted by Gaj *et al* [34]. In addition von Molnár *et al* found that their values of T_0 approached those determined in reference [34] as the carrier density was increased via PPC. These results were attributed to the influence of the local magnetisation experienced by the hopping conduction electrons, where the variation with carrier density results from the n dependence of the electron localisation length.

If we now consider the temperature dependence of the MR peak magnitude in figure 6.25, we can see that this peak height does not change monotonically. From the lowest temperature measured (T = 0.053 K) up to 0.336 K we see an increase in the MR peak height. In the higher temperature data (T = 0.535 K) we see that the MR peak magnitude is again reduced. Although the explanation for this is not clear, it is interesting to note that in this temperature region we are observing the rapid decrease in conductivity, due to the formation of BMP. It is likely that in this temperature region, where the sample crosses from weakly metallic to strongly localised and insulating, the exact mechanism for the MR changes, thus we may expect to see a difference in the relative magnitude of the MR peak, as observed in our experimental data.

Although the general features and shape of the MR appear to be similar in the work described above, closer examination of the data reveals that the magnitudes of the relative changes and other such details depend on the exact sample composition. Many different mechanisms have been invoked, by many different authors, in order to describe the behaviour of samples having a range of Mn concentrations and carrier densities. However, a complete description of the behaviour for samples both on the

metallic and on the insulating side of the MIT is required in order to explain all of the available experimental data. Clearly the important mechanisms relating to MR in DMS at low temperatures are spin disorder scattering, the effects of BMPs and also the redistribution of carriers between spin polarised subbands resulting from the exchange induced splitting of electronic states.

6.6.2 Low Field Negative Magnetoresistance

At very low temperatures (of the order T < 180 mK) we have measured a rather large low field MR. The figures below show this effect at different temperatures both before and after illumination.

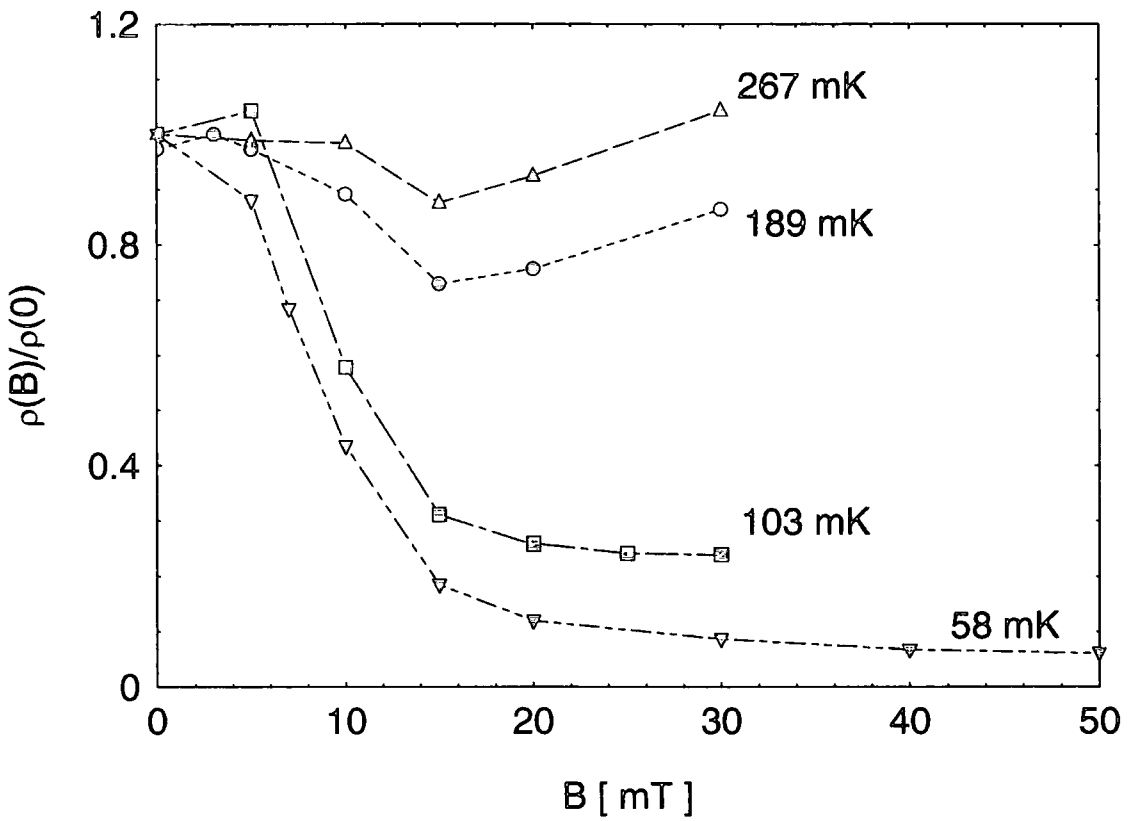

Figure 6.26 - Low field magnetoresistance of sample A1b at a number of different low temperatures prior to illumination.

Figure 6.26 shows the temperature dependence of the low field MR, data are presented for measurements made in very small applied magnetic fields (ie up to a few tens of mT). We see that at a temperature of 267 mK the changes in resistivity are very small for B < 30 mT. At lower temperatures a large negative MR is seen in fields less than

20 mT. The relative magnitude of the negative MR increases as the temperature decreases. This temperature dependence of the MR is again highlighted in figure 6.27 where we plot the temperature dependence of the resistivity for zero field and for an applied field of 50 mT. At this point it is important to make some comment about the zero field data. It should be noted that although every effort was made to minimise the magnetic field experienced by the sample during zero field measurements, due to the nature of our experiment the sample is essentially unshielded from the external influence of stray magnetic fields. Ordinarily such small stray fields would be expected to have very little affect on a measurement. However in our case, where at very low temperatures, we are observing such large changes in resistivity in very small fields it is important to take care to ensure that the field is as close to zero as possible. With this in mind an important technical detail is the remnant field exhibited by the superconducting magnet. All superconducting magnets show some remnant field immediately after the current is reduced to zero. The size of this remnant field is dependent on the field history of the magnet and decreases exponentially with time. For this reason after reduce the current in the magnet to zero it was necessary to wait many hours before a true zero field measurement of the resistivity could be obtained.

In addition to this problem of remnant field in the magnet great care had to be taken in order to rule out any possibility of locally heating the sample and thus producing an apparent negative MR. Examining the data of figure 6.27 we can see that at T = 60 mK in order to produce the same change in resistivity caused by a field of 50 mT we would require the temperature of the sample to increase to 100 mK. A change in temperature of this magnitude is clearly very unlikely and was not seen in the RuO_2 thermometer. In addition heating can occur as the magnetic field is swept due to eddy currents induced by a changing magnetic flux. For this reason measurements of the MR at low temperatures were repeated while varying the rate at which the magnetic field was swept. In all cases the MR measured was the same, ie independent of field sweep rate. For the reasons outlined above we can be very confident that the observed negative MR is a real effect and not just an artefact of our measurement technique.

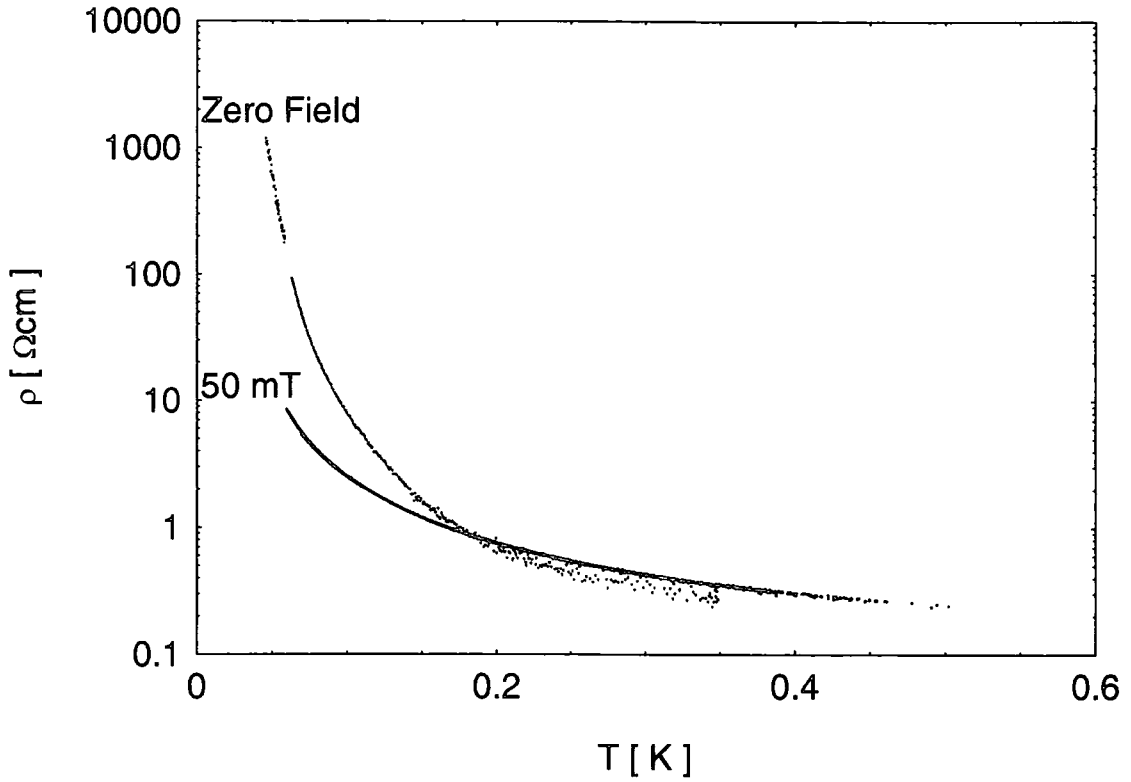

Figure 6.27 – Temperature dependence of low field magnetoresistance for sample A1b at low temperatures. Data are shown at both zero field and in a small applied magnetic field of B = 50 mT.

By examining the temperature dependence of the zero field data shown in figure 6.27 we suggested in section 6.3 that a gap in the DOS is responsible for the observed activated behaviour. This is not observed in an applied field of 50 mT so it seems likely that the gap has a magnetic origin, possibly related to the SG phase as suggested by Oppermann & Rosenow [15]. If the application of a small magnetic field could reduce the size of the gap (ie reduce E_H) then we would expect to observe negative MR as seen in the data presented above

One immediately apparent difficulty with this interpretation can be seen by examining the data of figure 6.26. Here we see that although the negative MR is greatly reduced at high temperatures, it appears that a small negative component persists at very low fields. We observe a small decrease in resistivity up to B ~ 30 mT even at a temperature of 267 mK, that is above the SG freezing temperature expected for a sample having a Mn fraction close to 0.05. As has already been mentioned the situation for a spin-cluster glass could be somewhat different, with the freezing process broadened over some temperature range. In this situation a gap in the DOS of states resulting from spin glass freezing could conceivably evolve from a higher temperature than any measured cusp in the magnetic susceptibility.

In the absence of any measurement of spin glass freezing at these very low temperatures we should offer an alternative interpretation of the experimental data that could result in the observed NMR. Our data shows that in the absence of an activated form for the conductivity, at very low temperatures we see evidence for ES VRH conduction. Previously NMR has been predicted and observed in the hopping conduction regime.

One mechanism for negative MR in the region of VRH has been described by Altshuler & Aronov [20]. Their model was based on a description of the effect of an applied magnetic field on a weakly localised electron. This theory was extended to the VRH regime by considering coherent hops over localised states close to the Fermi energy. At low fields they predicted that,

$$\ln\left[\frac{\rho(B)}{\rho(0)}\right] \propto B^2 \qquad \text{Equation 6.8}$$

Later, it was suggested by Shklovskii & Spivak [35] that this effect would be negligibly small in an insulating sample. They were able to give another description for negative MR in the VRH regime that predicts $\rho(B)/\rho(0)$ would have a linear dependence on the applied field, B.

From experimental data it is often difficult to extract the field dependence of the MR due to the existence of more than one competing mechanism. This is clearly true of our experimental data, where we can see that the observed positive MR is dominant at fields larger than 50 mT. As a result we are left with a very narrow range of fields over which to examine the field dependence. Despite the limitations described above, examination of our low field data suggests that the linear field dependence described in reference [35] is most appropriate.

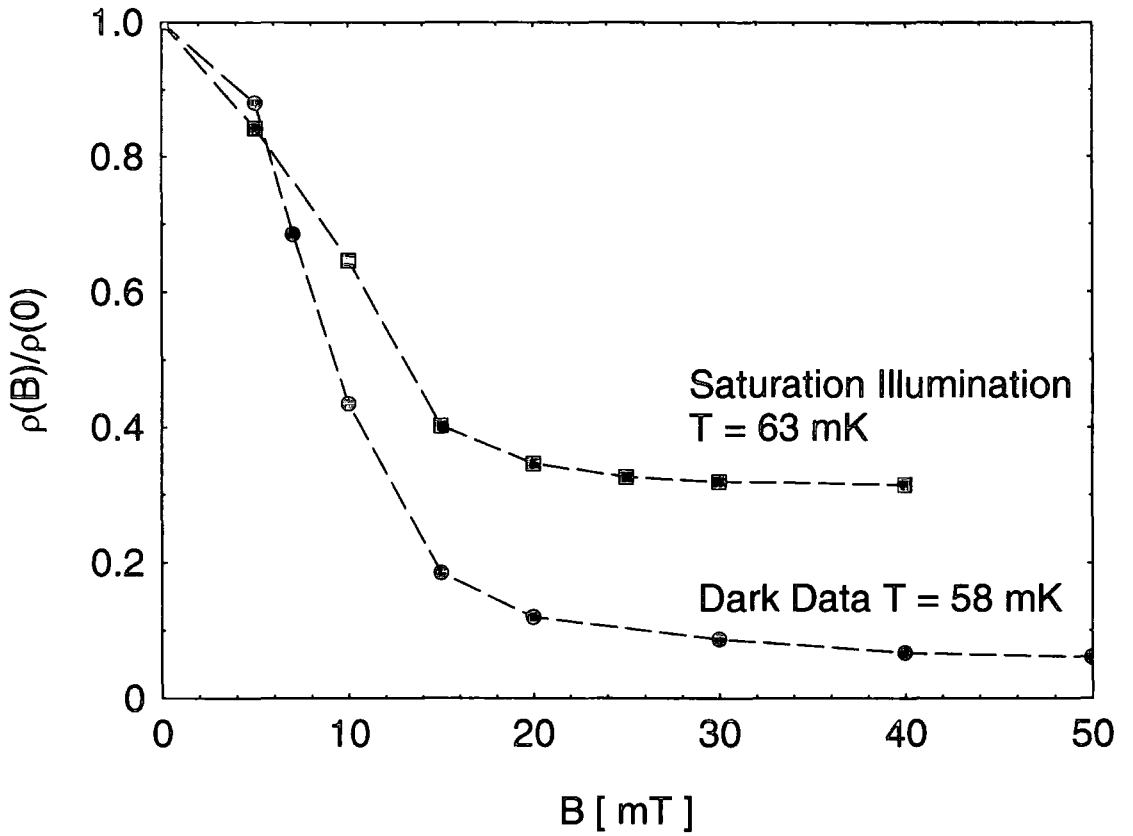

Figure 6.28 - Low field magnetoresistance of sample A1b at low temperatures. Data are shown for this sample both before and after illumination.

Finally in figure 6.28 we show MR data for both the dark and the saturation illumination level. We can see that the negative MR is qualitatively the same, however on increasing the carrier density the magnitude is decreased.

6.7 Summary and Conclusions

In this chapter we have present results of electrical transport measurements as a function of temperature, magnetic field and photogenerated carrier density. Measurements have been carried out on one sample of $Cd_{1-x}Mn_xTe$:In having a Mn concentration close to 5%. We have shown that the data obtained at relatively high temperatures are consistent with previous measurements made on similar samples.

At very low temperatures in zero applied magnetic field the sample has been shown to be an insulator for all obtainable carrier densities. This result is contrary to that expected from previous high temperature measurements and we have suggested that on going to lower temperatures increasingly strong electron localisation occurs due to the formation of BMPs.

It is possible to drive the sample into a metallic state by the application of a magnetic field ($B_c \sim 2$ T for the lowest carrier density prior to illumination). The observed insulator-metal phase transition appear to be described well by the scaling theory of electron localisation with a critical exponent, ν, close to one. On illuminating the sample to saturation and hence achieving the highest obtainable carrier density, we have seen the that IMT is shifted to lower fields ($B_c \sim 1.3$ T for the highest carrier density after illuminating to saturation.)

At low temperatures close to the transition from paramagnetic to spin glass phase we have seen a dramatic change in the resistivity anisotropy ratio. It is suggested that this unusual effect is intimately linked to the process of spin glass freezing.

Magnetoresistance measurements have shown behaviour similar to previous measurements of II-VI DMS close to the MIT, with the exception of a very large negative MR observed at low fields ($B < 50$ mT). It has been suggested that this large low field negative MR is due to effects of magnetic field on electrons in the variable range hopping regime.

6.8 References

1. Leighton, C., I. Terry, and P. Becla, *Persistent photoconductivity at elevated temperatures in $Cd_{1-x}Mn_xTe:In$.* Physical Review B-Condensed Matter, 1997. 56(11): p. 6689-6697.
2. Leighton, C., *Persistent Photoconductivity and the Metal-Insulator Transition in $Cd_{1-x}Mn_xTe:In$*, in *Physics*. 1997, University of Durham.
3. Leighton, C., I. Terry, and P. Becla, *Metallic conductivity near the metal-insulator transition in $Cd_{1-x}Mn_xTe$.* Physical Review B, 1998. 58(15): p. 9773-9782.
4. Ridley, B.K., *Quantum Processes in Semiconductors*. Third ed. 1993, Oxford: Clarendon Press.
5. Erginsoy, C., Phys. Rev., 1950. 79: p. 1013.
6. Dietl, T., *et al.*, *Interaction Effects Near the Metal-Insulator Transition in Semimagnetic Semiconductors*, in *Anderson Localization*, T. Ando and H. Fukuyama, Editors. 1987, Springer-Verlag. p. 58.
7. Read, D.E., *et al.*, *Conductivity of Weakly Metallic CdMnTe and the Influence of Bound Magnetic Polarons at Low Temperatures.* Annalen der Physik, 1999. 8(Special Issue): p. SI217-SI220.
8. Sawicki, M., *et al.*, *Influence of s-d Exchange Interaction On the Conductivity of $Cd_{1-x}Mn_xSe:In$ in the Weakly Localized Regime.* Physical Review Letters, 1986. 56(5): p. 508-511.
9. Leighton, C., I. Terry, and P. Becla, *Metal-insulator transition in the persistent photoconductor $Cd_{1-x}Mn_xTe:In$.* Europhysics Letters, 1998. 42(1): p. 67-72.
10. Shapira, Y., *et al.*, *Magnetoresistance and Hall-Effect Near the Metal-Insulator-Transition of n-Type $Cd_{0.95}Mn_{0.05}Te$.* Physical Review B-Condensed Matter, 1990. 41(9): p. 5931-5941.
11. Terry, I., *et al.*, *Magnetic-Field Dependence of the Dielectric-Constant in $Cd_{1-x}Mn_xTe:In$ On Approaching the Insulator-to-Metal Transition.* Philosophical Magazine B-Physics of Condensed Matter Statistical Mechanics Electronic Optical and Magnetic Properties, 1992. 65(6): p. 1245-1254.

12. Terry, I., T. Penney, and S. Vonmolnar, *Low-Temperature Transport-Properties of $Cd_{0.91}Mn_{0.09}Te$:In and Evidence For a Magnetic Hard Gap in the Density of States.* Physical Review Letters, 1992. 69(12): p. 1800-1803.

13. Dai, P.H., Y.Z. Zhang, and M.P. Sarachik, *Low-Temperature Transport in the Hopping Regime - Evidence For Correlations Due to Exchange.* Physical Review Letters, 1992. 69(12): p. 1804-1806.

14. Yakimov, A.I., *et al.*, *Magnetic Correlations On the Insulating Side of the Metal- Insulator-Transition in Amorphous $Si_{1-x}Mn_x$.* Physical Review B-Condensed Matter, 1995. 51(23): p. 16549-16552.

15. Oppermann, R. and B. Rosenow, *Magnetic gaps related to spin glass order in fermionic systems.* Physical Review Letters, 1998. 80(21): p. 4767-4770.

16. Novak, M.A., *et al.*, *Spin-Glass Behavior of $Cd_{1-x}Mn_xTe$ Below the Nearest-Neighbor Percolation Limit.* Journal of Applied Physics, 1985. 57(8): p. 3418-3420.

17. von Molnar, S., *et al.*, *Electron Localization in a Magnetic Semiconductor - $Gd_{3-x}v_xS4$.* Physical Review Letters, 1983. 51(8): p. 706-709.

18. Wojtowicz, T., *et al.*, *Metal-Insulator-Transition in Semimagnetic Semiconductors.* Physical Review Letters, 1986. 56(22): p. 2419-2422.

19. Teizer, W., F. Hellman, and R.C. Dynes, *Magnetic field induced insulator to metal transition in amorphous-Gd_xSi_{1-x}.* Solid State Communications, 2000. 114(2): p. 81-86.

20. Altshuler, B.L. and A.G. Aronov, *Electron-Electron Interaction in Disordered Conductors*, in *Electron-Electron Interactions in Disordered Systems*, A.L. Efros and M. Pollak, Editors. 1985, North-Holland: Amsterdam.

21. von Molnar, S., *et al.*, *The Metal-Insulator Transition in Magnetic Semiconductors - Transport in $Gd_{3-x}v_xS4$.* Solid-State Electronics, 1985. 28(1-2): p. 127-130.

22. Dai, P.H., Y.Z. Zhang, and M.P. Sarachik, *Electrical-Conductivity of Metallic Si-B Near the Metal- Insulator-Transition.* Physical Review B-Condensed Matter, 1992. 45(8): p. 3984-3994.

23. Katsumoto, S., *et al.*, *Fine Tuning of Metal-Insulator-Transition in $Al_{0.3}Ga_{0.7}As$ Using Persistent Photoconductivity.* Journal of the Physical Society of Japan, 1987. 56(7): p. 2259-2262.

24. Dietl, T., *et al.*, *Remarks On Localization in Semimagnetic Semiconductors.* Physica Scripta, 1986. T14: p. 29-36.

25. Washburn, S., *et al.*, *Absence of Minimum Metallic Conductivity in $Gd_{(3-x)}V_xS_4$ At Very Low-Temperature and Evidence For a Coulomb Gap.* Physical Review B-Condensed Matter, 1984. 30(10): p. 6224-6226.

26. Shklovskii, B.I. and A.L. Efros, *Electronic Properties of Doped Semiconductors.* 1984, Berlin: Springer-Verlag.

27. Terry, I., *et al.*, *Low temperature magnetoresistance of the persistent photoconductor $Cd_{0.9}Mn_{0.1}Te$:In.* Journal of Crystal Growth, 1996. 159(1-4): p. 1070-1074.

28. Shapira, Y., *et al.*, *Magnetoresistance of $Cd_{1-x}Mn_xSe$ Near the Mott Transition.* Journal of Applied Physics, 1985. 57(8): p. 3210-3212.

29. Shapira, Y., *et al.*, *Magnetoresistance Near the Metal-Insulator-Transition of $Cd_{0.99}Mn_{0.01}Se$.* Solid State Communications, 1985. 54(7): p. 593-596.

30. Shapira, Y., *et al.*, *Magnetoresistance and Hall-Effect Near the Metal-Insulator-Transition of $Cd_{1-x}Mn_xSe$.* Physical Review B-Condensed Matter, 1986. 34(6): p. 4187-4198.

31. Dietl, T., J. Antoszewski, and L. Swierkowski, *Hopping Conduction of the Bound Magnetic Polarons in n-CdMnSe.* Physica B & C, 1983. 117(MAR): p. 491-493.

32. von Molnar, S., *et al.*, *Local Magnetization and Magnetotransport in Magnetic Semiconductors.* Physica B, 1994. 197(1-4): p. 151-157.

33. von Molnar, S., *et al.*, *Localization and the Insulator Metal Transition in Magnetic Semiconductors.* Institute of Physics Conference Series, 1991(108): p. 29-39.

34. Gaj, J.A., R. Planel, and G. Fishman, *Relation of Magneto-optical Properties of Free Excitons to Spin Alignment of Mn^{2+} Ions in $Cd_{1-x}Mn_xTe$.* Solid State Comm, 1979. 29: p. 435-438.

35. Shklovskii, B.I. and B.Z. Spivak, *Scattering and Interference Effects in VRH Conduction*, in *Hopping transport in solids*, M. Pollak and B.I. Shklovskii, Editors. 1991, Elsevier: Amsterdam. p. 308.

7 Conclusions

7.1 Concluding Remarks

Both electrical transport and magnetic measurements have been made on a number of samples of the dilute magnetic semiconductor CdMnTe:In. The samples studied were measured to have manganese concentrations in the range $0.044 < x < 0.197$. Measurements have been made over a large temperature range ($300\ K > T > 40\ mK$). In general the results from high temperature measurements made have been consistent with previous measurements, whereas at the lower temperatures a number of new and original results have been obtained.

Magnetic measurements made at relatively high temperatures ($T > 4.2\ K$) and presented in section 5.3 represent the first study of highly doped samples of CdMnTe, and these are in good agreement with previous measurements for nominally undoped samples. At lower temperatures many samples have shown a transition from a paramagnetic to a spin glass phase. High sensitivity measurements have been made in very small magnetic fields using a custom designed and constructed SQUID susceptometer. The dependence of the spin glass freezing temperature on Mn fraction has been measured and compared to the limited amount of previous data available for undoped samples. The form of the magnetic susceptibility close to the spin glass freezing temperature has been shown to be consistent with a spin-cluster glass model.

At low temperatures photo-induced changes in magnetism have been measured in two different samples. These measurements have been made both in the paramagnetic phase and in the spin glass phase. These observed photo-induced changes have been attributed to the formation of bound magnetic polarons around quasi-localized s electron spins. In the spin glass phase, compared with the paramagnetic phase, the temperature dependence of the polaron susceptibility has been shown to be weaker. This result is in agreement with previous theoretical work describing the properties of magnetic polarons in a spin glass regime.

By illuminating at low temperatures, thereby increasing the free electron density, the number of neutral shallow donors and hence the number of bound magnetic polarons,

we have seen an increase in the spin glass freezing temperature. In addition to this increase we have shown that at higher carrier densities the transition is somewhat broadened.

Results of electrical transport measurements made as a function of temperature, magnetic field and photogenerated carrier density have been presented in chapter 6. These measurements have focused on one sample of $Cd_{1-x}Mn_xTe$:In having a Mn concentration $x = 0.047$. We have shown that the data obtained at relatively high temperatures are consistent with previous measurements made on similar samples.
Contrary to these previous measurements, at very low temperatures in zero applied magnetic field the sample has been shown to be an insulator for all obtainable carrier densities. This result suggests that we are observing some form of strongly temperature dependent localisation. It is suggested that this strong electron localisation on reducing the temperature occurs due to the formation of increasing numbers of bound magnetic polarons. This results in an increased spin disorder scattering rate and hence a temperature dependent localisation.

As a result of the application of a magnetic field at very low temperatures we have observed an insulator metal phase transition. The critical field for this transition was measured to be $B_c \sim 2$ T (for the lowest carrier density) prior to illumination. The observed insulator-metal phase transition appears to be described well by the scaling theory of electron localisation with a critical exponent, ν, close to unity. At higher photogenerated carrier densities we have observed a lower critical field. As a result of changing the position of the Fermi energy relative to the mobility edge. In this way we have used two independent parameters to tune the metal insulator transition in a single sample of a dilute magnetic system.

Analysis of the temperature dependence of the conductivity has shown both an activated form and a form consistent with Efros-Shklovskii variable range hopping. It has been shown that the activated conduction seen in zero applied magnetic fields can be suppressed by the application of a very small magnetic field ($B \sim 50$ mT)

At low temperatures close to the transition from paramagnetic to spin glass phase we have seen a dramatic change in the anisotropy ratio. This effect has not previously been observed in measurements made on magnetic systems in the spin glass phase. We

suggest that although the effect could be present in a number of similar material systems, the tendency for measurements to be made using samples in the Hall geometry could have resulted in previous studies failing to observe such a phenomena. Although the origin of the anisotropy has not been determined with complete certainty, it seems likely that it arises as a result of the process of spin glass freezing.

Magnetoresistance measurements at relatively high temperatures have shown behaviour consistent with previous measurements of II-VI DMS close to the metal insulator transition. A complete understanding of all the available experimental data (for samples on both side of the metal insulator transition) is not currently available.
At lower temperatures a very large negative MR is observed at low fields ($B < 50$ mT). It is suggested that this could be due to a hard gap in the density of states with a magnetic origin, resulting from a spin glass like phase. Alternatively a similar negative magnetoresistance could arise from a mechanism relating to hopping conduction. Further experimental work would be required in order to determine unambiguously the physics behind the observed low field negative magnetoresistance.

7.2 Future Work

Due to the extreme complexity of the problem, a subject that has previously received little attention is the nature of bound magnetic polarons within a spin glass phase. In particular the dynamics of such entities (which clearly play a crucial role in the low temperature transport) could benefit from further experimental or theoretical study.

In order to correlate directly the observed anisotropy and the spin glass freezing temperature magnetic measurements on samples with very low manganese concentration (hence, $T_g < 300$ mK) would be of great importance. We have observed the strong temperature dependent anisotropy in two samples cut from the same crystal, however measurements made on samples with slightly differing SG freezing temperatures would clearly add weight to this interpretation. In addition to this field dependent magnetization measurements made at low temperatures would be of interest in trying to obtain a more quantitative picture of the measured magnetoresistance.

Appendix A

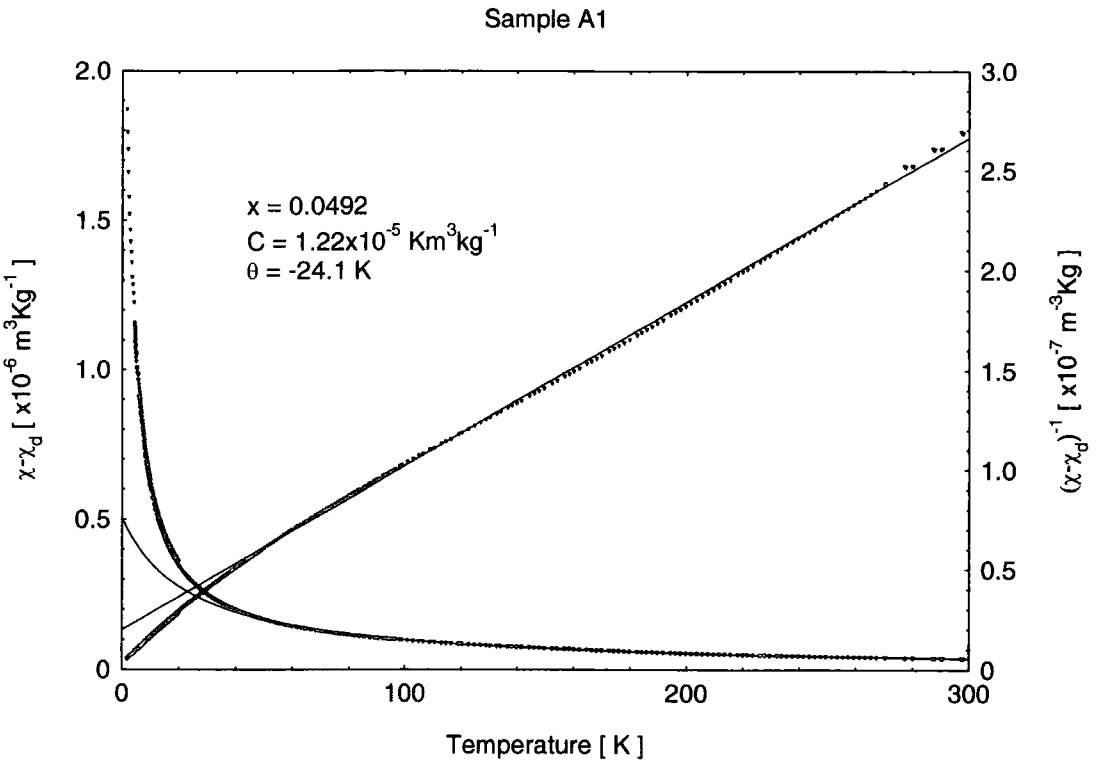

Figure A.1 – Magnetic susceptibility and inverse susceptibility as a function of temperature. For sample A1, x = 0.0492, measuring fields B = 10 mT & B = 100 mT. Plot shows experimental data and fits to Curie-Weiss law used to obtain values for C and θ.

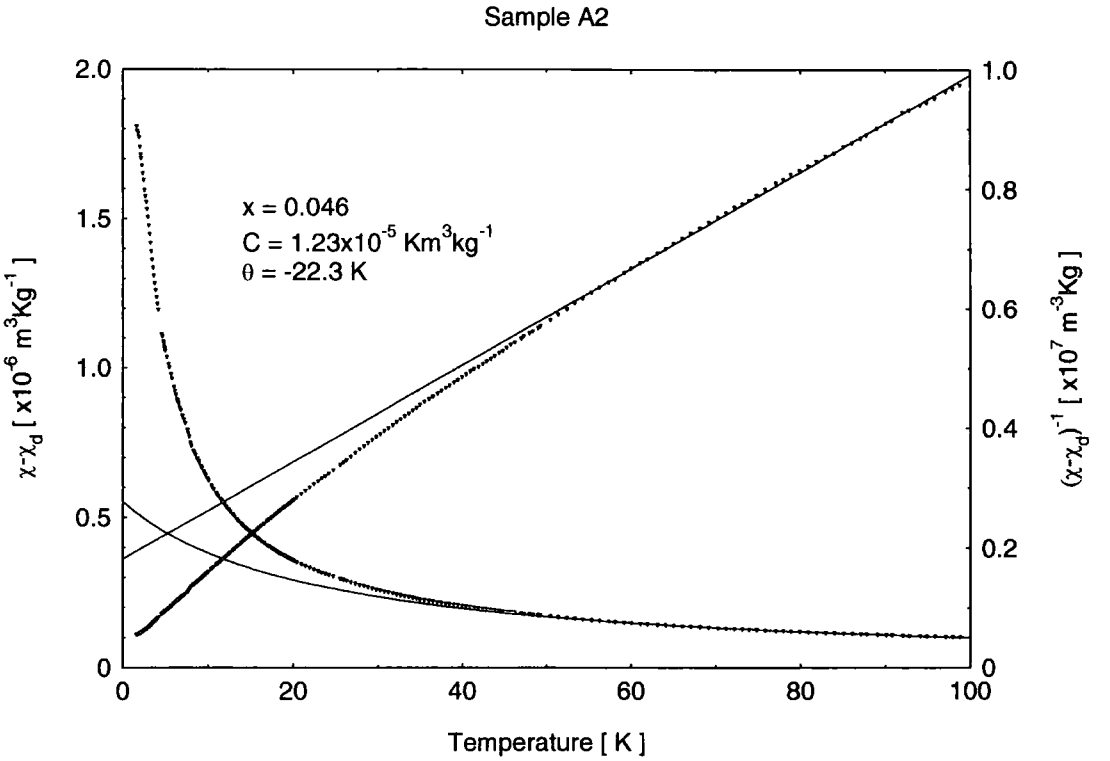

Figure A.2 – Magnetic susceptibility and inverse susceptibility as a function of temperature. For sample A2, x = 0.046, measuring field B = 10 mT. Plot shows experimental data and fits to Curie-Weiss law used to obtain values for C and θ.

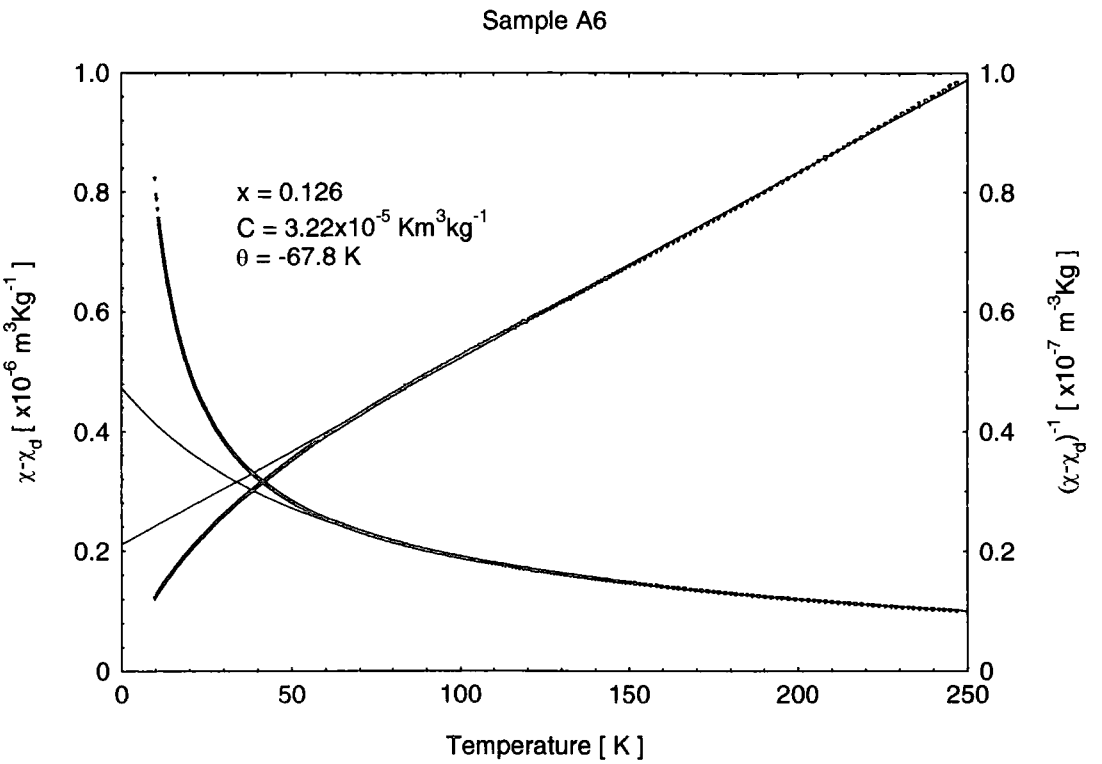

Figure A.3 – Magnetic susceptibility and inverse susceptibility as a function of temperature. For sample A6, x = 0.126, measuring field B = 50 mT. Plot shows experimental data and fits to Curie-Weiss law used to obtain values for C and θ.

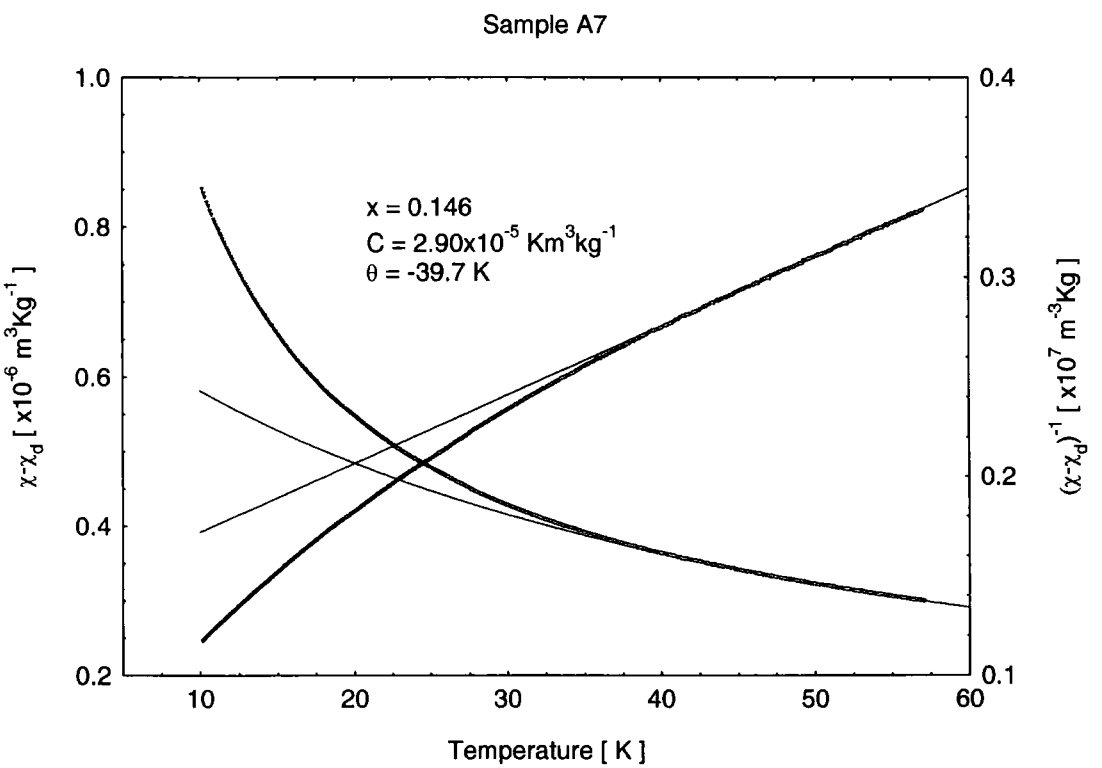

Figure A.4 – Magnetic susceptibility and inverse susceptibility as a function of temperature. For sample A7, x = 0.146, measuring field B = 50 mT. Plot shows experimental data and fits to Curie-Weiss law used to obtain values for C and θ.

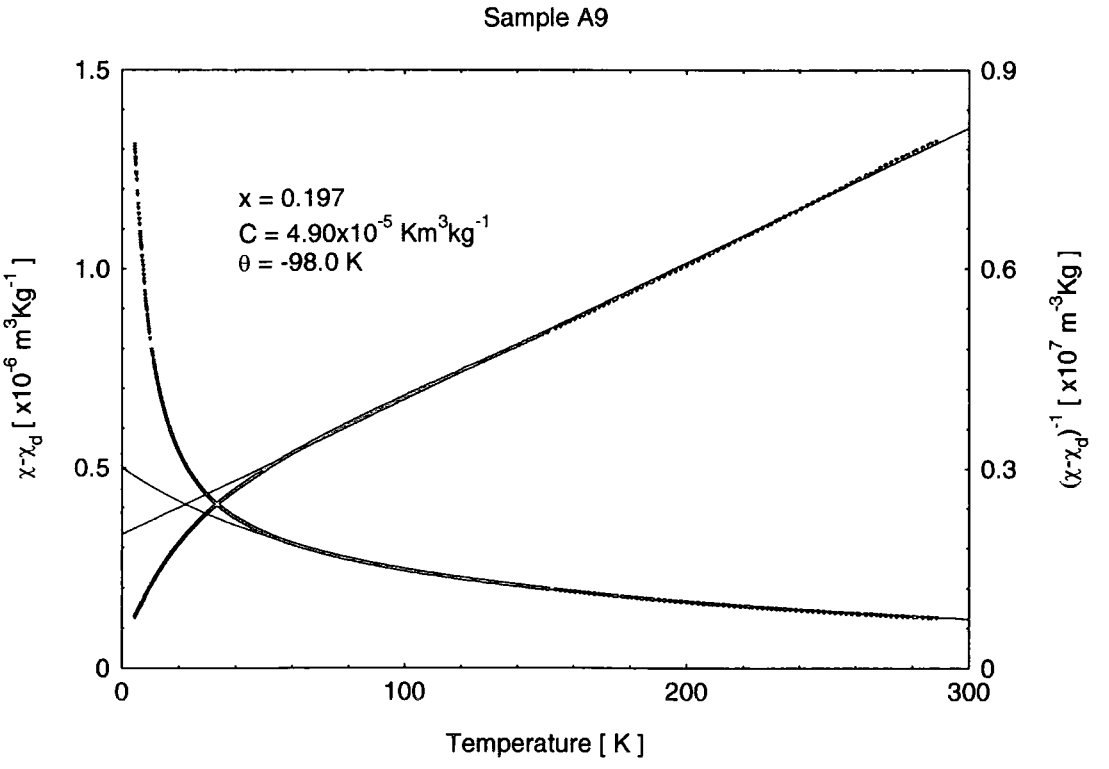

Figure A.5 – Magnetic susceptibility and inverse susceptibility as a function of temperature. For sample A9, x = 0.197, measuring field B = 50 mT. Plot shows experimental data and fits to Curie-Weiss law used to obtain values for C and θ.

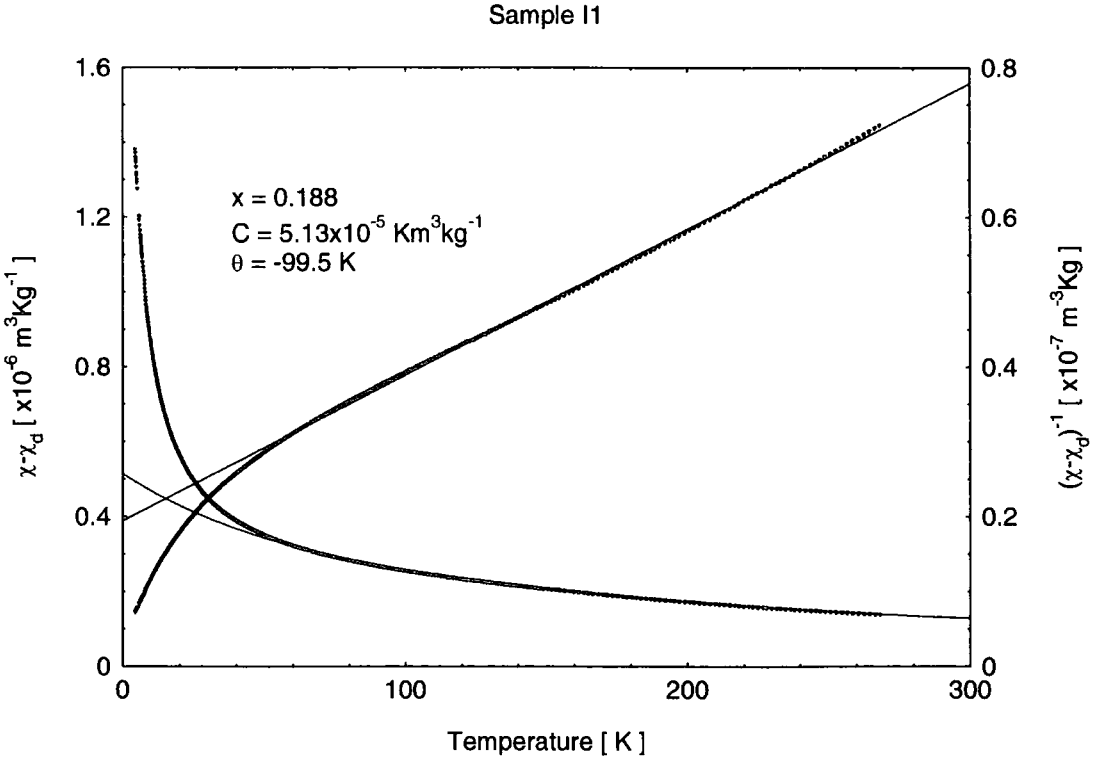

Figure A.6 – Magnetic susceptibility and inverse susceptibility as a function of temperature. For sample I1, x = 0.188, measuring field B = 50 mT. Plot shows experimental data and fits to Curie-Weiss law used to obtain values for C and θ.

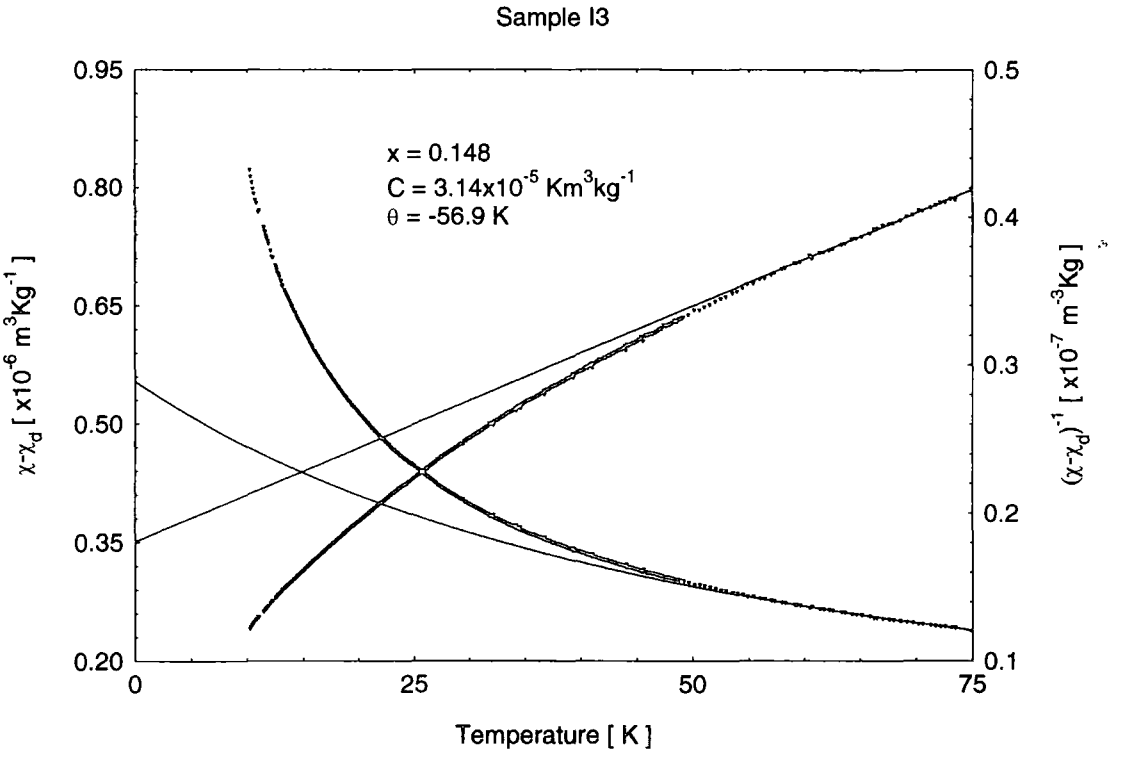

Figure A.7 – Magnetic susceptibility and inverse susceptibility as a function of temperature. For sample I3, x = 0.148, measuring fields B = 50 mT & B = 15 mT. Plot shows experimental data and fits to Curie-Weiss law used to obtain values for C and θ.

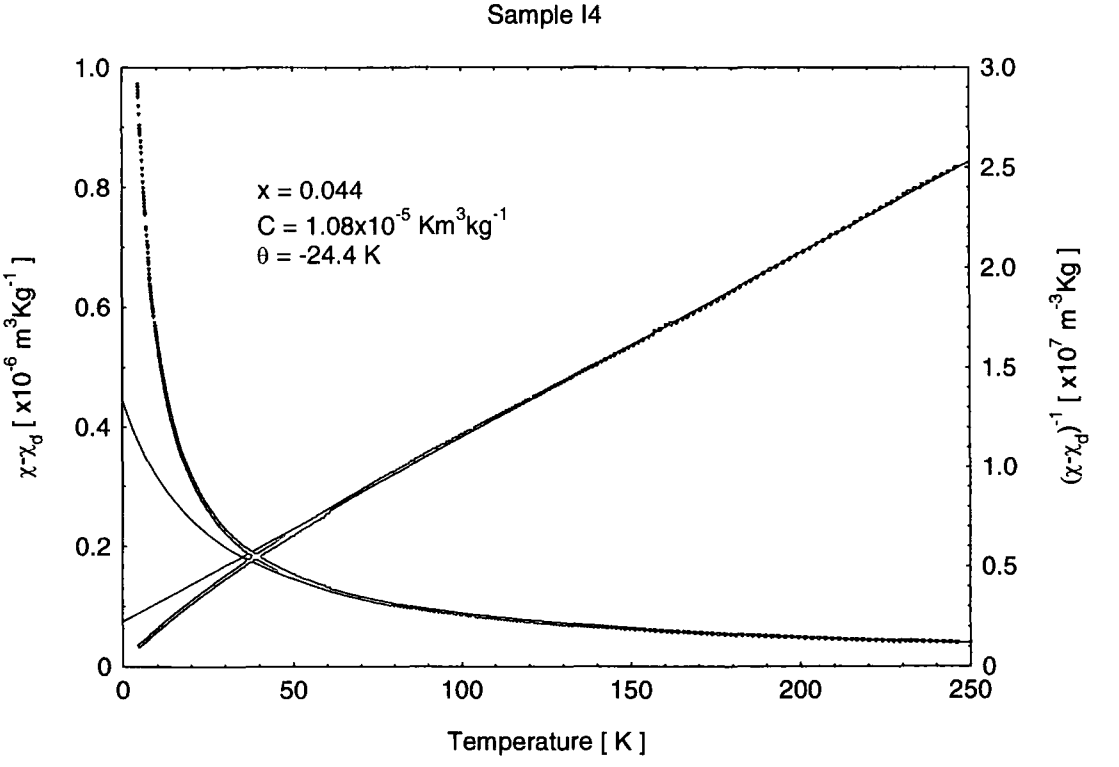

Figure A.8 – Magnetic susceptibility and inverse susceptibility as a function of temperature. For sample I4, x = 0.044, measuring fields B = 1 mT & B = 10 mT. Plot shows experimental data and fits to Curie-Weiss law used to obtain values for C and θ.